

REPORT DOCUMENTATION PAGE

Public reporting burden for this collection of information is estimated to average 1 hour per response, including and maintaining the data needed, and completing and reviewing the collection of information. Send comments, including suggestions for reducing this burden, to Washington Headquarters Services, Directorate for Information Operations and Reports, 1204, Arlington, VA 22202-4302, and to the Office of Management and Budget, Paperwork Reduction Project (0

AFRL-SR-BL-TR-98-

0799

athering
action of
y, Suite

1. AGENCY USE ONLY (Leave Blank)		2. REPORT DATE November, 1994		3. REPC Final	
4. TITLE AND SUBTITLE USAF Summer Research Program - 1993 Summer Research Extension Program Final Reports, Volume 5, AEDC, FJSRL, and WHMC				5. FUNDING NUMBERS	
6. AUTHORS Gary Moore					
7. PERFORMING ORGANIZATION NAME(S) AND ADDRESS(ES) Research and Development Labs, Culver City, CA				8. PERFORMING ORGANIZATION REPORT NUMBER	
9. SPONSORING/MONITORING AGENCY NAME(S) AND ADDRESS(ES) AFOSR/NI 4040 Fairfax Dr, Suite 500 Arlington, VA 22203-1613				10. SPONSORING/MONITORING AGENCY REPORT NUMBER	
11. SUPPLEMENTARY NOTES Contract Number: F4962-90-C-0076					
12a. DISTRIBUTION AVAILABILITY STATEMENT Approved for Public Release				12b. DISTRIBUTION CODE	
13. ABSTRACT (Maximum 200 words) The purpose of this program is to develop the basis for continuing research of interest to the Air Force at the institution of the faculty member; to stimulate continuing relations among faculty members and professional peers in the Air Force to enhance the research interests and capabilities of scientific and engineering educators; and to provide follow-on funding for research of particular promise that was started at an Air Force laboratory under the Summer Faculty Research Program. Each participant provided a report of their research, and these reports are consolidated into this annual report.					
14. SUBJECT TERMS AIR FORCE RESEARCH, AIR FORCE, ENGINEERING, LABORATORIES, REPORTS, UNIVERSITIES				15. NUMBER OF PAGES	
				16. PRICE CODE	
17. SECURITY CLASSIFICATION OF REPORT Unclassified	18. SECURITY CLASSIFICATION OF THIS PAGE Unclassified	19. SECURITY CLASSIFICATION OF ABSTRACT Unclassified	20. LIMITATION OF ABSTRACT UL		

UNITED STATES AIR FORCE
SUMMER RESEARCH PROGRAM -- 1993
SUMMER RESEARCH EXTENSION PROGRAM FINAL REPORTS

VOLUME 5

ARNOLD ENGINEERING DEVELOPMENT CENTER
FRANK J. SEILER RESEARCH LABORATORY
WILFORD HALL MEDICAL CENTER

RESEARCH & DEVELOPMENT LABORATORIES

5800 Uplander Way
Culver City, CA 90230-6608

Program Director, RDL
Gary Moore

Program Manager, AFOSR
Major David Hart

Program Manager, RDL
Scott Licoscas

Program Administrator, RDL
Gwendolyn Smith

Program Administrator, RDL
Johnetta Thompson

Submitted to:

AIR FORCE OFFICE OF SCIENTIFIC RESEARCH
Bolling Air Force Base
Washington, D.C.
November 1994

19981215 114

PREFACE

This volume is part of a five-volume set that summarizes the research of participants in the 1993 AFOSR Summer Research Extension Program (SREP). The current volume, Volume 5 of 5, presents the final reports of SREP participants at Arnold Engineering Development Center, Frank J. Seiler Research Laboratory and Wilford Hall Medical Center.

Reports presented in this volume are arranged alphabetically by author and are numbered consecutively -- e.g., 1-1, 1-2, 1-3; 2-1, 2-2, 2-3, with each series of reports preceded by a 35 page management summary. Reports in the five-volume set are organized as follows:

VOLUME	TITLE
1A	Armstrong Laboratory (part one)
1B	Armstrong Laboratory (part two)
2	Phillips Laboratory
3	Rome Laboratory
4A	Wright Laboratory (part one)
4B	Wright Laboratory (part two)
5	Arnold Engineering Development Center Frank J. Seiler Research Laboratory Wilford Hall Medical Center

1993 SREP FINAL REPORTS

Armstrong Laboratory

VOLUME 1A

Report #	Report Title Author's University	Report Author
1	Three-Dimensional Calculation of Blood Flow in a Thick -Walled Vessel Using the University of Missouri, Rolla, MO	Dr. Xavier Avula Mechanical & Aerospace AL/AO Engineering
2	A Study of the Contrast Detection Modeling for Human Eye and its Application to Wright State University, Dayton, OH	Dr. Jer-sen Chen Computer Science & AL/CF Engineering
3	An Approach to On-Line Assessment and Diagnosis of Student Troubleshooting Knowl New Mexico State University, Las Cruces, NM	Dr. Nancy Cooke Psychology AL/HR
4	An Experimental Investigation of Hand Torque Strength for Tightening Small Fast Tennessee Technological University, Cookeville, TN	Dr. Subramaniam Deivanayagam Industrial Engineering AL/HR
5	Determination of Total Peripheral Resistance, Arterial Compliance and Venous Com North Dakota State University, Fargo, ND	Dr. Dan Ewert Electrical Engineering AL/AO
6	A Computational Thermal Model and Theoretical Thermodynamic Model of Laser Induc Florida International University, Miami, FL	Dr. Bernard Gerstman Physics AL/OE
7	A Comparison of Various Estimators of Half-Life in the Air Force Health Study University of Maine, Orono, ME	Dr. Pushpa Gupta Mathematics AL/AO
8	The Effects of Exogenous Melatonin on Fatigue, Performance and Daytime Sleep Bowling Green State University, Bowling Green, OH	Mr. Rod Hughes Psychology AL/CF
9	A New Protocol for Studying Carotid Baroreceptor Function Georgia Institute of Technology, Atlanta, GA	Dr. Arthur Koblasz Civil Engineering AL/AO
10	Adaptive Control Architecture for Teleoperated Freflex System Purdue University, West Lafayette, IN	Dr. A. Koivo Electrical Engineering AL/CF
11	A New Construct for Interpreting the Fundamental Dilemma of Insufficient Tissue University of Tennessee, Memphis, TN	Dr. Robert Kundich Biomedical Engineering AL/CF
12	An Empirical Test of a Method for Comparison of Alternative Multiship Aircraft Arizona State University, Tempe, AZ	Dr. William Moor Industrial & Management AL/HR Engineering
13	Remote Monitoring and Reduction of Emotionality in Air Force Laboratory Primates University of Georgia Research, Athens, GA	Dr. B. Mulligan Psychology AL/OE

1993 SREP FINAL REPORTS

Armstrong Laboratory

VOLUME 1B

Report #	Report Title Author's University	Report Author
14	Simulation of the Motion of Single and Linked Ellipsoids Representing Human Body Wright State University, Dayton, OH	Dr. David Reynolds Biomedical & Human AL/CF Factors
15	Bioeffects of Microwave Radiation on Mammalian Cells and Cell Cultures Xavier University of Louisiana, New Orleans, LA	Dr. Donald Robinson Chemistry AL/OE
16	Analysis of Isocyanate Monomers and Oligomers in Spray Paint Formulations Southwest Texas State University, San Marcos, TX	Dr. Walter Rudzinski Chemistry AL/OE
17	Development of the "Next Generation" of the Activities Interest Inventory for Se Wayne State University, Detroit, MI	Dr. Lois Tetrick Industrial Relations Prog AL/HR
18	Investigations on the Seasonal Bionomics of the Asian Tiger Mosquito, Aedes Albo Macon College, Macon, GA	Dr. Michael Womack Natural Science and AL/OE Mathematics
19	Difficulty Facets Underlying Cognitive Ability Test Items Ohio State University, Columbus, OH	Dr. Mary Roznowski Psychology AL/HR
20	A Simplified Model for Predicting Jet Impingement Heat Transfer North Carolina A & T State University, Greensboro, NC	Mr. Mark Kitchart Mechanical Engineering AL/EQ
21	Geostatistical Techniques for Understanding Hydraulic Conductivity Variability Washington State University, Pullman, WA	Dr. Valipuram Manoranjan Pure and Applied AL/EQ Mathematics
22	An Immobilized Cell Fluidized Bed Bioreactor for 2,4-Dinitrotoluene Degradation Colorado State University, Fort Collins, CO	Dr. Kenneth Reardon Agricultural and Chemical AL/EQ Engineering
23	Applications of Superconductive Devices in Air Force Alfred University, Alfred, NY	Dr. Xingwu Wang Electrical Engineering AL/EQ

1993 SREP FINAL REPORTS

Phillips Laboratory

VOLUME 2

Report #	Report Title Author's University	Report Author
1	Optimal Passive Damping of a Complex Strut-Built Structure Iowa State University, Ames, IA	Dr. Joseph Baumgarten Mechanical Engineering PL/VT
2	Theoretical and Experimental Studies on the Effects of Low-Energy X-Rays on Elec University of Arizona, Tucson, AZ	Dr. Raymond Bellem Electrical & Computer Engineering PL/VT
3	Ultrawideband Antennas with Low Dispersion for Impulse Radars University of Alabama, Huntsville, AL	Dr. Albert Biggs Electrical Engineering PL/WS
4	Experimental Neutron Scattering Investigations of Liquid-Crystal Polymers Arkansas Technology University, Russellville, AR	Dr. David Elliott Engineering PL/RK
5	High Temperature Spectroscopy of Alkali Metal Vapors for Solar to Thermal Energy University of Iowa, Iowa City, IA	Mr. Paul Erdman Physics and Astronomy PL/RK
6	A Detailed Investigation of Low-and High-Power Arcjet Plume Velocity Profiles Us University of Southern California, Los Angeles, CA	Dr. Daniel Erwin Aerospace Engineering PL/RK
7	Measurements of Ion-Molecule Reactions at High Temperatures University of Puerto Rico, Mayaguez, PR	Dr. Jeffrey Friedman Physics PL/GP
8	Final Design and Construction of Lidar Receiver for the Starfire Optical Range Georgia Institute of Technology, Atlanta, GA	Dr. Gary Gimmestad Research Institute PL/LI
9	Dynamics of Gas-Phase Ion-Molecule Reactions Carnegie Mellon University, Pittsburgh, PA	Dr. Susan Graul Chemistry PL/WS
10	A Numerical Approach to Evaluating Phase Change Material Performance in Infrared University of Texas, San Antonio, TX	Mr. Steven Griffin Engineering PL/VT
11	An Analysis of ISAR Imaging and Image Simulation Technologies and Related Post University of Nevada, Reno, NV	Dr. James Henson Electrical Engineering PL/WS
12	Optical and Clear Air Turbulence Worcester Polytechnic Institut, Worcester, MA	Dr. Mayer Humi Mathematics PL/LI
13	Rotational Dynamics of Lageos Satellite North Carolina State University, Raleigh, NC	Dr. Arkady Kheyfets Mathematics PL/LI
14	Study of Instabilities Excited by Powerful HF Waves for Efficient Generation of Polytechnic University, Farmingdale, NY	Dr. Spencer Kuo Electrical Engineering PL/GP

1993 SREP FINAL REPORTS

Phillips Laboratory

VOLUME 2 cont'd

Report #	Report Title Author's University	Report Author
15	Particle Stimulation of Plasmas University of Missouri, Kansas City, MO	Dr. Richard Murphy Physics PL/WS
16	A Universal Equation of State for Shock in Homogeneous Materials California State University, Northridge, CA	Dr. Jon Shively Engineering & Computer Science PL/VT
17	Speed-Up of the Phase Diversity Method Via Reduced Region & Optimization Dimen. University of Houston, Victoria, TX	Dr. Johanna Stenzel Arts & Sciences PL/LI
18	Analysis of Solwind P-78 Fragmentation Using Empirical And Analytical Codes Alabama A & M University, Normal, AL	Dr. Arjun Tan Physics PL/WS
19	Experimental Investigations of Homogeneous and Heterogeneous Nucleation/Condensa University of Missouri, Rolla, MO	Dr. Philip Whitefield Physics PL/LI

1993 SREP FINAL REPORTS

Rome Laboratory

VOLUME 3

Report #	Report Title Author's University	Report Author
1	Analysis and Code for Treating Infinite Arrays of Tapered Antennas Printed on Bo California State University, Sacramento, CA	Dr. Jean-Pierre Bayard Electrical & Electronic RL/ER Engineering
2	Comparing Pattern Recognition Systems Syracuse University, Syracuse, NY	Dr. Pinyuen Chen Mathematics RL/IR
3	Wideband ATM Networks for the Dynamic Theater Environment University of Southwestern Louisiana, Lafayette, LA	Dr. Robert Henry Electrical & Computer RL/C3 Engineering
4	Congestion Control For ATM Network in a Tectical Theater Environment Polytechnic University, Brooklyn, NY	Mr. Benjamin Hoe Electrical Engineering RL/C3
5	Automated Natural Language Evaluators (ANLF) Southwest Texas State College, San Marcos, TX	Dr. Khosrow Kaikhah Computer Science RL/IR
6	System Analysis and Applications for a Photonic Delay Line Le Moyne College, Syracuse, NY	Dr. Evelyn Monsay Physics RL/OC
7	An Exploratory Investigaton of Multimedia Data Reinforcement for Large-Scale Inf Syracuse University, Syracuse, NY	Dr. Michael Nilan Information Studies RL/C3
8	Supporting Systematic Testing for Reusable Software Components University of Alabama, Tuscaloosa, AL	Dr. Allen Parrish Computer Science RL/C3
9	Use of Turnable Fiber Ring Lasers in Optical Communications SUNY/Institute of Technology, Utica, NY	Dr Salahuddin Qazi Optical Communications RL/OC
10	Further Monte Carlo Studies of a Theoretical Model for Non-Gaussian Radar Clutte SUNY College at Cortland, Cortland, NY	Dr. Jorge Romeu Assistant Prof. of RL/OC Mathematics
11	Hierarchical Modeling and Simulation Syracuse University, Syracuse, NY	Dr. Robert Sargent Engineering and Computer RL/XP Science
12	Metamodel Applications Using TAC Brawler Virginia Polytechnic Institute, Blacksburg, VA	Dr. Jeffery Tew Industrial & Systems RL/IR Engineering
13	Automatic Detection of Prominence in Spontaneous Speech New Mexico Institute of Mining, Socorro, NM	Dr. Colin Wightman Electrical Engineering RL/IR

1993 SREP FINAL REPORTS

Wright Laboratory

VOLUME 4A

Report #	Report Title Author's University	Report Author
1	Integrated Estimator/Guidance/Autopilot for Homing Missiles University of Missouri, Rolla, MO	Dr. S. Balakrishnan Mechanical & Aerospace WL/MN Engineering
2	Studies of NTO Decomposition Memphis State University, Memphis, TN	Dr. Theodore Burkey Chemistry WL/MN
3	Investigation of Ray-Beam Basis Functions for Use with the Generalized Ray Expan Ohio State University, Columbus, OH	Dr. Robert Burkholder Electrical Engineering WL/AA
4	Wave Mechanics Modeling of Terminal Ballistics Phenomenology Louisiana Tech University, Ruston, LA	Dr. Eugene Callens, Jr. Mechanical and Industrial WL/MN Engineer
5	Modeling for Aeroelastic Parameter Estimation of Flexing Slender Bodies in a Bal University of California, Berkeley, CA	Dr. Gary Chapman Mechanical Engineering WL/MN
6	Using VHDL in VSL Bist Design Synthesis and its Application to 3-D Pixel Graphic Wright State University, Dayton, OH	Dr. Chien-In Chen Electrical Engineering WL/EL
7	Study of Part Quality and Shrinkage for Injection Molded Aircraft Transparencies Florida International University, Miami, FL	Dr. Joe Chow Industrial and Systems WL/FI Engineering
8	Implementation of Noise-Reducing Multiple-Source Schlieren Systems Purdue University, West Lafayette, IN	Dr. Steven Collicott Aeronautics and WL/FI Astronautical Engineering
9	Performing Target Classification Using Fussy Morphology Neural Networks Iowa State University, Ames, IA	Dr. Jennifer Davidson Electrical Engineering WL/MN
10	Turbulent Heat Transfer In Counter-Rotating Disk System University of Dayton, Dayton, OH	Dr. Jamie Ervin Mechanical and Aerospace WL/ML Engineering
11	Modelling of Biomaterials for Non-Linear Optical Applications University of Virginia, Charlottesville, VA	Dr. Barry Farmer Materials Science and WL/ML Engineering
12	Passive Ranging, Roll-angle Approximation, and Target Recognition for Fuze Appli Florida State University, Tallahassee, FL	Dr. Simon Foo Electrical Engineering WL/MN
13	A Role of Oxygen and Sulfur Compounds in Jet Fuel Deposit Formation Eastern Kentucky University, Richmond, KY	Ms. Ann Gillman Chemistry WL/PO
14	Effect of Aeroelasticity on Experimental Nonlinear Indicial Responses Measured Ohio University, Athens, OH	Dr. Gary Graham Mechanical Engineering WL/FI

1993 SREP FINAL REPORTS

Wright Laboratory

VOLUME 4A cont'd

Report #	Report Title Author's University	Report Author
15	Virtual Reality Information Presentation Technology for Avionics New Mexico Highlands University, Las Vegas, NM	Dr. Elmer Grubbs Electrical Engineering WL/AA
16	An Investigation of the Thermal Stability of an AlC/Ti-22Al-23Nb Metal Matrix Co University of Delaware, Newark, DE	Dr. Ian Hall Materials Science WL/ML
17	Investigation of the Combustion Characteristics of Confined Coannular Jets with Brigham Young University, Provo, UT	Dr. Paul Hedman Chemical Engineering WL/PO
18	Morphology of High-Velocity Perforation of Laminated Plates University of New Orleans, New Orleans, LA	Dr. David Hui Mechanical Engineering WL/FI

1993 SREP FINAL REPORTS

Wright Laboratory

VOLUME 4B

Report #	Report Title Author's University	Report Author
19	Evaluation of Variable Structure Control for Missile Autopilots Using Reaction Auburn University, Auburn, AL	Dr. Mario Innocenti Aerospace Engineering WL/MN
20	Laser Imaging and Ranging (LIMAR) Processing Wright State University, Dayton, OH	Dr. Jack Jean Computer Science & WL/AA Engineering
21	Applications of Wavelet Subband Decomposition in Adaptive Arrays Lafayette College, Easton, PA	Dr. Ismail Jouny Electrical Engineering WL/AA
22	Micromechanics of Matrix Cracks In Brittle Matrix Composites With Frictional Int University of South Florida, Tampa, FL	Dr. Autar Kaw Mechanical Engineering WL/ML
23	A Physics-Based Heterojunction Bipolar Transistor Model Including High-Current, Universtiy of Central Florida, Orlando, FL	Dr. Juin Liou Electrical and Computer WL/EL Engineering
24	Electrical and Thermal Modeling of Switched Reluctance Machines San Francisco State Univesity, San Francisco, CA	Dr. Shy-Shenq Liou Engineering WL/PO
25	Process Migration Facility for the quest Distributed VHDL Simulator University of Cincinnati M.L., Cincinnati, OH	Mr. Dallas Marks Electrical and Computer WL/AA Engineering
26	Investigation of Third Order Non-Linear Optical Properties of Strained Layer Sem Columbia University, New York, NY	Dr. Mary Potasek Applied Physics WL/ML
27	Development of Control Design Methodologies for Flexible Systems with Multiple Arizona State University, Tempe, AZ	Dr. Armando Rodriguez Electrical Engineering WL/MN
28	Enhanced Liquid Fuel Atomization Through Effervescent Injection Virginia Polytechnic Inst & State Coll., Blacksburg, VA	Dr Larry Roe Mechanical Engineering WL/PO
29	Sensor Fusion for IR/MMW Dual-Mode Sensors Using Artificial Neural Networks Auburn University, Auburn, AL	Dr. Thaddeus Roppel Electrical Engineering WL/MN
30	Characterizing the Solid Fragment Population in a Debris Cloud Created by a Hype University of Alabama, Huntsville, AL	Dr. William Schonberg Civil and Environmental WL/MN Engineering
31	Digital Signal Processing Algorithms for Digital EW Receivers Wright State University, Dayton, OH	Dr. Arnab Shaw Electrical Engineering WL/AA
32	An Analytical Model of Laminated Composite Plates for Determination of Stresses University of Cincinnati, Cincinnati, OH	Mr. Robert Slater Mechanical & Industrial WL/FI Engineering

1993 SREP FINAL REPORTS

Wright Laboratory

VOLUME 4B

cont'd

Report #	Report Title Author's University	Report Author
33	Detection of Internal Defects in Multilayered Plates By Lamb Wave Acoustic Micro Universtiy of Arizona, Tucson, AZ	Dr. Kundu Tribikram Civil Engineering and WL/ML Engineering
34	Wavelet Analysis of Ultrasonic Signals for Non-Destructive Evaluation of Composi University of Dayton, Dayton, OH	Dr. Theresa Tuthill Electrical Engineering WL/ML
35	Stochastic Modeling of MBE Growth of Compoud Semiconductors University of Nevada, Las Vegas, NV	Dr. Ramasubrama Venkatasubraman Electrical and Computer WL/ML Engineering
36	Performance Evaluation And Improvement of a Resonant DC Link Inverter With A Lim North Dakota State University, Fargo, ND	Dr. Subbaraya Yuvarajan Electrical Engineering WL/PO
37	Three Component LDV Measurements in a Swirl Combustor North Carolina State University, Raleigh, NC	Dr. Richard Gould Mechanical and Aerospace WL/PO Engineering

1993 SREP FINAL REPORTS

VOLUME 5

Report #	Report Title Author's University	Report Author
Arnold Engineering Development Center		
1	Performance Enhancement for a TI TMS320C40 version of Multigraph Vanderbilt University, Nashville, TN	Mr. Ben Abbott Electrical Engineering AEDC/
2	System Integration Software for Parallel Hardware Architectures Vanderbilt University, Nashville, TN	Dr. Csaba Biegl Electrical Engineering AEDC/
3	Heat Load Structural Failure Prediction for the AEDC Heat-Hi Test Unit Nozzle Georgia Institute of Technology, Atlanta, GA	Dr. Kurt Gramoll Aerospace Engineering AEDC/
4	Coupling of an Inductive Generator with Plasma Erosion Opening Switch (PEOS) to Morehouse College, Atlanta, GA	Dr. Carlyle Moore Physics AEDC/
Frank J Seiler Research Laboratory		
5	Active and Passive Control Designs for the FJSRL Flexible Structure Testbeds Old Dominion University, Norfolk, VA	Dr. Thomas Alberts Mechanical Engineering FJSRL/
6	Three Dimensional Characterization of Non-Linear Optical Thin Films University of Colorado, Colorado Springs, CO	Dr. Thomas Christensen Physics FJSRL/
7	Electrochemistry of Lithium in Room Temperature Molten Salt Electrolytes Houghton College, Houghton, NY	Dr. Bernard Piersma Chemistry FJSRL/
Wilford Hall Medical Center		
8	Enhanced Physiologic Monitoring of Patients with Closed Head-Injury Memphis State, Memphis, TN	Dr. Michael Daley Electrical Engineering WHMC/
9	Rheological, Biochemical and Biophysical Studies of Blood at Elevated Temperatures University of Miami, Coral Gables, FL	Dr. Walter Drost-Hansen Chemistry WHMC

1993 SUMMER RESEARCH EXTENSION PROGRAM (SREP) MANAGEMENT REPORT

1.0 BACKGROUND

Under the provisions of Air Force Office of Scientific Research (AFOSR) contract F49620-90-C-0076, September 1990, Research & Development Laboratories (RDL), an 8(a) contractor in Culver City, CA, manages AFOSR's Summer Research Program. This report is issued in partial fulfillment of that contract (CLIN 0003AC).

The Summer Research Extension Program (SREP) is one of four programs AFOSR manages under the Summer Research Program. The Summer Faculty Research Program (SFRP) and the Graduate Student Research Program (GSRP) place college-level research associates in Air Force research laboratories around the United States for 8 to 12 weeks of research with Air Force scientists. The High School Apprenticeship Program (HSAP) is the fourth element of the Summer Research Program, allowing promising mathematics and science students to spend two months of their summer vacations working at Air Force laboratories within commuting distance from their homes.

SFRP associates and exceptional GSRP associates are encouraged, at the end of their summer tours, to write proposals to extend their summer research during the following calendar year at their home institutions. AFOSR provides funds adequate to pay for 75 SREP subcontracts. In addition, AFOSR has traditionally provided further funding, when available, to pay for additional SREP proposals, including those submitted by associates from Historically Black Colleges and Universities (HBCUs) and Minority Institutions (MIs). Finally, laboratories may transfer internal funds to AFOSR to fund additional SREPs. Ultimately the laboratories inform RDL of their SREP choices, RDL gets AFOSR approval, and RDL forwards a subcontract to the institution where the SREP associate is employed. The subcontract (see Appendix 1 for a sample) cites the SREP associate as the principal investigator and requires submission of a report at the end of the subcontract period.

Institutions are encouraged to share costs of the SREP research, and many do so. The most common cost-sharing arrangement is reduction in the overhead, fringes, or administrative charges institutions would normally add on to the principal investigator's or research associate's labor. Some institutions also provide other support (e.g., computer run time, administrative assistance, facilities and equipment or research assistants) at reduced or no cost.

When RDL receives the signed subcontract, we fund the effort initially by providing 90% of the subcontract amount to the institution (normally \$18,000 for a \$20,000 SREP). When we receive the end-of-research report, we evaluate it administratively and send a copy to the laboratory for a technical evaluation. When the laboratory notifies us the SREP report is acceptable, we release the remaining funds to the institution.

2.0 THE 1993 SREP PROGRAM

SELECTION DATA: A total of 719 faculty members (SFRP Associates) and 286 graduate students (GSRP associates) applied to participate in the 1992 Summer Research Program. From these applicants 185 SFRPs and 121 GSRPs were selected. The education level of those selected was as follows:

1992 SRP Associates, by Degree			
SFRP		GSRP	
PHD	MS	MS	BS
179	6	52	69

Of the participants in the 1992 Summer Research Program 90 percent of SFRPs and 25 percent of GSRPs submitted proposals for the SREP. Ninety proposals from SFRPs and ten from GSRPs were selected for funding, which equates to a selection rate of 54% of the SFRP proposals and of 34% for GSRP proposals.

1993 SREP: Proposals Submitted vs. Proposals Selected			
	Summer 1992 Participants	Submitted SREP Proposals	SREPs Funded
SFRP	185	167	90
GSRP	121	29	10
TOTAL	306	196	100

The funding was provided as follows:

Contractual slots funded by AFOSR	75
Laboratory funded	14
Additional funding from AFOSR	<u>11</u>
Total	100

Six HBCU/MI associates from the 1992 summer program submitted SREP proposals; six were selected (none were lab-funded; all were funded by additional AFOSR funds).

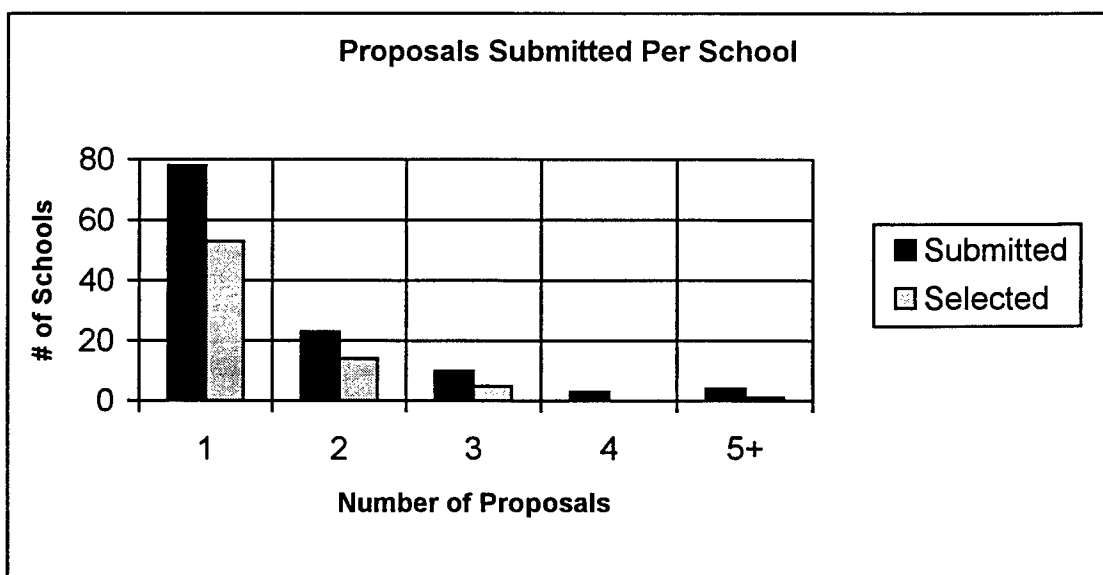
Proposals Submitted and Selected, by Laboratory		
	Applied	Selected
Air Force Civil Engineering Laboratory	9	4
Armstrong Laboratory	41	19
Arnold Engineering Development Center	12	4
Frank J. Seiler Research Laboratory	6	3
Phillips Laboratory	33	19
Rome Laboratory	31	13
Wilford Hall Medical Center	2	1
Wright Laboratory	62	37
TOTAL	196	100

Note: Phillips Laboratory funded 3 SREPs; Wright Laboratory funded 11; and AFOSR funded 11 beyond its contractual 75.

The 306 1992 Summer Research Program participants represented 135 institutions.

Institutions Represented on the 1992 SRP and 1993 SREP		
Number of schools represented in the Summer 92 Program	Number of schools represented in submitted proposals	Number of schools represented in Funded Proposals
135	118	73

Forty schools had more than one participant submitting proposals.



The selection rate for the 78 schools submitting 1 proposal (68%) was better than those submitting 2 proposals (61%), 3 proposals (50%), 4 proposals (0%) or 5+ proposals (25%). The 4 schools that submitted 5+ proposals accounted for 30 (15%) of the 196 proposals submitted.

Of the 196 proposals submitted, 159 offered institution cost sharing. Of the funded proposals which offered cost sharing, the minimum cost share was \$1000.00, the maximum was \$68,000.00 with an average cost share of \$12,016.00.

Proposals and Institution Cost Sharing		
	Proposals Submitted	Proposals Funded
With cost sharing	159	82
Without cost sharing	37	18
Total	196	100

The SREP participants were residents of 41 different states. Number of states represented at each laboratory were:

States Represented, by Proposals Submitted/Selected per Laboratory		
	Proposals Submitted	Proposals Funded
Air Force Civil Engineering Laboratory	8	4
Armstrong Laboratory	21	13
Arnold Engineering Development Center	5	2
Frank J. Seiler Research Laboratory	5	3
Phillips Laboratory	16	14
Rome Laboratory	14	7
Wilford Hall Medical Center	2	1
Wright Laboratory	24	20

Eleven of the 1993 SREP Principal Investigators also participated in the 1992 SREP.

ADMINISTRATIVE EVALUATION: The administrative quality of the SREP associates' final reports was satisfactory. Most complied with the formatting and other instructions provided to them by RDL. Ninety seven final reports and two interim reports have been received and are included in this report. The subcontracts were funded by \$1,991,623.00 of Air Force money. Institution cost sharing totaled \$985,353.00.

TECHNICAL EVALUATION: The form used for the technical evaluation is provided as Appendix 2. ninety-two evaluation reports were received. Participants by laboratory versus evaluations submitted is shown below:

	Participants	Evaluations	Percent
Air Force Civil Engineering Laboratory	*	*	*
Armstrong Laboratory	23 ¹	20	95.2
Arnold Engineering Development Center	4	4	100
Frank J. Seiler Research Laboratory	3	3	100
Phillips Laboratory	19 ²	18	100
Rome Laboratory	13	13	100
Wilford Hall Medical Center	1	1	100
Wright Laboratory	37	34	91.9
Total	100 ³	93	95.9

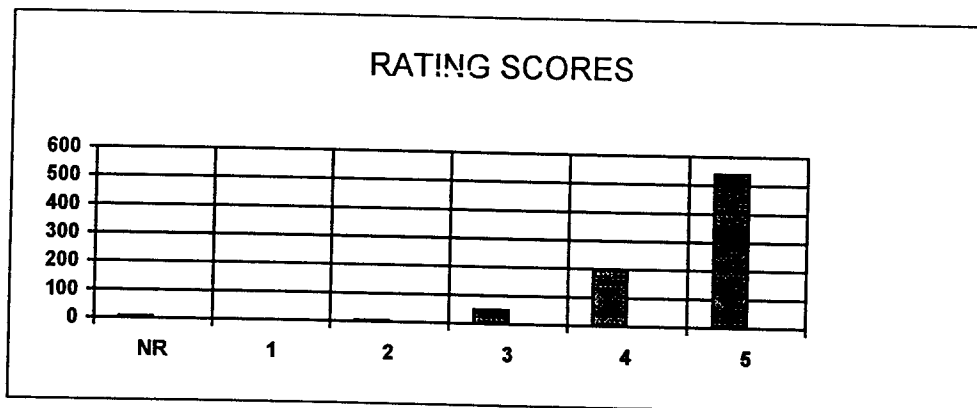
*AFCEL was combined with Wright Laboratory's Flight Dynamics Directorate and Armstrong Laboratories Environics Directorate in 1993. All four of AFCEL's SREP awards went to Armstrong Laboratories Environics Directorate, and their reports are included with Armstrong Lab.

Notes:

- 1: Research on two of the final reports was incomplete as of press time so there aren't any technical evaluations on them to process, yet. Percent complete is based upon 20/21=95.2%
- 2: One technical evaluation was not completed because one of the final reports was incomplete as of press time. Percent complete is based upon 18/18=100%
- 3: See notes 1 and 2 above. Percent complete is based upon 93/97=95.9%

The number of evaluations submitted for the 1993 SREP (95.9%) shows a marked improvement over the 1992 SREP submittals (65%).

PROGRAM EVALUATION: Each laboratory focal point evaluated ten areas (see Appendix 2) with a rating from one (lowest) to five (highest). The distribution of ratings was as follows:

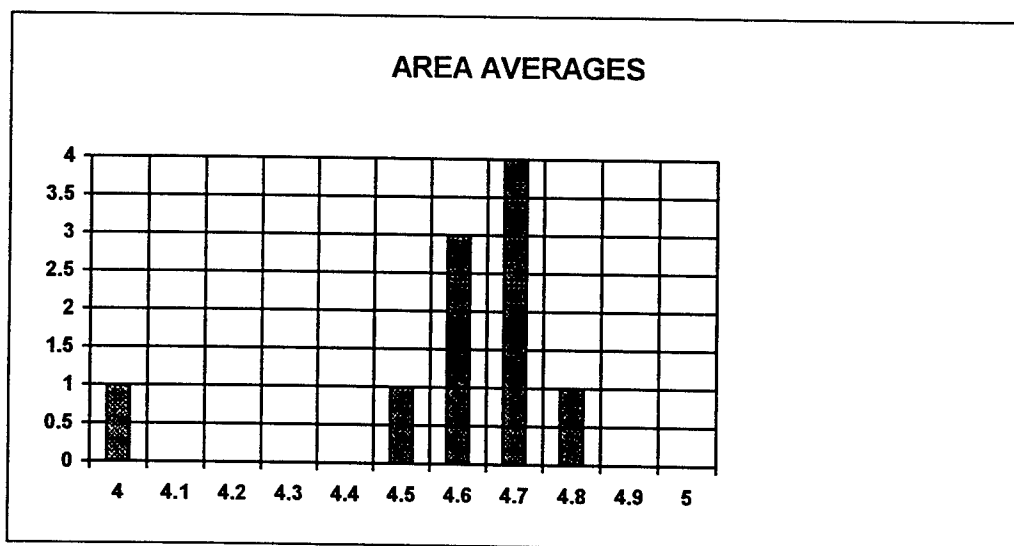


Rating	Not Rated	1	2	3	4	5
# Responses	7	1	7	62 (6%)	226 (25%)	617 (67%)

The 8 low ratings (one 1 and seven 2's) were for question 5 (one 2) "The USAF should continue to pursue the research in this SREP report" and question 10 (one 1 and six 2's) "The one-year period for complete SREP research is about right", in addition over 30% of the threes (20 of 62) were for question ten. The average rating by question was:

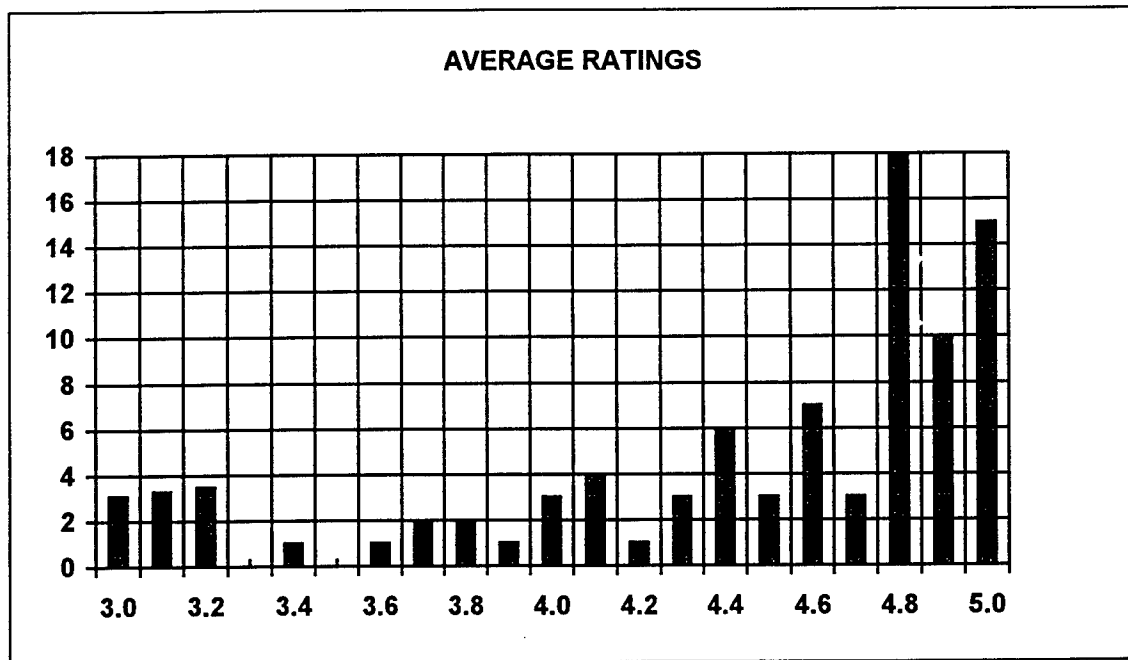
Question	1	2	3	4	5	6	7	8	9	10
Average	4.6	4.6	4.7	4.7	4.6	4.7	4.8	4.5	4.6	4.0

The distribution of the averages was:



Area 10 "the one-year period for complete SREP research is about right" had the lowest average rating (4.1). The overall average across all factors was 4.6 with a small sample standard deviation of 0.2. The average rating for area 10 (4.1) is approximately three sigma lower than the overall average (4.6) indicating that a significant number of the evaluators feel that a period of other than one year should be available for complete SREP research.

The average ratings ranged from 3.4 to 5.0. The overall average for those reports that were evaluated was 4.6. Since the distribution of the ratings is not a normal distribution the average of 4.6 is misleading. In fact over half of the reports received an average rating of 4.8 or higher. The distribution of the average report ratings is as shown:



It is clear from the high ratings that the laboratories place a high value on AFOSR's Summer Research Extension Programs.

3.0 SUBCONTRACTS SUMMARY

Table 1 provides a summary of the SREP subcontracts. The individual reports are published in volumes as shown:

<u>Laboratory</u>	<u>Volume</u>
Air Force Civil Engineering Laboratory	*
Armstrong Laboratory	1
Arnold Engineering Development Center	5
Frank J. Seiler Research Laboratory	5
Phillips Laboratory	2
Rome Laboratory	3
Wilford Hall Medical Center	5
Wright Laboratory	4A, 4B

*AFCEL was combined with Wright Laboratory's Flight Dynamics Directorate and Armstrong Laboratories Environics Directorate in 1993. All four of AFCEL's SREP awards went to Armstrong Laboratories Environics Directorate, and their reports are included with Armstrong Lab.

1993 SREP SUB-CONTRACT DATA

TABLE 1: SUBCONTRACTS SUMMARY

Report Author Author's University	Author's Degree	Sponsoring Lab	Performance Period		Contract Amount Univ. Cost Share
Abbott , Ben Electrical Engineering Vanderbilt University, Nashville, TN	M.S.	AEDC/	01/01/93	12/31/93	\$19619.00 \$0.00
Alberts , Thomas Mechanical Engineering Old Dominion University, Norfolk, VA	PhD	FJSRL/	01/01/93	04/15/94	\$20000.00 \$8000.00
Avula , Xavier Mechanical & Aerospace Engineering University of Missouri, Rolla, MO	PhD	AL/AO	01/01/93	04/15/94	\$20000.00 \$1836.00
Balakrishnan , S. Mechanical & Aerospace Engineering University of Missouri, Rolla, MO	PhD	WL/MN	12/01/92	12/14/93	\$20000.00 \$3996.00
Baumgarten , Joseph Mechanical Engineering Iowa State University, Ames, IA	PhD	PL/VT	01/01/93	04/01/94	\$19916.00 \$9083.00
Bayard , Jean-Pierre Electrical & Electronic Engineering California State University, Sacramento, CA	PhD	RL/ER	01/01/93	12/31/93	\$20000.00 \$7423.00
Bellem , Raymond Electrical & Computer Engineering University of Arizona, Tucson, AZ	PhD	PL/VT	01/01/93	02/28/94	\$19956.00 \$0.00
Biegl , Csaba Electrical Engineering Vanderbilt University, Nashville, TN	PhD	AEDC/	01/01/93	12/31/93	\$19999.00 \$0.00
Biggs , Albert Electrical Engineering University of Alabama, Huntsville, AL	PhD	PL/WS	01/01/93	12/31/93	\$19975.00 \$0.00
Burkey , Theodore Chemistry Memphis State University, Memphis, TN	PhD	WL/MN	01/01/93	12/31/93	\$20000.00 \$18648.00
Burkholder , Robert Electrical Engineering Ohio State University, Columbus, OH	PhD	WL/AA	01/01/93	12/31/93	\$20000.00 \$6727.00
Callens, Jr. , Eugene Mechanical and Industrial Engineer Louisiana Tech University, Ruston, LA	PhD	WL/MN	01/01/93	12/31/93	\$20000.00 \$5700.00
Chapman , Gary Mechanical Engineering University of California, Berkeley, CA	PhD	WL/MN	01/01/93	12/31/94	\$20000.00 \$0.00
Chen , Chien-In Electrical Engineering Wright State University, Dayton, OH	PhD	WL/EL	01/01/93	12/31/93	\$20000.00 \$32065.00
Chen , Jer-sen Computer Science & Engineering Wright State University, Dayton, OH	PhD	AL/CF	01/01/93	12/31/93	\$20000.00 \$31763.00

1993 SREP SUB-CONTRACT DATA

Report Author Author's University	Author's Degree	Sponsoring Lab	Performance Period		Contract Amount Univ. Cost Share
Chen , Pinyuen Mathematics Syracuse University, Syracuse, NY	PhD	RL/IR	01/01/93	12/31/93	\$20000.00 \$0.00
Chow , Joe Industrial and Systems Engineering Florida International University, Miami, FL	PhD	WL/FI	01/01/93	01/14/94	\$20000.00 \$2500.00
Christensen , Thomas Physics University of Colorado, Colorado Springs, CO	PhD	FJSRL/	01/01/93	12/31/93	\$20000.00 \$5390.00
Collicott , Steven Aeronautics and Astronautical Engineering Purdue University, West Lafayette, IN	PhD	WL/FI	01/01/93	12/31/93	\$20000.00 \$13307.00
Cooke , Nancy Psychology New Mexico State University, Las Cruces, NM	PhD	AL/HR	01/01/93	12/31/93	\$20000.00 \$6178.00
Daley , Michael Electrical Engineering Memphis State, Memphis, TN	PhD	WHMC/	01/01/93	12/31/93	\$20000.00 \$18260.00
Davidson , Jennifer Electrical Engineering Iowa State University, Ames, IA	PhD	WL/MN	01/01/93	02/28/94	\$19999.00 \$0.00
Deivanayagam , Subramaniam Industrial Engineering Tennessee Technological University, Cookeville, TN	PhD	AL/HR	02/01/93	12/31/93	\$20000.00 \$12491.00
Elliott , David Engineering Arkansas Technology University, Russellville, AR	PhD	PL/RK	10/01/92	08/15/93	\$20000.00 \$50271.00
Erdman , Paul Physics and Astronomy University of Iowa, Iowa City, IA	M.S.	PL/RK	01/01/93	12/31/93	\$20000.00 \$26408.00
Ervin , Jamie Mechanical and Aerospace Engineering University of Dayton, Dayton, OH	PhD	WL/ML	01/01/93	12/31/93	\$18632.00 \$3000.00
Erwin , Daniel Aerospace Engineering University of Southern California, Los Angeles, CA	PhD	PL/RK	01/01/93	12/31/93	\$19962.00 \$12696.00
Ewert , Dan Electrical Engineering North Dakota State University, Fargo, ND	PhD	AL/AO	01/01/93	12/31/93	\$20000.00 \$2100.00
Farmer , Barry Materials Science and Engineering University of Virginia, Charlottesville, VA	PhD	WL/ML	01/01/93	02/28/94	\$20000.00 \$2000.00
Foo , Simon Electrical Engineering Florida State University, Tallahassee, FL	PhD	WL/MN	01/01/93	12/31/93	\$19977.00 \$0.00

1993 SREP SUB-CONTRACT DATA

Report Author Author's University	Author's Degree	Sponsoring Lab	Performance Period		Contract Amount Univ. Cost Share
Friedman , Jeffrey Physics University of Puerto Rico, Mayaguez, PR	PhD	PL/GP	01/01/93	12/31/93	\$20000.00 \$10233.00
Gerstman , Bernard Physics Florida International University, Miami, FL	PhD	AL/OE	01/01/93	04/30/94	\$19947.00 \$2443.00
Gillman , Ann Chemistry Eastern Kentucky University, Richmond, KY	M.S.	WL/PO	01/01/93	12/31/93	\$20000.00 \$15618.00
Gimmestad , Gary Research Institute Georgia Institute of Technology, Atlanta, GA	PhD	PL/LI	01/01/93	12/31/93	\$20000.00 \$0.00
Gould , Richard Mechanical and Aerospace Engineering North Carolina State University, Raleigh, NC	PhD	WL/PO	01/01/93	12/31/93	\$20000.00 \$8004.00
Graham , Gary Mechanical Engineering Ohio University, Athens, OH	PhD	WL/FI	01/01/93	12/31/93	\$20000.00 \$5497.00
Gramoll , Kurt Aerospace Engineering Georgia Institute of Technology, Atlanta, GA	PhD	AEDC/	01/01/93	12/31/93	\$19707.00 \$14552.00
Graul , Susan Chemistry Carnegie Mellon University, Pittsburgh, PA	PhD	PL/WS	01/01/93	03/31/94	\$20000.00 \$0.00
Griffin , Steven Engineering University of Texas, San Antonio, TX	M.S.	PL/VT	01/01/93	12/31/93	\$20000.00 \$0.00
Grubbs , Elmer Electrical Engineering New Mexico Highlands University, Las Vegas, NM	PhD	WL/AA	01/01/93	12/31/93	\$20000.00 \$6747.00
Gupta , Pushpa Mathematics University of Maine, Orono, ME	PhD	AL/AO	01/01/93	12/31/93	\$20000.00 \$1472.00
Hall , Ian Materials Science University of Delaware, Newark, DE	PhD	WL/ML	01/01/93	12/31/93	\$20000.00 \$9580.00
Hedman , Paul Chemical Engineering Brigham Young University, Provo, UT	PhD	WL/PO	01/01/93	12/31/93	\$19999.00 \$7755.00
Henry , Robert Electrical & Computer Engineering University of Southwestern Louisiana, Lafayette, LA	PhD	RL/C3	12/01/92	05/31/93	\$19883.00 \$11404.00
Henson , James Electrical Engineering University of Nevada, Reno, NV	PhD	PL/WS	01/01/93	12/31/93	\$19913.00 \$9338.00

1993 SREP SUB-CONTRACT DATA

Report Author Author's University	Author's Degree	Sponsoring Lab	Performance Period		Contract Amount Univ. Cost Share
Hoe , Benjamin Electrical Engineering Polytechnic University, Brooklyn, NY	M.S.	RL/C3	09/01/92	05/31/93	\$19988.00 \$7150.00
Hughes , Rod Psychology Bowling Green State University, Bowling Green, OH	M.S.	AL/CF	01/01/93	04/15/94	\$20000.00 \$20846.00
Hui , David Mechanical Engineering University of New Orleans, New Orleans, LA	PhD	WL/FI	01/01/93	12/31/93	\$20000.00 \$0.00
Humi , Mayer Mathematics Worcester Polytechnic Institut, Worcester, MA	PhD	PL/LI	01/01/93	12/31/93	\$20000.00 \$5000.00
Innocenti , Mario Aerospace Engineering Auburn University, Auburn, AL	PhD	WL/MN	01/01/93	02/28/94	\$20000.00 \$12536.00
Jean , Jack Computer Science & Engineering Wright State University, Dayton, OH	PhD	WL/AA	01/01/93	12/31/93	\$20000.00 \$34036.00
Jouny , Ismail Electrical Engineering Lafayette College, Easton, PA	PhD	WL/AA	01/01/93	12/31/93	\$19381.00 \$4500.00
Kaikhah , Khosrow Computer Science Southwest Texas State College, San Marcos, TX	PhD	RL/IR	01/01/93	12/31/93	\$20000.00 \$0.00
Kaw , Autar Mechanical Engineering University of South Florida, Tampa, FL	PhD	WL/ML	01/01/93	12/31/93	\$20000.00 \$22556.00
Kheyfets , Arkady Mathematics North Carolina State University, Raleigh, NC	PhD	PL/LI	01/01/93	12/31/93	\$20000.00 \$2500.00
Kitchart , Mark Mechanical Engineering North Carolina A & T State University, Greensboro, NC	M.S.	AL/EQ	01/01/93	12/31/93	\$20000.00 \$0.00
Koblasz , Arthur Civil Engineering Georgia Institute of Technology, Atlanta, GA	PhD	AL/AO	01/01/93	12/31/93	\$19826.00 \$0.00
Koivo , A. Electrical Engineering Purdue University, West Lafayette, IN	PhD	AL/CF	01/01/93	06/30/94	\$20000.00 \$0.00
Kundich , Robert Biomedical Engineering University of Tennessee, Memphis, TN	PhD	AL/CF	01/01/93	12/31/94	\$20000.00 \$23045.00
Kuo , Spencer Electrical Engineering Polytechnic University, Farmingdale, NY	PhD	PL/GP	01/01/93	04/30/94	\$20000.00 \$9731.00

1993 SREP SUB-CONTRACT DATA

Report Author Author's University	Author's Degree	Sponsoring Lab	Performance Period		Contract Amount Univ. Cost Share
Liou , Juin Electrical and Computer Engineering Universtiy of Central Florida, Orlando, FL	PhD	WL/EL	01/01/93	12/31/93	\$20000.00 \$9073.00
Liou , Shy-Shenq Engineering San Francisco State Univesity, San Francisco, CA	PhD	WL/PO	01/01/93	12/31/93	\$20000.00 \$13387.00
Manoranjana , Valipuram Pure and Applied Mathematics Washington State University, Pullman, WA	PhD	AL/EQ	01/01/93	12/31/93	\$19956.00 \$10041.00
Marks , Dallas Electrical and Computer Engineering University of Cincinnati M.L., Cincinnati, OH	M.S.	WL/AA	10/01/92	06/30/93	\$20000.00 \$4731.00
Monsay , Evelyn Physics Le Moyne College, Syracuse, NY	PhD	RL/OC	01/01/93	12/31/93	\$19634.00 \$1510.00
Moor , William Industrial & Management Engineering Arizona State University, Tempe, AZ	PhD	AL/HR	01/01/93	12/31/93	\$20000.00 \$4833.00
Moore , Carlyle Physics Morehouse College, Atlanta, GA	PhD	AEDC/	01/01/93	12/31/93	\$20000.00 \$4880.00
Mulligan , B. Psychology University of Georgia Research, Athens, GA	PhD	AL/OE	01/01/93	04/15/94	\$19998.00 \$13936.00
Murphy , Richard Physics University of Missouri, Kansas City, MO	PhD	PL/WS	01/01/93	12/31/93	\$20000.00 \$13022.00
Nilan , Michael Information Studies Syracuse University, Syracuse, NY	PhD	RL/C3	01/01/93	12/31/93	\$19998.00 \$13016.00
Parrish , Allen Computer Science University of Alabama, Tuscaloosa, AL	PhD	RL/C3	01/01/93	12/31/93	\$19919.00 \$20599.00
Piersma , Bernard Chemistry Houghton College, Houghton, NY	PhD	FJSRL/	01/01/93	12/31/93	\$20000.00 \$4000.00
Potasek , Mary Applied Physics Columbia University, New York, NY	PhD	WL/ML	12/01/93	11/30/93	\$20000.00 \$7806.00
Qazi , Salahuddin Optical Communications SUNY/Institute of Technology, Utica, NY	PhD	RL/OC	01/01/93	12/31/93	\$20000.00 \$68000.00
Reardon , Kenneth Agricultural and Chemical Engineering Colorado State University, Fort Collins, CO	PhD	AL/EQ	01/01/93	01/31/94	\$19996.00 \$12561.00

1993 SREP SUB-CONTRACT DATA

Report Author Author's University	Author's Degree	Sponsoring Lab	Performance Period		Contract Amount Univ. Cost Share
Reynolds , David Biomedical & Human Factors Wright State University, Dayton, OH	PhD	AL/CF	01/01/93	06/30/94	\$20000.00 \$14063.00
Robinson , Donald Chemistry Xavier University of Louisiana, New Orleans, LA	PhD	AL/OE	01/01/93	06/30/94	\$20000.00 \$12935.00
Rodriguez , Armando Electrical Engineering Arizona State University, Tempe, AZ	PhD	WL/MN	01/01/93	12/31/93	\$20000.00 \$0.00
Roe , Larry Mechanical Engineering Virginia Polytechnic Inst & State Coll., Blacksburg, VA	PhD	WL/PO	01/01/93	12/31/93	\$20000.00 \$11421.00
Romeu , Jorge Assistant Prof. of Mathematics SUNY College at Cortland, Cortland, NY	PhD	RL/OC	01/01/93	12/31/93	\$19997.00 \$7129.00
Roppel , Thaddeus Electrical Engineering Auburn University, Auburn, AL	PhD	WL/MN	01/01/93	12/31/93	\$20000.00 \$21133.00
Roznowski , Mary Psychology Ohio State University, Columbus, OH	PhD	AL/HR	01/01/93	03/31/94	\$19953.00 \$6086.00
Rudzinski , Walter Chemistry Southwest Texas State University, San Marcos, TX	PhD	AL/OE	01/01/93	12/31/93	\$20000.00 \$10120.00
Sargent , Robert Engineering and Computer Science Syracuse University, Syracuse, NY	PhD	RL/XP	01/01/93	12/31/93	\$20000.00 \$11931.00
Schonberg , William Civil and Environmental Engineering University of Alabama, Huntsville, AL	PhD	WL/MN	01/01/93	12/31/93	\$19991.00 \$5083.00
Shaw , Arnab Electrical Engineering Wright State University, Dayton, OH	PhD	WL/AA	01/01/93	12/31/93	\$20000.00 \$4766.00
Shively , Jon Engineering & Computer Science California State University, Northridge, CA	PhD	PL/VT	01/01/93	12/31/93	\$20000.00 \$9782.00
Slater , Robert Mechanical & Industrial Engineering University of Cincinnati, Cincinnati, OH	M.S.	WL/FI	01/01/93	12/31/93	\$20000.00 \$8257.00
Stenzel , Johanna Arts & Sciences University of Houston, Victoria, TX	PhD	PL/LI	01/01/93	12/31/93	\$20000.00 \$9056.00
Tan , Arjun Physics Alabama A & M University, Normal, AL	PhD	PL/WS	01/01/93	12/31/93	\$20000.00 \$1000.00

1993 SREP SUB-CONTRACT DATA

Report Author Author's University	Author's Degree	Sponsoring Lab	Performance Period		Contract Amount Univ. Cost Share
Tetrick , Lois Industrial Relations Prog Wayne State University, Detroit, MI	PhD	AL/HR	01/01/93	12/31/93	\$20000.00 \$17872.00
Tew , Jeffery Industrial & Systems Engineering Virginia Polytechnic Institute, Blacksburg, VA	PhD	RL/IR	05/31/93	12/31/93	\$16489.00 \$4546.00
Tribikram , Kundu Civil Engineering and Engineering Universtiy of Arizona, Tucson, AZ	PhD	WL/ML	01/01/93	12/31/93	\$20000.00 \$9685.00
Tuthill , Theresa Electrical Engineering University of Dayton, Dayton, OH	PhD	WL/ML	01/01/93	12/31/93	\$20000.00 \$24002.00
Venkatasubraman , Ramasubrama Electrical and Computer Engineering University of Nevada, Las Vegas, NV	PhD	WL/ML	01/01/93	12/31/93	\$20000.00 \$18776.00
Wang , Xingwu Electrical Engineering Alfred University, Alfred, NY	PhD	AL/EQ	01/01/93	12/31/93	\$20000.00 \$10000.00
Whitefield , Philip Physics University of Missouri, Rolla, MO	PhD	PL/LI	01/01/93	03/01/94	\$20000.00 \$11040.00
Wightman , Colin Electrical Engineering New Mexico Institute of Mining, Socorro, NM	PhD	RL/IR	01/01/93	12/31/93	\$20000.00 \$1850.00
Womack , Michael Natural Science and Mathematics Macon College, Macon, GA	PhD	AL/OE	01/01/93	06/30/94	\$19028.00 \$6066.00
Yuvarajan , Subbaraya Electrical Engineering North Dakota State University, Fargo, ND	PhD	WL/PO	01/01/93	12/31/93	\$19985.00 \$22974.00

APPENDIX 1:
SAMPLE SREP SUBCONTRACT

AIR FORCE OFFICE OF SCIENTIFIC RESEARCH
1993 SUMMER RESEARCH EXTENSION PROGRAM SUBCONTRACT 93-133

BETWEEN

Research & Development Laboratories
5800 Uplander Way
Culver City, CA 90230-6608

AND

San Francisco State University
University Comptroller
San Francisco, CA 94132

REFERENCE: Summer Research Extension Program Proposal 93-133
Start Date: 01/01/93 End Date: 12/31/93
Proposal Amount: \$20,000.00

- (1) PRINCIPAL INVESTIGATOR: Dr. Shy Shenq P. Liou
Engineering
San Francisco State University
San Francisco, CA 94132
- (2) UNITED STATES AFOSR CONTRACT NUMBER: F49620-90-C-09076
- (3) CATALOG OF FEDERAL DOMESTIC ASSISTANCE NUMBER (CFDA): 12.800
PROJECT TITLE: AIR FORCE DEFENSE RESEARCH SOURCES PROGRAM
- (4) ATTACHMENTS 1 AND 2: SREP REPORT INSTRUCTIONS

*** SIGN SREP SUBCONTRACT AND RETURN TO RDL***

1. **BACKGROUND:** Research & Development Laboratories (RDL) is under contract (F49620-90-C-0076) to the United States Air Force to administer the Summer Research Programs (SRP), sponsored by the Air Force Office of Scientific Research (AFOSR), Bolling Air Force Base, D.C. Under the SRP, a selected number of college faculty members and graduate students spend part of the summer conducting research in Air Force laboratories. After completion of the summer tour participants may submit, through their home institutions, proposals for follow-on research. The follow-on research is known as the Summer Research Extension Program (SREP). Approximately 75 SREP proposals annually will be selected by the Air Force for funding of up to \$20,000; shared funding by the academic institution is encouraged. SREP efforts selected for funding are administered by RDL through subcontracts with the institutions. This subcontract represents such an agreement between RDL and the institution designated in Section 5 below.

2. **RDL PAYMENTS:** RDL will provide the following payments to SREP institutions:
 - 90 percent of the negotiated SREP dollar amount at the start of the SREP Research period.
 - the remainder of the funds within 30 days after receipt at RDL of the acceptable written final report for the SREP research.


3. **INSTITUTION'S RESPONSIBILITIES:** As a subcontractor to RDL, the institution designated on the title page will:
 - a. Assure that the research performed and the resources utilized adhere to those defined in the SREP proposal.
 - b. Provide the level and amounts of institutional support specified in the RIP proposal.
 - c. Notify RDL as soon as possible, but not later than 30 days, of any changes in 3a or 3b above, or any change to the assignment or amount of participation of the Principal Investigator designated on the title page.

- d. Assure that the research is completed and the final report is delivered to RDL not later than twelve months from the effective date of this subcontract, but no later than December 31, 1993. The effective date of the subcontract is one week after the date that the institution's contracting representative signs this subcontract, but no later than January 15, 1993.
- e. Assure that the final report is submitted in accordance with Attachment 1.
- f. Agree that any release of information relating to this subcontract (news releases, articles, manuscripts, brochures, advertisements, still and motion pictures, speeches, trade association meetings, symposia, etc.) will include a statement that the project or effort depicted was or is sponsored by: Air Force Office of Scientific Research, Bolling AFB, D.C.
- g. Notify RDL of inventions or patents claimed as the result of this research as specified in Attachment 1.
- h. RDL is required by the prime contract to flow down patent rights and technical data requirements in this subcontract. Attachment 2 to this subcontract contains a list of contract clauses incorporated by reference in the prime contract.

4. All notices to RDL shall be addressed to:

RDL Summer Research Program Office
5800 Uplander Way
Culver City, CA 90230-6608

5. By their signatures below, the parties agree to the provisions of this subcontract.



Abe S. Sopher
RDL Contracts Manager

Signature of Institution Contracting Official

Typed/Printed Name

Date

Title

Institution

(Date/Phone)

ATTACHMENT 2
CONTRACT CLAUSES

This contract incorporates by reference the following clauses of the Federal Acquisition Regulations (FAR), with the same force and effect as if they were given in full text. Upon request, the Contracting Officer or RDL will make their full text available (FAR 52.252-2).

<u>FAR CLAUSES</u>	<u>TITLE AND DATE</u>
52.202-1	DEFINITIONS (SEP 1991)
52.203-1	OFFICIALS NOT TO BENEFIT (APR 1984)
52.203-3	GRATUITIES (APR 1984)
52.203-5	COVENANT AGAINST CONTINGENT FEES (APR 1984)
52.304-6	RESTRICTIONS ON SUBCONTRACTOR SALES TO THE GOVERNMENT (JUL 1985)
52.203-7	ANTI-KICKBACK PROCEDURES (OCT 1988)
52.203-12	LIMITATION ON PAYMENTS TO INFLUENCE CERTAIN FEDERAL TRANSACTIONS (JAN 1990)
52.204-2	SECURITY REQUIREMENTS (APR 1984)
52.209-6	PROTECTING THE GOVERNMENT'S INTEREST WHEN SUBCONTRACTING WITH CONTRACTORS DEBARRED, SUSPENDED, OR PROPOSED FOR DEBARMENT (NOV 1992)
52.212-8	DEFENSE PRIORITY AND ALLOCATION REQUIREMENTS (SEP 1990)
52.215-1	EXAMINATION OF RECORDS BY COMPTROLLER GENERAL (APR 1984)
52.215-2	AUDIT - NEGOTIATION (DEC 1989)
52.222-26	EQUAL OPPORTUNITY (APR 1984)
52.222-28	EQUAL OPPORTUNITY PREAWARD CLEARANCE OF SUBCONTRACTS (APR 1984)

- 52.222-35 AFFIRMATIVE ACTION FOR SPECIAL DISABLED AND VIETNAM ERA VETERANS (APR 1984)
- 52.222-36 AFFIRMATIVE ACTION FOR HANDICAPPED WORKERS (APR 1984)
- 52.222-37 EMPLOYMENT REPORTS ON SPECIAL DISABLED VETERAN AND VETERANS OF THE VIETNAM ERA (JAN 1988)
- 52.223-2 CLEAN AIR AND WATER (APR 1984)
- 52.232-6 DRUG-FREE WORKPLACE (JUL 1990)
- 52.224-1 PRIVACY ACT NOTIFICATION (APR 1984)
- 52.224-2 PRIVACY ACT (APR 1984)
- 52.225-13 RESTRICTIONS ON CONTRACTING WITH SANCTIONED PERSONS (MAY 1989)
- 52.227-1 AUTHORIZATION AND CONSENT (APR 1984)
- 52.227-2 NOTICE AND ASSISTANCE REGARDING PATENT AND COPYRIGHT INFRINGEMENT (APR 1984)
- 52.227-10 FILING OF PATENT APPLICATIONS - CLASSIFIED SUBJECT MATTER (APR 1984)
- 52.227-11 PATENT RIGHTS - RETENTION BY THE CONTRACTOR (SHORT FORM) (JUN 1989)
- 52.228-6 INSURANCE - IMMUNITY FROM TORT LIABILITY (APR 1984)
- 52.228-7 INSURANCE - LIABILITY TO THIRD PERSONS (APR 1984)
- 52.230-5 DISCLOSURE AND CONSISTENCY OF COST ACCOUNTING PRACTICES (AUG 1992)
- 52.232-23 ASSIGNMENT OF CLAIMS (JAN 1986)
- 52.237-3 CONTINUITY OF SERVICES (JAN 1991)

52.246-25	LIMITATION OF LIABILITY - SERVICES (APR 1984)
52.249-6	TERMINATION (COST-REIMBURSEMENT) (MAY 1986)
52.249-14	EXCUSABLE DELAYS (APR 1984)
52.251-1	GOVERNMENT SUPPLY SOURCES (APR 1984)

APPENDIX 2:
SAMPLE TECHNICAL EVALUATION FORM

1993 SUMMER RESEARCH EXTENSION PROGRAM

RIP NO.: 93-0092

RIP ASSOCIATE: Dr. Gary T. Chapman

Provided are several evaluation statements followed by ratings of (1) through (5). A rating of (1) is the lowest and (5) is the highest. Circle the rating level number you best feel rates the statement. Document additional comments on the back of this evaluation form.

Mail or fax the completed form to :

RDL

Attn: 1993 SREP TECH EVALS
5800 Uplander Way
Culver City, CA 90230-6608
(FAX: 310 216-5940)

- | | | | | | | |
|-----|---|---|---|---|---|---|
| 1. | This SREP report has a high level of technical merit. | 1 | 2 | 3 | 4 | 5 |
| 2. | The SREP program is important to accomplishing the labs's mission | 1 | 2 | 3 | 4 | 5 |
| 3. | This SREP report accomplished what the associate's proposal promised. | 1 | 2 | 3 | 4 | 5 |
| 4. | This SREP report addresses area(s) important to the USAF | 1 | 2 | 3 | 4 | 5 |
| 5. | The USAF should continue to pursue the research in this SREP report | 1 | 2 | 3 | 4 | 5 |
| 6. | The USAF should maintain research relationships with this SREP associate | 1 | 2 | 3 | 4 | 5 |
| 7. | The money spent on this SREP effort was well worth it | 1 | 2 | 3 | 4 | 5 |
| 8. | This SREP report is well organized and well written | 1 | 2 | 3 | 4 | 5 |
| 9. | I'll be eager to be a focal point for summer and SREP associates in the future. | 1 | 2 | 3 | 4 | 5 |
| 10. | The one-year period for complete SREP research is about right | 1 | 2 | 3 | 4 | 5 |

****USE THE BACK OF THIS FORM FOR ADDITIONAL COMMENTS****

LAB FOCAL POINT'S NAME (PRINT): _____

OFFICE SYMBOL: _____ PHONE: _____

PERFORMANCE ENHANCEMENT FOR
A TI TMS320C40 VERSION OF MULTIGRAPH

Ben A. Abbott
Research Faculty
Department of Electrical Engineering

Vanderbilt University
400 24th Avenue South
Nashville, TN 37235

Final Report for:
Research Initiation Program
Arnold Engineering Development Center

Sponsored by:
Air Force Office of Scientific Research
Bolling Air Force Base, Washington, D.C.

December 1993

PERFORMANCE ENHANCEMENT FOR
A TI TMS320C40 VERSION OF MULTIGRAPH

Ben A. Abbott
Research Faculty
Department of Electrical Engineering

Abstract

This research concentrated on completing the Multigraph port to the Texas Instruments TI320C40, enhancing its performance, providing needed tools, and reevaluating the result. Results from our prior work were used to guide the choice of areas in need of significant improvement.

The need for this research became apparent through participation in the 1992 Summer Research Program (SRP) at Arnold Engineering Development Center (AEDC). A major goal of the research was to provide tools for the Computer Assisted Dynamic Data Monitoring and Analysis System (CADDMAS) project. Results of this work include several tools for the TI TMS320C40 aiding in many of the AEDC parallel instrumentation/Multigraph problems.

PERFORMANCE ENHANCEMENT FOR A TI TMS320C40 VERSION OF MULTIGRAPH

Ben A. Abbott

INTRODUCTION

This research concentrated on completing the Multigraph port to the Texas Instruments TI TMS320C40, enhancing its performance, providing needed tools, and reevaluating the result. Results from our prior work were used to guide the choice of areas in need of significant improvement.

The need for this research became apparent through participation in the 1992 Summer Research Program (SRP) at Arnold Engineering Development Center (AEDC). This report documents the results of a follow-up grant (mini-grant) awarded as an extension of the SRP.

For the reader unfamiliar with CADDMAS or the Multigraph Programming Environment, background information may be found in the final reports delivered at the end of the Summer Faculty Research Programs (1988 through 1992) written by this same author. That reader may wish to read that background information before tackling the specific steps and results sections of this document. However, a quick description of the CADDMAS project and motivation for this research is found in the next section.

Further, while this study performed tests on and developed code for the TI TMS320C40 (C40) processor, it would be out of scope and quite lengthy for this document to try to describe all of the details of programming the C40. Rather, the reader will want to be familiar with the information found in the C40 data book [5].

MOTIVATION

Although programming environments and tools are fundamental research issues of parallel processing, a large-scale parallel application, CADDMAS, is responsible for the current focus. AEDC has developed and is currently using this large (200 Mega-Flops), transputer-based, parallel data acquisition and analysis system for turbine engine tests. However, a future system providing real-time monitoring with a performance in excess of 2 Giga-Flops is desired.

Several thousand sensors are commonly used during a turbine engine test. These devices generate large quantities of data that must be quickly analyzed and stored for later recall. On-line computations include: conversion to engineering units, filtering sensor readings, and computation of performance parameters such as Mach number, flow rates, and aggregate pressures. The previous Arnold computation platform consisting of a Cray 1-S and several Modcomp computers was incapable of meeting the real-time demands of current turbine tests.

Vanderbilt has cooperated in this effort since the Summer of 1988. The role of Vanderbilt is to provide a flexible/graphical programming environment (Multigraph) for this parallel system. The key principals of the Multigraph include:

- Providing a virtual machine consisting of a set of heterogeneous connected processors. The user should not be overburdened with the complexity of all the processors and their interconnections.
- Provide a multiple aspect modeling environment allowing the instrumentation system desired to be programmed (or modeled) in a declarative fashion rather than an algorithmic fashion. The declarative models are used by a special interpretation process to automatically generate the executable system.

The Multigraph has proven to be a quite valuable tool aiding the development of the CADDMAS software. Further, the TI TMS320C40 will provide a tremendous growth

path beyond the transputer system.

However, moving to the TI processor will encounter difficulties (and has already). In fact, the weak TI software environment is reminiscent of the early transputer environments. Using combined experience from this early TI performance research, as well as our extensive use of transputers, the following list of problem areas was compiled:

1. There is no equivalent of the transputer utility programs:

- *check* for verifying network configuration.
- *ld-net* for loading a set of programs onto the processors.
- *ckmon* for networked based, low level, debugging.

These programs were crucial for the successful deployment of the transputer based AEDC systems. A software environment sold by 3L provides the *ld-net* function; however, is deeply rooted in an Occam-like style and is difficult to use with the Multigraph (as well as the JTAG debugger). The other tools simply did not exist at the beginning of this research effort. Transtech has recently released a tool similar to the INMOS check, "tcheck".

2. Porting existing C code to the TI often proves to be difficult due to the "non-standard" `sizeof(long) / sizeof(char)` ratio. On the TI, the only addressable memory unit is a 32 bit word resulting in: `sizeof(double) == sizeof(float) == sizeof(long) == sizeof(int) == sizeof(char) == 1`. It is a common assumption of C programmers that: `sizeof(double) == 8`, `sizeof(float) == sizeof(long) == 4`, `sizeof(int) == 4 or 2`, and `sizeof(char) == 1`. This assumption has proven to be reasonable, until the TI. The result is that reuse of public / pre-existing code for the TI will often require a major rework. As well, all expected TI communication with other processors such as PCs or transputers must be carefully worked.

3. Use of the TI communication links in a half-duplex fashion (only sending one direction at a time) provides a 16 MegaBytes/Second bandwidth under DMA control. However, using full duplex transfers drops the aggregate bandwidth to 12 MegaBytes/Second (6 each direction). All of the AEDC/Multigraph applications regularly perform bidirectional transfers.

This nonlinear bandwidth drop will have dramatic effects on programs that load the communications heavily (even if the load is only a peak load). Linear prediction models will fail to correctly predict actual performance. Consider an application requiring 10 Mbytes/second in one direction and only 4 Mbytes/second in the opposite direction. This system might run perfectly for hours; as long as timing does not request a bidirectional transferring of data. However, if timing edges slowly such that a small bidirectional transfer overlap begins to occur, the overlap can then grow in an accelerated fashion since each added overlap portion decreases the overall possible bandwidth. At the overlap limit case for this example, the system would fail since 14 Mbytes/second exceeds the bidirectional bandwidth available.

This problem did not exist in the transputer platforms since it provides “true” full duplex transfers.

The research concentrated on breaking ground for the anticipated TI based AEDC applications by attempting to tackle these problems in a way that provided software development tools.

This document proceeds by providing a step by step description and result discussions of the research steps performed. Then, the conclusion section attempts to combine this information into a concise summary.

DEVELOP UTILITY PROGRAMS: CHECK, LD-NET, and CKMON

The bulk of this research effort was expended developing the TICK (TI Check) utility program for TI TMS320C40 networks. In cooperation with a team of programmers spread across the world and connected by the internet, a C40 network test program was developed and enhanced, TICK. Due to the multiple programmer approach adopted, this tool is now robust, well tested, and supported on several platforms: Sun VME Hunt boards, Transtech TDMB408 and TDMB409 (a port was made to the Transtech TRAM based C40 module but dropped due to lack of interest), Sang MegaLink, SunOs, Unix, Linux, DJGCC, and VxWorks.

TICK provides all of the functionality formerly provided by check and ld-net for the transputers with the exception of a memory test suite. However, it was recently reported that Sang computers has provided such functionality. If so, it will soon be incorporated into TICK.

In an effort to provide a tool like ckmon, TID (TICK Debugger) was developed. When there are over three processors, the TI JTAG based debugging environment begins to fall apart: long chains of processors are not allowed, loading time dramatically increases, processor names do not track loader names, and the emulator software becomes cumbersome. TID is a simple tool that allows residual global variables of a suspected program running on a processor to be inspected. TID is based on the loader portions of TICK, however, loading functions have been replaced with inspection functions (reading and writing memory). Therefore, processor names/node numbers follow exactly the same names as were used by the TICK utility to load the network. Testing of the TID program has been sparse, however, it has proven to be quite useful for debugging and appears to work correctly.

Details of the TICK and TID programs follow:

- The TICK program provides three basic functions: network exploration, network loading, and dumb terminal output.

When exploring, the TICK program is responsible for resetting a C40 network from the host computer interface, squirting a program onto the network of processors that will “worm” around and find what is out there, and collecting and tallying the results of the worm’s search. In order to write a network check program, care must be taken to assume as little as possible about the processors that will be found in the network. For this purpose, only on-chip RAM is utilized by TICK. This restriction puts a serious size limitation on the “worm” portion. When network loading, TICK is responsible for placing executables on each of the processors of a known network. A similar size requirement occurs here as well. That is, the network must be bootstrapped by a small “worm” that will subsequently take commands from the host to fill portions of processor memory with the correct values. Obviously, it is best if the “worm” code itself does not use up part of the off-chip RAM. The TICK loader provides automatic ID ROM based initialization and memory zeroing functions. These functions were not needed on transputer networks since the DRAM refresh timing and memory size support is not provided by software. However, for the C40 TIM standard, the network loader is responsible for reading the TIM ID ROM and initializing the processor accordingly before any external bus operations (ie. not accessing the internal Ram or registers) are used. Additionally, TICK provides a dumb terminal (output only) mode for debug. In this case, raw words read from the C40 to Host port are displayed on standard out as a series of characters or numbers. This functionality is nice when debugging simple programs such as a data generator that is trying to simulate an A/D coming in a communication port.

TICK has been given version numbers. Version 1.0 could only find a network of less than 16 processors. Version 1.2 was ported to the Sun and cleaned up. Version 2.0 is the current version and supports network loading.

TICK uses INMOS style link drivers as a standard way to access host to root

C40 functions. This makes it easy to port to other hardware platforms. The link driver code is typically less than 100 lines of C. Functions to reset the network and test and read/write words through the interface are all that need to be provided.

Only TI C and a native Ansi C for the host environment are necessary to compile TICK.

The following output illustrates how to run the program under DOS to search a network:

```
c:\> tick

TICK v2.0  TMS320C40 parallel network detection utility
Copyright (c) 1993 Vanderbilt University
```

#	TYPE	MHz	LINK0	LINK1	LINK2	LINK3	LINK4	LINK5	GMEM	LMEM	FMEM
1	00120001-000C	40	'2:3	''''	''''	HOST	''''	'2:2	4096Kb	4096Kb	8Kb
2	00120002-000A	40	'3:3	''''	'1:5	'1:0	''''	'3:2	4096Kb	4096Kb	8Kb
3	00120002-000A	40	''''	''''	'2:5	'2:0	''''	''''	4096Kb	4096Kb	8Kb

This output indicates that the network connected to this PC has 3 C40's in it. They have been numbered 1 to 3. C40 #1 is connected to the PC host through its link 3. Link 0 of C40 #1 is hooked to Link 3 of C40 #2, etc.

Several items read from the TIM ID Rom are displayed:

1. The type identifier says that Processor #1 has a manufacturer id of 0012 (Hex), model id is 0001 (Hex), Revision level is 000C (Hex).
2. The speed is indicated under the MHz label.
3. The Memory size values for Global, Local, and on chip RAM are also provided.

The full TICK syntax appears below:

Syntax:

```
tick [-v] [-Fsss | -Lsss | -T | -TL | -i | -N] [-pXXX]
```

-i = print C40 IDROM Information

-v = verbose mode

-pXXX = use hex i/o port XXX, 150, 300, etc.

-T = provide a dumb output port of ascii to stdout

-TL = provide a dumb output port of longs to stdout

-Lsss = load a network as described by contents of file sss

-Fsss = build a network load file to flood with file sss

-J = pause before starting programs to allow JTAG breakpoints

-N = do not zero C40 memory during load

Using the “-i” switch provides a full ID ROM print out of each module.

We have patterned this interface after the INMOS “check” program. (All code here is new and is not based on the INMOS code.) Therefore use of the Vanderbilt APNA tool to graphically inspect/modify TI C40 networks is now possible.

- This section illustrates the capabilities and features of the loader by describing some examples.

The loader works in a two stage broadcast based fashion. That is, it first bootstraps the network (using the TICK functions provided for exploration). The bootstrap code, stack, and data all fit within the two on chip RAM sections

of the C40 (yet it is all C code, good job TI). Once the network has been bootstrapped, the C40s begin to process loader messages. The bootstrap process has left the network connected in an acyclic tree starting from the host. This tree is used for the broadcast functions. The host sends packets out that indicate the recipients (via a bit field), the function to be performed, and the data to perform the function with. All packets go to all processors. If a packet recipient field does not match a particular node number, that node ignores the packet. There are really only two types of packets used during the loading process: DATA packets, and the START packet.

Most people like examples to understand how to use a software tool. We have provided a few simple examples to help in a subdirectory examples¹. To build the examples use Turbo C make "make -fmakefile.dos". You may have to modify the .cmd files if your TIMs do not have RAM on the local bus or if it is in a strange place (like on strobe 1). To run an example type exam1.bat or exam2.bat or exam3.bat (I trust unix guys know the drill here). Exam1 is a simple argc, argv, string output example. It should print out the args described in the exam1.bt file. Exam2 uses the flood load functions of TICK to use all of your processors to count prime numbers (give it some time to finish). Exam3 also uses the flood load functions but in this case it checks to see what processors have checked in.

Look at the examples, then look at the documentation, then look at the examples again. This should help you understand how to use the loader.

In order to provide a simple output interface, TICK can go into a dumb display terminal mode. "tick -T" tells the host to go into this mode. Each TI character (4 bytes) received by the host will be sent to standard out. In this case, the most significant 3 bytes are dumped. "tick -TL" is similar but prints the value of the longs (4 bytes) received by the host to standard out. In this case, the

¹Listings of the source code are provided as a special appendix to this document

values are printed in both HEX and base 10.

Loading code onto a network of processors is done by calling: *tick -Lfile.bt*. Where *file.bt* is a text file indicating how to load the network. Its format is described below. The booting process involves two stages:

1. Stage one sets up an acyclic broadcast tree to receive download commands on all C40s. During this bootstrap stage, all local and global RAM described in the ID ROM of each TIM bootstrapped is initialized to the 0 integer value. As well, ID ROM information is used to initialize the control register values of each TIM as necessary.
2. Stage two accepts download packets through the broadcast tree that direct each processor to fill memory with its code as needed.

The loader only uses on chip RAM of the C40s for its functions. However, it uses almost all of the on chip RAM. Therefore, initialized user code must NOT use the on chip RAM area. Results of doing so will be quite strange lock ups, etc.

Since stage 1 initializes the processor control register values, the file loaded onto each processor need only match the available memory constraints. Beware, there is no run time checking to see that the user has not exceeded his available memory. However, the TI linker allows you to do a good job here at link time. Files to be loaded may be generated with the TI linker *lnk30*. The “makeload” program described below is used to transform output files from the *lnk30* into “.dwn” files acceptable to the loader.

After we started using the JTAG debugger, a “-J” switch was added to pause loader execution just before user program execution begins. In this way, the TI emulator may be started after the code has been initialized and downloaded. Therefore, breakpoints may be set correctly. There are several issues that must be considered when using JTAG and TICK:

- After EMU40 has been used, EMURST must be executed before TICK can access the C40 since the emulator grabs the reset.
- The EMU40 “sload” command should be used rather than the “load” command since the code is already in the processor.
- No processor hardware reconfiguration commands should be issued (watch out for these in your emuinit.cmd)
- When EMU40 comes up the processor will be executing code in the on chip RAM, this is the loader code. If you want to single step through your application set a breakpoint at main (“ba main”) and then “run”. Next, release the tick loader by typing a key in that window. Your breakpoint will then be hit.

The boot file tells the loader the specific C40 executable file (.dwn file made with the makeload “-B” switch) to place on each of the different processors in the network. The boot file also indicates the path the loader should use to bootstrap the network. The boot path information makes the format of boot file somewhat complicated. We use a graphical tool to generate these files (as well as, 3L wire list files) directly, GCM.

Rules concerning “.bt” file format follow:

- Comment lines are allowed in the .bt file. Valid comment lines must have a “;” character in the first column.
- No lines should be longer than 132 characters (including all parameters)
- All other lines have the following format:

```
<booter> <booty> <booter_channel>    <.dwn file> [arguments]
```

Only the arguments are optional. These are the values that the C program on the processor **booty** will see as arg(1), arg(2), etc. Arg(0) is the “.dwn”

file name.

Booter is the node number of the processor that will boot node **booty**. There must be a physical communication port connection between the **booter** and the **booty**. **Booter_channel** is the communication port number 0 to 5 that **booter** should use to boot **booty**. **Dwn file** is the executable that will be loaded onto **booty**.

Node numbers (the values given to **booter** and **booty**) must begin with 1 and end with the number of processors to be loaded. No gaps are allowed. The host computer (the PC or SUN) is always indicated as node number 0. On a PC, the only valid **booter_channel** is 0, the PC to C40 link adaptor. We do not have a SUN, however, we think it may be possible to specify different **booter_channels** for the host. The rest of this documentation ignores this possibility.

The order of **booter-booty-booter_channel** triples must describe a valid depth first search of a spanning tree of the network to be loaded starting from the host. This means that the **booter** on the first non-comment line should be 0 and its **booter_channel** should also be 0. **booty** of this first line is typically given a value of 1 but may be any number that fits the previously given requirements. The next line should indicate the first processor that **booty** is to boot as well as the communication port of the first **booty** that must be used to boot the next processor. And so on.

Incorrect boot files will typically fail in one of two ways:

1. The loader will hang while trying to bootstrap a particular processor because no response is given. This is the failure mode that is seen when there is no processor connected to a port that was indicated as a **booter_channel**.
2. A message saying something about an error bootstrapping node "X" because node "Y" was found in its place. This happens when the boot file

indicates two paths to the same node. In this case, the attempted second bootstrap of the node causes the error. This error also happens when the “depth first spanning tree” rule is not followed.

A simple way to generate a correct boot file for a network is to use the “tick -Ftest.dwn” command. This command will spit out a valid boot file for the network found. In this case, the boot file automatically generated will be set up to flood the network of C40s with the executable “test.dwn”.

At the end of the booting process, the global variables defined in the C startup code (“low_main.c”) are set. These variables include:

```
long  _node_number;  /* the number assigned to a <booty>  */
long  _boot_chan;    /* the comm port booty was booted from.
                     This is NOT the <booter_channel>.
                     Rather, it indicates an acyclic path
                     toward the host and can be most
                     powerful for farming applications. */
long  _broadcast_mask; /* a bit field indicating each of the
                     comm ports that were used by this
                     node number as <booter_channel>s.
                     Bit 0 (the least significant bit)
                     indicates whether or not comm port 0
                     was used to boot a processor, and so
                     on.  The broadcast mask is also
                     useful for farming applications in
                     that it describes an acyclic tree
                     that may be used to broadcast packets
                     out to worker processors.          */
```

As well, argc and argv are set in the usual C fashion. By allowing the user

to provide unique arguments for each loaded processor, the personality of the loaded code may be customized without having to load a unique “.dwn” file for each processor. The big advantage of using this technique is load time. Each unique “.dwn” file need only be downloaded once regardless of the number of processors that should be loaded with its code.

Further, to make it easy to write simple low level programs, a few simple I/O functions are provided by “low_main”:

```
void _low_put_long( long port, long value );
/* sends a long out a comm port.  It will hang if the queue is
   full until room is made for the new long to be inserted.  */

void _low_put_string( long port, char *str );
/* sends a string.  */

long _low_get_long( long port );
/* reads a long from a port.  It will hang until the read is
   complete.  */

long _low_test_read( long port );
/* checks to see if a call to _low_get_long() will hang */

long _low_test_write( long port );
/* checks to see if a call to _low_put_long() will hang */

void _low_config(int on)
/* A routine to toggle the light (or whatever) */
```

TICK can be used to act like a flood loader, a loader that automatically finds and fills all processors of a network regardless of its size or connection structure. However, it really is not a flood loader. Rather, flood loading involves two unique invocations of TICK. Invocation one searches the network with the standard TICK functions to find all of the processors and their interconnection structure. These results are output to a file in the format of a valid “.bt” file for the network. Invocation 2 loads the network as indicated by the just generated “.bt” file.

Invocation one:

```
tick -Ffile.dwn >flood.bt
```

will generate a “.bt” file that will flood the network with the file “file.dwn”.

Invocation two:

```
tick -Lflood.bt
```

will actually load the network.

A side effect of invocation 1 is the generation of a file “ti.mp” in the current directory. This file describes a shortest path type of virtual communication path that we use for our internal Vanderbilt message passing system.

The makeload program transforms output from the TI linker lnk30 into various download formats. The input file should always be a fully referenced, absolutely located COFF file with a start address. It should have been linked with the ROM initialization option (by doing this you can slip the constants for your FFT into the on-chip RAM). Further, if you are trying to use the loader portion of TICK, you will want to link to the low_main.o40 file provided.

Syntax:

```
makeload [switches] lnk30.out makeload.out
```

Switches:

- B produce a file acceptable to the TICK loader.
- T produce a file in the format valid to bootstrap a reset TI down a raw link.
- C produce a file of C code of an initialized array of longs describing the boot stream of data.
- Z add explicit code to the download file to initialize the stack, bss, and heap sections to integer value 0.

Typical call for use with the TICK loader:

```
makeload -B user_prg.out user_prg.dwn
```

The “-Z” switch is useful if your ID ROM is strange and does not really tell how much RAM you have. In this case, the loader can not always figure out how much RAM to initialize to 0.

The “-C” and “-T” switches are used to generate the executable TICK program. In this case, C code is produced that is included for execution on the host. That code is an array of longs that when spit into a reset C40 causes it to come to life and run the TICK and loader functions. If you plan to hack in this area, please look at the code for tick and makeload.

- The TID program is based on the TICK program and is used to provide *ckmon*

like functions. In particular, it may be used to read and write memory of any processor in a C40 network. A TICK ".bt" file must be provided by the user to direct TID to the node of interest. Typical use is illustrated below:

```
C:>\release\bin\tid -Dafire.bt
```

```
TID v2.0    TMS320C40 parallel network detection/loader utility
```

```
Copyright (c) 1993 Vanderbilt University
```

```
Using <afire.bt> for boot information
```

```
Node to debug? 3
```

```
Attempting to Bootstrap    3 Nodes
```

```
Bootstrapping Node    1 via Node    0's link 0
```

```
Bootstrapping Node    2 via Node    1's link 1
```

```
Bootstrapping Node    3 via Node    1's link 4
```

```
TICK Debugger
```

```
Node[3]> ?
```

```
Commands:
```

```
    r <hex address>                [ to read a value ]
```

```
    w <hex address> <hex value>    [ to write a value ]
```

```
    return uses incremented address with previous value
```

```
    q                                [ to quit ]
```

```
Node[3]> r 300000
```

```
300000 -> 0x3434343 == 17219
```

```
Node[3]>
```

The full TID syntax appears below:

Syntax:

```
tid [-v] [-Fsss | -Lsss | -T | -TL | -i] [-pXXX]
```

-i = print C40 IDROM Information

-v = verbose mode

-pXXX = use hex i/o port XXX, 150, 300, etc.

-T = provide a dumb output port of ascii to stdout

-TL = provide a dumb output port of longs to stdout

-Dsss = debug a network as described by contents of file sss

-Fsss = build a network load file to flood with file sss

The “-Dafle.bt” switch tells TID to use the “.bt” file to direct its way down to the processor of interest. The syntax of this file is exactly the same as that of a “.bt” file for TICK. For TID “.bt” files, the “.dwn” file position must be filled but the actual “.dwn” file need not exist since it will not actually be loaded. The syntax was chosen in this way to allow a user to use the same “.bt” file for loading and debugging. TID asks for the node of interest during initialization. It only loads the sub-network described by the “.bt” file before reaching the processor of interest.

Due to the availability of TID, “n9_2_fatal()”, the error catching routine of the Multigraph communication network, was modified so that TID can be used to catch run time errors on all processors. “n9_2_fatal()” now writes to the location “n9_2_fatal_value”. Find this value in your map and use TID to check the error code.

Some warnings about the use of TID:

- DRAM is not always going to hold the old values since the network is reset and then restarted. Thus, processors that are far away from the root (ie. take a long time before they are bootstrapped) will often lose their contents while the refresh is stopped. Important values can be copied into the on-chip RAM.
- Since TID uses the on-chip RAM to “worm” itself across the network, only the last 16 words of the second on-chip RAM bank may be recovered by TID.

TID is source code and functionality is identical to TICK with the exception of loader DOWN and START packets. Instead, these have been replaced with READ and WRITE packets.

LOOK FOR A SOLUTION TO THE BYTE SIZE PROBLEM

In an effort find a reasonable solution to the word only addressing of the TI C compiler, the Helios C compiler for the Sun was purchased. The Helios compiler uses, at the cost of performance a code generator that produces code that accesses actual bytes via “shifts”, “masks”, and “or’s”.

Upon looking at the code output by the compiler it was easily apparent that this solution would be quite difficult to implement since the compiler relies heavily upon runtime functions provide only within the Helios environment.

Rather than continue striving after such a difficult (and unreachable during the current time frame) goal, engineering solutions were developed to ease the byte transition problem for CADDMAS code. The solutions include:

- The file I/O functions of the Multigraph communication look at the file type (ascii or binary) and pack bytes accordingly.
- C macros using a multipler of sizeof(int)/sizeof(char) are used throughout the CADDMAS code wherever communication or I/O occur.
- All interface routines requiring parameters defining the size of an object of interest always use BYTES regardless of the platform: transputer, PC, or C40.
- Very fast byte read accessing of variables on the C40 may be accomplished with C bitfields. That is:

```
typedef struct word_struct
{
    char byte_a:8;
    char byte_b:8;
    char byte_c:8;
    char byte_d:8;
```

} WORD;

With these simple rules, and a painful walking through all of the CADDMAS, communication, and Multigraph code, the byte problem is now gone for the TI CAD-DMAS. Future applications need to follow this same approach.

CONCLUSIONS

The code produced during this research effort is already in use on the CADDMAS project. We have used it a countless number of times. The solutions given for the byte size problem although not elegant do work. It is still worthwhile to watch for a better solution to these problems since the TI network seems to be targetted toward non-CADDMAS projects.

ACKNOWLEDGEMENTS

I wish to thank the Air Force Material Command and the Air Force Office of Scientific Research for sponsorship of this research. Research Development Labs must also be commended for their concern and help to us in all administrative and directional aspects of this program. My experience was rewarding and enriching because of many different influences. The help of Tom Tibbals was invaluable in overcoming many technical roadblocks.

* A separate source code appendix includes:

boot.asm	: basic entry point for C40 codes
boot.o40	
check.c	: Host computer codes directing C40 search and load functions
check.obj	
checkti.c	: C40 codes to handle host requests in search and load
checkti.map	: lnk30 output map for C40 executable
checkti.o40	
checkti.out	: lnk30 output COFF for C40 executable
defaults.h	: Common flags for host and C40 side
dos.cmd	: C40 lnk30 command file for PC versions
hes.cmd	: C40 lnk30 command file for Hunt Sun version
hesio.h	
heslink.c	: Device driver interface routine for Sun version
hevlink.c	: Device driver interface routine for other Sun version
linkio.h	: Device driver interface routine prototypes for all versions
low_main.c	: Basic C40 startup program to handle argc, argv, etc.
low_main.o40	
makefile.gcc	: Makefile for DJGCC a 32 bit DOS C compiler
makefile.hes	: Makefile for Sun
makefile.lnx	: Makefile for Linux (pc Unix)

```

makefile.sun      : Makefile for other Sun
makefile.tcc      : Makefile for DOS (Turbo C)
makeload.c        : The makeload utility for transforming TI COFF
                   to .dwn files
makeload.exe      : MAKELOAD for DOS compiled with Turbo C
makeload.obj
readme            : Some documentation
ship.bat
sun.cmd           : C40 lnk30 command file for other Sun version
swap4.c           : Out of date utility to flip byte order for
                   old Sun version
t408link.c        : Device driver interface routines for all
                   PC versions
t408link.obj
tick.c            : Top level Host computer side (parses args etc.)
tick.exe          : TICK V2.0 for DOS compiled with Turbo C
tick.h            : The file CHECKTI.OUT transformed to C code array
tick.obj

```

* Examples

```

examples\exam1
examples\exam1.bat
examples\exam1.bt
examples\exam1.c
examples\exam1.cmd
examples\exam1.dwn
examples\exam1.map

```

examples\exam1.o40
examples\exam1.out
examples\exam2
examples\exam2.bat
examples\exam2.c
examples\exam2.cmd
examples\exam2.dwn
examples\exam2.map
examples\exam2.o40
examples\exam2.out
examples\exam3
examples\exam3.bat
examples\exam3.c
examples\exam3.cmd
examples\exam3.dwn
examples\exam3.map
examples\exam3.o40
examples\exam3.out
examples\makefile.dos

References

- [1] Biegl, C.: "Design and Implementation of an Execution Environment for Knowledge-Based Systems" Ph.D. thesis, Department of Electrical Engineering, Vanderbilt University, Nashville, TN., Dec., 1988.
- [2] Abbott, B., Biegl, C., Sztipanovits, J.: "Multigraph for the Transputer", Proc. of 3rd Conf. The North Amer. Transputer Users Group, Santa Clara, Calif., April 1990.
- [3] INMOS Limited: Transputer Reference Manual, 1989.
- [4] SONITECH International, Inc: SPIRIT-40/ISA User's Guide, June, 1992.
- [5] Texas Instruments Incorporated: TMS20C40 User's Guide, 1992.
- [6] Zoran Corporation: ZR34345 32-Bit IEEE Floating-Point Vector Signal Processor User's Manual.

SYSTEM INTEGRATION SOFTWARE FOR PARALLEL
HARDWARE ARCHITECTURES

Csaba Biegl
Research Assistant Professor
Vanderbilt University
Department of Electrical Engineering
Box 1649 Station B
Nashville, TN 37235
(615) 343 - 8197

Final Report for:
Research Initiation Program
Arnold Engineering Development Center

Sponsored by:
Air Force Office of Scientific Research
Bolling Air Force Base, Washington, D.C.

January 1993

SYSTEM INTEGRATION SOFTWARE FOR PARALLEL
HARDWARE ARCHITECTURES

Csaba Biegl
Research Assistant Professor
Vanderbilt University

Abstract

This report describes work done on the issue of system integration on parallel hardware architectures. First an overview is given of the CADDMAS system which is the application domain for the results of this work. Results from prior work in the areas of model-based system specification, hardware modeling, and parallel execution environments are described to provide a context for the work performed. Finally, additional new tools to this environment are described which were implemented in order aid the creation of large scale parallel processing systems, like CADDMAS. A summary of the results and possible future research directions conclude this report.

SYSTEM INTEGRATION SOFTWARE FOR PARALLEL HARDWARE ARCHITECTURES

Csaba Biegl

Introduction

During ongoing research efforts, parts of the Multigraph Architecture have been used in various parallel applications at the Arnold Engineering Development Center (AEDC). These AEDC research efforts include: the Computer Aided Dynamic Data Monitoring and Analysis System (CADDMAS), a Transient Data Processing System, and feasibility studies in image processing applications. A common feature of all these applications is that they implement a highly parallel complex computational network using a large number of parallel processors. For example, the largest CADDMAS system currently uses on the order of 100 processors (Inmos Transputers, Texas Instruments TMS320C30 and TMS320C40 processors, and high speed special purpose digital signal processing chips). Planned future configurations will have several hundred processors. The work described in the report is based on the needs of the CADDMAS system, but it may have applications in the other domains as well.

The Multigraph Architecture is a comprehensive software environment developed at Vanderbilt University for building large-scale parallel engineering systems like signal processing, process monitoring, etc.. applications. It aids the creation of such applications in several ways:

- 1) Macro-dataflow parallel execution environment: A component of the Multigraph Architecture, the Multigraph Kernel, provides an execution environment in which parallel applications can be built from sequential user-supplied procedures (also known as scripts) using the dataflow computational model. The Kernel supports parallel execution on a variety of multiprocessor hardware architectures: shared memory systems, networks of UNI workstations, and transputer networks. Code written for the Kernel

is highly portable as all programming details of the underlying parallel hardware (such as memory management, communications, etc..) are hidden from the application programmer. The Kernel permits the dynamic building of dataflow computational graphs, i.e. a running system can be altered, expanded during execution.

2) High-level modeling of computations: Another component of the Multigraph Architecture is a set of high-level modeling languages and their interpreters. These languages permit the user to describe the target system in an application-specific language. Interpreters for these languages are used to dynamically build run-time configurations from the high-level models under the control of the Multigraph Kernel. One such language is the Hierarchical Description Language (HDL) which can be used to describe complex signal processing systems. This language has been used in AEDC applications. A graphical model editor supplements the high-level modeling support in the Multigraph Architecture.

3) Hardware modeling: The third aspect of support provided by the Multigraph Architecture for parallel applications is a set of tools to model and analyze networks of parallel processors. A high-level modeling language (Multiprocessor Modeling Language, MPDL) is used to describe hierarchical networks of processors. The graphical model editor can also be used to edit MPDL models. Two associated analysis tools (the Automatic Parallel Network Analyzer, APNA and the Graphical Configuration Manager, GCM) are used to automatically generate optimal routing maps for the communication layer of the Multigraph kernel from high-level graphical representations of processor architectures.

It is anticipated that AEDC will build several versions of the CADDMAS system and possibly the spreadsheet and image processing applications, as well. These versions will use the existing operating system (Multigraph Kernel) and

application (data processing modules) software, but might run on different hardware architectures containing varying number and type of processors. This means that the system integration process has to be repeated any time a new system is built (or when the hardware configuration of an existing system changes).

Much of this task is performed automatically by the modeling and system integration components of the Multigraph Architecture. However, there are a few areas where the coverage of the previously available tools was not sufficient. The goal of this project was to implement the necessary software to permit fully automatic configuration of CADDMAS-like systems.

Problem Domain: the CADDMAS System

The Computer Assisted Dynamic Data Analysis and Monitoring System (CADDMAS) [3] [4] [5] has been developed for on-line data analysis of turbine engine tests in altitude test cells. During actual operation, the current 24 channel system continuously delivers 200 MFLOPS. This performance index, measured on the actual application program, exceeds the capabilities of many conventional high performance computers.

Testing turbine engines involves running an instrumented version of the engine through various operational maneuvers. These tests are typically conducted while the engine is in a wind tunnel capable of simulating altitude, atmospheric, and air speed conditions. In order to analyze dynamic vibrations, strain gauges are attached to the turbine fan blades. A typical aeromechanic stress test instruments the engine with several hundred stress sensors along with a variety of temperature, pressure, flow, and revolution per second sensors (see Figure 1). Stress sensors can generate signals with bandwidth in the tens of KiloHertz.

Historically, analysis of turbine engine stress data has been an off-line process. On-line capabilities were limited to oscilloscopes showing unprocessed amplitude vs. time information, and a small number of signal analyzers for simple spectral analysis on single channels. The bulk of the raw information was recorded onto analog tapes. Later, the data were digitized for analysis on

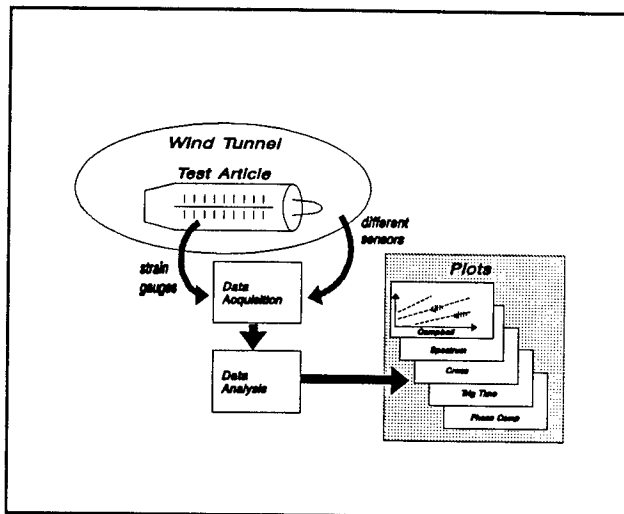


Figure 1. The CADDMAS system

conventional computers. The processing of this data was extremely compute intensive, and consequently, only a selected portion of the data was reduced. The analysis imposed a delay of several weeks on the availability of final results. Thus, vital information was not available for on-line test planning and evaluation.

The CADDMAS system was developed to provide these capabilities on-line. The system processes all sensor readings and presents the results both graphically and in hard copy form during the test. The immediate availability of results opens the possibility for interactive test planning.

A graphical user interface allows the user to configure various visualization screens interactively. The user can select the number of visible windows on a screen, the contents of each plot window, and the parameters of each plot, such as titles, labels, axis ranges, plot type, and update rate. Stored configurations automate the operation of the user interface. The user can also print these plots. The types of on-line plots generated by the CADDMAS system include:

- 1) Amplitude vs. Time plots represent the absolute stress on a blade over time. Calculation involves scaling the sampled A/D counts to engineering units and triggering the beginning of a display plot with a once per revolution pulse of the engine.
- 2) Spectral display with Full-Time Envelope Capture shows the energy of vibrations over a range of frequencies. The envelope continuously captures the historical maximum to ensure that no spectral activity is missed. FFT's are used to generate the spectral estimates. Frequency Tracking display shows the spectrum corrected by engine RPM. This is useful to observe synchronous vibrations over a range of engine speeds.
- 3) The Campbell diagram is a very important tool in the analysis of engine stress data. It is a three dimensional scatter plot of stress amplitude vs. frequency vs. RPM. It represents historical information over an entire test maneuver and provides a summary of the blade behavior in a single chart. Generation of a Campbell diagram involves sorting the peaks of all of the spectral estimates of a strain gauge across a test maneuver and keeping the "interesting" peaks. Interesting is defined per test maneuver and includes: minimum, maximum, and delta RPM of interest, minimum, maximum, and delta frequency of interest, and minimum stress amplitude of interest.
- 4) Phase Campbell diagrams show the phase angle relationship between two sensors vs. frequency vs. RPM. They incorporate information from two related sensors and can be used to help determine vibratory modes of an engine component.
- 5) Modified Campbell diagrams allow the engineer to visualize the stress behavior of the engine components as a function of any engine or

environmental parameter (instead of RPM) such as temperature, pressure, or time.

The CADDMAS system is used for testing different types of turbine engines. Since engine capabilities are constantly improving, testing scenarios are updated on a test-by-test basis. For each test, aeromechanical engineers specify the number, types, and accuracy of the desired plots. The CADDMAS must be open and scalable to meet these changing and unknown needs. Moreover, several engine tests may be performed in different wind tunnels at the same time. Therefore, the hardware resources available for a test may vary. The CADDMAS hardware consists of various computational building blocks which are modular so as to allow systems of various size and personality to be "plugged" together. These blocks include:

- 1) An INMOS transputer network for general purpose computing and to provide a basic message passing fabric. Some of these blocks have parallel port adapters for driving printers or reading a special real-time clock.
- 2) The Front End Processor (FEP) consists of a high speed 12 bit A/D converter multiplexed to sample four independent analog streams, and three Motorola 56001 processors for time and frequency domain threshold alarm generation, anti-alias filtering, and down sampling. The down sampled four data streams are broken into 1024 point ensembles and shuffled through a FIFO into a special parallel to serial converter chip, so they may be easily used as an input by other CADDMAS processing blocks.
- 3) The Numeric Processing Element (NPE) consists of an INMOS T800 floating point transputer with a Zoran 34325 floating point Vector Signal Processor in shared memory. 38 MFLOPS are achieved when computing 1024 point FFT's on the Zoran. The actual packaging of the NPE is such that 2 independent NPE's share a single VME board.

- 4) The user interface and system integrator capabilities are provided through Intel based 486 PC's with INMOS serial to PC Bus adaptor cards. Such PC-s are also used as high speed graphics displays for the generated plots.

The Multigraph Architecture

The Multigraph Architecture (MA) has been developed for building a broad category of model-based systems operating in real-time environments. The MA has been used as a framework for intelligent instrumentation [7] [8] [11], automatic test configuration [10], and process control [9] [12] systems.

Implementation of hierarchical control and signal processing systems requires the integration of symbolic and numerical programming techniques, different models of parallel computations, and various programming paradigms. A significant amount of research has been invested in the development of a real-time parallel execution environment, the Multigraph Architecture (MA). The purpose of this research has been the creation of a computing model and programming environment that allows the model-based dynamic configuration of real-time, parallel systems on various hardware architectures.

The MA is a layered architecture consisting of a builder layer, a module layer, a system layer, and a hardware layer. In current implementations, the hardware layer and the system layer are provided by a particular computing environment and are "external elements" to MA. Specific software components have been developed for the module and builder layers.

- 1) The hardware layer may include single processor systems, multiprocessor configurations, loosely coupled computer networks, and their combinations. The elements of the higher layers can take advantage of special hardware components, such as hardware accelerators and peripherals provided by this layer.

- 2) The system layer includes an operating system providing standardized access mechanisms to the hardware resources. In multiple processor configurations, the system layer facilitates task management, inter-task (inter-processor) communication, synchronization and real-time services. In current implementations of MA, the system layer is comprised of a message passing system running either under commercially available operating systems such as various Unix versions and MS-DOS, or stand-alone on processors like the Inmos Transputer or the Texas Instruments TMS320C40.
- 3) The module layer is an intermediate layer between the builder layer and system layer. Its primary function is to provide a virtual machine for the Multigraph Computational Model (MCM). The MCM is a parallel graph model of computation which supports medium or large computational granularity. In the MCM, the computations are mapped onto a bipartite control graph built from actor nodes and data nodes. The actor nodes represent individually scheduled computational units. The data nodes are associated with data structures moving along the graph. MCM is supported by a run-time system, called the Multigraph Kernel. This kernel allows the dynamic configuration and control of computational graphs and provides a data-flow scheduler, which schedules the elementary computational units (actor nodes) and allocates the processing resources to them.
- 4) The builder layer supports symbolic computations. A generic programming methodology has been developed for the design and implementation of hierarchical control and signal processing systems. The basic components of the methodology are as follows:
 - a) Declarative representation languages (and associated graphic editors) are specified for modeling the environment and different subsystems of hierarchical controllers,

- b) Interpreters are designed for the declarative languages which,
- c) Map the representations into an executable system in the Multigraph execution environment.

The Implementation of CADDMAS Using the Multigraph Architecture

CADDMAS is just one of the complex large-scale system implemented within the framework of the MA. However, its special requirements in the areas of computing performance and hardware architectures significantly influenced the way the tools of the MA were used to build it.

CADDMAS and the Multigraph Kernel

In order to understand the special coding techniques which were used to implement the CADDMAS system it is necessary to briefly overview the main features of the Multigraph Kernel [1] [2] [6] [13]. The Kernel can be considered as the distributed operating system under which CADDMAS executes.

The Multigraph Kernel is a system integration tool for building complex applications from precoded software modules using an extended macro-dataflow computational model. The parallel execution of these systems is possible in implementations where the underlying hardware architecture supports parallelism - either shared memory or distributed. The Kernel provides a full set of C interface functions for building, controlling and executing dataflow-based applications. It also includes an interactive command interpreter for stand-alone applications, and a Lisp interface for integration with symbolic programming environments.

Multigraph Kernel applications are specified in terms of their control graphs containing actor nodes, data nodes, and node connections, and an execution structure for assigning resources to run the nodes.

The actor nodes are the active components of the control graphs. These nodes perform transformations on the data being propagated in the control graph. The transformations performed by the actor nodes are called scripts. Scripts are implemented as procedures written in some high-level language (most frequently "C"). To create a Multigraph application, the user must provide a library of scripts and link them with the Kernel. The Kernel has a set of script interface functions for propagating data in the control graph, making it possible to write position-independent code for the scripts. The code of a script can be shared between several actor nodes provided that it was written in a re-entrant fashion. Each actor node has a local parameter structure called context, which can be used to customize the operation of the script or to store local data between successive activations of the node.

The function of the data nodes is to store the data produced by the actors. There are two data node types: stream and scalar nodes. The first type has a data stream attached to it which stores all incoming data in the order of arrival, while the scalar nodes store only the last data propagated to them. Data nodes may be connected to multiple input and output actor nodes. In the case of multiple inputs they merge the incoming data from all connected sources into a single stream which will then be read in parallel by all connected consumer nodes.

Both actor and data nodes have ports (either input or output), which are used to set up connections between them. The ports of the data nodes are not distinguishable, and their number is not limited. The number of ports of the actor nodes is determined when the node is created. The actor ports are distinguishable, since it is presumed that the script will use each port for a given function.

It is also possible to create a control graph in a distributed system with node connections across process boundaries. The Kernel will automatically

recognize these connections and use the message passing software libraries available on the host system to propagate the data in the control graph. These different communicating dataflow processes are called tasks and they have separate address spaces, schedulers and possibly even multiple threads.

Implementing the CADDMAS system using the Multigraph Kernel required several tasks to be performed:

- 1) Design of the signal flow graphs: The data processing requirements of the CADDMAS system (Fourier transforms, data collection steps, plot formatting, etc..) were analyzed and functional blocks which implement these were defined.
- 2) The functional blocks specified in Step 1 were implemented as Multigraph Kernel scripts. Many of the scripts are universal, they can be compiled and executed on any of the processor types from which the CADDMAS system is built.
- 3) Implementation of the signal flow graphs: Based on the available signal flow interconnect requirements, script execution speed and processor performance characteristics a Multigraph Kernel control graph was designed which, together with the elementary script codes implements the data processing required by the CADDMAS system. This control graph specifies all actor and data nodes, their interconnections and their placement on the available processors.

In theory, all of the above steps could be performed using the Multigraph Kernel alone. However, Step 3, the building of the Multigraph Application is a very complex and error prone task. The modeling techniques described next made this task manageable.

Modeling Environment for CADDMAS

In order to aid the creation of the distributed Multigraph Kernel control graph implementing the CADDMAS system two aspects of the system were modeled using the high-level graphical modeling tools provided by the MA:

- 1) Signal flow modeling: Every channel of the CADDMAS system is implemented with a signal flow graph containing several (on the order of 10) processing modules. Implementing this graph for every signal channel (24 or more) results in a quite large distributed signal flow graph. Using hierarchical modeling techniques the complexity of this graph can be made manageable. This is the approach supported by the Hierarchical Description Language (HDL) which was developed to model complex signal flow graphs. HDL is a so called Very High Level Language (VHLL) written for a narrow, very specific problem domain: modeling signal processing systems. The syntax of the HDL - as of any other VHLL of the MA - is based on the Lisp language. HDL models are built of primitives and compounds. Primitives are models of elementary signal processing routines. Primitive models represent the input and output data streams and the configuration parameters of these routines. Compound structures are built from primitives and other compounds and represent increasingly larger portions of the signal flow in a hierarchical manner. The graphical model builder of the Multigraph Architecture supports the creation of HDL models. There is also an HDL interpreter module which can be included in the run-time version of the application. The task of this interpreter is the building of the Multigraph Kernel control graph from the HDL models developed off-line. The HDL approach has proven extremely suitable for modeling the CADDMAS signal flow graph as there is a considerable regularity in it, due to the similarity of the processing required by each channel.
- 2) Hardware modeling: The same hierarchical modeling techniques which were used to model the signal flow can also be used to model the CADDMAS

hardware. Most processors in the system can be found in a few different sub-assemblies (i.e. cards). Modeling these cards in a hierarchical fashion reduced the overall complexity of the hardware model significantly. An other Very High Level Language, the Multiprocessor Description Language (MPDL) was used for this purpose, together with the generic graphical model building tools of the Multigraph Architecture. The MPDL models are used by a tool called the Automatic Parallel Network Analyzer (APNA). APNA can interpret the MPDL models, and using its hardware detection facilities it can verify that the models accurately reflect the available processors and interconnections. Another useful feature of APNA is the generation of communications maps for the message passing system used by the Multigraph Kernel. Although the original CADDMAS maps were generated by APNA, by now it has been replaced with a newer more advanced tool, the Graphical Configuration Manager (GCM).

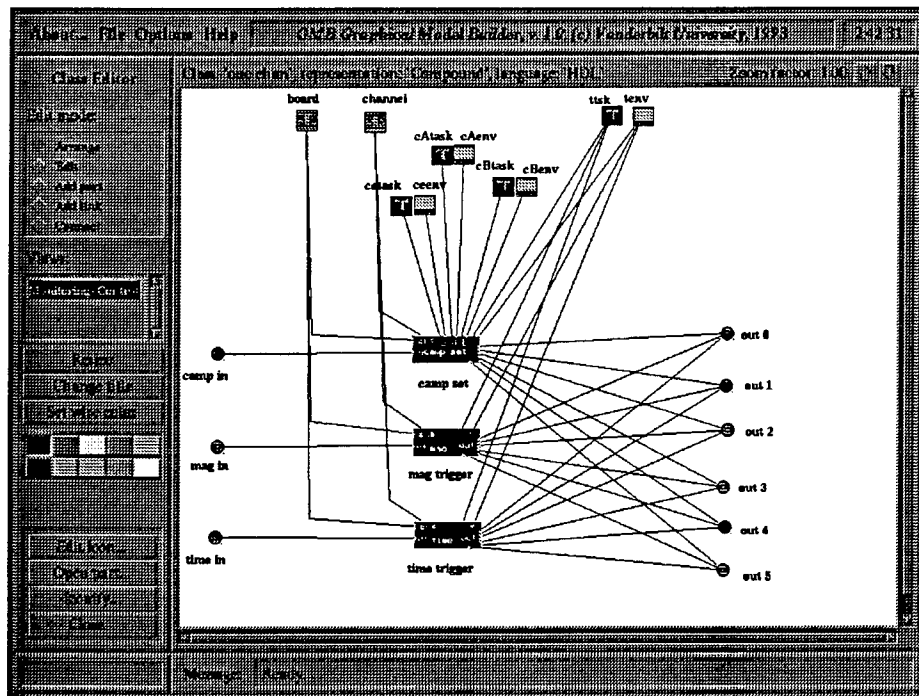
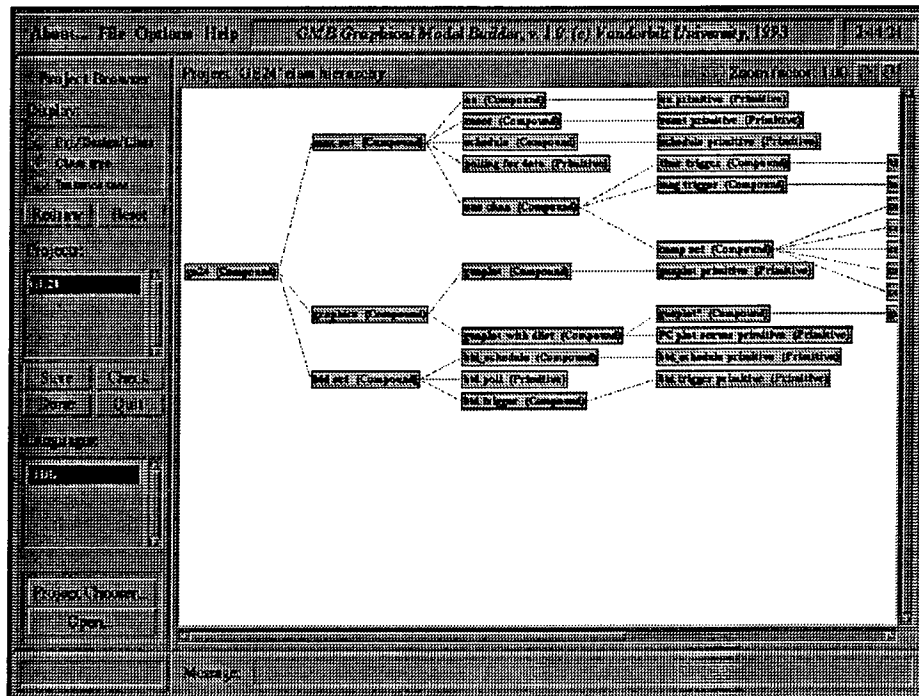
In summary, the signal flow and hardware modeling techniques made it possible to manage the complex signal processing graphs and hardware architectures of the CADDMAS system. The common feature of the two modeling aspects are the off-line graphical development of the models and the run-time interpretation of them in order to properly coordinate the operation of the various software modules on the parallel processor network.

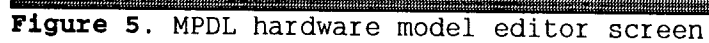
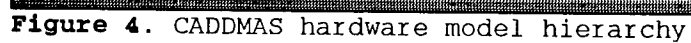
However, the modeling tools available in the Multigraph Architecture did not cover all aspects of the integration of the CADDMAS system. The implementation of the missing tools was the subject of this research.

New Tools for Parallel System Integration

The tools developed in the framework of this research address two open issues related to the CADDMAS system integration process:

- 1) Fully DOS-hosted development: The graphical modeling tools of the MA were originally developed on Unix workstations running the X Windows system for process monitoring and diagnosis applications. The first CADDMAS models were developed using these model building tools. Since the CADDMAS run-time environment is hosted by a DOS-based PC, the lack of a DOS-based model editor was inconvenient. The CADDMAS host PC has to run DOS for various reasons, including performance (no overhead of a multitasking scheduler) and easier access to special hardware (for example, the communication interface of the other processors). Since the original model building tool of the MA (XGEM) was very X and Unix specific, it was not worthwhile to attempt to port it. A completely new graphical editor (the Graphical Model Builder, GMB) was created which was designed to be portable. GMB is a customizable model editor: it can edit declarations in any of the available representation languages (including, of course, HDL and MPDL). GMB achieves this flexibility by providing a generic editing interface which can be customized by loading a descriptor package (called Editor Definition File, EDF) for the currently used modeling language. Such editor definition files can easily be created for new modeling languages if needed. The format of these definition files is common between GMB and the old MA model editor, XGEM. One significant improvement in GMB is the ability to load several language definitions in one session. (XGEM could work only with one language at a time.) After GMB was completed, the CADDMAS models were ported to DOS. (GMB is available under UNIX and X as well, but the CADDMAS models are best maintained under DOS for reasons described above.) This merely required changing some file names to conform to the DOS file length limits. Figures 2 through 5 show example GMB screens when working with the signal flow and hardware models of CADDMAS. Figure 2 shows the HDL declaration hierarchy of the CADDMAS signal flow models. The leaves of the tree are the elementary signal processing modules (primitives) from which compound modules of increasing complexity are built. GMB can display the declaration hierarchies of a





large system in the fashion shown in Figure 2 to aid the user in navigating the system. Other types of displays (for example, ordered by the file structure of the project) are also available. Figure 3 shows one of the compound declarations opened for editing. In this mode GMB allows the user to make changes using familiar graphical operations (click, drag, menus, etc...). Figure 4 shows the declarations hierarchy of the CADDMAS hardware models, while Figure 5 shows an MPDL multiprocessor declaration opened for editing.

- 2) Improvements to the HDL language: During the integration of the CADDMAS system a shortcoming of the HDL language was discovered: it did not provide sufficient control over the creation of the Multigraph Kernel data nodes. (The 'signal' concept in the HDL language roughly corresponds to the data nodes in MGK.) The Kernel allows extensive customization of data node behavior in order to meet the application's needs. From the point of view of CADDMAS the two most important customization options are the placement of the data node (i.e. on which distributed processor is it created) and the maximum allowed data stream length stored in the node. In previous applications of the HDL language these options were not important, thus the control of them is not part of the language. On the other hand, many processors in the CADDMAS system execute a set of signal processing modules whose total memory requirements is very close to the amount of available memory on the given processor. For this reason it is very important to control how these modules use memory via the Multigraph Kernel's data node control options. The necessary additions to the HDL language were defined and implemented. Additionally, the HDL editor definition file and run-time model interpreter were also updated to support these options.
- 3) Integration of signal flow and hardware models: In previous CADDMAS versions the hardware models were not used in the run-time environment for

building the Multigraph control graph of the system. This task was performed manually using a configuration file which predefined the processor assignments used by the HDL interpreter. The hardware models were used only by the APNA and GCM tools to create a communication maps for the message passing system. This fact made changing system configurations somewhat more difficult, since graphical techniques were not usable for this purpose. To support fully graphical modeling of the CADDMAS architecture using the MA two possible approaches were available:

- a) Develop a new modeling language which contains the features of both HDL and MPDL and rebuild the models in this language.
- b) Develop a modeling language which allows the creation of links between HDL and MPDL structures while leaving the respective languages intact.

While both approaches were feasible, the second solution was chosen in order to avoid rebuilding all existing models. There is precedent for this approach in the Multigraph Architecture: the Physical to Process model Language (PPL). That language was used in a model-based industrial process monitoring and diagnosis system. To model such a system two vastly different aspects (and languages) were used. One aspect was the Process Model (modeled by the Process Model Language, PML) which described all activities in the plant and their interactions, failure states, etc... The other modeling aspect was the Physical Model (modeled by the PHYSical system modeling language, PHY) which represented the component and assembly hierarchies of the system. To provide a functional diagnosis it was necessary to link the two hierarchies, that is, to define which functionalities were implemented by which components. This idea, i.e. the idea of creating a link language which establishes associations between model hierarchies of vastly different domain is also usable for the signal

flow and hardware model domains of CADDMAS. A new language called Signal flow to Processor Assignment Language (SPAL) was defined for this purpose. Unlike PPL, SPAL also allows the creation of hierarchical links between two declaration trees. To see why this is advantageous it is best to consider the signal flow and hardware model hierarchies of the CADDMAS system (Figures 2 and 4). For example, the hardware hierarchy contains a declaration called 'ALTA' which models a group of six Transputer processors which are mounted on a common board. The signal flow models contain a declaration called 'MUX_SET' which is the signal flow model for a group of four input channels. It turns out that there are exactly six 'ALTA' processor groups and six 'MUX_SET' signal flow sub-graphs in the 24 channel CADDMAS system. Additionally, each 'MUX_SET' compound is implemented on the processors of one 'ALTA' group. Using SPAL it is possible to define the mapping of the processors of the 'ALTA' group to the computing elements in the 'MUX_SET' compound just once. Using these assignments it is sufficient to create a single link between each of the six 'ALTA' and 'MUX_SET' modules in the top-level declaration trees. This is in contrast to the "original" link languages of the MA (like PPL) which can only work with the fully expanded hierarchies. Implementing support for this kind of link editing necessitated adding new services in the language definition interface of GMB. This means that declarations written in languages like SPAL cannot be edited any more using the "old" MA graphical model builder (XGEM).

The necessary editor configuration file for the SPAL language was added to GMB. An example editor screen can be seen in Figure 6. In this figure links are being created between the hardware and signal flow aspects of the CADDMAS models.

A run-time interpreter module was also developed for the SPAL language. In order to minimize the effect on the CADDMAS run-time system building

process, the SPAL interpreter is not directly interfaced to the HDL interpreter. Instead, the SPAL interpretation just runs before the HDL builder starts, and declares all those processor assignments expected by HDL which were done manually before.

The result of the above work is that the CADDMAS system now can be fully integrated using model-based graphical tools. At this time it is unclear when all research and production versions of CADDMAS will use this technology due to other ongoing development efforts.

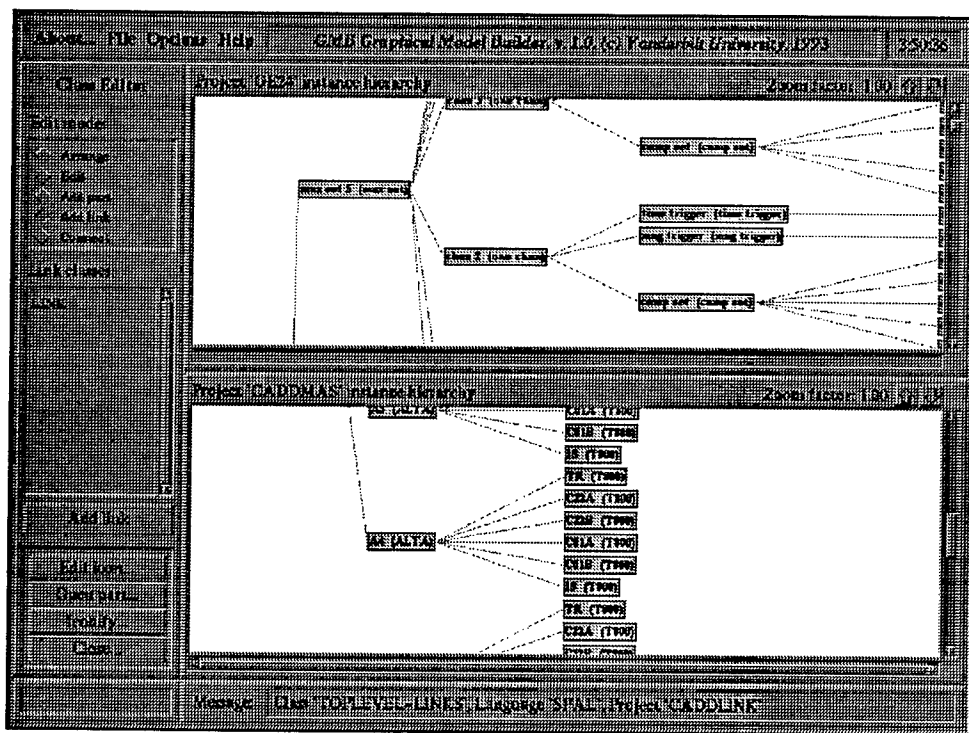


Figure 6. Signal processing to hardware link editor screen

Conclusions, Future Research

The additions to the Multigraph Architecture described in the previous sections can significantly simplify the system integration process for a large parallel system like CADDMAS. There are still a few open issues remaining:

- 1) Synthesis of Multigraph scripts from HDL models: One of the potential pitfalls of the HDL language is that it is possible for a modeled signal flow routine not to match the actual code which implements it. This can lead to hard to track bugs in the system. The solution is to integrate the source code of the signal processing modules into the HDL models. Whenever the models are changed, the HDL interpreter would compile the embedded sources and rebuild the executable(s) for the affected processor(s).
- 2) Automatic load image building: It is possible to determine which processing modules are needed on which processor from the HDL, MPDL and SPAL models of a distributed parallel system. The model interpretation process could automatically configure executable images for the various processors in the network based on this information. For the current CADDMAS systems this capability is not necessary because the memory space which could be gained by this approach is negligible. However, future parallel applications may require the optimization of download images.

The results of this work should be applicable in other large-scale parallel distributed data processing applications, like AEDC's simulation and image processing efforts.

References:

- [1] Abbott, B.: "Multigraph Kernel for the Transputer", Master's thesis Dept. of Electrical Engineering, Vanderbilt University, Nashville, TN., Dec. 1989.
- [2] Abbott, B.: "MULTIGRAPH Kernel for Transputer Based Systems", Final Report for USAF-UES SRP, Contract no. F49620-88-C-0053, Sept, 1988.

- [3] Abbott, B., Bapty T.: "High Speed Parallel Signal Processing", Final Report for USAF-UES SRP, Contract no. F49620-90-C-0053, Sept, 1990.
- [4] Bapty T., Abbott, B: "Parallel Signal Processing Architecture for Turbine Engine Testing", Final Report for USAF-RDL SRP, Sept, 1990.
- [5] Bapty T., Abbott, B: "Real-Time Turbine Engine Data Visualization", Transputer Research and Applications, ed.: D. L. Fielding, IOS Press, 1990.
- [6] Biegl, C.: "Design and Implementation of an Execution Environment for Knowledge-Based Systems", Ph.D. thesis Dept. of Electrical Engineering, Vanderbilt University, Nashville, TN., Dec. 1988.
- [7] Biegl, C., Karsai, G., Sztipanovits, J., Bourne, J., Mushlin, R., Harrison, C.: "Execution Environment for Intelligent Real-Time Systems", Proc. of the 8th Annual IEEE/EMBS Conference, Dallas, TX, pp. 807-811, 1986.
- [8] Karsai, G., Biegl, C., Sztipanovits, J., Bourne, J., Mushlin, R., Harrison, C.: "Experiment Design Language for Intelligent MRI Systems", Proc. of the 8th Annual IEEE/EMBS Conference, Dallas, TX, pp. 803-807, 1986.
- [9] Padalkar, S., Karsai, G., Sztipanovits, J.: "Graph-Based Real-Time Fault Diagnostics", Proc. of the Fourth Conference on Artificial Intelligence for Space Applications, pp. 115-124, Huntsville, AL.
- [10] Sztipanovits, J., Padalkar, S., Krishnamurthy, C., and Purves, R.: "Testing and Validation in Artificial Intelligence Programming", in Proc. of the Third Conference. on A.I. for Space Applications, pp. 21-32,

Huntsville, AL, 1987.

- [11] Sztipanovits, J., Biegl, C., Karsai, G., Bourne, J., Mushlin, R., Harrison, C.: "Knowledge-Based Experiment Builder for Magnetic Resonance Imaging (MRI) Systems", Proc. of the 3rd IEEE Conference on Artificial Intelligence Applications, Orlando, FL, pp. 126-133, 1987.

- [12] Sztipanovits, J., et. al.: "Cooperative Systems for Real-Time Process Monitoring and Process Diagnostics", Proc. of the AI 87 JAPAN, Osaka, Japan, pp. 419-416, 1988.

- [13] Wilkes, D. Abbott, B.: "MULTIGRAPH Kernel for Transputer Based Systems", Final Report for USAF-UES Mini-Grant, Contract no. F49620-88-C-0053/SB5881-0378, May, 1989.

**HEAT LOAD STRUCTURAL FAILURE PREDICTION FOR
THE ARNOLD ENGINEERING DEVELOPMENT CENTER
HEAT-H1 TEST UNIT NOZZLE**

**Michael A. Weaver
Graduate Research Assistant**

**Faculty Advisor:
Kurt C. Gramoll
Assistant Professor**

**School of Aerospace Engineering
Georgia Institute of Technology
Atlanta, Georgia 30332-0150**

**Final Report for:
AFOSR Summer Research Extension Program
Arnold Engineering Development Center
Arnold Air Force Base, Tennessee**

**Sponsored by:
Air Force Office of Scientific Research
Bolling Air Force Base, Washington, DC**

and

Georgia Institute of Technology

**Project Period:
1 January 1993 to 31 December 1993**

**Final Report Date:
18 March 1994**

**HEAT LOAD STRUCTURAL FAILURE PREDICTION FOR
THE ARNOLD ENGINEERING DEVELOPMENT CENTER
HEAT-H1 TEST UNIT NOZZLE**

Michael A. Weaver
Graduate Research Assistant
School of Aerospace Engineering
Georgia Institute of Technology

Abstract

A method for unsteady, axisymmetric, conjugate heat transfer analysis was developed. The conjugate heat transfer domain comprises co-flowing high temperature air and subcooled water coolant on opposite sides of a copper-zirconium, converging nozzle. Heat transfer through the nozzle wall is characterized by solid-body conduction with convection boundary conditions along the air side and water side of the nozzle wall. The air-side heat transfer is characterized by forced convection with a turbulent boundary-layer. The water-side heat transfer is characterized by forced convection, subcooled, nucleate boiling. Convective heat transfer coefficients on each side of the nozzle wall are functions of the wall temperature and the respective flow properties, thus coupling the three regions of the domain. The solution method marches in time, solving at each time step for the nozzle wall temperature distribution, the flow properties on each side of the nozzle wall, and for the convective heat transfer coefficients. The algorithm terminates when either the steady state is achieved or nozzle wall failure conditions are reached. Solutions are obtained for four test cases culled from the run history of the Arnold Engineering Development Center HEAT-H1 Test Unit. Results show that the recorded test case failures were not caused by pre-critical boiling effects. Conclusive failure analysis for the HEAT-H1 test cases awaits application of an appropriate convective boiling critical heat flux model, along with creep and stress-rupture models for the nozzle wall.

HEAT LOAD STRUCTURAL FAILURE PREDICTION FOR THE ARNOLD ENGINEERING DEVELOPMENT CENTER HEAT-H1 TEST UNIT NOZZLE

Michael A. Weaver

Introduction

The Arnold Engineering Development Center (AEDC) HEAT-H1 Test Unit is an arc-heated, free jet test facility, providing extremely high enthalpy air flow. Flows with enthalpies ranging from 2,000 to 8,500 Btu/lbm and pressures ranging from 20 to 115 atm are routinely produced [1]. Mach numbers ranging from 1.8 to 3.5 are achieved with interchangeable nozzles. These nozzles are actively cooled with backside co-flowing water undergoing subcooled nucleate boiling.

Proposed future applications for the HEAT-H1 Test Unit require operating conditions beyond the current survival envelope. These applications will need pressures of up to 200 atm, while nozzle wall heat load failures have been observed at pressures in the range 120 to 130 atm. The ability to identify and predict the heat load failure modes of the nozzle wall is crucial to extending operation of the HEAT-H1 Test Unit beyond its current capabilities.

Heat load in the HEAT-H1 nozzle wall can be categorized as a coupled or conjugate heat transfer phenomenon. The conjugate heat transfer domain comprises co-flowing high temperature air and subcooled water coolant on opposite sides of a copper-zirconium, converging/diverging nozzle wall. Heat transfer through the nozzle wall is characterized by solid-body conduction with convection boundary conditions along the air side and water side of the nozzle wall. The air-side heat transfer is characterized by forced convection with a turbulent boundary layer. The water-side heat transfer is characterized by forced convection, subcooled, nucleate boiling. Convective heat transfer coefficients on each side of the nozzle wall are functions of the wall temperature and the respective flow properties, thus coupling the three regions of the domain.

The AEDC operating contractor for the HEAT-H1 Test Unit (Calspan Corporation/AEDC Operations) has conducted a heat load failure analysis by assuming one-dimensional (radial) conjugate heat transfer through the nozzle wall [2, 3]. This approach gives good results for the thin-walled region of the

nozzle, but failure analysis for the complete nozzle must consider multidimensional conjugate heat transfer. With sponsorship from the Air Force Office of Scientific Research (AFOSR), the author pursued such a multidimensional approach while participating in the 1992 AFOSR Summer Research Program [4]. This multidimensional heat load failure analysis subsequently received additional funding through the 1993 AFOSR Summer Research Program [5], and the 1993 AFOSR Summer Research Extension Program.

The multidimensional approach requires numerical models (based on either analytic methods or engineering mathematical correlations) for the unsteady solid-body heat transfer in the copper-zirconium nozzle, the flow properties and heat transfer coefficients on the air side of the nozzle, and the flow properties and heat transfer coefficients on the water side of the nozzle. During the 1992 AFOSR Summer Research Program, the author assembled the numerical models, developed a fully-coupled solution algorithm, and demonstrated the feasibility of the solution scheme. The 1993 AFOSR Summer Research Program was devoted to improvement of the flow properties model on the water side of the nozzle. The 1993 AFOSR Summer Research Extension Program provided nine months of funding for refining the numerical models, and obtaining solutions for comparison with four experimentally derived test cases.

Discussion of Problem

In the HEAT-H1 Test Unit, tangentially injected air flows between an anode and a cathode for heating by an electric arc. The tangentially injected air creates swirling flow which serves to keep the electric arc from making contact with the wall in the region between the anode and cathode. The high temperature, subsonic air passes from the cathode, through a conical contraction, to the nozzle inlet, then expands through the nozzle to parallel, supersonic flow at the nozzle exit. The HEAT-H1 arc-heater configuration is shown in Figure 1, with an idealized nozzle and cooling jacket shown in Figure 2.

The current and previous studies focus on the HEAT-H1 Mach 1.8 nozzle. This axisymmetric, copper-zirconium nozzle has a length of 2.3 inches with a throat diameter of 0.9 inches. Water flow between the nozzle wall and cooling jacket provides backside cooling for the nozzle wall. Away from the end regions (refer to Figure 2), solid-body heat transfer through the nozzle wall is approximately radial, becoming both radial and axial near the flanged ends of the nozzle.

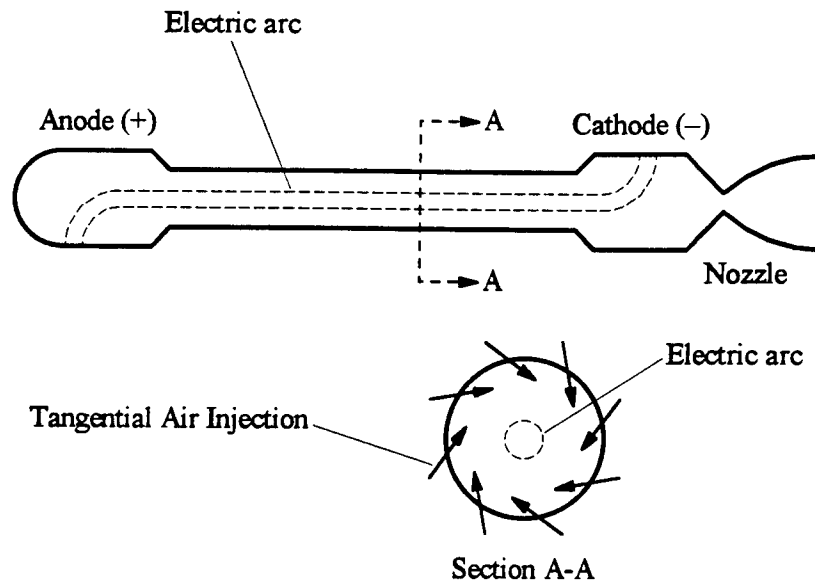


Figure 1. Schematic representation of the HEAT-H1 arc-heated wind tunnel.

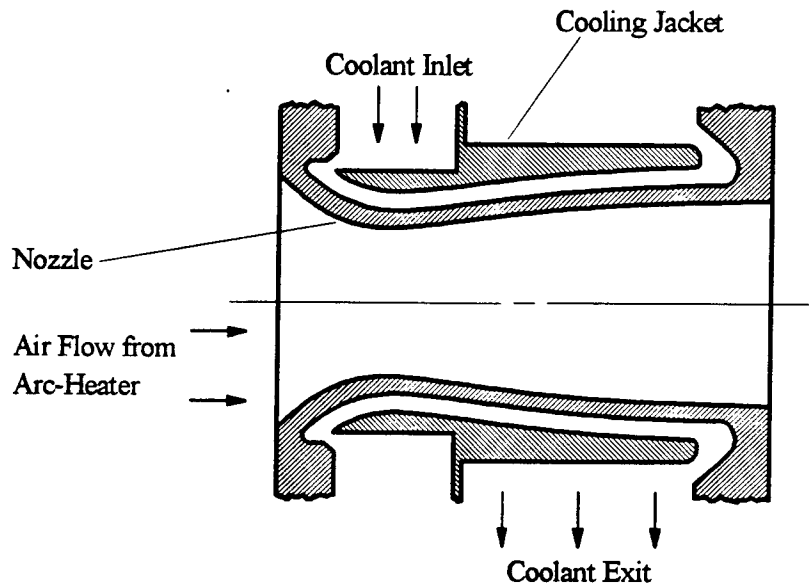


Figure 2. Idealization of a nozzle and cooling jacket for the HEAT-H1 Test Unit.

Air flow over the nozzle wall is assumed steady, compressible, and turbulent, with a high temperature boundary-layer. Outside the boundary-layer, flow is assumed to be steady, compressible, nonuniform, dissociated, equilibrium air, with decreasing total temperature approaching the wall.

Transport properties for the high temperature, high pressure air are strong functions of temperature and weak functions of pressure.

Water flow through the cooling passage is assumed steady, incompressible, viscous, and turbulent. The water enters and exits the active cooling region in the subcooled state. Subcooled nucleate boiling is assumed to occur at the nozzle wall, while the outer cooling jacket wall is assumed adiabatic. Transport properties for the subcooled water are functions of temperature and pressure. Due to high flow convection rates, the momentum properties of the flow (density, velocity, and pressure) are decoupled from the temperature distribution of the flow.

Four test cases have been taken from the HEAT-H1 Test Unit run history [2]. Summarized in Table I, two of the test cases show nozzle wall survival, and two show nozzle wall failure. These test cases include variation in the air total pressure, total temperature, and total enthalpy. Also included are variations in the water mass flow rate and inlet temperature.

Table I. Heat Load Failure Test Cases for the HEAT-H1 Mach 1.8 Nozzle.

Test Case Number	I	II	III	IV
Water inlet total pressure (psia)	1,000	1,000	1,000	1,000
Water mass flow rate (lbm/s)	11.54	11.54	7.09	7.063
Water inlet temperature (°R)	557	552	520	520
Water temperature rise (°R)	25	27	34	36
Air total pressure (atm)	126.5	137	104.4	94.3
Air total temperature (°R)	9,000	9,432	8,280	9,180
Air total enthalpy (Btu/lbm)	3,480	3,750	3,062	3,644
Survival/Failure	Survived	Failed	Survived	Failed

Method of Analysis

Heat load structural deformation and failure in the HEAT-H1 nozzles has been observed in the region between the nozzle inlet and the nozzle throat. Nozzle wall failure has not been observed downstream of the nozzle throat. For this reason, the current analysis is limited to the HEAT-H1 Mach 1.8

nozzle geometry from the inlet to the throat. This simplification leads to a nonphysical longitudinal boundary at the nozzle throat. Due to the approximately one-dimensional (radial) nature of heat transfer at the throat, this longitudinal throat boundary is assumed adiabatic. The three regions of the conjugate heat transfer domain (nozzle, air, and water) are summarized in Figure 3 with the adiabatic boundary conditions indicated.

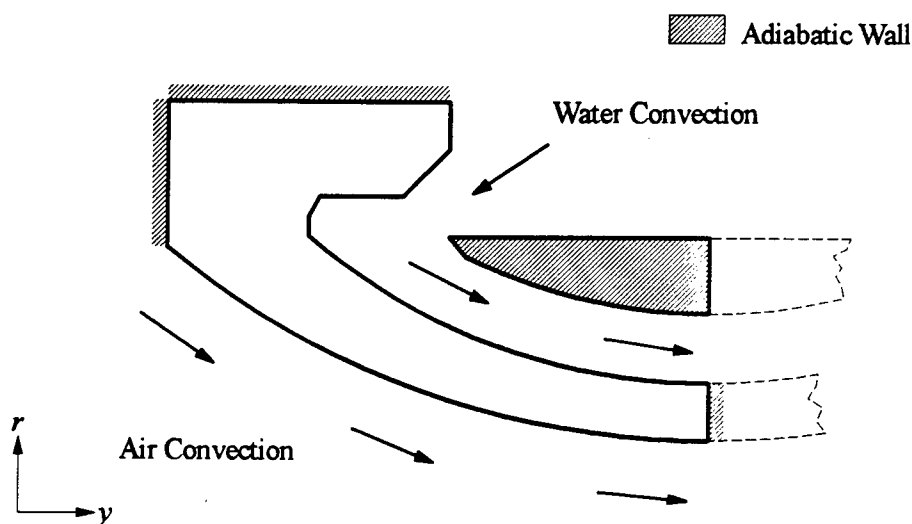


Figure 3. Conjugate heat transfer domain for the HEAT-H1 nozzle.

At least three modes of heat load failure exist for the nozzle wall. The nozzle wall temperature may reach the material melting point, due to insufficient heat load removal through nucleate boiling (pre-critical) heat flux. Also, the melting point may be reached through insufficient transition boiling (post-critical) heat flux. Last, the time span and magnitude of the heat load may permit plastic deformation (creep) great enough to produce structural failure, even though the nozzle wall temperature remains below the material melting point.

The failure mode being examined determines the appropriate analysis method. The first two failure modes can be analyzed with either a steady or an unsteady approach. The steady conjugate heat transfer problem could be solved, and then the solution checked for either nozzle wall temperature exceeding the material melting point, or boiling heat flux exceeding the critical heat flux. Alternatively, the unsteady conjugate heat transfer problem could be marched in time until either the nozzle wall temperature exceeds

the material melting point, the boiling heat flux exceeds the critical heat flux, or the steady state is obtained. The third failure mode, by its unsteady nature, must be analyzed with an unsteady approach. The unsteady method already described could be used for the third failure mode, with the inclusion of an additional step to determine structural deformation, and a check for structural yield.

In the current study, only the first two failure modes are considered, but the unsteady approach has been adopted for its future applicability to plasticity analysis for the third failure mode. The algorithm developed is as follows:

- a) Assume an initially constant nozzle wall temperature distribution equal to the water inlet temperature.
- b) Calculate the initial water flow properties along the water side and the initial air flow properties along the air side of the nozzle.
- c) Calculate the initial heat transfer coefficients for the water side and the air side of the nozzle.
- d) Use the heat transfer coefficients and effective fluid temperatures for the air side and water side of the nozzle in the initial time step of an unsteady heat transfer analysis of the copper-zirconium nozzle to obtain the new temperature distribution.
- e) Calculate the new water flow properties along the water side and the new air flow properties along the air side of the nozzle.
- f) Calculate the new heat transfer coefficients for the water side and the air side of the nozzle.
- g) Use the heat transfer coefficients and effective fluid temperatures for the air side and water side of the nozzle in the next time step of an unsteady heat transfer analysis of the copper-zirconium nozzle to obtain the new temperature distribution.
- h) Return to step e), until either the nozzle wall temperature exceeds the copper-zirconium melting point, the boiling heat flux exceeds the critical heat flux, or the steady state is obtained.

At each time step, this algorithm calculates the steady-state flow and heat transfer properties of air and water, assuming the wall temperature distribution is in thermal equilibrium after each time step. For this assumption to remain valid, the time step size must be less than or equal to the characteristic time for heat transfer in the nozzle wall material.

The required numerical models for the unsteady solid-body heat transfer in the copper-zirconium nozzle, the flow properties and heat transfer coefficients on the air side of the nozzle, and the flow properties and heat transfer coefficients on the water side of the nozzle, are now described for the three regions of the conjugate heat transfer domain.

(i) Copper-zirconium nozzle wall:

Unsteady, axisymmetric, solid-body heat conduction, with no internal heat generation, and with temperature dependent thermal conductivity is governed by

$$\rho c_p \frac{\partial T}{\partial t} = \frac{1}{r} \left[\frac{\partial}{\partial r} \left(kr \frac{\partial T}{\partial r} \right) + \frac{\partial}{\partial y} \left(kr \frac{\partial T}{\partial y} \right) \right].$$

The adiabatic wall boundary condition is given by

$$\left. \frac{\partial T}{\partial n} \right|_{wall} = 0.$$

The convection boundary condition is given by

$$-k \left. \frac{\partial T}{\partial n} \right|_{wall} = h(T_{wall} - T_{eff}).$$

Here,

c_p	= isobaric specific heat,
k	= thermal conductivity,
h	= heat transfer coefficient,
n	= boundary normal coordinate,
r	= radial coordinate,
t	= time,
T	= solid-body temperature,

T_{eff} = effective fluid temperature,

T_{wall} = wall temperature,

y = longitudinal coordinate,

ρ = mass density.

The heat transfer analysis finite element program TRAX [6] is used to solve this problem. At each time step, the heat transfer coefficients and effective fluid temperatures are specified. The effective fluid temperature for the water side is the local static temperature. For the air side, the effective fluid temperature is the local adiabatic wall temperature. Using these values, program TRAX reads the nodal temperature distribution from the previous time step and calculates the new nodal temperature distribution.

Three finite element models, with differing mesh resolutions, were created for the investigation of algorithm convergence as a function of mesh resolution. The *coarse* model contains 71 nodes with 51 elements, and represents the lower limit for the mesh resolution study. The *medium* model contains 99 nodes with 72 elements. The *fine* model contains 119 nodes with 87 elements, and represents the upper limit for the mesh resolution study. The three finite element models in Figure 4 show the geometry for the HEAT-H1 Mach 1.8 nozzle. The fine model has twice the resolution of the coarse model in the wetted-wall regions (air and water) of the nozzle. The medium model resolution is approximately the mean between the coarse and fine model resolutions in the wetted-wall regions.

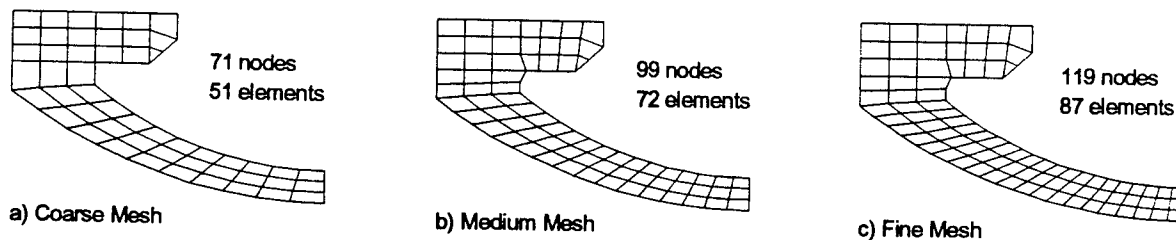


Figure 4. Three finite element models for the HEAT-H1 Mach 1.8 nozzle.

Temperature dependent material properties for the copper-zirconium nozzle are suitably approximated by those of elemental copper. For elemental copper, the available data [7, 8] show a linear

variation of c_p in the range from 491.67°R to 1931.67°R; a linear variation of k in the range 491.67°R to 1571.67°R; and a linear variation of ρ in the range 491.67°R to 1059.67°R. Beyond these available upper limits, material property values were linearly extrapolated to 2,500°R. The melting point for elemental copper is approximately 2,410°R.

(ii) Air side of the nozzle wall:

Steady-state heat transfer through a turbulent, compressible boundary-layer in accelerating, axisymmetric duct flow is given by the method of Ambrok [9],

$$St_{CP} = \frac{A}{Pr} \frac{R^{(1-n)/n} (T_{aw} - T_{wall})^{(1-n)/n}}{\left[\frac{1}{\mu_0} \int_0^x R^{1/n} (T_{aw} - T_{wall})^{1/n} G d\xi \right]^{1-n}} = \frac{h}{G c_{p,eff}}$$

- Here,
- $c_{p,eff}$ = effective isobaric specific heat = $(i_o - i_{wall}) / (T_{aw} - T_{wall})$,
 - G = mass flux,
 - h = heat transfer coefficient,
 - i_o = boundary-layer edge total enthalpy,
 - i_{wall} = enthalpy at the wall,
 - Pr = Prandtl number,
 - $R(\xi)$ = wall radius (function of arc length),
 - R_t = turbulent recovery factor,
 - St_{CP} = constant-property Stanton number,
 - T_{aw} = adiabatic wall temperature = $T_s + R_t (T_o - T_s)$,
 - T_o = boundary-layer edge total temperature,
 - T_s = boundary-layer edge static temperature,
 - T_{wall} = wall temperature,
 - x = wall arc length at position of interest,
 - μ = absolute viscosity,
 - ξ = variable of integration (wall arc length).

This method is based on solving the boundary-layer energy integral equation in terms of the thermal boundary-layer momentum thickness. The thermal boundary-layer originates at the lower limit of the integral.

Parameters A and n are obtained by an auxiliary relation for the wall-length Nusselt number and Reynolds number:

$$Nu_x = A Re_x^n.$$

For the turbulent boundary-layer flow of a compressible gas, a suitable expression is given by the Reynolds-Kays-Kline equation [10],

$$Nu_x = 0.0287 Pr^{0.6} Re_x^{0.8}.$$

As formulated above, Ambrok's approach is valid for smoothly varying wall temperature, and assumes a thin boundary-layer with constant fluid properties. A correction to the constant-property Stanton number accounting for temperature-dependent fluid properties can be expressed as [11],

$$St = St_{CP} \left(\frac{T_s}{T_{wall}} \right)^m \text{ with } 0 \leq m \leq 0.1,$$

for the case of a turbulent gas flowing through a tube with cooled walls. In the current analysis, the maximum value of 0.1 is used for m .

Applied to the HEAT-H1 nozzle analysis, the method of Ambrok takes the final form,

$$St = \frac{0.0287}{Pr^{0.4}} \frac{R^{0.25} (T_{aw} - T_{wall})^{0.25}}{\left[\frac{1}{\mu} \int_0^x R^{1.25} (T_{aw} - T_{wall})^{1.25} G d\xi \right]^{0.2}} \left(\frac{T_s}{T_{wall}} \right)^{0.1} = \frac{h}{Gc_{p,eff}}.$$

Here, all fluid properties are evaluated at the local boundary-layer edge temperature. For the determination of adiabatic wall temperature, a recovery factor of 0.9 for turbulent, subsonic, tube flow was used [12]. The thermal boundary layer is assumed to originate at the point of conical contraction of the HEAT-H1 cathode exit (refer to Figure 1). This assumption is based upon speculation that velocity and thermal boundary-layers entering the cathode will be sufficiently disrupted by the rotating electric arc striking the cathode wall.

The flow properties for dissociated, equilibrium air, as required for the HEAT-H1 application, are obtained by mathematical correlation. An effective gas constant of 0.07400 Btu/lbm/°R and a specific heat ratio of 1.24 are used in the quasi-one-dimensional, isentropic flow equations to obtain mass flux, static temperature, and static pressure. The effective constants were chosen such that the correlated flow variables compare well with flow variables from predetermined equilibrium gas solutions [13]. The effective values of gas constant and specific heat ratio are also used to determine the effective isobaric specific heat. The effective isobaric specific heat appearing in the above formulation of Ambrok's method serves only as an unscaling parameter, and does not equal the equilibrium air isobaric specific heat.

Due to nonuniform flow over the cross-section, the bulk and boundary-layer edge total temperatures are unequal. A bulk-to-edge total enthalpy ratio of 1.211 was obtained through experimental measurements in the HEAT-H1 Test Unit [2]. Edge total enthalpy was obtained by scaling the nominal bulk total enthalpy with this experimental value. Edge total temperature was then calculated from equilibrium gas tables [14] using the edge total enthalpy, and the nominal total pressure. This edge total temperature, and the nominal total pressure are used as effective total conditions in the isentropic flow equations.

The air transport properties are obtained from equilibrium gas tables. Absolute viscosity and Prandtl number are bilinearly interpolated from values tabulated as functions of pressure and temperature. The local pressure and temperature used for interpolation are obtained from the flow properties correlation.

The heat transfer coefficients h , and adiabatic wall temperatures T_{aw} , are determined along the air side of the nozzle wall using these models. These values are then used to specify the air-side boundary conditions for one time step of the finite element heat conduction analysis.

(iii) Water side of the nozzle wall:

Steady-state heat transfer during forced convection, subcooled nucleate boiling in an annular passage is predicted by the correlation of Shah [15, 16, 17]. This correlation assumes the total convection heat flux is the sum of the single-phase convection heat flux and the nucleate boiling convection heat flux,

$$q = q_{spc} + q_{nb},$$

where, q = two-phase (total) convection heat flux,
 q_{spc} = single-phase convection heat flux,
 q_{nb} = nucleate boiling convection heat flux.

The single-phase convection heat flux, for turbulent flow, is determined from the Dittus-Boelter equation,

$$\frac{q_{spc}}{(T_{wall} - T_s)} = 0.023 \left(\frac{GD_{eq}}{\mu} \right)^{0.8} Pr^{0.4} \left(\frac{k}{D_{eq}} \right) = h_{sp},$$

where, D_{eq} = equivalent annulus diameter,
 G = mass flux,
 h_{sp} = single-phase convection heat transfer coefficient,
 k = thermal conductivity,
 Pr = Prandtl number,
 T_s = static temperature,
 T_{wall} = wall temperature,
 μ = absolute viscosity.

All quantities are evaluated at the local static temperature.

The nucleate boiling convection heat flux is determined from the correlation of experimental data for fully developed flow boiling. This follows the recommendation of Bergles and Rohsenow [18] that nucleate boiling convection heat flux should not be determined with a pool boiling correlation.

The Shah correlation for forced convection, subcooled nucleate boiling in an annular passage is expressed as,

$$\frac{q}{(T_{wall} - T_s)} = h_{sp} \left[(T_{wall} - T_{sat}) \max(230 Bo^{0.5}, 1) + \sigma(T_{sat} - T_s) \right] = h_{tp},$$

where, Bo = boiling number = $q/(i_{fg} G)$,
 i_{fg} = heat of vaporization,
 h_{tp} = two-phase convection heat transfer coefficient,
 T_{sat} = saturation temperature at local static pressure.

Also,

$$\sigma = \begin{cases} 0, & \text{for fully developed boiling (low subcooling regime)} \\ 1, & \text{for local or partial boiling (high subcooling regime)} \end{cases}$$

Here, local or partial boiling occurs when,

$$\frac{(T_{sat} - T_s)}{(T_{wall} - T_{sat})} > 2, \text{ or } \frac{(T_{sat} - T_s)}{(T_{wall} - T_{sat})} > 6.3 \times 10^4 Bo^{1.25},$$

otherwise, fully developed boiling is assumed.

If no boiling is present (i.e. when $T_{wall} < T_{sat}$), then the single-phase convection heat transfer coefficient h_{sp} is used. When boiling is present, the two-phase convection heat transfer coefficient h_{tp} from the Shah correlation is used. The Shah two-phase convection heat transfer coefficient includes the contribution from single-phase convection.

The turbulent, steady-state velocity and pressure distributions for water through the annular cooling passage are determined with the incompressible form of the three-dimensional Navier-Stokes equations. The governing equations are formulated in the research flow solver INS3D-UP from NASA Ames Research Center [19]. This flow solver uses the pseudo-compressibility method, first introduced by Chorin [20], and successfully applied by Kwak et al. [21], Rogers and Kwak [22], and others.

Briefly summarizing this approach [23], the continuity equation for the incompressible Navier-Stokes equations reduces to

$$\vec{\nabla} \cdot \vec{V} = 0.$$

The steady-state momentum conservation equation, without body forces, becomes

$$\vec{\nabla} \cdot (\vec{V} \otimes \vec{V}) = \frac{1}{\rho} \vec{\nabla} \cdot (-p\vec{I} + \vec{\tau}),$$

where, \vec{V} = Cartesian velocity vector $(u, v, w) = (V_1, V_2, V_3)$,
 ρ = constant mass density,
 p = static pressure,
 \vec{I} = unit tensor,

$$\begin{aligned}\bar{\tau} &= \text{shear stress tensor} = \tau_{ij} = \mu \left(\frac{\partial V_j}{\partial x_i} + \frac{\partial V_i}{\partial x_j} \right), \\ \mu &= \text{absolute viscosity.}\end{aligned}$$

The pseudo-compressibility method then replaces the continuity equation with the time-dependent expression

$$\frac{1}{\beta^2} \frac{\partial p}{\partial t} + \rho \vec{\nabla} \cdot \vec{V} = 0.$$

The parameter β represents a pseudo-speed of sound for the transformed system, with pseudo-pressure waves propagating at finite speed. Thereby, the elliptic governing equations have taken on a hyperbolic character. The pseudo-speed of sound β must be adjusted for optimum convergence to the steady-state solution. The apparent transient behavior of the transformed system has no physical meaning until the divergence-free condition, and thus convergence, is reached. As implemented in INS3D-UP, an upwind differencing scheme based on flux-difference splitting is used to compute the convective terms, and second-order central differencing is used for the viscous terms [19, 22]. Also, the governing equations are nondimensionalized, and solved in a generalized curvilinear coordinate system.

An axisymmetric flow solution is obtained from INS3D-UP by solving the full three-dimensional problem on three azimuthally rotated planes. Axial symmetry boundary conditions are enforced on the lateral walls of the resulting wedge-shaped configuration, thus giving an axisymmetric solution on the center plane. For the HEAT-H1 problem, each of the two outer planes are rotated by 1° from the center plane.

Examination of the four HEAT-H1 test cases (refer to Table I) shows the similarity between the water flow parameters. All four cases have identical values for the water inlet total pressure. Cases I and II have identical values for water mass flow rate. In addition, the water mass flow rates for Cases III and IV differ by less than 0.4 percent. For these reasons, only two flow solutions are required for all four test cases: one solution for Cases I & II, and an additional solution for Cases III & IV. Due to the high flow convection rates, the velocity and pressure distributions are decoupled from the temperature distribution of the flow. This permits obtaining the water velocity and pressure solutions prior to the heat load analysis,

rather than obtaining the flow solutions within the iterative heat load algorithm.

The temperature distribution of water through the annular cooling passage is determined by application of steady-state, one-dimensional energy conservation, in combination with the thermodynamic relations for subcooled water. An elemental control volume is assumed with the known quantities,

- \dot{m} = mass flow rate into the control volume,
- p_{in} = control volume inlet static pressure,
- p_{out} = control volume exit static pressure,
- \dot{Q} = heat transfer rate into the control volume,
- T_{in} = control volume inlet bulk temperature,
- V_{in} = control volume inlet bulk velocity,
- V_{out} = control volume exit bulk velocity.

Then, assuming no work being done, conservation of energy for the control volume is given by

$$\left(i_{out} + \frac{V_{out}^2}{2} \right) - \left(i_{in} + \frac{V_{in}^2}{2} \right) = \frac{\dot{Q}}{\dot{m}},$$

- where,
- i_{in} = control volume inlet specific enthalpy,
 - i_{out} = control volume exit specific enthalpy.

The thermodynamic relations for water give specific enthalpy as a function of pressure and temperature

$$i_{in} = f(p_{in}, T_{in}) \text{ and } i_{out} = f(p_{out}, T_{out}),$$

from which T_{out} , the exit static temperature of the elemental control volume, is then obtained.

Note that the Shah correlation and the method for determining local flow temperature are coupled, due to the equivalence of the two-phase convection heat flux and the control volume heat transfer rate per unit heated area. For this reason, iteration between determining the local flow temperature and determining the two-phase convection heat flux is required.

The water thermodynamic and transport properties are obtained from the standard thermodynamic relations for subcooled water [24, 25].

The heat transfer coefficients h , and local static temperatures T_s , are determined along the water

side of the nozzle wall using these models. These values are then used to specify the water side boundary conditions for one time step of the finite element heat conduction analysis.

Results

Before proceeding with solutions for the test cases presented in Table I, water flow solutions are obtained at inlet conditions for Cases I & II, and Cases III & IV. The convergence characteristics of the unsteady solution algorithm are then examined for varying time step-size, and mesh resolution. From these algorithm convergence studies, an appropriate step-size and mesh resolution are selected for the conjugate heat transfer analysis. The details of these preliminary steps are now described, followed by solutions for the four HEAT-H1 Mach 1.8 nozzle test cases.

Water Flow Solutions:

Navier-Stokes solutions at inlet conditions for Cases I & II (equivalent), and Cases III & IV (also equivalent) were obtained for the axisymmetric, turbulent, steady-state flow of water through the annular HEAT-H1 Mach 1.8 nozzle cooling passage. Bulk velocity and nozzle wall pressure distributions were extracted from the flow solutions, and fitted to the Mach 1.8 nozzle finite element models using cubic-spline interpolation. For the fine resolution model, bulk velocity and nozzle wall pressure distributions are shown in Figures 5 and 6.

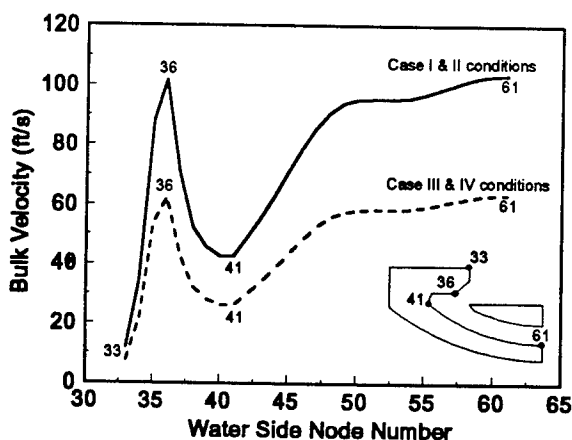


Figure 5. Bulk velocity distribution for the HEAT-H1 Mach 1.8 nozzle cooling passage.

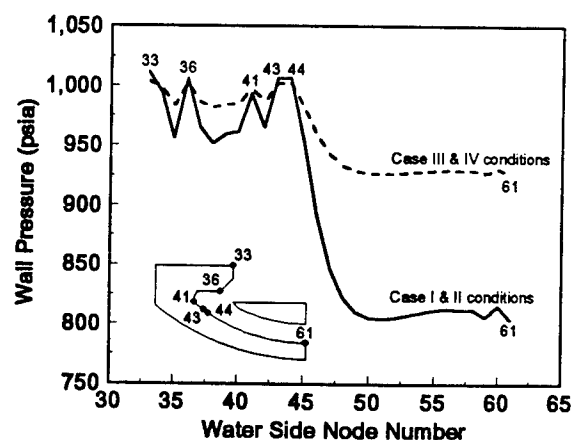


Figure 6. Wall pressure distribution for the HEAT-H1 Mach 1.8 nozzle cooling passage.

The bulk velocity (Figure 5) peaks as it accelerates through the initial flow constriction (node 36), and then dips as the flow enters the region of maximum flow area (node 41). Bulk velocity then steadily increases as the annular flow area decreases approaching the cooling passage throat (node 61). The two bulk velocity solutions display qualitatively similar results, with quantitative differences reflecting the higher mass flow rate for Cases I & II.

The wall pressure (Figure 6) initially drops as flow accelerates through the constriction, but then peaks (node 36) as flow near the wall decelerates in the proximity of a stagnation point (just downstream of node 36 in the complete flow solution). Wall pressure again drops, through a flow recirculation region, and then peaks in a region of corner flow (node 41). From here a second stagnation point is encountered, producing a final pressure peak (nodes 43 and 44). Pressure then falls precipitously as the flow near the wall becomes smoother approaching the throat (node 61). As with the bulk velocity solutions, the two wall pressure solutions display qualitatively similar results, with quantitative differences again reflecting the higher mass flow rate for Cases I & II.

The full velocity solution for Cases I & II illustrates the complexity of the cooling passage flow field. Velocity vectors scaled by magnitude in Figure 7 show acceleration as the flow approaches the

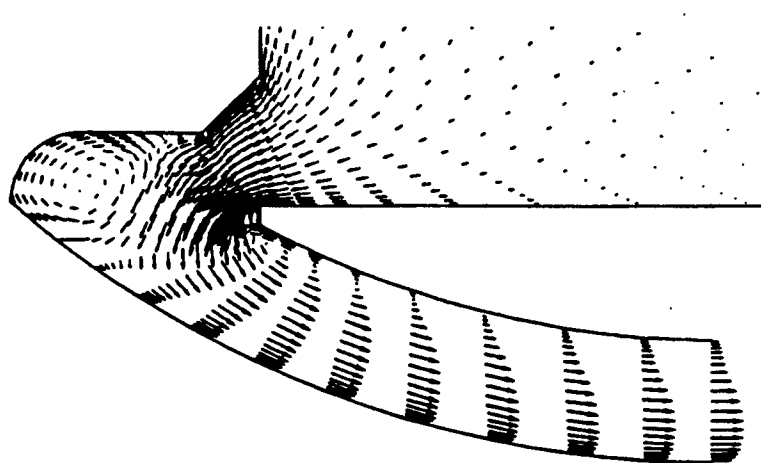


Figure 7. Velocity vectors in the HEAT-H1 Mach 1.8 nozzle cooling passage (Cases I & II).

constriction at the beginning of the turn. As the flow negotiates the hairpin turn, two separation regions develop. The first separation region hugs the inside corner of the turn, and contributes to the elongated recirculation pattern carried partially downstream. The second separation region occurs on the outside edge of the turn, and leads to the large circular recirculation pattern.

Of particular interest, a stagnation point lies on the nozzle-side (hot side) of the cooling passage wall at the edge of the second separation region. An enlarged view of this second region is shown in Fig. 8 with constant magnitude vectors. The existence of a recirculation region and a stagnation point on the hot wall reduces the efficiency of heat transfer from the wall. In the HEAT-H1 nozzle cooling passage, heat is swept away from the nozzle wall by continuously flowing cool water. Flow recirculation slows the replenishment of cool water, possibly leading to a local temperature rise. In addition, the stagnation region slows the local flow velocity, also contributing to temperature rise.

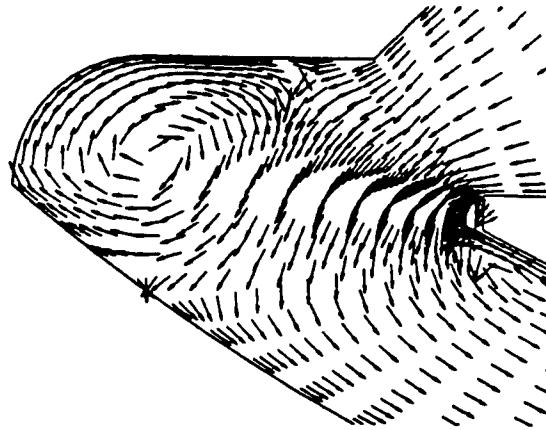


Figure 8. Recirculation patterns in the HEAT-H1 Mach 1.8 nozzle cooling passage (Cases I & II).

Note that the wall pressure distribution of Figure 5 presents the complexity of the flow near the nozzle wall better than the bulk velocity distribution of Figure 6. This is because the averaging process inherent in a bulk property calculation effectively smooths away local flow phenomena. To remedy this, the use of velocity values at the nozzle wall would not be practical (or very interesting) since relative velocities vanish at solid walls in a viscous flow problem. A more representative velocity distribution (i.e.

a distribution capable of reflecting stagnation flow effects) might be obtained by calculating bulk velocity near the nozzle wall, and excluding the flow region away from the nozzle wall. Recall that these velocity and pressure values are ultimately used for the determination of heat flux from the nozzle wall, lending credence that wall effects could be more important than bulk effects for this analysis. Unfortunately, rigorously determining the extent of the flow region to exclude from the bulk calculation is not straightforward, and so the "wall-weighted" bulk velocity is not used here. Conversely, nozzle wall pressures are easily obtained from the flow solutions, and therefore are used.

Time step-size convergence study:

Convergence characteristics for the unsteady solution algorithm were investigated as a function of time step-size. Case I run conditions were used with the fine resolution mesh to obtain steady-state solutions for three different step-sizes: 0.005 s, 0.001 s, and 0.0005 s. The convergence history for the three solutions is shown in Figure 9.

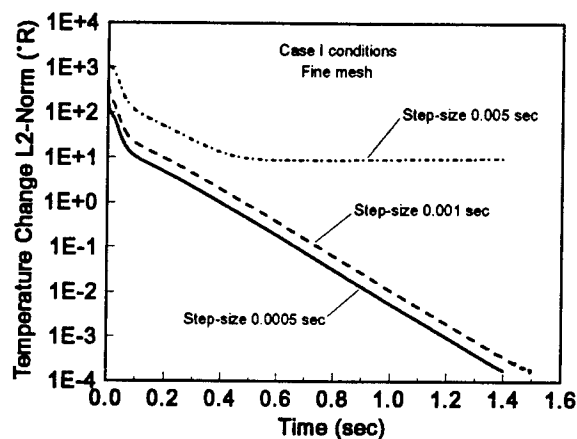


Figure 9. Convergence history for the solution algorithm time step-size study.

The L2-norm (Euclidean norm) of nodal temperature change is shown versus total solution time. For time step-sizes 0.001 s and 0.0005 s, the solutions converge smoothly through seven orders of magnitude of the L2-norm. On a per-node basis, the convergence level corresponds to effective machine zero. The 0.001 s step-size requires about 0.1 s longer to converge to the same level as the 0.0005 s step-size, but this corresponds to 1,500 total steps for the 0.001 s case, compared with 2,800 total steps for the

0.0005 s case. For time step-size 0.005 s, the solution initially converges, but reaches a minimum level near 0.6 s, and then begins slowly diverging as error accumulates. For comparison purposes, the unconverged results from the 0.005 s case are taken at the minimum convergence point.

Air-side solution results show excellent agreement among all three step-size cases. Solution comparisons for the air side of the HEAT-H1 Mach 1.8 nozzle are shown in Figures 10, 11, 12, and 13. Distributions for heat flux, heat transfer coefficient, adiabatic wall temperature, and wall temperature agree equally well for each of the three step-sizes.

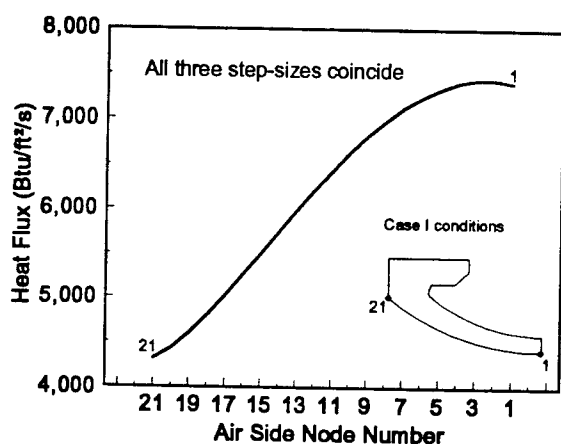


Figure 10. Air-side heat flux distribution for the HEAT-H1 Mach 1.8 nozzle.

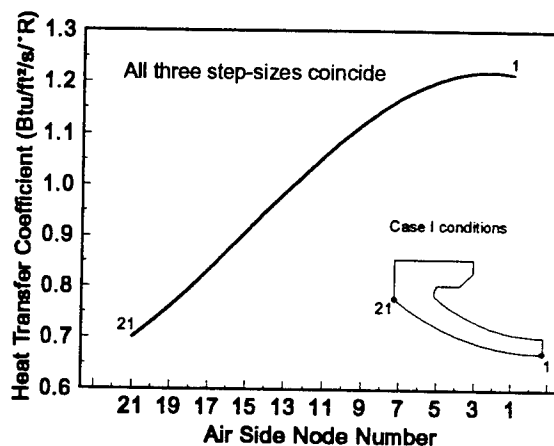


Figure 11. Air-side heat transfer coefficient distribution for the HEAT-H1 Mach 1.8 nozzle.

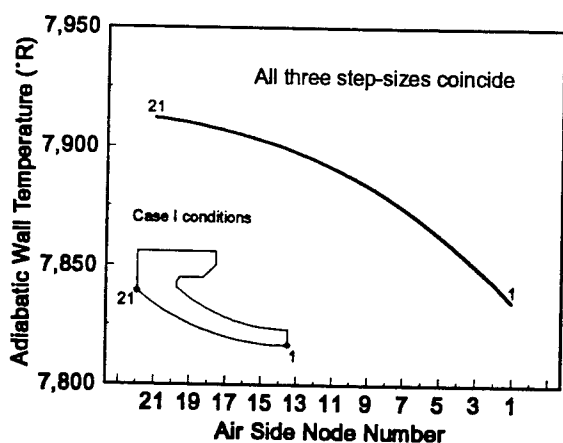


Figure 12. Air-side adiabatic wall temperature distribution for the HEAT-H1 Mach 1.8 nozzle.

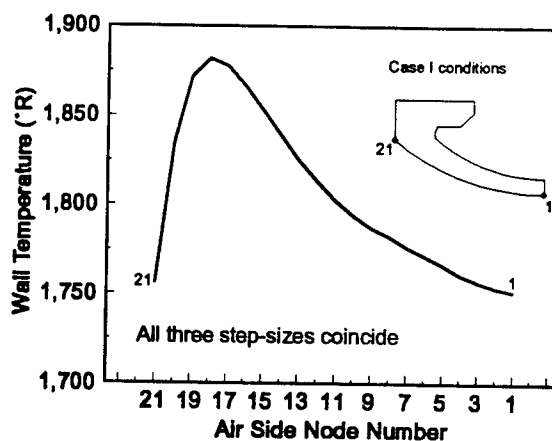


Figure 13. Air-side wall temperature distribution for the HEAT-H1 Mach 1.8 nozzle.

Water-side solution results show excellent agreement between the 0.001 s and 0.0005 s cases. Solution comparisons for the water side of the HEAT-H1 Mach 1.8 nozzle are shown in Figures 14, 15, 16, and 17. Distributions for heat flux, and heat transfer coefficient show the departure of the 0.005 s case results from those of the other two cases. The differences are most pronounced at the cooling passage throat (node 61). Distributions for bulk temperature and wall temperature agree equally well for each of the three step-sizes. As the 0.005 s solution proceeds beyond the minimum convergence point, all water-side results eventually depart from the 0.001 s and 0.0005 s results (not shown here).

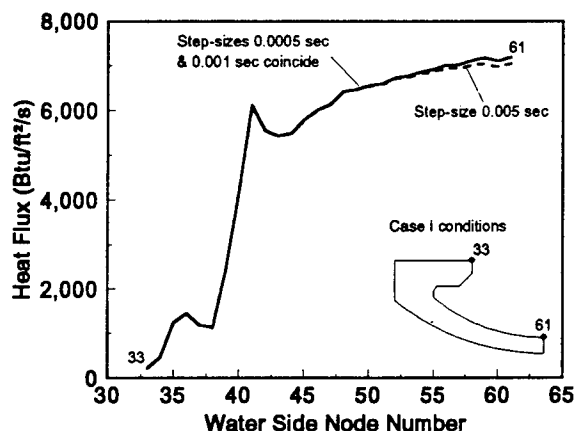


Figure 14. Water-side heat flux distribution for the HEAT-H1 Mach 1.8 nozzle.

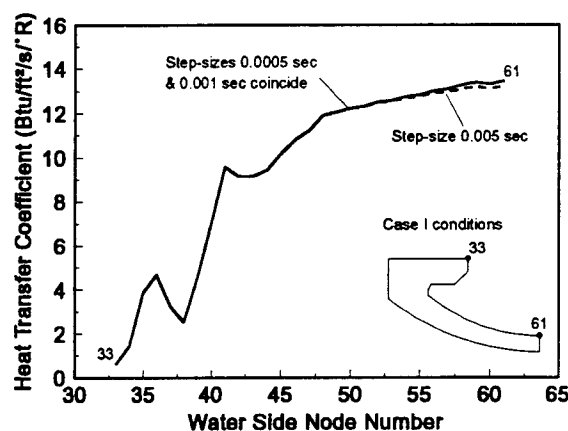


Figure 15. Water-side heat transfer coefficient distribution for the HEAT-H1 Mach 1.8 nozzle.

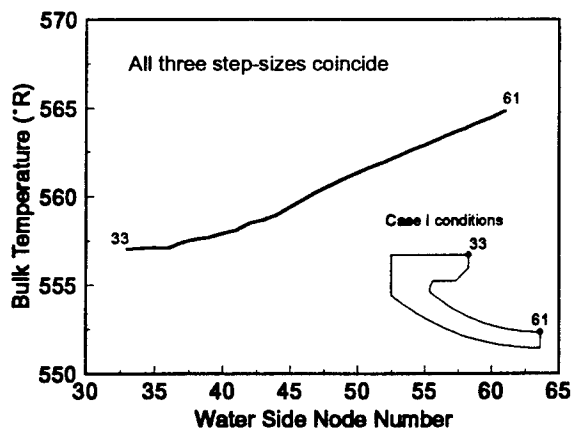


Figure 16. Water-side bulk temperature distribution for the HEAT-H1 Mach 1.8 nozzle

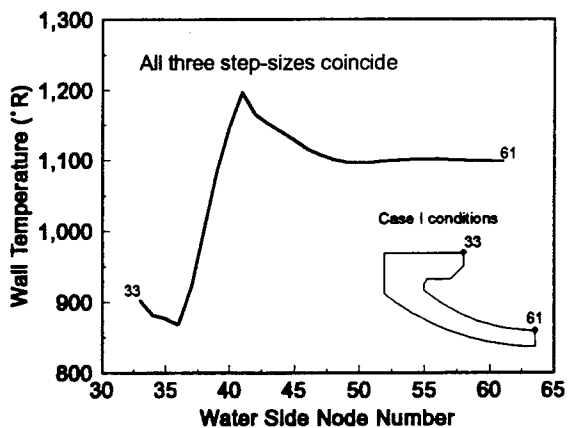


Figure 17. Water-side wall temperature distribution for the HEAT-H1 Mach 1.8 nozzle.

Mesh resolution convergence study:

Convergence characteristics for the unsteady solution algorithm were investigated as a function of finite element mesh resolution. Case I run conditions were used with the 0.0005 s time step-size to obtain steady-state solutions for three different mesh resolutions (refer to Figure 4): coarse, medium, and fine. The convergence history for the three solutions is shown in Figure 18.

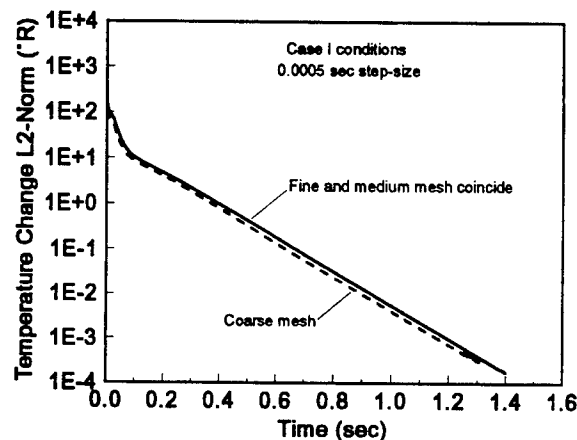


Figure 18. Convergence history for the solution algorithm mesh resolution study.

As in the time step-size convergence study, the L2-norm of the nodal temperature change is shown versus total solution time. For all three mesh resolutions, the solutions converge smoothly through seven orders of magnitude of the L2-norm. On a per-node basis, the convergence level corresponds to effective machine zero. The medium and fine meshes follow coincident convergence paths, with the coarse mesh differing only slightly from the medium and fine mesh cases. The mesh resolution convergence histories for all three meshes display essentially the same behavior as the convergence histories for the 0.001s and 0.0005 s step-size histories. In fact, the same data are used for both the fine mesh convergence curve on Figure 18, and the 0.0005 s step-size convergence curve on Figure 9.

Air-side solution results show excellent agreement between the medium and fine mesh cases. Solution comparisons for the air side of the HEAT-H1 Mach 1.8 nozzle are shown in Figures 19, 20, 21, and 22. Distributions for heat flux, heat transfer coefficient, and adiabatic wall temperature agree equally

well for all three mesh resolutions. The wall temperature distribution shows the departure of the coarse mesh solution from the medium and fine mesh results, while the medium and fine mesh results still compare equally well to each other. The coarse mesh result for wall temperature falls slightly below the medium and fine mesh results at all points along the nozzle wall, but the greatest difference appears at the point of maximum wall temperature.

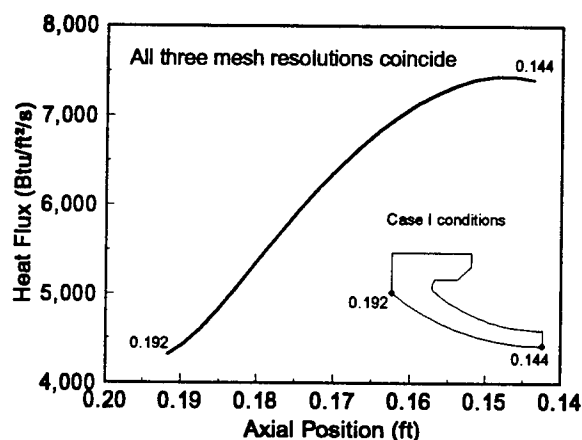


Figure 19. Air-side heat flux distribution for the HEAT-H1 Mach 1.8 nozzle.

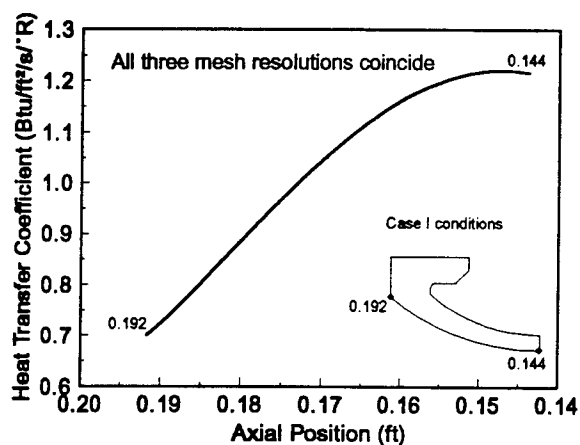


Figure 20. Air-side heat transfer coefficient distribution for the HEAT-H1 Mach 1.8 nozzle.

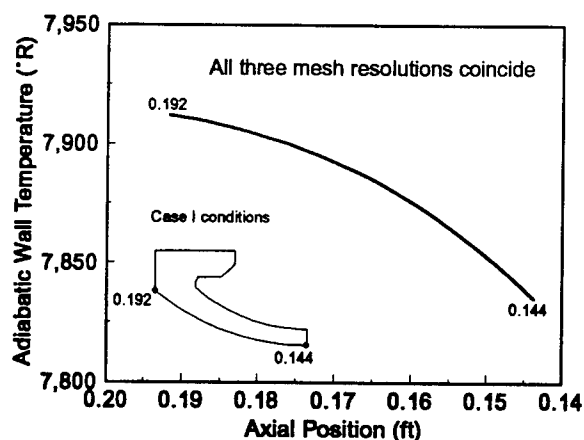


Figure 21. Air-side adiabatic wall temperature distribution for the HEAT-H1 Mach 1.8 nozzle.

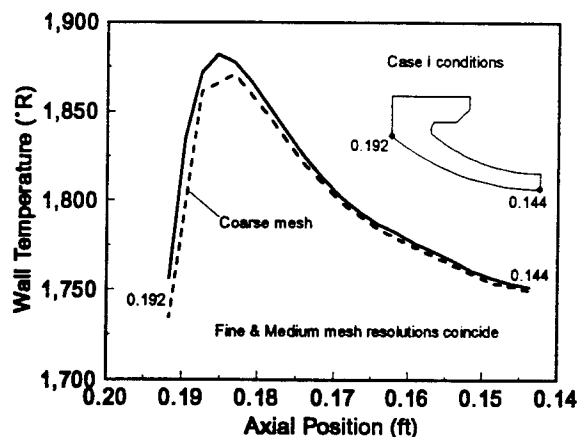


Figure 22. Air-side wall temperature distribution for the HEAT-H1 Mach 1.8 nozzle.

Water-side solution results show excellent agreement between the medium and fine mesh cases. Solution comparisons for the water side of the HEAT-H1 Mach 1.8 nozzle are shown in Figures 23, 24, 25, and 26. Distributions for heat flux, and heat transfer coefficient show the slight departure of the coarse mesh results from those of the medium and fine mesh results. The medium and fine mesh solutions compare equally well for the heat flux, and heat transfer coefficient distributions. All three mesh resolutions compare equally well for the bulk temperature, and wall temperature distributions.

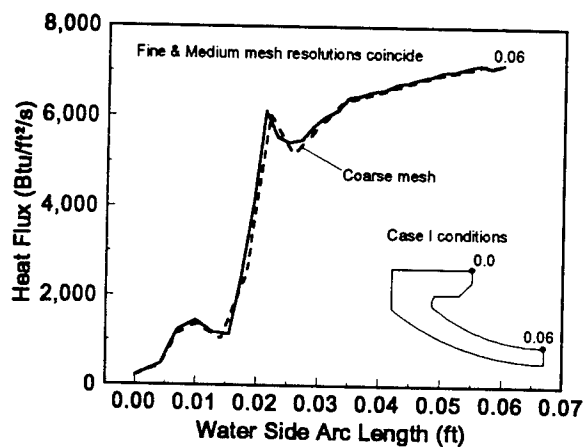


Figure 23. Water-side heat flux distribution for the HEAT-H1 Mach 1.8 nozzle.

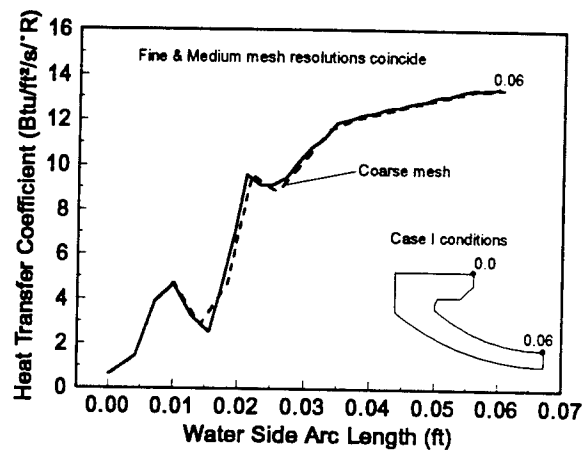


Figure 24. Water-side heat transfer coefficient distribution for the HEAT-H1 Mach 1.8 nozzle.

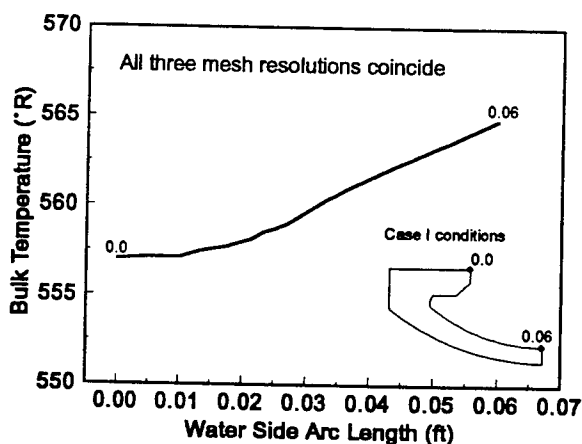


Figure 25. Water-side bulk temperature distribution for the HEAT-H1 Mach 1.8 nozzle

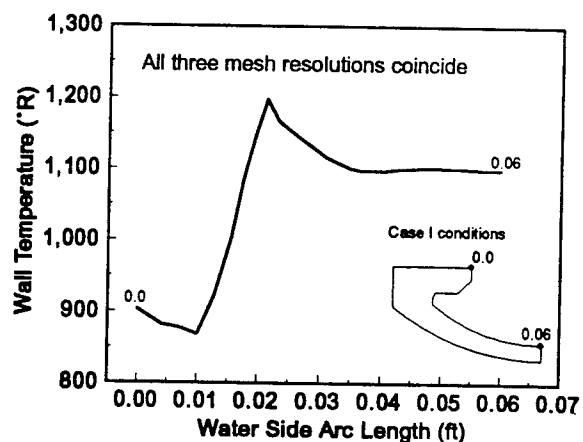


Figure 26. Water-side wall temperature distribution for the HEAT-H1 Mach 1.8 nozzle.

HEAT-H1 Mach 1.8 nozzle solutions:

The unsteady solution algorithm was used to obtain four axisymmetric, steady-state, conjugate heat transfer solutions for the HEAT-H1 Mach 1.8 nozzle. The run conditions used for the four cases are shown in Table II. With the exception of the air boundary-layer edge total temperatures, all values shown in Table II are identical to those in Table I.

**Table II. Run Conditions for Conjugate Heat Transfer
Analysis of the HEAT-H1 Mach 1.8 Nozzle.**

Test Case Number	I	II	III	IV
Water inlet total pressure (psia)	1,000	1,000	1,000	1,000
Water mass flow rate (lbm/s)	11.54	11.54	7.09	7.063
Water inlet temperature (°R)	557	552	520	520
Air total pressure (atm)	126.5	137	104.4	94.3
Air total temperature (°R)	9,000	9,432	8,280	9,180
Air edge total temperature (°R)	7,920	8,271	7,432	8,239
Air total enthalpy (Btu/lbm)	3,480	3,750	3,062	3,644

The results of the time step-size convergence study and the mesh resolution convergence study indicate that adequate solution convergence will be achieved by using the fine resolution finite element mesh with a time step-size of 0.001 s. The mesh resolution study also implies that equivalent results will be obtained by using the medium resolution mesh instead of the fine mesh. However, the fine mesh is chosen for this analysis because it offers smoother variation of solution results than the medium mesh, but at only slightly higher computational cost. The 0.001 s time step-size is used for this analysis because it offers a twofold savings in computation time over the 0.0005 s step-size.

Air-side results show that Case II run conditions present the most severe environment to the air side of the HEAT-H1 Mach 1.8 nozzle. Case solution comparisons for the air side of the nozzle are shown in Figures 27, 28, 29, and 30. The highest heat flux distribution (Figure 27) is achieved by Case II, followed by Case I, Case IV, and then Case III. Heat flux distributions for all but Case IV reach maximum values at mesh node 3, which is 0.0623 inches axially upstream from the nozzle throat. Heat flux for Case

IV reaches a maximum value at node 2, which is 0.0312 inches axially upstream from the nozzle throat. Heat transfer coefficient results (Figure 28) again show Case II having the highest values, followed by Case I, Case III, and Case IV. This ranking of heat transfer coefficients follows the same trend as that for air total pressure (refer to Table II). Heat transfer coefficient distributions for all four cases reach maximum values at node 2. Adiabatic wall temperature results (Figure 29) follow the same trend as air total temperature (and air boundary-layer edge total temperature), with Case II the highest, trailed closely by Case IV, then Case I, and Case III. Wall temperature results (Figure 30) share the same trend as the

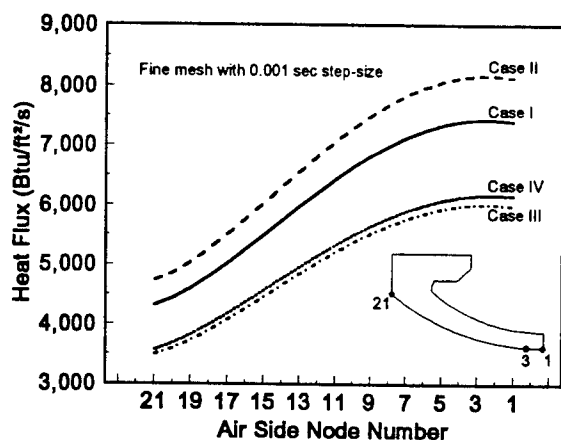


Figure 27. Air-side heat flux distribution for the HEAT-H1 Mach 1.8 nozzle.

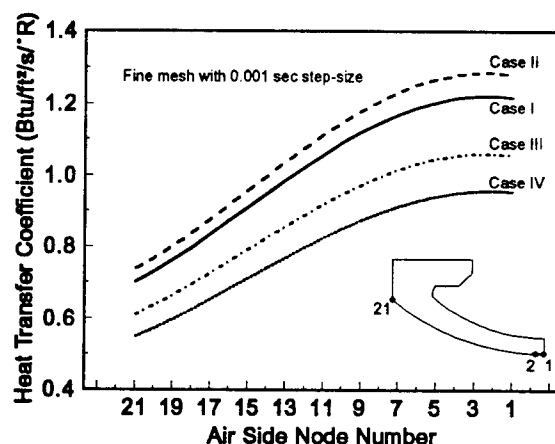


Figure 28. Air-side heat transfer coefficient distribution for the HEAT-H1 Mach 1.8 nozzle.

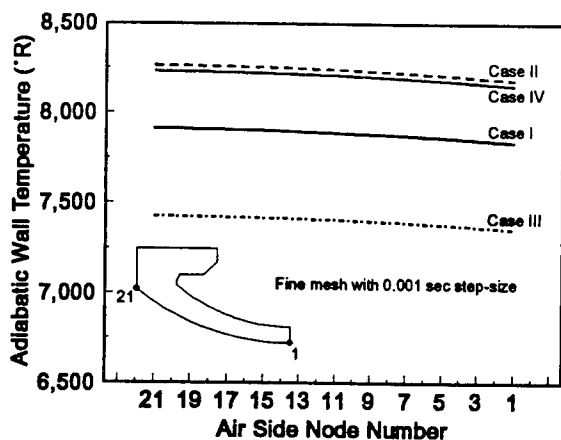


Figure 29. Air-side adiabatic wall temperature distribution for the HEAT-H1 Mach 1.8 nozzle.

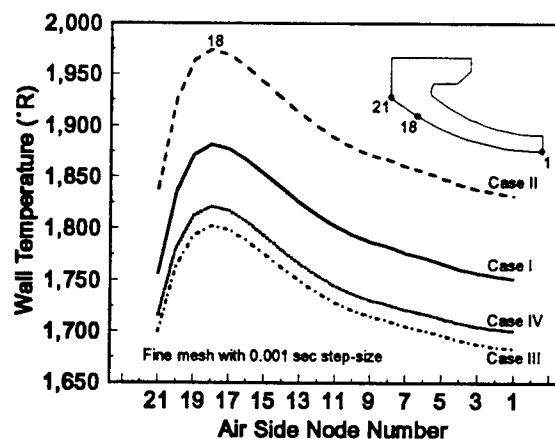


Figure 30. Air-side wall temperature distribution for the HEAT-H1 Mach 1.8 nozzle.

heat flux results, with Case II leading Case I, Case IV, and Case III, respectively. Wall temperatures for all four cases reach maximum values at node 18 on the nozzle wall. Note that the location of node 18 on the air-side nozzle wall is opposite the region on the water-side nozzle wall associated with bulk velocity and wall pressure extrema (refer to Figures 5 and 6). Maximum wall temperatures for all four cases fall well below the nozzle material melting point of 2,410°R.

Water-side results for the HEAT-H1 Mach 1.8 nozzle demonstrate the influence of the cooling passage flow profile, and subcooled boiling. Case solution comparisons for the water side of the nozzle are

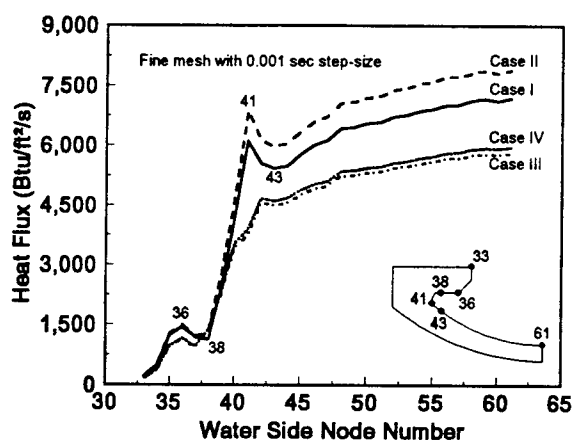


Figure 31. Water-side heat flux distribution for the HEAT-H1 Mach 1.8 nozzle.

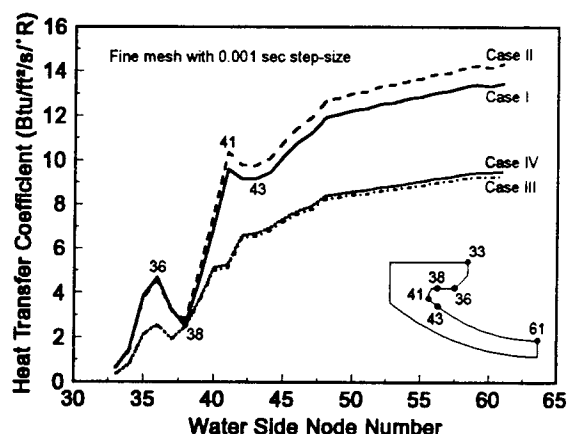


Figure 32. Water-side heat transfer coefficient distribution for the HEAT-H1 Mach 1.8 nozzle.

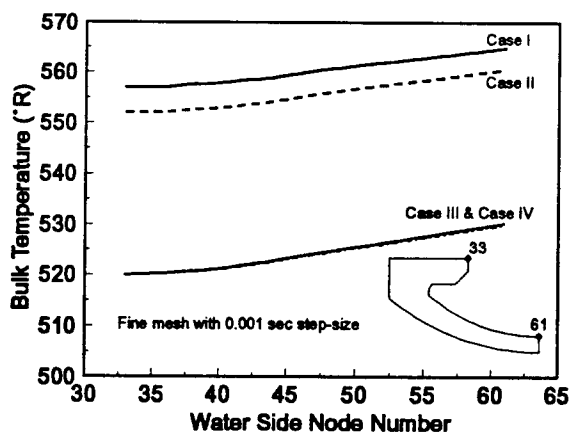


Figure 33. Water-side bulk temperature distribution for the HEAT-H1 Mach 1.8 nozzle

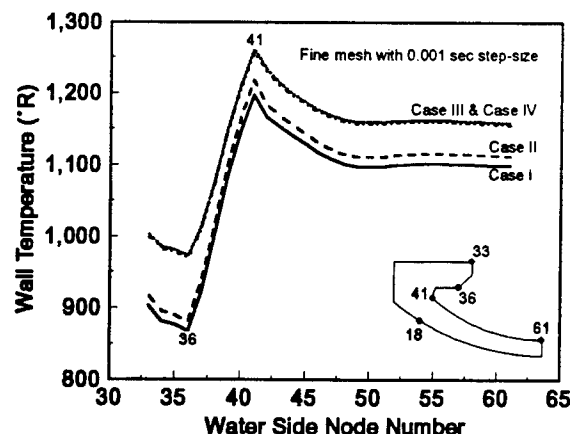


Figure 34. Water-side wall temperature distribution for the HEAT-H1 Mach 1.8 nozzle.

shown in Figures 31, 32, 33, and 34. The highest heat flux distribution (Figure 31) is achieved by Case II, followed by Case I, Case IV, and then Case III. This order reflects that of the air-side heat flux distributions (Figure 27). Water-side heat flux distributions for all four cases reach maximum values at the cooling passage throat (node 61). Heat flux local peaks at node 36 correspond to the water bulk velocity peaks at the same location (refer to Figure 5). Boiling begins at node 38 for Cases I and II, and at node 37 for Cases III and IV. Under the influence of boiling, the heat flux then rapidly increases for all four cases. While the heat flux local maxima at node 41 (Case I and Case II only) correspond to local extrema for both the water bulk velocity (refer to Figure 5), and the wall pressure (refer to Figure 6), the relative contribution of each flow extremum remains unknown. The heat flux local minimum at node 43, present in all four cases, results from the stagnation-flow induced pressure peak at the same location. Heat transfer coefficient results (Figure 32) show the same overall trends as the heat flux results, displaying identical features. Bulk temperature results (Figure 33) display smoothly increasing values as flow proceeds through the cooling passage. Case IV has the maximum temperature rise at the throat with 10.3 R, followed closely by Case III with 10.1 R. Case II shows a temperature rise at the throat of 8.6 R, and Case I has the lowest temperature rise at 7.9 R. Water-side wall temperature results (Figure 34) for all four cases place the maximum water-side wall temperature at node 41. This location on the water side of the nozzle wall is opposite to the location for the air-side maximum wall temperature at node 18 (Figure 30). Maximum wall temperatures for all four test cases are compared in Table III. Also shown are values

Table III. Maximum Wall Temperatures for the HEAT-H1 Mach 1.8 Nozzle Test Case Solutions.

Test Case Number	I	II	III	IV
Air-side maximum wall temperature (R)	1,882	1,974	1,802	1,821
Water-side maximum wall temperature (R)	1,197	1,218	1,256	1,261
Average of maximum wall temperatures (R)	1,540	1,596	1,529	1,541

of the air-side and wall-side maximum temperatures. Note that the two highest average values are those for Case II and Case IV, which are the same test cases for which wall failure has been observed (refer to Table I). The Case I average value trails the Case II value extremely closely, possibly indicating Case I conditions are near the failure threshold.

These four conjugate heat transfer solutions for the HEAT-H1 Mach 1.8 nozzle are obtained without regard to a convective boiling critical heat flux model. Since none of the nozzle wall temperatures for any of the four solutions exceed the nozzle material melting point (2,410 R), this analysis implies that the nozzle failures recorded in Table I are not due to insufficient heat load removal through nucleate boiling heat flux (pre-critical failure). The two remaining candidates for heat load failure are then: insufficient heat load removal through transition boiling heat flux (post-critical failure); and submelting-point plastic deformation to the point of structural yield (creep failure).

Consideration of post-critical failure requires comparison of a critical heat flux (CHF) prediction to the water-side heat flux distribution. If the water-side distribution anywhere exceeds the CHF prediction, then failure may be assumed. No theoretical approach yet exists for CHF prediction in convective subcooled boiling [26], thus requiring the use of mathematical correlations. Many candidate CHF correlation models applicable to the HEAT-H1 problem are reviewed in Ref. 26.

Some relevant factors to consider when choosing or developing a CHF model for the HEAT-H1 application are: an annular flow channel, a subcooled fluid, high flow velocities (up to 100 ft/s), high static pressures (up to 1,000 psia), high heat flux values (approaching 8,000 Btu/ft²/s), and high centrifugal flow acceleration (up to 5,700 g). While no single model accounts for all of these factors, Shope [3] has suggested a hybrid of the Rousar and Van Huff model [27] (further verified by Rousar and Chen [28]), and the model of Gu, Chow, and Beam [29].

The Rousar-Van Huff-Chen correlation accounts for subcooled, high velocity, high pressure flow through a straight tube, while the Gu-Chow-Beam correlation accounts for centrifugally accelerated flow through a curved tube (though for low velocity and low pressure). Shope applied the hybrid CHF model to the one-dimensional conjugate heat transfer analysis of the HEAT-H1 Mach 1.8 nozzle. Adjustable

constants were added to agree with test case failure results (those in Table I) in light of his one-dimensional analysis solutions. The Shope hybrid CHF model awaits experimental refinement in the High Temperature Wall Laboratory [30] at AEDC.

Differences in the cooling passage geometry, and the cooling passage flow solutions for the one-dimensional conjugate heat transfer analysis and the current analysis prevent direct application of the Shope CHF model. The one-dimensional analysis models the nozzle cooling passage as a smoothly varying, constant-gap annulus. Contrast this with the severe turns, and varying gap-size present in the current multidimensional analysis. Due to this difference in geometry, the flow velocity patterns and pressure distributions also differ for the two approaches, thus requiring modification of the adjustable constants. Alternatively, and more palatable from an analytical perspective, the adjustable constants could be obtained from the already mentioned experimental refinement in the High Temperature Wall Laboratory.

Analysis results show that the creep mechanism remains a viable failure mode. Creep effects become significant when material temperatures exceed one-half the melting temperature. Air-side wall temperatures (refer to Figure 30), and the transmural average of maximum temperatures (refer to Table III) for all four HEAT-H1 Mach 1.8 nozzle test cases exceed one-half of the material melting temperature (1,205°R).

Consideration of creep failure requires inclusion of nozzle wall viscoplastic and stress-rupture models in the unsteady solution algorithm. A viscoplastic model applicable to the HEAT-H1 nozzle is given in Reference 32. This model requires specification of material constants which characterize the temperature-dependent elastic properties, thermal diffusivity properties, steady-state plastic properties, temperature-dependent transient plastic properties, and the plastic initial conditions for the material (constants for copper are provided in [32]). These constants, along with stress, strain, and heat transfer histories, are then used to determine internal stress and strain values. A typical stress-rupture model correlates the current stress and temperature of the material, along with various material-dependent parameters, to predict a rupture time. Reference 33 summarizes many classic stress-rupture correlation models.

Conclusion

The development of a method for unsteady, axisymmetric, conjugate heat transfer analysis has been achieved. This approach features solid-body heat conduction with coupled, forced convection boundary conditions. The method was applied to heat load failure prediction for the HEAT-H1 Mach 1.8 nozzle at run conditions from four experimentally derived test cases. The solutions obtained indicate that nozzle wall failures recorded for two of the test cases are not the result of pre-critical boiling heat flux phenomena.

Two additional heat load failure modes remain to be investigated. Analysis of the post-critical failure mode is possible with the current method and the addition of a CHF model. A candidate CHF model has been identified, and awaits implementation. The creep failure mode can also be examined using the current method with the addition of viscoplastic and stress-rupture models for the HEAT-H1 Mach 1.8 nozzle. Both the air-side and water-side nozzle wall temperatures lie well within the range for the occurrence creep effects, warranting implementation of such a model.

One caveat for the results of this analysis is the neglect of two-phase flow effects in the water-side flow solutions. Two-phase flow arises from the presence of subcooled nucleate boiling on the hot wall of the nozzle cooling passage. Water vapor bubbles would act to decrease the effective flow area, and thus might lead to higher flow velocities than would be expected in single-phase flow. However, since the Shah correlation attempts to partially account for this effect, and because solution results show bulk water temperatures remaining highly subcooled, the effects of two-phase flow are believed to be negligible for the test cases examined.

Future work on this conjugate heat transfer analysis method should include investigation of improvements to the air-side and water-side flow models. The feasibility of replacing the current correlational air-side flow model with an equilibrium air solution should be examined. This air flow solution could be obtained externally to the analysis method algorithm, in the same manner as the current water-side flow solution. The water-side flow solution may benefit from consideration of two-phase flow effects. Several methods with varying degrees of accuracy (and difficulty) are available for consideration

[31]. Also, the water-side flow solution might be more accurately represented by developing a "wall-weighted" velocity distribution to replace the current bulk velocity distribution.

Complete heat load failure prediction (i.e. consideration of all three failure modes) for the HEAT-H1 Mach 1.8 nozzle can be readily achieved with the current analysis method and the suggested modifications. The pre-critical mode of failure has been eliminated from consideration. Remaining viable failure mechanisms are the post-critical mode and the creep mode. Inclusion of the post-critical failure mode awaits selection and application of an appropriate boiling critical heat flux model. Inclusion of the creep failure mode awaits the application of readily available thermoviscoplastic modeling techniques.

Acknowledgment

This work was funded by AFOSR through the 1993 Summer Research Extension Program at AEDC. The coordinating officer for the 1993 AFOSR Summer Research Extension Program at AEDC was Maj. Hal Martin, USAF. The project coordinator at the Georgia Institute of Technology was Dr. K. C. Gramoll. The author wishes to express gratitude to and acknowledge the contributions of Mr. F. L. Shope (Calspan Corporation/AEDC Operations) for his technical expertise in the field of conjugate heat transfer, and his extensive analysis effort on the HEAT-H1 Test Unit; and of Dr. B. R. Circelli (Calspan Corporation/AEDC Operations) for his knowledge of the INS3D-UP code, and his advance work on the cooling passage flow solution. The author also wishes to express gratitude to Dr. K. C. Gramoll for his considerable administrative assistance.

References

- [1] *Test Facilities Handbook*, Arnold Engineering Development Center, Arnold AFB, TN, Vol. 3, May 1992, p. 3.125.
- [2] Shope, Frederick L., "Conjugate Conduction/Convection/Nucleate-Boiling Heat Transfer with a High-Speed Boundary Layer," AIAA-91-5033, AIAA 3rd International Aerospace Planes Conference, Orlando, Dec. 1991.
- [3] Shope, Frederick L., "Conceptual Thermal Design of a 200-atm, Water-Cooled Arc Heater Nozzle," AIAA-93-2879, AIAA 28th Thermophysics Conference, Orlando, July 1993.

- [4] Weaver, Michael A., "Multidimensional Conjugate Heat Transfer Analysis for the Arnold Engineering Development Center HEAT-H1 Test Unit Nozzle," 1992 AFOSR Summer Research Program Final Report, Sept. 1992.
- [5] Weaver, Michael A., "Incompressible Navier-Stokes Flow Analysis for the Arnold Engineering Development Center HEAT-H1 Test Unit Nozzle Cooling Passage," 1993 AFOSR Summer Research Program Final Report, Sept. 1993.
- [6] Rochelle, J. K., "TRAX: A Program for 2D Heat Transfer Analysis," Master's Thesis, University of Tennessee Space Institute, 1973.
- [7] Raznjevic, Kuzman, *Handbook of Thermodynamic Tables and Charts*, Hemisphere Publishing Corporation, 1976, pp. 13,24.
- [8] Messinger, B. L. ed., *Aero-Space Applied Thermodynamics Manual*, Society of Automotive Engineers, Inc., 1962, p. D-1.
- [9] Ambrok, G. S., "Approximate Solution of Equations for the Thermal Boundary Layer with Variations in Boundary Layer Structure," *Soviet Physics/Technical Physics*, Vol. 2, No. 9, Sept. 1957, pp. 1979-1986.
- [10] Reynolds, W. C., W. M. Kays, and S. J. Kline, NASA Memo 12-2-58W, Washington D. C., 1958.
- [11] Kays, W. M., and M. E. Crawford, *Convective Heat and Mass Transfer*, McGraw-Hill Book Company, 1980, pp. 275-282.
- [12] Shapiro, Ascher H., *The Dynamics and Thermodynamics of Compressible Fluid Flow, Volume II*, Robert E. Kreiger Publishing Company, 1983, pp. 1135-1136.
- [13] Shope, Frederick L., Calspan Corporation/AEDC Operations, Arnold AFB, TN, unpublished project analysis.
- [14] Yos, J. M., "Revised Transport Properties for High Temperature Air and Its Components," Technical Release, Avco Systems Division, Nov. 1967, pp. 41-44.
- [15] Shah, M. Mohammed, "A General Correlation for Heat Transfer during Subcooled Boiling in Pipes and Annuli," *ASHRAE Transactions*, Vol. 83, Pt. 1, 1977, pp. 202-217.

- [16] Shah, M. Mohammed, "Generalized Prediction of Heat Transfer during Subcooled Boiling in Annuli," *Heat Transfer Engineering*, Vol. 4, No. 1, Jan.-Mar. 1983, pp. 24-31.
- [17] Shah, M. Mohammed, "Prediction of Heat Transfer during Forced-Convection Subcooled Boiling," *Handbook of Heat and Mass Transfer, Volume 1: Heat Transfer Operations*, Cheremisinoff, N. P., ed., Gulf Publishing Company, 1986, pp. 387-391.
- [18] Bergles, A. E., and W. M. Rohsenow, "The Determination of Forced Convection Surface Boiling Heat Transfer," *Trans. ASME, Journal of Heat Transfer*, Aug. 1964, pp. 305-311.
- [19] Rogers, S. E., "Numerical Solution of the Incompressible Navier-Stokes Equations," NASA TM 102199, 1990.
- [20] Chorin, A. J., "A Numerical Method for Solving Incompressible Viscous Flow Problems," *Journal of Computational Physics*, vol. 2, 1967, pp. 12-26.
- [21] Kwak, D., J. L. C. Chang, S. P. Shanks, and S. R. Chakravarthy, "A Three-Dimensional Incompressible Navier-Stokes Solver Using Primitive Variables," *AIAA Journal*, vol. 24, no. 3, 1986, pp. 390-396.
- [22] Rogers, S. E., and D. Kwak, "Upwind Differencing Scheme for the Time-Accurate Incompressible Navier-Stokes Equations," *AIAA Journal*, vol. 28, no. 2, 1990, pp. 253-262.
- [23] Hirsch, C., *Numerical Computation of Internal and External Flows, Volume 2: Computational Methods for Inviscid and Viscous Flows*, John Wiley & Sons Ltd., 1990, pp. 654-656.
- [24] *The 1967 IFC Formulation for Industrial Use*, International Formulation Committee of the International Conference on the Properties of Steam, Feb. 1967.
- [25] *Supplementary Release on Transport Properties*, Sixth International Conference on the Properties of Steam, Nov. 1964.
- [26] Beitel, G. R., "Boiling Heat-Transfer Processes and Their Application in the Cooling of High Heat Flux Devices," AEDC-TR-93-3, June 1993, pp. 34-50.
- [27] Rousar, D. C., and N. E. Van Huff, "Heat-Transfer Characteristics of 98% H_2O_2 at High Pressure and High Velocity," AFRPL-TR-66-263 (AGC Report 10785-SR-1), August 1966.

- [28] Rousar, D. C., and F. F. Chen, "Cooling High Pressure Combustion Chambers with Super Critical Pressure Water," AIAA-88-2845, AIAA 24th Joint Propulsion Conference, Boston, July 1988.
- [29] Gu, C. B., L. C. Chow, and J. E. Beam, "Flow Boiling in a Curved Channel," ASME Winter Meeting, San Francisco, 1989.
- [30] Beitel, G. R. and M. J. McConnell, "A High Heat Flux Boiling Apparatus for the Study of Cooling Effectiveness," AIAA-93-2741, AIAA 28th Thermophysics Conference, Orlando, July 1993.
- [31] Collier, J. G., *Convective Boiling and Condensation*, McGraw-Hill, New York, 1972.
- [32] Freed, Alan D., "Thermoviscoplastic Model with Application to Copper," NASA TP 2845, December 1988.
- [33] Meyers, Mark André, and Krishan Kumar Chawla, *Mechanical Metallurgy*, Prentice-Hall, Englewood Cliffs, New Jersey, 1984, pp. 662-667.

**COUPLING OF AN INDUCTIVE STORAGE GENERATOR WITH PLASMA EROSION
OPENING SWITCH (PEOS) TO A PLASMA RADIATION SOURCE (PRS) LOAD**

**Carlyle E. Moore
Associate Professor
Department of Physics**

**Morehouse College
830 Westview Drive, S.W.
Atlanta, GA 30314**

**Final Report for:
Research Initiation Program
Arnold Engineering Development Center**

**Sponsored by:
Air Force Office of Scientific Research
Arnold Air Force Base, Tullahoma, TN**

and

Morehouse College

December, 1993

COUPLING OF AN INDUCTIVE STORAGE GENERATOR WITH PLASMA EROSION OPENING SWITCH (PEOS) TO A PLASMA RADIATION SOURCE (PRS) LOAD

Carlyle E. Moore
Associate Professor
Department of Physics
Morehouse College

ABSTRACT

This Report examines the coupling of an inductive storage generator with Plasma Erosion Opening Switch (*PEOS*) to an imploding Plasma Radiation Source (*PRS*) load, using *MHD* single-fluid equations. Two models of the *PRS* are discussed. A simplified power flow model, which ignores the dynamics of internal plasma behavior, nonetheless allows an evaluation of the effects of the load impedance and other system parameters. A more realistic model takes account of internal dynamic processes, such as plasma pressure, magnetic compression, ohmic heating and radiation. The implosion dynamics, energetics and current history obtained with the simple model are close to those provided by the more sophisticated model, for similar system parameters and appropriate initial conditions, except that the latter model predicts a series of compressions and re-expansions late in the implosion process. If the initial radius is reduced sufficiently, the plasma collapses rapidly to high density and the *PRS* behaves like a resistance rather than an oscillating inductance. Less than 10% of the energy initially contained in the storage inductor is coupled to the *PRS* load in the form of kinetic energy, and nearly 35% is dissipated in the *PEOS*.

COUPLING OF AN INDUCTIVE STORAGE GENERATOR WITH PLASMA EROSION OPENING SWITCH (PEOS) TO A PLASMA RADIATION SOURCE (PRS) LOAD

Carlyle E. Moore

I. INTRODUCTION

It has been demonstrated experimentally^{1,2} that the implosion of annular, high-atomic-number material loads using high-power, low-impedance generators produces high-energy-density plasmas which have proven to be valuable intense laboratory sources of soft X-radiation. Theoretical studies suggest that these sources may be instrumental in achieving a number of defense-related objectives when driven by generators of even higher power. A proposal to build a facility at the ARNOLD ENGINEERING DEVELOPMENT CENTER (*AEDC*) for the purpose of testing space-bound military equipment has been under consideration for some time. In order to implement this program, X-ray simulators capable of meeting the next generation of *DNA* objectives must be used. *AEDC* will be the site of a large, inductive storage system capable of producing power yields ten times higher than those of the old generation. Construction of this X10 or "decade" facility has already begun.

This Report presents a review of the coupling of an inductive storage generator with Plasma Erosion Opening Switch (*PEOS*) to an imploding Plasma Radiation Source (*PRS*) load. The Plasma Erosion Opening Switch is a fast-opening switch that has been used successfully with a variety of pulsed power generators³⁻⁷, and will no doubt be used with the new X10-level inductive storage devices⁸. The overall effect of the *PEOS* is the transfer of current and energy to the load. A number of experiments, using generators such as GAMBLE I and GAMBLE II, as well as the new generation of X10-level systems, have been evaluated with diode loads. Acceptably efficient transfer of current and energy has been achieved, as a result of low impedance on the downstream side of the switch and predictable impedance behavior of the diode. This Report discusses an evaluation of the generator/switch combination used as a driver for plasma radiation source (*PRS*) loads.

Because of the dynamic characteristics of the *PEOS* and the plasma load, they form a more highly interactive system than an inductive system coupled to a diode load or a standard transmission-line system coupled to a *PRS* load. A description of the behavior of the coupled generator-load system must therefore be described in terms of a model of the dynamic impedance characteristics of the *PRS*. Special attention will be given to the following aspects of the operation of the system:

- Efficiency of transfer of energy from X10 systems into *PRS* loads.
- Effects of varying generator design parameters.
- Effects of internal plasma dynamics, ohmic heating and radiation on compact *PRS* load coupling.

II. Model of an Imploding Plasma Radiation Source

We describe below a simple theoretical model, due to S. W. McDonald and P. F. Ottinger⁹, of a cylindrically imploding gas-puff plasma radiation source. It is based on *MHD* single-fluid equations, and will be of crucial importance in our subsequent discussion of the coupling of the generator to the *PRS* load.

Consider a *gas-puff plasma* confined to a cylindrical annulus of length H , outer radius b and inner radius a , with a co-axial outer skin of skin depth δ . The plasma is contained within a co-axial wall of radius W , as shown in Figure 1. Current in the plasma flows only in the outer skin, of inner radius c , with uniform current density J . Positive ions in the plasma are assumed to have mass M and number density N . The corresponding quantities for the electrons are denoted by m and n , respectively. The model is developed by making a number of assumptions about the behavior of the plasma, and these will be spelled out as the discussion proceeds.

Conservation of mass in the plasma is represented by the equation of continuity

$$\frac{\partial \rho}{\partial t} + \nabla \cdot \mathbf{j} = 0 \quad (2.1)$$

where ρ is the mass density and

$$\mathbf{j} = \rho \mathbf{v} \quad (2.2)$$

is the mass current density vector, \mathbf{v} being the local velocity of the plasma. Using the vector identity

$$\nabla \cdot g \mathbf{A} = g \nabla \cdot \mathbf{A} + \mathbf{A} \cdot \nabla g \quad (2.3)$$

Equation (2.1) may be written as

$$\frac{\partial \rho}{\partial t} + \rho \nabla \cdot \mathbf{v} + \mathbf{v} \cdot \nabla \rho = 0 \quad (2.4)$$

We now make the assumption that the mass density ρ is uniform inside the plasma:

$$\nabla \rho = 0 \quad (2.5)$$

Equation (2.4) then reduces to

$$\frac{1}{\rho} \frac{\partial \rho}{\partial t} + \nabla \cdot \mathbf{v} = 0 \quad (2.6)$$

Now

$$\rho = NM + nm \quad (2.7)$$

and, if Z is the charge state of the positive ions, quasi-neutrality of the plasma gives

$$n \approx ZN \quad (2.8)$$

whence

$$\rho = NM + ZNm = NM(1 + Zm/M) \approx NM \quad (2.9)$$

since $m \ll M$. Equation (2.6) may then be written as

$$\frac{1}{N} \frac{\partial N}{\partial t} + \frac{1}{r} \frac{d}{dr}(rv) = 0 \quad (2.10)$$

where r is the cylindrical coordinate radius, and we have assumed that the velocity v is radial. The number density N may be written in terms of λ , the mass per unit length of the plasma:

$$N = \frac{\lambda}{M\pi(b^2 - a^2)} \quad (2.11)$$

and Equation (2.10) becomes

$$\frac{1}{r} \frac{d}{dr}(rv) = \frac{2}{b^2 - a^2} \left(b \frac{db}{dt} - a \frac{da}{dt} \right) \quad (2.12)$$

Assume, further, that the inner radius a and the outer radius b both move with the same speed U , i.e.

$$\frac{da}{dt} = \frac{db}{dt} = U \quad (2.13)$$

Equation (2.12) then reduces to

$$\frac{1}{r} \frac{d}{dr}(rv) = 2 \left(\frac{U}{b+a} \right) \quad (2.14)$$

which may be integrated to yield the velocity profile

$$v(r) = \left[\left(\frac{ab}{b+a} \right) U \right] \frac{1}{r} + \left(\frac{U}{b+a} \right) r \quad (2.15)$$

This velocity profile is equally valid for both $a > 0$ and $a = 0$ (annulus collapses into a cylinder). We shall therefore write the profile in the form

$$v(r) = \frac{C_1}{r} + C_2 r \quad (2.16)$$

$$C_1 = \begin{cases} abU / (b+a) ; a > 0 \\ 0 ; a = 0 \end{cases} ; C_2 = \begin{cases} U / (b+a) ; a > 0 \\ U / b ; a = 0 \end{cases} \quad (2.17)$$

However, there is a singularity in the velocity of the inner radius at the point $a = 0$, since for $a > 0$, $v(a) = U$ whereas for $a = 0$ the velocity must be zero.

So far, the velocity U of the outer radius has not been determined. To do so, we use the equation of motion

$$\rho \frac{d\mathbf{v}}{dt} = -\nabla p + \mathbf{J} \times \mathbf{B} \quad (2.18)$$

where p is the fluid pressure. The magnetic field due to the current I_p in the plasma is given by

$$B(r) = \begin{cases} 0 ; 0 < r < c \text{ (inner vacuum and core)} \\ [\mu_o I_p / 2\pi r] [(r^2 - c^2) / (b^2 - c^2)] ; c < r < b \text{ (skin)} \\ \mu_o I_p / 2\pi r ; b < r < W \text{ (outer vacuum)} \end{cases} \quad (2.19)$$

Note that the time derivative on the Left Hand Side of Equation (2.18) is the so-called convective derivative

$$\frac{d}{dt} = \frac{\partial}{\partial t} + \frac{\partial x_i}{\partial t} \frac{\partial}{\partial x_i} = \frac{\partial}{\partial t} + v_i \frac{\partial}{\partial x_i} = \frac{\partial}{\partial t} + \mathbf{v} \cdot \nabla \quad (2.20)$$

where the summation convention (a summation over each repeated index is to be performed; Latin indices i, j etc = 1, 2, 3) has been used. The equation of motion then takes the form

$$\rho \left[\frac{\partial}{\partial t} + \mathbf{v} \cdot \nabla \right] \mathbf{v} = -\nabla p + \mathbf{J} \times \mathbf{B} \quad (2.21)$$

Taking the scalar product of the velocity \mathbf{v} with Equation (2.21), we get

$$\rho \left[\mathbf{v} \cdot \frac{\partial \mathbf{v}}{\partial t} + v_i (\mathbf{v} \cdot \nabla) v_i \right] = -\mathbf{v} \cdot \nabla p + \mathbf{v} \cdot \mathbf{J} \times \mathbf{B} \quad (2.22)$$

Now
$$\mathbf{v} \cdot \frac{\partial \mathbf{v}}{\partial t} = \frac{\partial}{\partial t} \left(\frac{1}{2} v^2 \right) \quad (2.23)$$

and
$$v_i (\mathbf{v} \cdot \nabla) v_i = v_i \left[v_j (\partial_j v_i) \right] = \frac{1}{2} v_j \left[v_i (\partial_j v_i) + (\partial_j v_i) v_i \right] \quad (2.24)$$

$$= v_j \partial_j \left(\frac{1}{2} v_i v_i \right) = (\mathbf{v} \cdot \nabla) \frac{1}{2} v^2 \quad (2.25)$$

where we have used the notation $\partial_j \equiv \frac{\partial}{\partial x_j}$ ($j = 1, 2, 3$). Equation (2.22) then becomes

$$\rho \left[\frac{\partial}{\partial t} + \mathbf{v} \cdot \nabla \right] \frac{1}{2} v^2 = -\mathbf{v} \cdot \nabla p + \mathbf{v} \cdot \mathbf{J} \times \mathbf{B} \quad (2.26)$$

Recall that

$$\frac{\partial \rho}{\partial t} + \rho \nabla \cdot \mathbf{v} = 0 \quad (2.6)$$

or
$$\frac{1}{2} v^2 \left(\frac{\partial \rho}{\partial t} \right) + \frac{1}{2} v^2 (\rho \nabla \cdot \mathbf{v}) = 0 \quad (2.27)$$

Adding Equations (2.26) and (2.27), we get

$$\frac{\partial}{\partial t} \left(\frac{1}{2} \rho v^2 \right) + \rho (\mathbf{v} \cdot \nabla) \frac{1}{2} v^2 + \frac{1}{2} \rho v^2 (\nabla \cdot \mathbf{v}) = -\mathbf{v} \cdot \nabla p + \mathbf{v} \cdot \mathbf{J} \times \mathbf{B} \quad (2.28)$$

Now since the mass density ρ is assumed to be uniform, this may be written as

$$\frac{\partial}{\partial t} \left(\frac{1}{2} \rho v^2 \right) + \mathbf{v} \cdot \nabla \left(\frac{1}{2} \rho v^2 \right) + \frac{1}{2} \rho v^2 (\nabla \cdot \mathbf{v}) = -\mathbf{v} \cdot \nabla p + \mathbf{v} \cdot \mathbf{J} \times \mathbf{B} \quad (2.29)$$

or, using the vector identity

$$\nabla \cdot g \mathbf{A} = g \nabla \cdot \mathbf{A} + \mathbf{A} \cdot \nabla g \quad (2.3)$$

$$\frac{\partial}{\partial t} \left(\frac{1}{2} \rho v^2 \right) + \nabla \cdot \left(\frac{1}{2} \rho v^2 \mathbf{v} \right) = -\mathbf{v} \cdot \nabla p + \mathbf{v} \cdot \mathbf{J} \times \mathbf{B} \quad (2.30)$$

i.e.
$$\frac{\partial \kappa}{\partial t} + \nabla \cdot (\kappa \mathbf{v}) = -\mathbf{v} \cdot \nabla p + \mathbf{v} \cdot \mathbf{J} \times \mathbf{B} \quad (2.31)$$

where the quantity

$$\kappa = \frac{1}{2} \rho v^2 \quad (2.32)$$

is the kinetic energy density.

Since the Right Hand Side of Equation (2.31) is not equal to zero, the kinetic energy of the plasma is not conserved, i.e. the change in kinetic energy is not due to an influx of particles through the boundary surfaces at $r = a$ and $r = b$. The rate of change of the kinetic energy is obtained by integrating Equation (2.31) over the entire time-dependent volume of the plasma, using the divergence theorem and the result

$$\frac{d}{dt} \int_{V(t)} \kappa dV = \int_{V(t)} \frac{\partial \kappa}{\partial t} dV + \oint_{S(t)} \kappa \mathbf{v}_s \cdot d\mathbf{S} \quad (2.33)$$

where $S(t)$ is the boundary surface of the time-varying volume $V(t)$ and \mathbf{v}_s is the velocity of the surface element $d\mathbf{S}$. This gives

$$\left[\frac{d}{dt} \int_{V(t)} \kappa dV - \oint_{S(t)} \kappa \mathbf{v}_s \cdot d\mathbf{S} \right] + \oint_{S(t)} \kappa \mathbf{v}_s \cdot d\mathbf{S} = - \int_{V(t)} (\mathbf{v} \cdot \nabla p) dV + \int_{V(t)} [\mathbf{v} \cdot \mathbf{J} \times \mathbf{B}] dV \quad (2.34)$$

$$\boxed{\frac{dK}{dt} = - \int_{V(t)} (\mathbf{v} \cdot \nabla p) dV + \int_{V(t)} [\mathbf{v} \cdot \mathbf{J} \times \mathbf{B}] dV} \quad (2.35)$$

where K is the total kinetic energy. We shall evaluate each of the terms in Equation (2.35) in turn.

The total kinetic energy K is obtained from Equation (2.15) as

$$K = \int \frac{1}{2} \rho v^2 dV = \int_a^b \frac{\lambda}{2\pi(b^2 - a^2)} \left(\frac{U}{b+a} \right)^2 \left(\frac{ab}{r} + r \right)^2 2\pi r H dr \quad (2.36)$$

or

$$K = \frac{\lambda U^2 H}{(b^2 - a^2)(b+a)^2} \int_a^b r \left(\frac{a^2 b^2}{r^2} + 2ab + r^2 \right) dr \quad (2.37)$$

and upon evaluating the integral, we get

$$K = \frac{1}{4} \lambda U^2 H \left[1 + \frac{2ab}{(b+a)^2} + \frac{4a^2 b^2 \ln(b/a)}{(b^2 - a^2)(b+a)^2} \right] \quad (2.38)$$

This expression remains valid for $a = 0$, i.e.

$$K_{a=0} = \frac{1}{4} \lambda U^2 H \quad (2.39)$$

The time derivative of the kinetic energy is given by

$$\begin{aligned} \left. \frac{dK}{dt} \right|_{a>0} &= \frac{\lambda U H}{2(b+a)^2} \frac{dU}{dt} \left[b^2 + a^2 + 4ab + 4 \frac{a^2 b^2 \ln(b/a)}{b^2 - a^2} \right] + \\ &+ \frac{\lambda U^3 H}{2(b+a)^3} \left[b^2 + a^2 - 4ab + \frac{4ab(b^2 + a^2 - ab) \ln(b/a)}{b^2 - a^2} \right] \end{aligned} \quad (2.40)$$

$$\left. \frac{dK}{dt} \right|_{a=0} = \frac{1}{2} \lambda U H \frac{dU}{dt} \quad (2.41)$$

The first integral on the Right Hand Side of Equation (2.35) may be evaluated by using the vector identity (2.3):

$$\int_V (\mathbf{v} \cdot \nabla p) dV = \int_V [\nabla \cdot p \mathbf{v} - p \nabla \cdot \mathbf{v}] dV \quad (2.42)$$

$$\text{or} \quad \int_V (\mathbf{v} \cdot \nabla p) dV = \oint_S p \mathbf{v} \cdot d\mathbf{S} - (\nabla \cdot \mathbf{v}) \int_V p dV \quad (2.43)$$

where we have used the divergence theorem and the fact that

$$\nabla \cdot \mathbf{v} = -\frac{1}{\rho} \frac{\partial \rho}{\partial t} \quad (2.6)$$

is independent of position, since ρ is assumed to be uniform. Note also that the pressure p is equal to zero at the boundary surface of the plasma, hence the first integral on the Right Hand Side of Equation (2.43) is zero. The second integral on the Right is evaluated by dividing the volume V of the plasma into the volume V_c of the core and the volume V_s of the skin. We then have

$$\int_V (\mathbf{v} \cdot \nabla p) dV = -(\nabla \cdot \mathbf{v}) \left[\int_{V_c} p dV_c + \int_{V_s} p dV_s \right] = -(\nabla \cdot \mathbf{v}) [p_c V_c + p_s V_s] \quad (2.44)$$

where p_c and p_s are the average values of the pressure in the core and skin, respectively. Recall that

$$\nabla \cdot \mathbf{v} = 2 \left(\frac{U}{b+a} \right) \quad (2.14)$$

If the plasma is treated like a mixture of ideal gases (ions and electrons), the partial pressure exerted by the ions is equal to $\aleph_{c,s} k T_{c,s} / V_{c,s}$, where \aleph is the total number of ions, k is the Boltzmann constant and T is the absolute temperature. If Z represents the charge state of the ions, the number of electrons is equal to $Z \aleph$ (quasi-neutrality), and if it is assumed that the ions and electrons in each region have the same temperature, the partial pressure exerted by the electrons is equal to $\aleph_{c,s} Z k T_{c,s} / V_{c,s}$. Thus the total plasma pressure in the core or skin is given by

$$p_{c,s} V_{c,s} = \aleph_{c,s} (1 + Z) k T_{c,s} \quad (2.45)$$

Combining Equations (2.14), (2.44) and (2.45), we get

$$\boxed{\int_V (\mathbf{v} \cdot \nabla p) dV = 2k \left(\frac{U}{b+a} \right) (1+Z) (\aleph_c T_c + \aleph_s T_s)} \quad (2.46)$$

The $\mathbf{J} \times \mathbf{B}$ term in Equation (2.35) is

$$\int_V \mathbf{v} \cdot \mathbf{J} \times \mathbf{B} dV = - \int_V v |\mathbf{J} \times \mathbf{B}| dV \quad (2.47)$$

Using the expression (2.16) for v , and Equation (2.19) for the magnetic field, we get

$$\int_V \mathbf{v} \cdot \mathbf{J} \times \mathbf{B} dV = - \int_c^b \left(\frac{C_1}{r} + C_2 r \right) \left[\frac{I_p}{\pi(b^2 - c^2)} \right] \left[\frac{\mu_o I_p}{2\pi r} \left(\frac{r^2 - c^2}{b^2 - c^2} \right) \right] 2\pi r H dr \quad (2.48)$$

$$\text{or} \quad \int_V \mathbf{v} \cdot \mathbf{J} \times \mathbf{B} dV = - \left(\frac{\mu_o}{4\pi} \right) H I_p^2 \left[2C_1 \left\{ \frac{b^2 - c^2 [1 + 2 \ln(b/c)]}{(b^2 - c^2)^2} \right\} + C_2 \right] \quad (2.49)$$

The "coefficients" C_1 and C_2 are given in Equation (2.17) for both $a > 0$ and $a = 0$.

We note, in particular, that for $a = 0$ Equation (2.35) reduces to

$$\boxed{\frac{1}{2} \lambda U H \frac{dU}{dt} = 2k \frac{U}{b} (1+Z) (\aleph_c T_c + \aleph_s T_s) - \left(\frac{\mu_o}{4\pi} \right) H I_p^2 \frac{U}{b}} \quad (2.50)$$

This may be further simplified by neglecting the pressure term on the Right Hand Side, to give

$$\boxed{\frac{dU}{dt} = -\left(\frac{\mu_o}{2\pi}\right)\left(\frac{I_p^2}{\lambda b}\right)} \quad (2.51)$$

which describes the load dynamics of the $\mathbf{J} \times \mathbf{B}$ driven implosion of a gas puff plasma of radius b and linear mass density λ carrying a current I_p .

III. Simple Power Flow Model

In this Section, we shall describe the coupling of an inductive storage generator with Plasma Erosion Opening Switch to a *PRS* load. The treatment presented here is due to D. Mosher and R. J. Comisso¹⁰. We consider a much simplified version of the gas-puff model of the Plasma Radiation Source discussed in the previous Section, neglecting the effects of plasma pressure and focusing our attention on the implosion of the plasma annulus only after assembly time ($a = 0$). In spite of the simplicity of this approach, a number of useful conclusions can be drawn and the effects of variations of the generator design parameters may be examined.

A geometrical illustration of the power flow into the *PRS* load is given in Figure 2. We shall not attempt here to discuss the effects of such factors as internal plasma dynamics, ohmic heating or radiation. Instead, we shall rely on a lumped circuit analysis of the behavior of the system, based on the circuit shown in Figure 3. This approach is somewhat similar to the theoretical modeling of the Plasma Erosion Opening Switch by Ottinger, Goldstein and Meger³. It is assumed that at time $t = 0$ the storage inductor L_S is current charged to $I(0) = I_o$ by the generator, whose open circuit voltage then drops to zero. The Plasma Erosion Opening Switch is modelled as a resistance which is initially zero, but rises linearly with time as $R_S = \alpha t$, unlike the treatment of Ottinger et al³, where the switch resistance rises instantaneously from zero to a constant value. The large-radius vacuum region immediately downstream of the switch has a fixed inductance L_V . Power from the switch region is funneled into the small-radius *PRS* load by the addition of a radial vacuum feed with an inter-electrode gap large enough to insulate charged particle flow. The radial feed introduces substantial inductance L_d in series with the load, and a large-area, high electric field region in which significant current flow I_C can take place prior to insulation by the load current. The switch and load currents are denoted by I_S and I_P , respectively, and a current I_V flows in the vacuum inductance L_V . Conservation of charge is therefore represented by the Equations

$$I = I_s + I_v \quad (3.1)$$

$$I_v = I_c + I_p \quad (3.2)$$

In the analysis of Mosher and Comisso¹⁰, the following system parameters are kept fixed:

Storage inductance $L_s = 16$ nH

Initial current in storage inductance $I(0) = I_o = 30$ MA

Vacuum inductance $L_v = 2$ nH

This vacuum inductance is comparable to the total downstream inductance assumed in studies of *decade* systems with diode loads. Other parameters are varied in order to determine the optimum performance of the system.

The inductance of the radial feed is determined by equating the quantity $L_d I_p^2 / 2$ to the energy of the magnetic field. The energy density in the field is

$$w_B = \frac{1}{2\mu_o} B^2 = \frac{1}{2\mu_o} \left(\frac{\mu_o I_p}{2\pi x} \right)^2 \quad (3.3)$$

where x is the distance from the plasma axis. Hence

$$\frac{1}{2} L_d I_p^2 = \int_{b_o}^{r_s + \delta_s} \frac{\mu_o I_p^2}{8\pi^2 x^2} (2\pi x \delta_d) dx = \frac{1}{2} \left[\frac{\mu_o}{2\pi} \delta_d \ln \left(\frac{r_s + \delta_s}{b_o} \right) \right] I_p^2 \quad (3.4)$$

where

r_s = vacuum feed radius

δ_s = vacuum feed gap

δ_d = radial feed gap

b_o = initial plasma radius

Thus

$$L_d = \frac{\mu_o}{2\pi} \delta_d \ln \left(\frac{r_s + \delta_s}{b_o} \right) \quad (3.5)$$

Similarly, it may be shown that the load inductance is given by

$$L_p = \frac{\mu_o}{2\pi} z_p \ln \left[\frac{b_o + \delta_p}{b(t)} \right] \quad (3.6)$$

where

$$z_p = \text{load plasma length}$$

$$b(t) = \text{instantaneous radius of the imploding plasma}$$

and it is assumed, in the context of the annular gas-puff plasma discussed in the previous Section, that the annulus has already collapsed to a cylinder ($a = 0$).

The velocity U of the radius of the plasma is obtained from Equation (2.35). Neglecting the effects of plasma pressure, this reduces to

$$\frac{dK}{dt} = \int \mathbf{v} \cdot \mathbf{J} \times \mathbf{B} \, dV \quad (3.7)$$

and using Equations (2.41) and (2.49), we get

$$\frac{1}{2} \lambda U H \frac{dU}{dt} = -\frac{\mu_o}{4\pi} \left(\frac{U H I_p^2}{b} \right) \quad (3.8)$$

$$\frac{dU}{dt} = -\frac{\mu_o}{2\pi} \left(\frac{I_p^2}{\lambda b} \right) \quad (3.9)$$

where

$$U = \frac{db}{dt} \quad (2.14)$$

An important consideration in the discussion of the power flow model is the flow of charged particles in the radial feed. Electrons are emitted from the edge of the radial feed, at radius r_s , where the instantaneous voltage is V_d . This emission radius remains constant as the power pulse evolves, but the anode contact radius decreases with time from the initial value r_s , at a rate which is determined by electron heating of the anode. Ion emission from plasma on the heated portion of the anode leads to charge neutralization, and this causes the electron beam to pinch, thereby heating a new region of the anode^{11,12}. The instantaneous anode contact radius r_i is determined by equating the power supplied by the electron current I_e (in Amps) to the product of the electron energy flux F (in Joules/m²) required to produce plasma and the rate of change of the circular area of radius r_i . This gives

$$I_e V_d = F \left[-\frac{d}{dt} (\pi r_i^2) \right] = -2\pi F r_i \frac{dr_i}{dt} \quad (3.10)$$

The minus sign appears because the radius r_i decreases.

The electron current is assumed to be zero as long as the electric field V_d / δ_d in the radial feed is less than the breakdown value of 3×10^7 V / m. Once this field is exceeded, the emission current is given by the equation¹³

$$I_{emit} = 1.13 \times 10^4 S (\gamma^2 - 1)^{1/2} \quad (3.11)$$

where

$$S = r_s / \delta_d \quad (3.12)$$

is the geometrical aspect ratio of the radial feed, and the relativistic factor γ is obtained by equating the quantity $e V_d$ to the kinetic energy gained by the electrons:

$$e V_d = (\gamma - 1) m c^2 \quad (3.13)$$

$$\gamma = 1 + \frac{e V_d}{m c^2} \quad (3.14)$$

Now the rest energy of the electron is

$$m c^2 = 0.511 \text{ MeV} \quad (3.15)$$

Hence (3.14) reduces to

$$\gamma = 1 + \left(\frac{V_d}{0.511} \right) \times 10^{-6} \quad (3.16)$$

V_d being measured in volts. Magnetic insulation of electrons is estimated by comparing the current I_p in the PRS load to the critical current I_{crit} . The critical current is reached when the width δ_d of the radial feed gap is equal to the Larmor radius of the electron, and is obtained from the relation

$$\gamma m \left(\frac{v^2}{\delta_d} \right) = e v B = e v \left(\frac{\mu_o I_{crit}}{2 \pi r_s} \right) \quad (3.17)$$

where the velocity v of the electron is given by

$$v = \left[(\gamma^2 - 1)^{1/2} / \gamma \right] c \quad (3.18)$$

Hence

$$I_{crit} = \left(\frac{m c}{e} \right) \left(\frac{2 \pi}{\mu_o} \right) (\gamma^2 - 1)^{1/2} \left(\frac{r_s}{\delta_d} \right) \quad (3.19)$$

Inserting the values of the numerical constants, this reduces to

$$I_{crit} = 8.5 \times 10^3 S (\gamma^2 - 1)^{1/2} \text{ Amps} \quad (3.20)$$

The emission current is adjusted according to¹⁴

$$I_e = I_{emit} \exp \left[- \left(I_p / I_{crit} \right)^4 \right] \quad (3.21)$$

so that the electron current is "cut off" when the load current I_p exceeds the critical current I_{crit} .

The ion current is calculated by assuming that ions are emitted from the heated portion of the anode between radii $r_i(t)$ and r_s . The electron current density J_e and the ion current density J_i are related, under conditions of Child-Langmuir flow, by¹⁶

$$\frac{J_i}{J_e} = \left(\frac{Zm}{M} \right)^{1/2} \left(1 + \frac{e V_d}{2mc^2} \right)^{1/2} = \left(\frac{Zm}{M} \right)^{1/2} \left[\frac{1}{2} (\gamma + 1) \right]^{1/2} \quad (3.22)$$

where m , M are the electron and ion masses, respectively and Z represents the charge state of the ions. The electron current density can be shown to be¹⁶

$$J_e = \frac{\epsilon_o}{4} \left(\frac{2e}{m} \right)^{1/2} \frac{V_d^{3/2}}{\delta_d^2} g^2(\alpha) \quad (3.23)$$

where

$$g(\alpha) = \int_0^1 \frac{d\xi}{\left[\xi^{1/2} (1 + \alpha\xi)^{1/2} + (1 + \alpha)^{1/2} \{ (1 - \xi)^{1/2} - 1 \} \right]^{1/2}} \quad (3.24)$$

$$\alpha = \frac{e V_d}{2mc^2} \quad (3.25)$$

The ion current is therefore

$$I_i = J_i \left[\pi (r_s^2 - r_i^2) \right] = \left(\frac{Zm}{M} \right)^{1/2} \left[\frac{1}{2} (\gamma + 1) \right]^{1/2} \left[\frac{\epsilon_o}{4} \left(\frac{2e}{m} \right)^{1/2} \left(\frac{V_d^{3/2}}{\delta_d^2} \right) g^2(\alpha) \right] \left[\pi (r_s^2 - r_i^2) \right] \quad (3.26)$$

or

$$I_i = \frac{\epsilon_o}{4} \left(\frac{2Ze}{M} \right)^{1/2} \left[\frac{1}{2} (\gamma + 1) \right]^{1/2} V_d^{3/2} \left[\pi \frac{(r_s^2 - r_i^2)}{\delta_d^2} \right] g^2(\alpha) \quad (3.27)$$

which reduces, in the non-relativistic limit, to

$$I_i = \frac{\epsilon_0}{4} \left(\frac{2Ze}{M} \right)^{1/2} V_d^{3/2} \left[\pi \frac{(r_s^2 - r_i^2)}{\delta_d^2} \right] g^2(0) \quad (3.28)$$

In Reference 10, the ion current for Child-Langmuir flow is given as

$$I_i(CL) = 1.7 \times 10^{-7} V_d^{3/2} \left\{ 1 + \exp \left[- \left(I_p / I_{crit} \right)^4 \right] \right\} (r_s^2 - r_i^2) / \delta_d^2 \quad (3.29)$$

and the exponential term is included to increase CL emission by a factor of two when electron space charge is close to the anode surface. In addition to CL flow, Goldstein-Lee flow, induced by the pinched electron beam, is also considered. The GL ion current¹⁵ is

$$I_i(GL) = 2.3 \times 10^{-5} V_d^{1/2} [(r_s - r_i) / \delta_d] I_e \quad (3.30)$$

At any time, the ion current is taken to be larger of the expressions in (3.29) and (3.30).

For the purposes of circuit analysis, the charged particle current is taken to be

$$I_c = I_e + I_i \quad (3.31)$$

Equations (3.1) and (3.2), which represent conservation of charge, must be supplemented by the following Loop Equations, which represent conservation of energy:

$$-L_s \frac{dI}{dt} = I_s R_s \quad (3.32)$$

$$-L_s \frac{dI}{dt} - L_v \frac{dI_v}{dt} - L_d \frac{dI_p}{dt} - \frac{d}{dt} (L_p I_p) = 0 \quad (3.33)$$

$$-L_v \frac{dI_v}{dt} = V_d - I_s R_s \quad (3.34)$$

subject to the initial conditions

$$I(0) = I_o ; I_v(0) = 0 ; I_p(0) = 0 \quad (3.35)$$

Integrating Equation (3.33) with respect to time gives

$$-L_s \int_0^t \frac{dI}{dt} dt = L_v \int_0^t \frac{dI_v}{dt} dt + L_d \int_0^t \frac{dI_p}{dt} dt + \int_0^t \frac{d}{dt} (L_p I_p) dt \quad (3.36)$$

or

$$L_s [I_o - I(t)] = L_v I_v(t) + L_d I_p(t) + L_p I_p(t) \quad (3.37)$$

and using the relation

$$I_v = I_c + I_p \quad (3.2)$$

we get

$$L_V [I_c + I_p] + [L_d + L_p] I_p = L_S [I_o - I(t)] \quad (3.38)$$

or

$$L_V I_c + L_T I_p = L_S [I_o - I(t)] \quad (3.39)$$

where

$$L_T = L_V + L_d + L_p \quad (3.40)$$

Now eliminating I_S between (3.1) and (3.32). we get

$$-L_S \frac{dI}{dt} = R_S (I - I_V) = \alpha t (I - I_V) \quad (3.41)$$

$$\frac{dI}{dt} + \left(\frac{\alpha}{L_S} t \right) I = \left(\frac{\alpha}{L_S} t \right) I_V \quad (3.42)$$

Multiplying through by the integrating factor $\exp(\alpha t^2 / 2L_S)$ and integrating with respect to time, we get

$$\int_0^t \frac{d}{dt} [I(t) \exp(\alpha t^2 / 2L_S)] dt = \frac{1}{L_S} \int_0^t \alpha t I_V(t) \exp(\alpha t^2 / 2L_S) dt \quad (3.43)$$

$$I(t) \exp(\alpha t^2 / 2L_S) - I_o = \frac{1}{L_S} \int_0^t \alpha t I_V(t) \exp(\alpha t^2 / 2L_S) dt \quad (3.44)$$

$$I(t) = \exp(-\alpha t^2 / 2L_S) \left[I_o + \frac{1}{L_S} \int_0^t \alpha t I_V(t) \exp(\alpha t^2 / 2L_S) dt \right] \quad (3.45)$$

The current I_V is obtained from Equations (3.2) and (3.39) as

$$I_V = I_C + \frac{L_S [I_o - I(t)] - L_V I_C}{L_T(t)} \quad (3.46)$$

and the integral in Equation (3.45) is evaluated numerically. Recall that the implosion of the plasma is governed by the equation

$$\frac{dU}{dt} = \frac{d^2 b}{dt^2} = -\frac{\mu_o}{2\pi} \left(\frac{I_p^2}{\lambda b} \right) \quad (2.51)$$

which is integrated numerically up to time τ_i , when the radius b of the imploding plasma reaches some pre-determined fraction of its initial value b_o . In the analysis by Mosher and Comisso¹⁰, this has been taken to be $b / b_o = 0.1$.

Considerable simplification of the analysis can be achieved by assuming that the inductance

$$L_T = L_v + L_d + L_p \quad (3.40)$$

is fixed, and by neglecting the charged-particle flow in the radial feed (i.e. by taking $I_c = 0$). In this case, the circuit equations can be solved analytically. Equations (3.2) and (3.39) give

$$I_v = I_p = \frac{L_s [I_o - I(t)]}{L_T} \quad (3.47)$$

and (3.42) becomes

$$\frac{dI}{dt} + \left(\frac{\alpha}{L_s} t \right) I = \frac{\alpha}{L_T} t [I_o - I(t)] \quad (3.48)$$

or

$$\frac{dI}{dt} + \left(\frac{\alpha}{\beta} t \right) I = \left(\frac{\alpha}{L_T} I_o \right) t \quad (3.49)$$

where

$$\frac{1}{\beta} = \frac{1}{L_s} + \frac{1}{L_T} \quad (3.50)$$

Multiplying through by the integrating factor $\exp(\alpha t^2 / 2\beta)$ and integrating, we get

$$\int_0^t \frac{d}{dt} [I(t) \exp(\alpha t^2 / 2\beta)] dt = \frac{\alpha}{L_T} I_o \int_0^t t \exp(\alpha t^2 / 2\beta) dt \quad (3.51)$$

$$I(t) \exp(\alpha t^2 / 2\beta) - I_o = \frac{\beta}{L_T} I_o \int_0^t d[\exp(\alpha t^2 / 2\beta)] = \frac{\beta}{L_T} I_o [\exp(\alpha t^2 / 2\beta) - 1] \quad (3.52)$$

or

$$I(t) = I_o \left[(\beta / L_T) + (1 - \beta / L_T) \exp(-\alpha t^2 / 2\beta) \right] \quad (3.53)$$

The load current is obtained by substituting (3.53) into (3.47), to give

$$I_p(t) = \frac{L_s}{L_T} I_o (1 - \beta / L_T) [1 - \exp(-\alpha t^2 / 2\beta)] \quad (3.54)$$

where

$$\frac{L_s}{L_T} \left(1 - \frac{\beta}{L_T} \right) = \frac{L_s}{L_T} \left[1 - \frac{1}{L_T} \left(\frac{L_s L_T}{L_s + L_T} \right) \right] = \frac{L_s}{L_s + L_T} = \frac{\beta}{L_T} \quad (3.55)$$

or

$$I_p(t) = \frac{\beta}{L_T} I_o [1 - \exp(-\alpha t^2 / 2\beta)] \quad (3.56)$$

Equation (3.56) may be written in the form

$$I_p(t^2) = \frac{\beta}{L_T} I_o [1 - \exp(-t^2 / \tau)] \quad (3.57)$$

where the time constant τ is given by

$$\tau = \frac{2\beta}{\alpha} = \frac{2L_S L_T}{\alpha(L_S + L_T)} \quad (3.58)$$

The load current thus reaches the asymptotic value

$$I_p(\infty) = \left(\frac{L_S}{L_S + L_T} \right) I_o \quad (3.59)$$

after about 5 time constants, i.e. at a time t given by

$$t^2 \approx 5 \tau = 10 \left[\frac{L_S L_T}{\alpha(L_S + L_T)} \right] \quad (3.60)$$

The switch current I_S is equal to $I - I_p$. Using Equations (3.53) and (3.56), this gives

$$I_S(t) = I_o e^{-\alpha t^2 / 2\beta} \quad (3.61)$$

We note, in passing, that Equation (3.53) shows that the storage inductor current I also reaches the asymptotic value

$$I(\infty) = \frac{\beta}{L_T} I_o = \frac{L_S}{L_S + L_T} I_o \quad (3.62)$$

as the switch current becomes magnetically insulated.

We are now in a position to compare the predictions of this simplified power flow model with observations of the coupling of an inductive pulse generator with plasma erosion opening switch to a plasma radiation source. Experimental observations have been made by Mosher and Comisso¹⁰ for the parameter set listed in Table 1. For this set of parameters, the storage inductor current $I(t)$, switch current $I_S(t)$ and load current $I_p(t)$ predicted by the model are shown in Figure 4. The experimentally observed currents are shown in Figure 5. The load current predicted by the model rises to a value of 7.77 MA in 25 ns, 16.69 MA in 50 ns and 18.81 MA in 75 ns, essentially duplicating the observed rise in load current. As the end of the implosion is approached, the experimental load current decreases, as a result of the increasing inductance of the PRS load, while the load current predicted by the model (which assumes a constant load inductance equal to its initial value of 0.8 nH) continues to increase, reaching its

asymptotic value of 18.97 MA after about 108 ns. Incidentally, if the final value of 5.4 nH of the load inductance is used in the model, the final load current is found to be 16 MA, in good agreement with the experimentally observed value. The model predicts that the storage inductor current and the load current both reach the same asymptotic value of 18.97 MA, as the switch current decreases exponentially to zero. This model behavior is similar to what is observed experimentally, except that late in the implosion phase the switch current increases slightly, with a corresponding decrease in the load current. It is significant that such good agreement with experiment is obtained by this simple model, which neglects the effects of plasma pressure and charged-particle flow in the radial feed and assumes that the load inductance is fixed.

The observed behavior of the plasma radius $b(t)$, the radial feed voltage V_d and the load current $I_p(t)$ are shown in Figure 6. The load current shows a strong resemblance to the current I_v , deviating slightly early on and late in the power pulse, when charged particle flow in the radial feed is appreciable. From Equation (3.34), the radial feed voltage is given by

$$V_d = I_s R_s - L_v \frac{dI_v}{dt} = I_s (\alpha t) - L_v \frac{dI_v}{dt} \quad (3.63)$$

As can be seen from Figure 5, during the early part of the power pulse (up to about 50 ns), both the switch current $I_s(t)$ and the current $I_v(t)$ have relatively constant slopes, so Equation (3.63) can be written, approximately, as

$$V_d = (I_o - ct)(\alpha t) - d = -d + I_o \alpha t - c \alpha t^2 \quad (3.64)$$

where c and d are constants. This takes the form of a parabola, and the voltage rises above 3 MV after about 25 ns, then falls to about 2 MV at 50 ns. Subsequently, both currents I_s and I_v begin to level off, becoming flat at about 75 ns, when the voltage reaches its minimum value. The switch current then rises slightly and I_v falls slightly, resulting in an increase in the voltage V_d . Charged particle flow in the radial feed is depicted in Figure 7.

The energy in the storage inductor at any time t is given by

$$E(t) = \frac{1}{2} L_s I^2 = \frac{1}{2} L_s I_o^2 \left[(\beta / L_T) + (1 - \beta / L_T) \exp(-\alpha t^2 / 2\beta) \right]^2 \quad (3.65)$$

where we have used Equation (3.53), and the amount of energy extracted from the storage inductor at the end of the implosion phase $t = \tau_i$ is

$$\Delta E = E(0) - E(\tau_i) = 4.85 \text{ MJ} ; E(0) = 7.2 \text{ MJ} \quad (3.66)$$

This energy is distributed as follows:

$E_{R_s} = 2.5$ MJ is the energy dissipated in the switch

$E_C = 0.22$ MJ is the beam energy created in the radial feed

$E_k = 0.63$ MJ is the implosion kinetic energy of the load

$E_d = 1.5$ MJ is the magnetic energy stored downstream of the switch

where

$$E_{R_s} = \int_0^{\tau_i} I_s^2 R_s dt = \alpha I_o^2 \int_0^{\tau_i} t \left[\exp(-\alpha t^2 / \beta) \right] dt \quad (3.67)$$

and

$$E_k = \frac{1}{4} \lambda U^2 H \quad (2.39)$$

the speed U of the plasma radius being determined from the relation

$$\frac{dU}{dt} = -\frac{\mu_o}{2\pi} \left(\frac{I_p^2}{\lambda b} \right) \quad (3.9)$$

and

$$E_d = \frac{1}{2} L_v I_v^2 + \frac{1}{2} L_p I_p^2 \quad (3.68)$$

The distribution of energy during the implosion phase is shown in Figure 8.

The effects of various parameters on system performance may be examined by altering the values of the parameters listed in Table 1. This was done by Mosher and Commisso¹⁰, keeping the first five parameters in the Table fixed and altering the values of the remainder. The results of this exercise are contained in Table II. Several points of interest emerge from this tabulation. The first two entries demonstrate the effect of neglecting charged-particle flow in the radial feed. The load current and radial feed voltage remain essentially unchanged, as do the implosion time and implosion kinetic energy. In other words, both the circuit response and implosion dynamics are insensitive to energy losses in the radial feed, with the sole exception that if the charged-particle current is neglected, these losses appear as increased energy dissipation in the switch. This observation is of considerable theoretical importance, since a simplified lumped circuit analysis may be used to describe the coupling of the the generator through a *PEOS* to a *PRS* load.

The next five entries show the effect of doubling and of halving the system parameters. We see that the implosion kinetic energy increases with the plasma length, but that this is accompanied by a decrease in peak load current which is particularly strong for the largest plasma length. A quantity of some interest is the specific kinetic energy, defined as the kinetic energy per unit mass, $E_k / \lambda z_p$, where

λ is the linear density of the plasma. For the fixed linear density $\lambda = 3$ mg/cm, the specific kinetic energy takes the values 240 MJ/gm, 210 MJ/gm and 165 MJ/gm for plasma lengths of 0.5 cm, 1.0 cm and 2.0 cm, respectively. In other words, the specific kinetic energy decreases with plasma length, for fixed linear density. High specific kinetic energy is required in PRS loads designed to radiate at high photon energy, hence the radiation yield is maximized by using the minimum plasma length allowed.

One of the most significant features of the results presented in Table II is the strong correlation between the maximum load current $I_p(\text{max})$ and the coupled implosion kinetic energy E_k . Mosher and Commisso have obtained an empirical relation between E_k and the change in magnetic energy stored in the load inductor:

$$\Delta E_m = \frac{1}{2} \Delta L_p I_p^2(\text{max}) \quad (3.69)$$

assuming that the implosion of the PRS load occurs at peak current. The change in inductance of the load is obtained from the formula

$$L_p = \frac{\mu_o}{2\pi} z_p \ln \left[\frac{b_o + \delta_p}{b(t)} \right] \quad (3.6)$$

whence
$$\Delta L_p = 2 \left(\frac{\mu_o}{4\pi} \right) z_p \left\{ \ln \left[\frac{b_o + \delta_p}{b_f} \right] - \ln \left[\frac{b_o + \delta_p}{b_o} \right] \right\} = 2 \left(\frac{\mu_o}{4\pi} \right) z_p \ln \left(\frac{b_o}{b_f} \right) \quad (3.70)$$

where $b_f = b_o / 10$ is the final plasma radius. Detailed examination of the results in Table II leads to the relation

$$E_k \approx [0.76 \Delta E_m + 0.06] \text{ MJ} \quad (3.71)$$

The implosion kinetic energy E_k is, as we should expect, less than ΔE_m , which is computed on the basis of the maximum load current. Inserting the numerical values in Equation (3.71), we obtain the result

$$E_k = [0.00175 z_p I_p^2(\text{max}) + 0.06] \text{ MJ} \quad (3.72)$$

where z_p is measured in cm and $I_p(\text{max})$ is measured in MA. This relation holds for all the entries in the Table except those for which $z_p = 2$ cm (this gives $E_k = 0.57$ MJ instead of the observed value of 0.99 MJ) and $\delta_d = 0.5$ cm (which gives $E_k = 0.78$ MJ instead of the observed value of 0.72 MJ).

Of particular importance in the analysis is the efficiency of energy transfer from the storage inductor to the *PRS* load, defined as the ratio of implosion kinetic energy to the energy initially stored in the inductor L_S :

$$\eta = \frac{E_k}{E_S(0)} \quad (3.73)$$

For the purpose of estimating the efficiency, we shall neglect the term 0.06 in Equation (3.71), and write

$$E_k \approx 0.76 \times 0.5 \times \Delta L_p \times I_p^2(\text{max}) \quad (3.74)$$

or

$$E_k = 0.38 \times \Delta L_p \times \left(\frac{L_S}{L_S + L_T} \right)^2 I_o^2 \quad (3.75)$$

where we have used the expression

$$I_p(\infty) = \left(\frac{L_S}{L_S + L_T} \right) I_o \quad (3.59)$$

for the maximum load current, obtained earlier by assuming that all the inductances are fixed and charged-particle flow in the radial feed is neglected. It will be recalled that the load current obtained in this way is strikingly similar to the observed current. The energy initially contained in the storage inductor is

$$E_S(0) = \frac{1}{2} L_S I_o^2 \quad (3.76)$$

hence

$$\eta = \frac{0.76 L_S \Delta L_p}{[L_S + L_T(0)]^2} = \frac{2 \times 0.76 L_S (\mu_o / 4\pi) z_p \ln(r_o / r_f)}{[L_S + L_T(0)]^2} \quad (3.77)$$

substituting for ΔL_p from Equation (3.70). Note that z_p is measured in cm and the inductances are in nH. Inserting the parameter values $z_p = 1$ cm, $r_o / r_f = 10$, $L_S = 16$ nH and $L_T(0) = 9.3$ nH, we get

$$\eta = 0.087 \quad (3.78)$$

IV. POWER FLOW WITH Z-PINCH LOAD MODELING

In the previous Section, a simple model was used to describe the coupling of the generator to a *PRS* load which takes the form of an annular gas puff. This model ignores the effect of plasma pressure and other internal dynamic processes, but is suitable because most of the energy is inductively deposited in the load as kinetic energy of implosion. Loads for which these considerations play a significant role,

such as the compact PRS loads which may be used in DNA decade systems, cannot be treated with this model. In addition to plasma pressure, such processes as adiabatic compression, ohmic heating and radiation need to be taken into account. These are included in the so-called *gas-bag model*, which considers a titanium plasma at uniform (ion) density $N(t)$ and temperature $T(t)$ within the boundary radius $b(t)$. This radius is affected by the expansion force due to plasma pressure as well as the compressional magnetic force produced by the current flowing in the plasma. The determination of the radial velocity profile is based on the assumption that the plasma motion is self-similar:

$$v(r,t) = \left(\frac{db}{dt} \right) \frac{r}{b} = U \frac{r}{b} \quad (4.1)$$

where r is the cylindrical coordinate radius and $U = db/dt$ is the (radial) velocity of the boundary surface. Conservation of mass may be written in the form

$$N = \frac{\lambda}{M\pi b^2} = \text{constant} \quad (4.2)$$

where M is the ion mass, λ is the mass per unit length of the plasma and $N(t)$ its number density, and we have put $a = 0$ in Equation (2.11). In Section II the equation of motion was used to obtain an equation for the velocity of the radius b of the plasma. This is given in Equation (2.50). A modified form of this equation is given by Mosher and Comisso¹⁰ as

$$\frac{1}{2} \lambda \left[b \frac{dU}{dt} + g c_s U \right] = 2(1+Z) \left(\frac{\aleph}{H} \right) kT - \left(\frac{\mu_o}{4\pi} \right) I_p^2 \quad (4.3)$$

where λ is the mass of the plasma per unit length, Z is the charge state of the ions and \aleph their total number, H is the length of the plasma, k is the Boltzmann constant and T the temperature in the core of the plasma (the presence of a skin is neglected), and I_p is the load current. In the second term in square brackets, g is a constant ≤ 1 and c_s is the speed of sound. This term represents the thermalization of kinetic energy through propagation of sound waves in the plasma. Conservation of energy may be expressed as

$$\frac{d}{dt}(E_i + E_k) = P_{ohm} + P_{mag} - P_{rad} \quad (4.4)$$

where E_i and E_k are, respectively, the internal energy and the kinetic energy per unit length, P_{ohm} is the power per unit length in ohmic heating, P_{mag} is the power per unit length due to magnetic compression of the plasma, and P_{rad} is the power radiated by the plasma per unit length. The kinetic energy per unit length is obtained from

$$dE_k = \frac{1}{2} [M N(t) (2\pi r dr)] v^2(r, t) = \pi M N(t) r dr \left[\frac{r^2}{b^2} U^2 \right] \quad (4.5)$$

$$E_k(t) = \pi M N(t) \frac{U^2}{b^2} \int_0^b r^3 dr = \frac{1}{4} M [\pi b^2 N(t)] U^2 \quad (4.6)$$

$$E_k = \frac{1}{4} \lambda U^2 \quad (4.7)$$

The power per unit length due to magnetic compression is

$$P_{mag} = -I_p B v = -\frac{\mu_o I_p^2 v}{2\pi r} = -\frac{\mu_o I_p^2 U}{2\pi b} \quad (4.8)$$

and

$$P_{ohm} = \eta(T) \frac{I_p^2}{\pi b^2} \quad (4.9)$$

is the power per unit length in ohmic heating¹⁷, where η is the resistivity of the plasma. The radiated power per unit length is given by¹⁰

$$P_{rad}^{-1} = P_t^{-1} + P_b^{-1} \quad (4.10)$$

$$P_t = S(T) Z(T) \frac{\lambda^2}{M^2 \pi b^2} \quad (4.11)$$

is an optically thin rate and

$$P_b = (\sigma T^4)(2\pi b) \quad (4.12)$$

where σ is the Stefan-Boltzmann constant, is the black-body rate.

As before, we rely on a lumped circuit analysis of the behavior of the system, based on the circuit shown in Figure 9. The plasma load is coupled inductively to the generator, as in the simple power flow model, and resistively through the time-varying resistance $R_p(t)$ in series with the load inductance L_p . Conservation of charge is again represented by the equations

$$I = I_s + I_v \quad (3.1)$$

$$I_v = I_c + I_p \quad (3.2)$$

and the Loop Equation

$$-L_s \frac{dI}{dt} = I_s R_s \quad (3.32)$$

is retained, but because of the resistive coupling, Equation (3.33) is replaced by

$$-L_s \frac{dI}{dt} - L_v \frac{dI_v}{dt} - L_d \frac{dI_p}{dt} - \frac{d}{dt}(L_p I_p) = I_p R_p \quad (4.13)$$

The initial conditions are, as before,

$$I(0) = I_o ; I_v(0) = 0 ; I_p(0) = 0 \quad (3.35)$$

Using (3.2), Equation (4.13) may be written as

$$\frac{d}{dt}(L_s I) + \frac{d}{dt}[L_v(I_c + I_p)] + \frac{d}{dt}(L_d I_p) + \frac{d}{dt}(L_p I_p) = -I_p R_p \quad (4.14)$$

or

$$\frac{d}{dt}(L_s I + L_v I_c) + \frac{d}{dt}(L_T I_p) = -I_p R_p \quad (4.15)$$

where

$$L_T = L_v + L_d + L_p \quad (3.40)$$

Equation (4.15) may be re-written as

$$\frac{d}{dt}(L_T I_p) + \frac{R_p}{L_T}(L_T I_p) = -\frac{d}{dt}(L_s I + L_v I_c) = -\frac{d}{dt}G(t) \quad (4.16)$$

where

$$G(t) = (L_s I + L_v I_c) \quad (4.17)$$

The integrating factor is $\exp[F(t)]$, where

$$F(t) = \int_0^t \frac{R_p}{L_T} dt \quad (4.18)$$

$$\int_0^t \frac{d}{dt}[L_T I_p e^{F(t)}] dt = - \int_0^t \frac{dG}{dt} e^{F(t)} dt \quad (4.19)$$

$$L_T I_p e^{F(t)} = - \int_0^t e^{F(t)} dG = - \left[e^{F(t)} G(t) \Big|_0^t - \int_0^t G(t) \frac{dF}{dt} e^{F(t)} dt \right] \quad (4.20)$$

$$L_T I_p e^{F(t)} = - \left[e^{F(t)} G(t) - G(0) - \int_0^t \frac{R_p}{L_T} G(t) e^{F(t)} dt \right] \quad (4.21)$$

$$L_T I_p = - \left[G(t) - G(0) e^{-F(t)} - e^{-F(t)} \int_0^t \frac{R_p}{L_T} G(t) e^{F(t)} dt \right] \quad (4.22)$$

$$= - [L_S I + L_V I_C] + L_S I_o e^{-F(t)} + e^{-F(t)} \int_0^t \frac{R_p}{L_T} (L_S I + L_V I_C) e^{F(t)} dt \quad (4.23)$$

$$L_S [I_o e^{-F(t)} - I] = L_T I_p + L_V I_C - e^{-F(t)} \int_0^t \frac{R_p}{L_T} (L_S I + L_V I_C) e^{F(t)} dt \quad (4.24)$$

The results of this calculation are displayed in Figure 10, using the parameter values of Table I, except that the plasma now has an initial radius $b_o = 5.66$ cm and contains 5×10^{18} ions. These values are chosen so that the nominal implosion time is the same as for the parameters of Table I. A dimensional analysis of Equation (4.3) shows that the implosion time does not change if λb_o^2 is kept fixed. The load current I_p is obtained by numerical integration of Equation (4.24), neglecting the charged-particle flow in the radial feed (i.e. assuming that $I_c = 0$) and using the value of the inductor current $I(t)$ obtained from Equation (3.45), which ignores the resistive coupling of the load to the inductor. The time variation of the plasma radius and load current (during the nominal implosion time $0 \leq t \leq 118$ ns) are quite similar to the results obtained with the simple power flow model, using annular mass calculations. The internal energy peaks at about 118 ns, at a value which is close to the kinetic energy of implosion of the simpler calculation. Early on in the implosion process, ohmic heating raises the temperature of the plasma to about 10 eV. Subsequent compressional heating results in a further rise in temperature to over 10 keV. At these high temperatures, plasma resistivity is low, and therefore ohmic heating is small, as can be seen from Equation (4.9). Peak compression of the plasma is achieved at about 118 ns, after which the kinetic pressure exceeds magnetic pressure, and the plasma expands and cools. Note that an implosion time of 118 ns leads to a radial compression of about 10, this being achieved through self-consistent internal plasma dynamics whereas, in the simpler model, a compression ratio of 10 is imposed as a boundary condition. This similarity in the compression ratios means that the implosion dynamics, energetics and current history derived from the gas-bag model are close to those obtained from the annular mass calculations.

During the expansion phase, the plasma radius is large and the temperature remains relatively high (resistivity is relatively low). Equation (4.9) shows that, under these conditions, ohmic dissipation is low. As the radius increases, the load inductance decreases, the current remains high and the plasma undergoes a second compression. This behaviour continues as time progresses, i.e. the plasma experiences a series of compressions and expansions, with decreasing radial amplitude.

A different type of *PRS* load behaviour is observed when the initial plasma radius is decreased to 0.5 cm and the line density increased to 10^{19} ions/cm. The plasma radius decreases rapidly, and radiation becomes a predominant feature of the implosion process. After peak compression has occurred, a quasi-equilibrium process takes place, in which black-body radiation is emitted at a rate which is determined by the accompanying ohmic heating, as the plasma expands slowly. This behavior is illustrated in Figure 11.

V. Summary

This Report presents a description of the coupling of a X10 (decade) level inductive storage generator using a Plasma Erosion Opening Switch (*PEOS*) to a Plasma Radiation Source (*PRS*) load. For simplicity, the *PEOS* is modeled as a resistance R_s which is proportional to the time t (it is assumed that at time $t = 0$ the storage inductor is current charged to $I(0) = 30$ MA by the generator). The large-radius *PEOS* is coupled to the small-radius *PRS* by the addition of a radial feed, which introduces considerable inductance downstream of the switch. This power flow model takes account of loss currents due to charged particle flow in the radial feed. Two models of the *PRS* are used. The first is a simplified version of a cylindrically imploding gas puff plasma, in which the effects of plasma pressure and other dynamic processes are neglected. The second is the so-called "gas-bag" model, in which plasma pressure, adiabatic compression, ohmic heating and radiation are all taken into account.

Using the simplified model, the behaviour of the coupled generator-load system was examined by varying certain selected system parameters and keeping the others fixed. On the basis of this analysis, the following conclusions may be drawn:

- (1) Loss currents due to charged particle flow in the radial feed have only a minor effect on the energy coupled to the load. Neglect of these currents simplifies the lumped circuit analysis, and has the effect of increasing the energy dissipated in the switch.
- (2) The efficiency of transfer of energy from the storage inductor to the load increases with length of the plasma load. However, the increased inductance of the longer plasma length causes a reduction in peak load current. For a storage inductor of 16 nH coupled to an imploding *PRS* load of 1 cm length

(assuming that charged particle flow in the radial feed can be neglected and that there is a *fixed* inductance of 9.3 nH downstream of the switch), the efficiency of energy transfer is roughly 8.7%.

(3) Nearly 35% of the energy initially contained in the storage inductor (2.5MJ out of 7.2MJ) is dissipated in the *PEOS*.

(4) Coupled implosion energy depends more weakly on the linear density λ and initial radius b_o of the plasma than in conventional generators. This indicates that there may be greater flexibility in the choice of these parameters when using inductive generators.

The results obtained with the gas-bag model are similar to those of the simpler model, for appropriately chosen values of the linear density λ and initial radius b_o of the plasma. However, when the initial radius is reduced sufficiently, the plasma radius collapses rapidly and a quasi-equilibrium pinch evolution results. Under these conditions, ohmic heating is balanced by black-body radiation and the *PRS* behaves like a resistance, as opposed to an oscillating inductance, and the electrical circuit is highly damped. The gas-bag model therefore exhibits two different types of load behaviour, depending on the initial conditions, and these represent limiting cases of the dynamic evolution of the *PRS* load inductively coupled to the generator.

Acknowledgments

I would like to express my gratitude to the Air Force Office of Scientific Research for sponsoring this research, and to the Arnold Engineering Development Center for its hospitality during the 1992 Summer Faculty Research Program, out of which this project developed. In particular, I would like to thank Mr. Tim Cotter for suggesting this topic and my Focal Point at *AEDC*, Mr. Lavell Whitehead, for his unwavering help and encouragement.

References

1. C. Stallings, K. Nielsen and R. Schneider, *Appl. Phys. Lett.*, **29**, 404 (1976).
2. D. Mosher and S. J. Stephanakis, *NRL Memorandum Rep.* 3321 (1976).
3. P. F. Ottinger, S. A. Goldstein and R. A. Meger, *J. Appl. Phys.*, **56**, 224 (1984).
4. R. J. Commisso, G. Cooperstein, R. A. Meger, J. M. Neri, P. F. Ottinger and B. V. Weber, *NRL Memorandum Rep.* 5560 (1985).
5. G. Cooperstein and P. F. Ottinger, *IEEE Trans. Plasma Sci*, **PS-15**, No. 6, 629 (1987).
6. B. V. Weber, R. J. Commisso, G. Cooperstein, J. M. Grossmann, D. D. Hinshelwood, M. Mosher, J. M. Neri, P. F. Ottinger and S. J. Stephanakis, *IEEE Trans. Plasma Sci*, **PS-15**, No. 6, 635 (1987).

References (cont'd)

7. B. V. Weber, R. J. Commisso, P. J. Goodrich, J. M. Grossmann, D. D. Hinshelwood, J. C. Kellogg and P. F. Ottinger, IEEE Trans. Plasma Sci, PS-19, No. 5, 757 (1991).
8. Meeting Record, DNA Pulsed Power Review and SDIO Update, Las Vegas, NV (1986), E. E. Stobbs, R. J. Commisso and J. M. Neri, Eds., p 5.
9. S. W. McDonald and P. F. Ottinger, NRL Memorandum Rep. 5785 (1986).
10. D. Mosher and R. J. Commisso, NRL Memorandum Rep. (1989).
11. E. Blaugrund, G. Cooperstein and S. A. Goldstein, Phys. Fluids, 20, 1185 (1977).
12. E. Blaugrund and G. Cooperstein, Phys. Rev. Lett., 34, 461 (1975).
13. D. J. Johnson, S. A. Goldstein, R. Lee and W. F. Oliphant, J. Appl. Phys., 49, 4634 (1978).
14. D. Mosher, NRL Memorandum Rep. 3883 (1978).
15. S. A. Goldstein and R. Lee, Phys. Rev. Lett, 35, 1079 (1975).
16. J. W. Poukey, Appl. Phys. Lett., 26, 145 (1975).
17. S. C. Braginskii, Rev. Plasma Phys., Vol. I, Consultants Bureau, New York (1975).

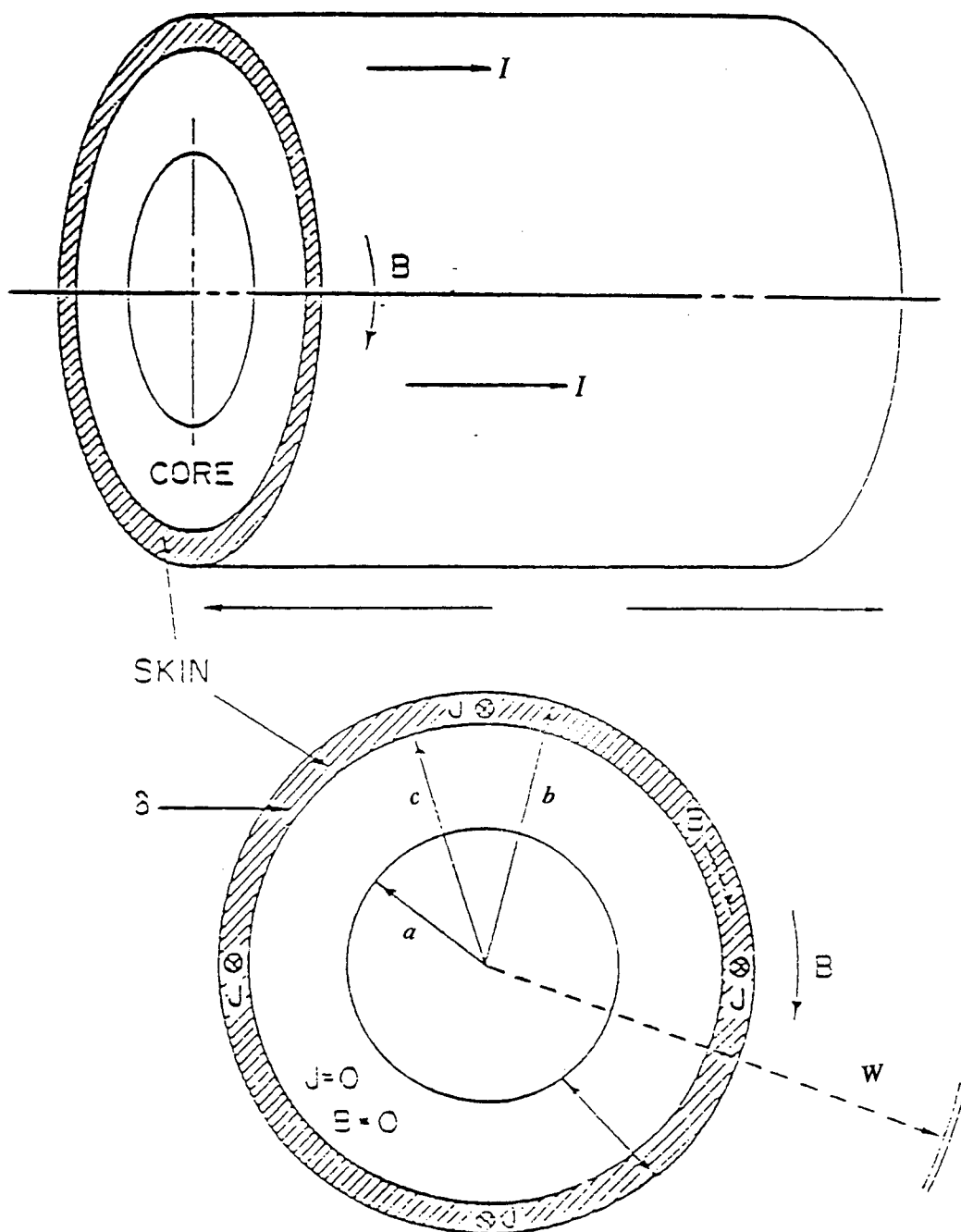


Figure 1. Geometry of model gas puff (from Ref. 9)

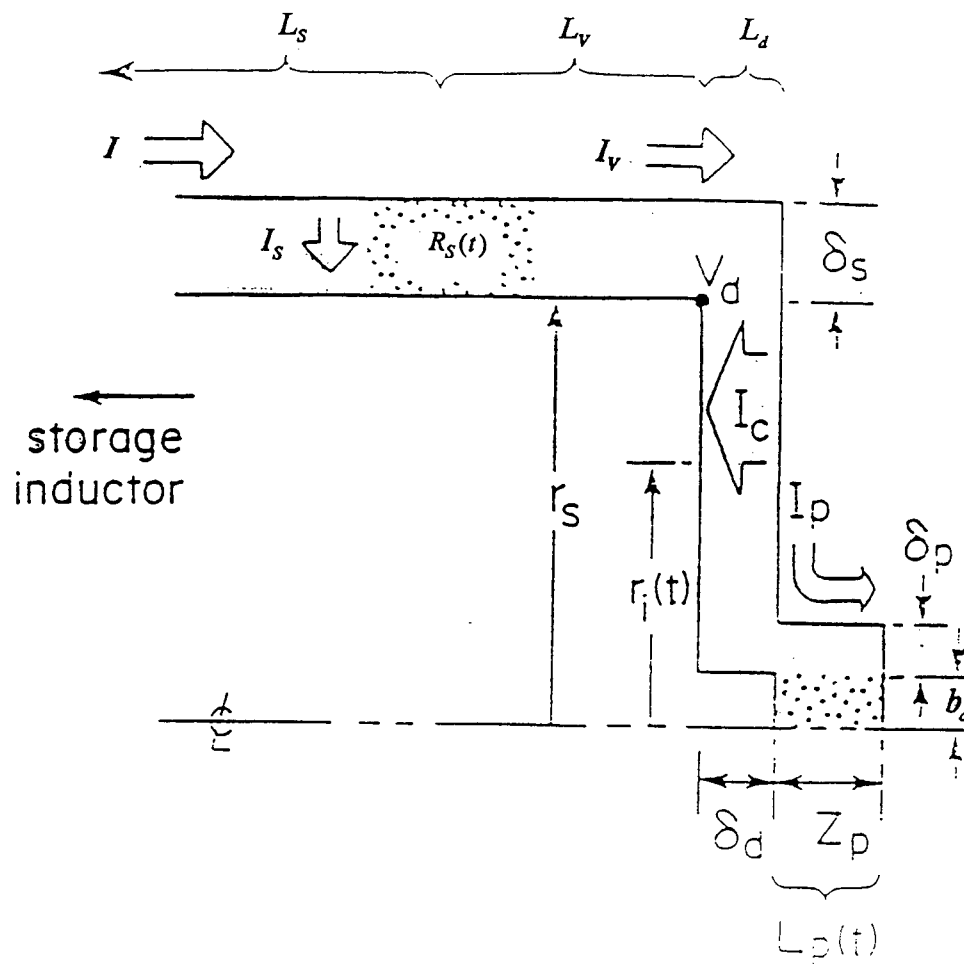


Figure 2. Geometry of power flow (from Ref. 10)

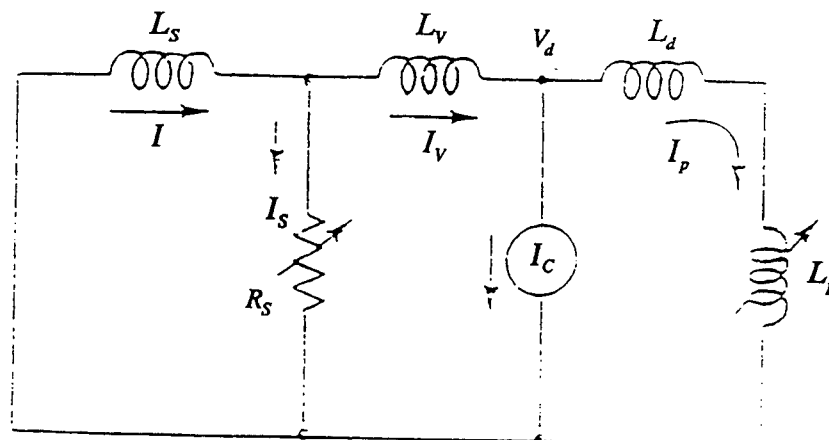


Figure 3. Lumped circuit for simple power flow model

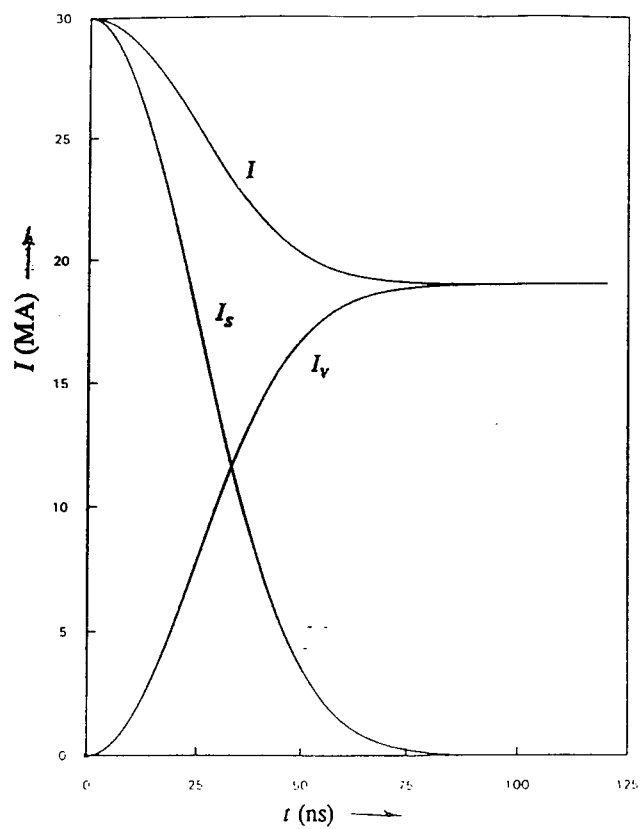


Figure 4. Current histories predicted by the simple model for parameters of Table 1.

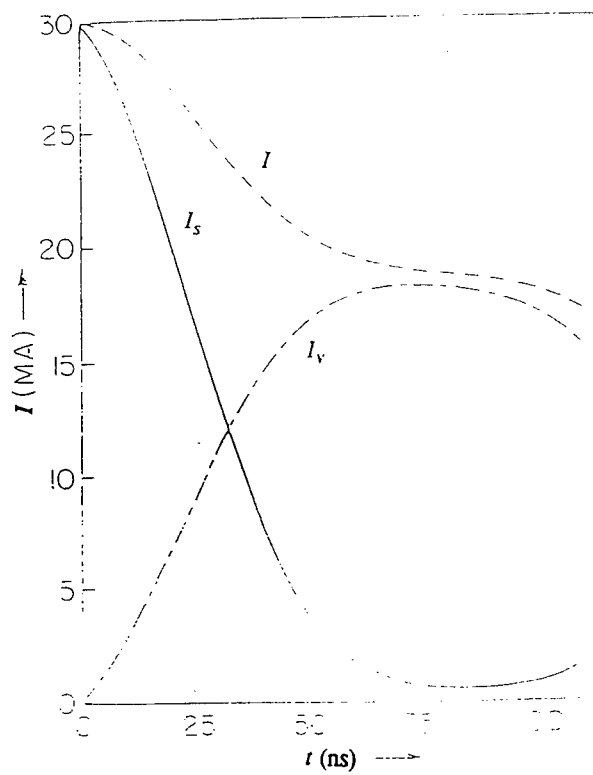


Figure 5. Experimental current histories for parameters of Table 1 (from Ref. 10).

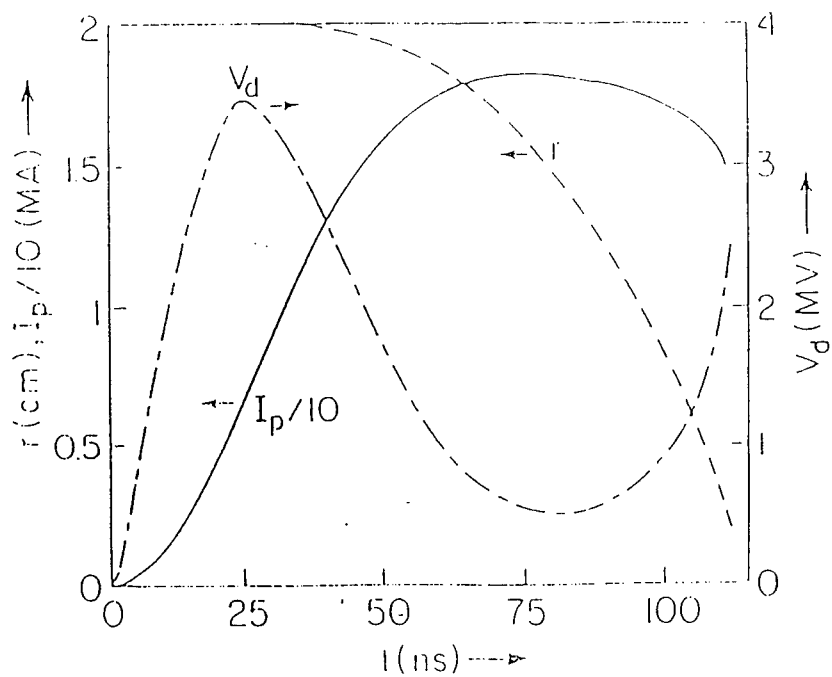


Figure 6. Load History (from Reference 10).

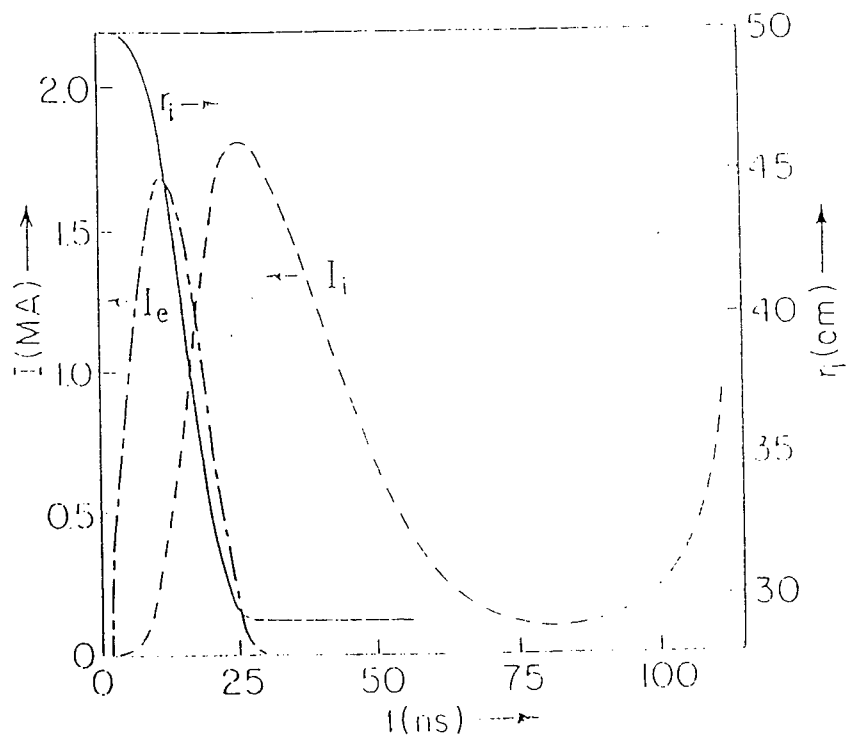


Figure 7. Charged Particle Emission History (from Reference 10).

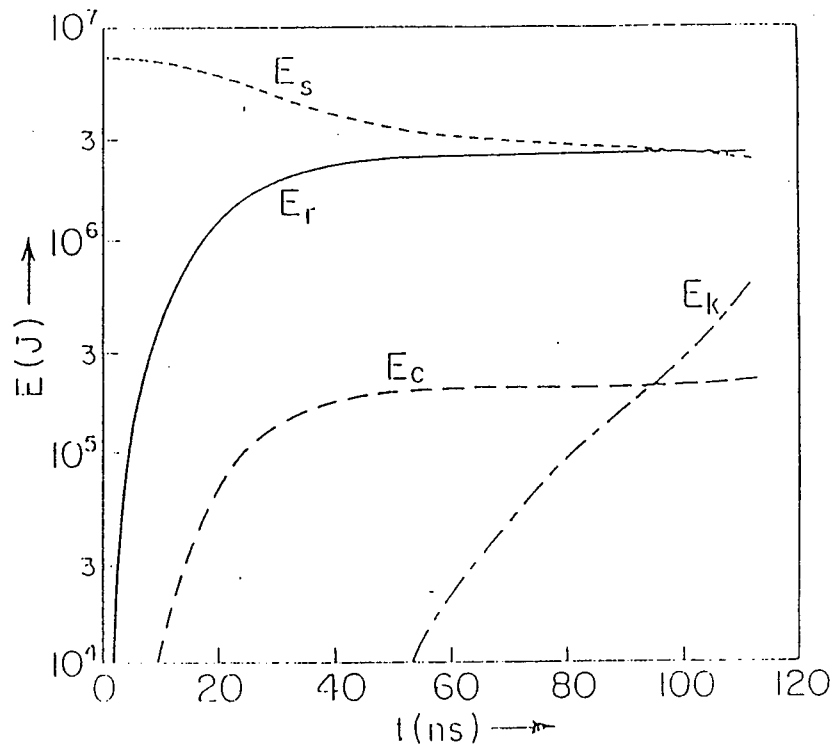


Figure 8. Energy History (from Reference 10).

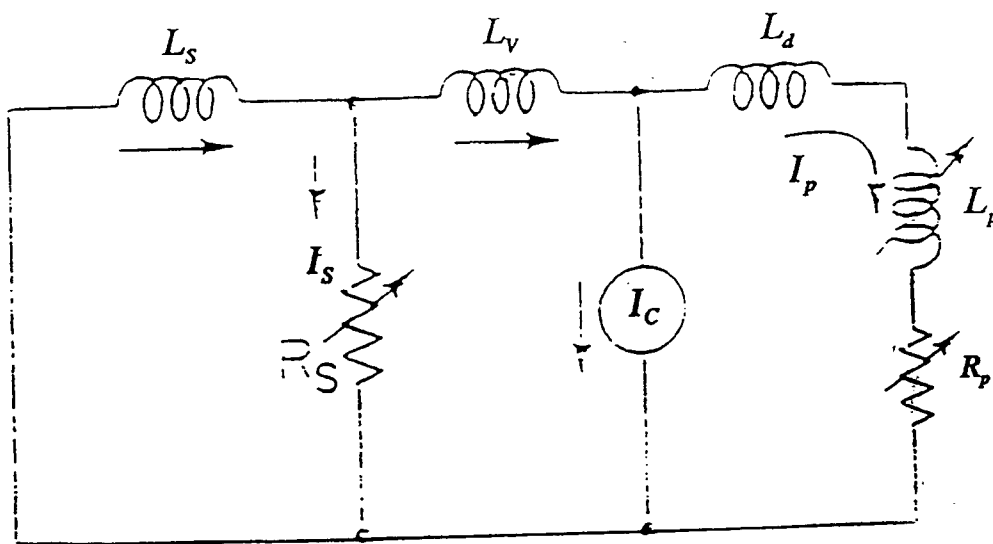


Figure 9. Lumped Circuit for Dynamic Power Flow Model.

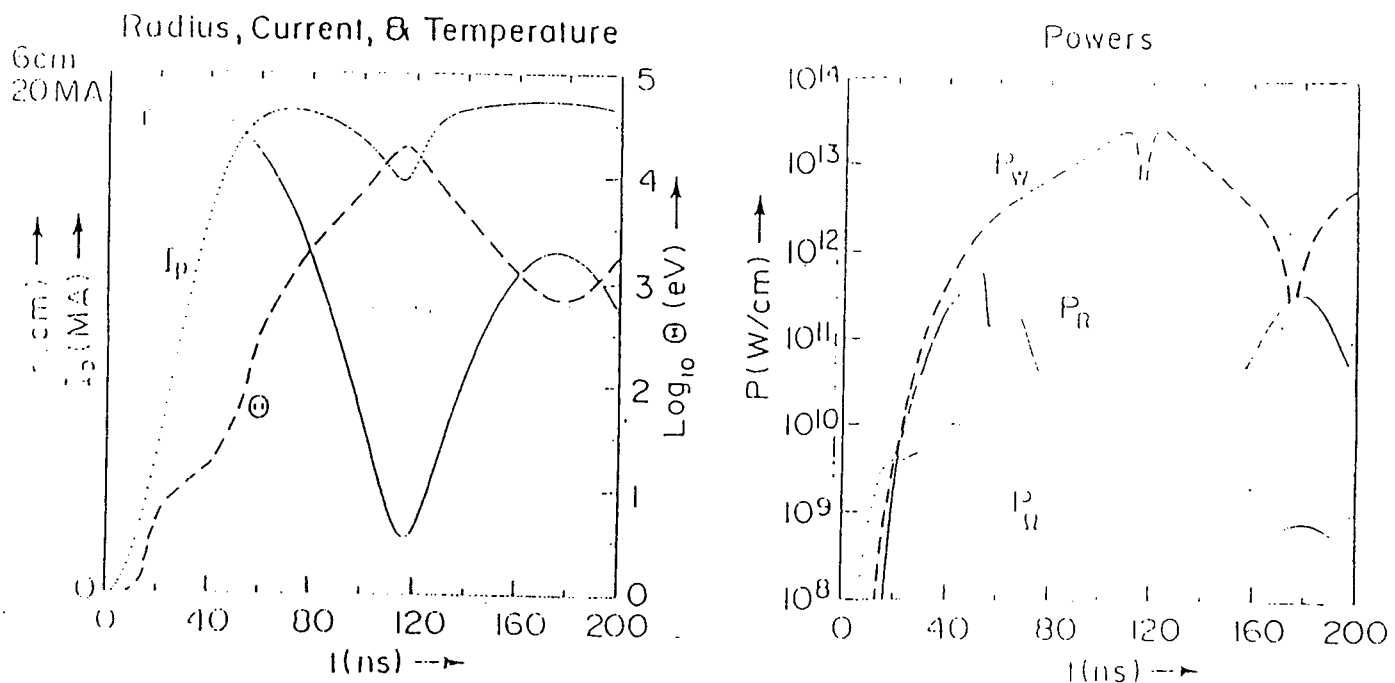


Figure 10. Discharge History - $b_0 = 0.5$ cm, $N = 1 \times 10^{19}$ ions (from Reference 10).

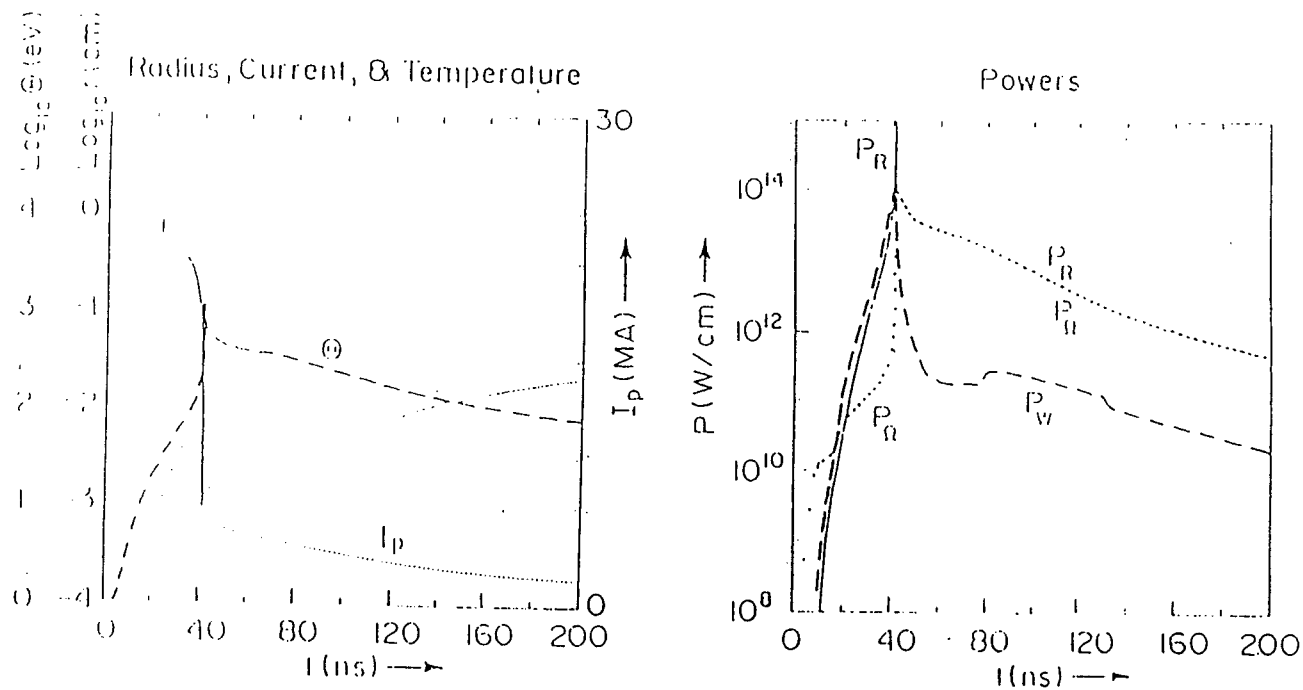


Figure 11. Discharge History - $b_0 = 0.5$ cm, $N = 1 \times 10^{19}$ ions (from Reference 10).

Parameter	Symbol	Value
Storage inductance	L_s	16 nH
Initial current in L_s	I_o	30 MA
Vacuum inductance	L_v	2 nH
Vacuum feed gap	δ_s	2.5 cm
Load plasma wall gap	δ_p	1 cm
Switch resistance rate-of-rise	α	$10^7 \Omega/s$
Vacuum feed radius	r_s	50 cm
Radial feed gap	δ_d	1 cm
Load plasma length	z_p	1 cm
Initial plasma radius	b_o	2 cm
Plasma line mass	λ	3 mg/cm

Table 1. Parameter values for description of system behavior.

(from Reference 10)

Changed Parameter	τ_i (ns)	I_{pmax} (MA)	V_{dmax} (MV)	E_k (MJ)	E_r (MJ)	E_c (MJ)
Table I	112	18.1	3.43	0.63	2.49	0.22
Table I, $I_c = 0$	109	18.2	3.47	0.64	2.70	--
$z_p = 0.5$ cm	109	18.7	3.37	0.36	2.42	0.19
$z_p = 2.0$ cm	117	17.1	3.54	0.99	2.62	0.28
$\lambda = 1.5$ mg/cm	90	17.5	3.43	0.59	2.51	0.22
$\lambda = 6.0$ mg/cm	142	18.5	3.45	0.65	2.48	0.21
$\delta_d = 0.5$ cm	101	20.3	2.37	0.72	1.75	0.33
$\delta_d = 2.0$ cm	134	14.6	4.49	0.43	3.49	0.12
$\alpha = 0.5 \times 10^7 \Omega/s$	126	17.6	2.47	0.60	2.62	0.10
$\alpha = 2.0 \times 10^7 \Omega/s$	103	18.4	4.48	0.64	2.31	0.39
$r_s = 100$ cm	125	17.0	3.01	0.56	2.22	0.71
$r_s = 25$ cm	104	19.1	3.16	0.69	2.44	0.03
$b_o = 1.5$ cm	96	17.1	3.53	0.57	2.59	0.27
$b_o = 3.0$ cm	142	19.3	3.25	0.70	2.35	0.16

Table 2. Variations in system performance due to changes in parameter values.

(from Reference 10)

ACTIVE AND PASSIVE CONTROL DESIGNS FOR THE FJSRL FLEXIBLE STRUCTURE TESTBEDS

Thomas E. Alberts
Associate Professor

Department of Mechanical Engineering and Mechanics
Old Dominion University
Norfolk, Virginia 23529-0247, USA
Phone: (804) 683-3736
Email: talberts@mem.odu.edu

Final Report for:
Summer Research Extension Program
Frank J. Seiler Research Laboratory

Sponsored by:
Air Force Office of Scientific Research
Bolling Air Force Base, Washington, D.C.

March 13, 1994

ACTIVE AND PASSIVE CONTROL DESIGNS FOR THE FJSRL FLEXIBLE STRUCTURE TESTBEDS

Thomas E. Alberts
Department of Mechanical Engineering and Mechanics
Old Dominion University

Abstract

The research performed involves the development and testing of synergistic active and passive control designs for the piezoelectric laminate beam, and planar truss experiments at FJSRL. Under the AFOSR 1992 Summer Research Program, the Principal Investigator developed and experimentally verified a multi-input, multi-output transfer matrix model for a slewing beam system with piezoelectric actuators and sensors. The piezoelectric beam system at FJSRL was used for this work.

In the first phase of the project, the transfer functions previously established piezoelectric laminate beam experiment are to be used to develop and experimentally validate a simultaneously optimal active and passive damping design for the experimental system. Active and passive control measures are simultaneously optimized to interact in the most effective possible way.

The second phase involves preliminary exploration of a similar active/passive design strategy for the FJSRL planar truss structure. As a truss structure, the passive damping design is fundamentally different than that for a beam like structure in that surface treatments are not suitable, but rather discrete dampers designed into the load path are required. The required work for this structure includes finite element dynamic analysis, dynamic dissipative controller design, passive damping design, and simultaneous numerical optimization of the active/passive control system. To date, the modeling and simulation and preliminary control design have been completed. This work will serve as a precursor to anticipated research in nonlinear dissipative control of the same system, modified through the addition of a slewing arm at its endpoint.

ACTIVE AND PASSIVE CONTROL DESIGNS FOR THE FJSRL FLEXIBLE STRUCTURE TESTBEDS

Thomas E. Alberts

1 Introduction

It is well known that the achievable performance of active control designs can be limited by a number of practical factors, including spillover effects [2] which could lead to instability. Indeed, in initial experiments with the JPL precision truss, Fanson, et.al. [4] found that simple controllers successfully attenuated lower frequency modes but inadvertently destabilized higher modes. The augmentation of active control with passive damping provides a practical solution [5] to such problems. Viscoelastic passive damping treatments can be designed to perform well in a prescribed frequency range and are particularly well suited for the control of higher modes of structural vibration. Moreover, active control of higher modes is seldom required for purposes of, for example, shape control. Rather, enhanced damping of the higher modes is the desired property. Active control measures, are normally viewed as being well suited only for lower frequency structural modes, due to actuator bandwidth and computational speed limitations. Considered together, these facts suggest that a synergistic approach employing active control for lower frequency modes and passive control for higher frequency modes deserves serious consideration. Passive damping can enhance the performance of active controllers while easing the burden of active control and providing enhanced system stability [5]. Desirable properties of passive control approaches include simplicity, reliability, low cost and light weight. The research performed involves the development and testing of synergistic active and passive control designs for two FJSRL testbeds — the piezoelectric laminate beam, and the planar truss. While the combination of active and passive damping has been demonstrated before, the active and passive components has generally been designed independent of one another, with passive damping often being applied as an afterthought, for example to eliminate spillover induced instabilities. The unique characteristic of this approach is that the active and passive control measures have been optimized simultaneously to achieve an integrated design for optimal active/passive control interaction.

2 PHASE I: Piezoelectric Laminate Beam

In the first phase of the project, a simultaneously optimal active and passive damping design for the experimental system was developed, simulated, and validated. The control designs for the beam experiment were based on the models developed and verified during the summer of 1992 at FJSRL. The initial approach to optimal active/passive control synergism employed the Independent Modal Space Control (IMSC) [6], [7],

[8] method for active control. IMSC was chosen due to its simplicity and the intuitive feel that it lends to the active control design problem. This phase of the work is regarded as a *proof of concept effort*.

2.1 The Experimental Piezoelectric Laminate Beam System

The beam system considered is pinned at the proximal end, an endpoint motion sensor is attached at the distal end, and patches of thin piezoelectric laminates attached to its surface. A schematic illustration of the system modeled is shown in Figure 1.

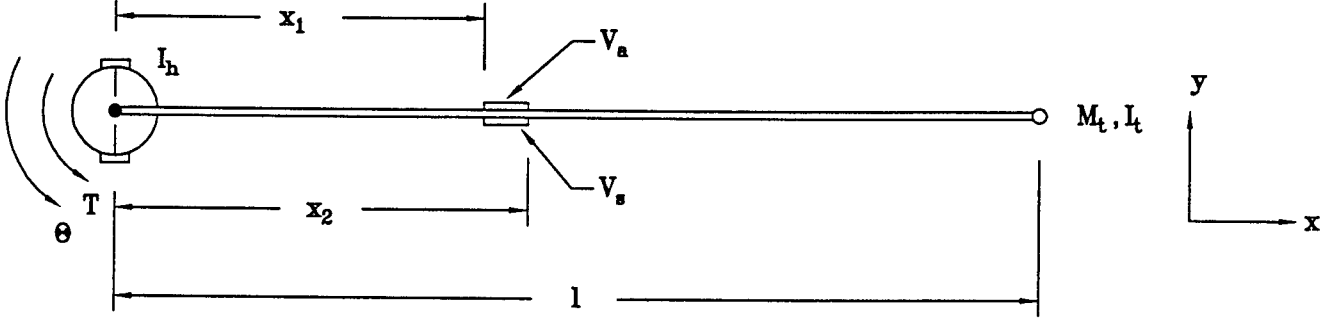


Figure 1: Schematic of Slewing Beam System

The system modeled has three discrete inputs, V_{a1} , V_{a2} and T , and four outputs, Y_{tip} , θ , V_{s1} and V_{s2} . The V_{ai} 's are actuator voltages at position i , T is applied torque, Y_{tip} is tip position, θ is hub angle, and the V_{si} 's are voltage sensed at position i . The piezoelectric elements are located at position 1, at the beam root, and position 2, near the beam midpoint. The transfer matrix can be expressed:

$$\begin{bmatrix} \theta(s) \\ V_{s1}(s) \\ V_{s2}(s) \\ Y_{tip}(s) \end{bmatrix} = \begin{bmatrix} G_{\theta,V_{a1}}(s) & G_{\theta,V_{a2}}(s) & G_{\theta,T}(s) \\ G_{V_{s1},V_{a1}}(s) & G_{V_{s1},V_{a2}}(s) & G_{V_{s1},T}(s) \\ G_{V_{s2},V_{a1}}(s) & G_{V_{s2},V_{a2}}(s) & G_{V_{s2},T}(s) \\ G_{Y,V_{a1}}(s) & G_{Y,V_{a2}}(s) & G_{Y,T}(s) \end{bmatrix} \begin{bmatrix} V_{a1}(s) \\ V_{a2}(s) \\ T(s) \end{bmatrix} \quad (1)$$

The subscripts p and q of each element $G_{p,q}(s)$ identify the associated output and input variable respectively.

The experimental system existing at FJSRL consists of a 2 m long uniform aluminum beam of rectangular cross section (76.2 mm \times 6.35 mm), hanging vertically from a very low friction hinge. The hinge is in a knife edge arrangement as illustrated in Figure 2, and is situated in such a way that the root of the flexible beam is coincident with the hinge axis. This also allows PZT actuator/sensor pairs to be located with one edge coincident with the hinge axis. The hinge arrangement has effectively zero inertia, however, a hub inertia has been added in order to increase pole-zero separation. Although the system has no torque motor, for purposes of modal testing, torque inputs are achieved by applying impulsive force to a rigid moment arm extending from the hinge axis. A PCB Piezotronics force hammer is used to provide the force. Because the angular displacements of the hinged joint are very small during modal testing, it was possible to get an adequate measurement of hub angle by measuring translational displacement of a point on the arm extending from the

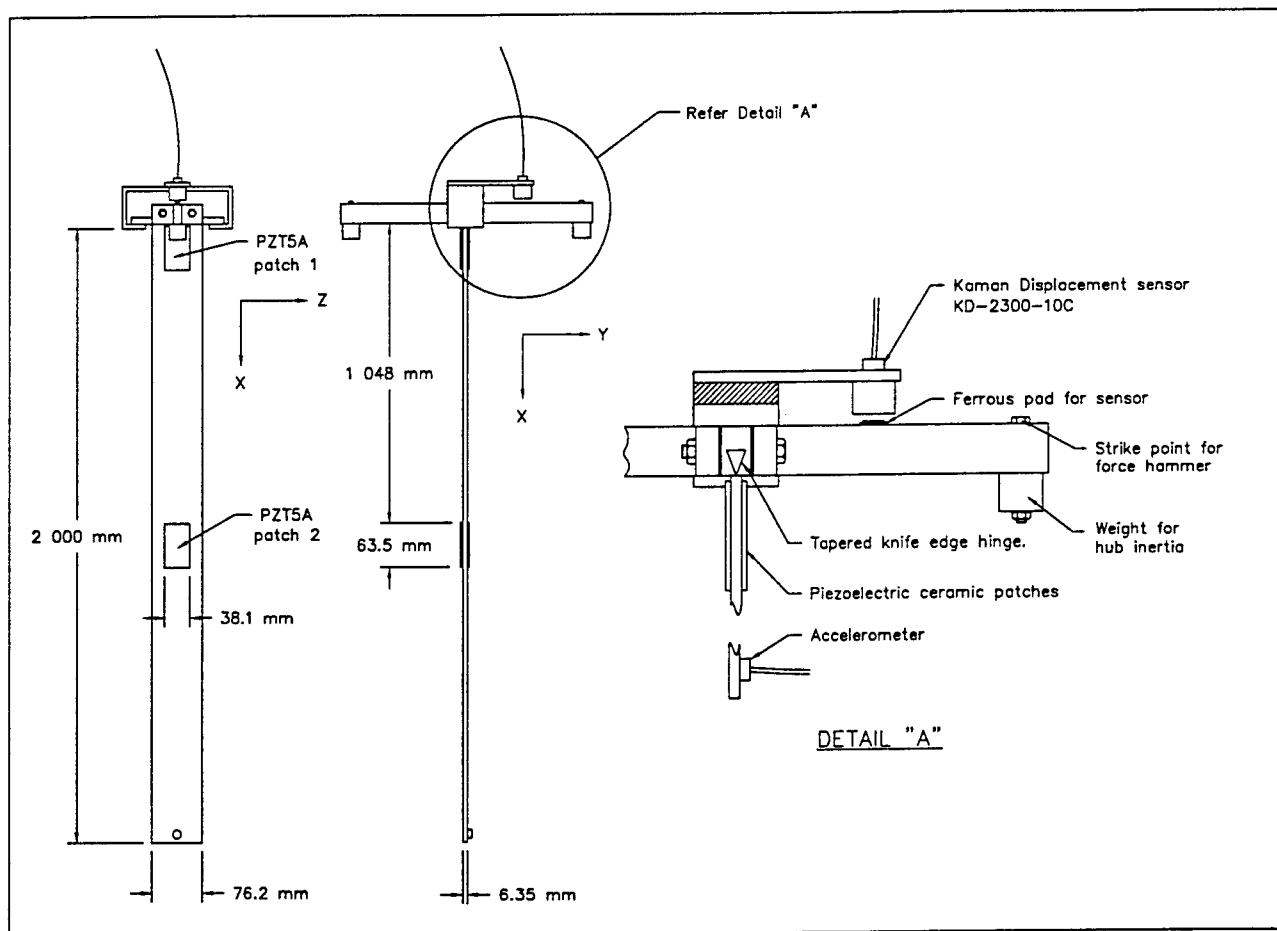


Figure 2: The Experimental Beam

Hub inertia, I_h	0.0348 N-m-s ²	Beam length, l	2.0 m
Volumetric mass density, ρ	2712.6 Kg /m ³	Cross sectional area, A	483.87 $\times 10^{-6}$ m ²
Young's Modulus, E	69.0 $\times 10^9$ N/m ²	Area moment of inertia, I	1.63 $\times 10^{-9}$ m ⁴

Table 1: Experimental Beam Parameters

Charge Constant, d_{31}	-171×10^{-12} m/v	Voltage Constant, g_{31}	-11.4×10^{-3} Vm/N
Coupling Coefficient, k_{31}	-0.340	Capacitance, C	68.35 μ F/m ²
Surface area, $w \times (x_2 - x_1)$	0.0024 m ²	Thickness t_a	3.05 $\times 10^{-4}$ m
Young's Modulus, E_a	69.0 $\times 10^9$ N/m ²		

Table 2: PZT5A Parameters

hinge. A Kaman KD-2300-10CU non-contact displacement measuring system was used for this measurement. This sensor has a rated 3dB frequency response range of static to 50 kHz.. a measurement range of 25.4 mm, and 0.254 mm midrange resolution. The piezoelectric ceramic elements are Vernitron PZT5A patches mounted in pairs on opposite faces of the beam. A 63.5 mm long by 38.1 mm wide piezoelectric material patch is attached to each side of the root of the beam so $x_1 = 0$, $x_2 = 63.5$ mm, and $w = 38.1$ mm. A second pair is located roughly midway down the beam at $x_1 = 1.048$ m, $x_2 = 1.111$ m. The PZT patches used for both actuation and sensing are identical, and hence $t_a = t_c$.

The parameters for experimental system are tabulated in Table 1. Table 2 contains the parameters of the piezoelectric material.

3 IMSC Control

The name 'Independent Modal Space Control' very nicely describes what it is all about. Particular vibratory modes of a structure can be controlled independently. One also has to keep in mind that the number of controlled modes has to be the same (or less) than the number of actuators and that the system must be represented in modal coordinates.

Given a linear transfer function representation of a flexible structure system in the form:

$$Y(s) = G(s)F(s) \quad (2)$$

where:

$F(s)$ is a vector of control input forces,

$G(s)$ is a matrix of transfer functions,

$Y(s)$ is a vector of outputs,

The system output can be expressed as,

$$Y(s) = \sum_{i=1}^n \left(\frac{(B_i s + C_i)U(s)}{(s + c_i)^2 + d_i^2} \right) + \delta U(s) \quad (3)$$

This implies that in the time domain the i th modal differential equation of a system with proportional damping and multiple inputs can be written as

$$\ddot{\eta}_i(t) + 2\zeta_i p_i \dot{\eta}_i(t) + p_i^2 \eta_i(t) = B_i \dot{u}(t) + C_i u(t) + f_i(t) \quad (4)$$

where ζ_i is the i th modal damping ratio, $f_i(t)$ the i th modal independent control force, $u(t)$ the $n \times 1$ disturbance input vector, and $B_i = [B_{i1} B_{i2} \dots B_{in}]$ the i^{th} modal participation vector corresponding to the inputs derivative and C_i being likewise for just the inputs. Since each element f_i of the modal control vector is designed to depend only upon the corresponding i^{th} modal displacement and velocity, n representing the number of actively controlled modes, then the closed loop system remains decoupled and the control is referred to as Independent Modal Space Control (IMSC). If the modal control law is defined as

$$f_i(t) = -g_i \eta_i(t) - h_i \dot{\eta}_i(t) \quad (5)$$

the i th modal equation of the closed loop system becomes

$$\ddot{\eta}_i(t) + (2\zeta_i p_i + h_i) \dot{\eta}_i(t) + (p_i^2 + g_i) \eta_i(t) = B_{ij} \dot{u}_j(t) + C_{ij} u_j(t) \quad (6)$$

For independent modal space control, the performance index can be expressed as a linear combination of modal performance indices as

$$J^{opt} = \sum_{i=1}^n J_i \quad (7)$$

where each modal index J_i can be minimized independently. In the work presented here, the modal performance indices are defined as

$$J_i = \int_0^\infty \left[\dot{\eta}_i^2 + (p_i^2 + g_i) \eta_i^2 + \frac{1}{2\alpha^2} f_i^2 \right] dt \quad (8)$$

The first two terms in the integral in (8) represent the total mechanical energy corresponding to the i th mode of the closed loop system defined in (6), and the third term in the integral is the control effort with a penalty factor α . As α is increased, the penalty on control is decreased. Appropriate substitution and integration yields

$$\begin{aligned} J_i = & \frac{1}{4\alpha^2(g_i + p_i^2)(h_i + 2p_i\zeta_i)} \left(\left(\sum_{j=1}^n B_{ij} \right)^2 (g_i + p_i^2)(4\alpha^2 g_i + g_i^2 + 2\alpha^2 h_i^2 - \right. \\ & g_i h_i^2 + h_i^4 + 4\alpha^2 p_i^2 + h_i^2 p_i^2 + 8\alpha^2 h_i p_i \zeta_i - 4g_i h_i p_i \zeta_i + 4h_i^3 p_i \zeta_i + \\ & 8\alpha^2 p_i^2 \zeta_i^2 + 4h_i^2 p_i^2 \zeta_i^2) + \left(\sum_{j=1}^n B_{ij} \right) \left(-2 \left(\sum_{j=1}^n C_{ij} \right) (2\alpha^2 + h_i^2)(g_i + p_i^2)(h_i + 2p_i\zeta_i)) + \right. \\ & \left. \left(\sum_{j=1}^n C_{ij} \right)^2 (4\alpha^2 g_i + g_i^2 + g_i h_i^2 + 4\alpha^2 p_i^2 + h_i^2 p_i^2) \right) \end{aligned} \quad (9)$$

If we were to have assumed light damping, $\zeta_i \ll 1$ then the B_{ij} terms would be gone and (9) reduces to

$$J_i = \left[2 + \frac{h_i^2}{2\alpha^2} + \frac{g_i^2}{2\alpha^2(p_i^2 + g_i)} \right] \frac{c_i^2}{4\zeta_i p_i + 2h_i} \quad (10)$$

which is the result found in [15]. The modal index J_i can be minimized with respect to g_i and h_i by setting the corresponding first partial derivatives equal to zero. These partial derivatives consist of a numerator and a denominator. All we have to deal with is the numerator since we are setting the derivative term equal to zero. The numerator for the partial derivative of J_i with respect to g_i is

$$\begin{aligned} 0 = & g_i^3(2B^2) + g_i^2(4\alpha^2 B^2 + C^2 - B^2 h_i^2 + 4B^2 p_i^2 - 4B^2 h_i p_i \zeta_i) + \\ & g(8\alpha^2 B^2 p_i^2 + 2C^2 p_i^2 - 2B^2 h_i^2 p_i^2 + 2B_i^2 p_i^4 - 8B^2 h_i p_i^3 \zeta_i) + \\ & 4\alpha^2 B^2 p_i^4 - B^2 h_i^2 p_i^4 - 4B^2 h_i p_i^5 \zeta_i \end{aligned} \quad (11)$$

The numerator for the partial derivative of J_i with respect to h_i is

$$\begin{aligned} 0 = & h_i^3(4B(g_i + p_i^2)(-c_i + 4B p_i \zeta_i) + h_i^2((g_i + p_i^2)(2\alpha^2 B^2 + C^2 - \\ & B^2 g_i + B^2 p_i^2 - 16BC p_i \zeta_i + 28B^2 p_i^2 \zeta_i^2)) + h_i(4p_i(g_i + p_i^2)\zeta_i(2\alpha^2 B^2 + \\ & C^2 - B^2 g_i + B^2 p_i^2 - 4BC p_i \zeta_i + 4B^2 p_i^2 \zeta_i^2)) - (C^2 g_i^2) - B^2 g_i^3 - \\ & B^2 g_i^2 p_i^2 + 3B^2 h_i^4(g_i + p_i^2) - 8B^2 g_i^2 p_i^2 \zeta_i^2 - 8b_i^2 g_i p_i^4 \zeta_i^2 + 4\alpha^2(g_i + \\ & p_i^2)(-C^2 - B^2 g_i - B^2 p_i^2 + 2B^2 p_i^2 \zeta_i^2)) \end{aligned} \quad (12)$$

In these two expressions,

$$B = \sum_{j=1}^n B_{ij} \quad (13)$$

and

$$C = \sum_{j=1}^n C_{ij} \quad (14)$$

The two denominator expressions (11) and (12) contain the desired control gains, g_i^{opt} and h_i^{opt} . Upon observation of these equations one notices the first is a cubic of g_i and the other is a fourth order. Only one of the roots can be the optimal in each case. Luckily what happens when the equations are solved is that one root will be a positive real number and the others will be imaginary and/or negative. Obviously the positive real roots are the ones desired. It is apparent that these gains are dependent on each other. To get a closed symbolic expression for the gains is not feasible. However these two equations can be solved numerically, in an iterative fashion. The total performance index for the optimally controlled structure, J_a^{opt} , can be obtained by substituting (9), g_i^{opt} and h_i^{opt} into (7). This index, J_a^{opt} , which unfortunately is only numeric, is optimized with respect to the control gains. Further optimization will include a designed-in viscoelastic passive damping treatment. Now if there is no damping present then the optimal gains turn out to be

$$g_i^{opt} = 0 \quad (15)$$

$$h_i^{opt} = -2\zeta_i p_i + 2\sqrt{\zeta_i^2 p_i^2 + \alpha^2} \quad (16)$$

This was a result from [15].

3.1 Implementation of IMSC

For implementation we want to take the developed equations from above and represent them in a State-Space formulation. From (3) it is possible to convert the transfer function to a partial fraction expansion form:

$$Y = \sum_{j=1}^m \left(\sum_{i=1}^n \frac{B_{ij}s + C_{ij}}{(s + c_i)^2 + d_i^2} + \delta_j \right) F_j = \sum_{i=1}^n \eta_i + \sum_{j=1}^m \delta_j F_j \quad (17)$$

where n is the number of modes and m is the number of inputs and once again F_i is a vector of input control forces. From here we can deduce that:

$$\eta_i(s) = \sum_{j=1}^m \frac{B_{ij}s + C_{ij}}{(s + c_i)^2 + d_i^2} F_j(s) \quad (18)$$

In this particular experiment there are two inputs, so to simplify this development, let $j = 1, 2$ and

$$\eta_i(s) = \frac{(B_{i1}s + C_{i1})F_1(s) + (B_{i2}s + C_{i2})F_2(s)}{(s + c_i)^2 + d_i^2} \quad (19)$$

using Laplace Transform rules, this can be converted directly to the second order, time domain modally decoupled form:

$$\ddot{\eta}_i(t) + 2c_i\dot{\eta}_i(t) + (c_i^2 + d_i^2)\eta_i(t) = B_{i1}F_1(t) + B_{i2}F_2(t) + C_{i1}\dot{F}_1(t) + C_{i2}\dot{F}_2(t) \quad (20)$$

where, B and C come from the partial fraction expansion, and F and \dot{F} being the input force and its time derivative, respectively. From (20), the independent modal forces are:

$$f_i(t) = B_{i1}\dot{F}_1(t) + B_{i2}\dot{F}_2(t) + C_{i1}F_1(t) + C_{i2}F_2(t) \quad (21)$$

Solving (20) for $\ddot{\eta}_i$ and integrating twice:

$$\begin{aligned} \eta_i(t) = & -2c_i \int_0^\infty \eta_i(t)dt + B_{i1} \int_0^\infty F_1(t)dt + B_{i2} \int_0^\infty F_2(t)dt - \\ & (c_i^2 + d_i^2) \int_0^\infty \int_0^\infty \eta_i(t)dtdt + C_{i1} \int_0^\infty \int_0^\infty F_1(t)dtdt + \\ & C_{i2} \int_0^\infty \int_0^\infty F_2(t)dtdt \end{aligned}$$

Now if we let

$$\begin{aligned} \dot{x}_1 &= -2c_i\eta_i + B_{i1}F_1 + B_{i2}F_2 + x_2 \\ \dot{x}_2 &= -(c_i^2 + d_i^2)\eta_i + C_{i1}F_1 + C_{i2}F_2 \\ x_1 &= \eta_i \end{aligned}$$

This is illustrated in block diagram form in figure (3).

Note that $x_2 \neq \dot{\eta}_i$, but \dot{x}_1 can be formed in the observer. It is easy to see the following State-Space representation:

$$\begin{aligned} A_{pl} &= \begin{bmatrix} -2c_i & 1 \\ -(c_i^2 + d_i^2) & 0 \end{bmatrix} & B_{pl} &= \begin{bmatrix} B_{i1} & B_{i2} \\ C_{i1} & C_{i2} \end{bmatrix} \\ C_{pl} &= \begin{bmatrix} 1 & 0 \end{bmatrix} & D_{pl} &= \begin{bmatrix} 0 & 0 \end{bmatrix} \end{aligned}$$

where A_{pl} , B_{pl} , C_{pl} , and D_{pl} were used for the state-space form, to avoid confusion with the same symbols used previously. Also note here that A_{pl} should be represented in block-diagonal form with dimension $2i \times 2i$. B_{pl} , C_{pl} , and D_{pl} are in column form and have dimensions $2i \times 2$, $1 \times 2i$, and 1×2 respectively. Next an observer is needed to get $\dot{\eta}_i$. Therefore we want the output of the observer to be

$$y_i = \begin{bmatrix} \eta_i \\ \dot{\eta}_i \end{bmatrix} \quad (22)$$

So referring back to figure (3), the C_{ob} , and D_{ob} matrices for the observer are

$$C_{ob} = \begin{bmatrix} 1 & 0 \\ -2c_i & 1 \end{bmatrix} \quad D_{ob} = \begin{bmatrix} 0 & 0 \\ B_{i1} & B_{i2} \end{bmatrix}$$

Now we should develop the rest of the observer. From [12]

$$\dot{\hat{x}} = (A - KC)\hat{x} + Bu + Ky \quad (23)$$

where \hat{x} is an estimate of x , the state variables A , B , and C are the plant's A , B , C matrices, K is a matrix of Kalman gains, and u and y are the plants input and output. We already know that the input vector is

$$u = -G\hat{x} \quad (24)$$

where G contains the optimal gains from (11) and (12) and D is the plant D matrix. Therefore (23) becomes

$$\dot{\hat{x}} = (A - KC - BG)\hat{x} + Ky \quad (25)$$

Now representing the observer in State-Space form

$$A_{ob} = [(A_{pl} - KC_{pl} - B_{pl}G)] \quad B_{ob} = [KC_{pl}]$$

So thus far we have the plant model, which has an output of modal displacements and an observer which has an output of modal displacements and modal velocities, η_i and $\dot{\eta}_i$. The sum of the modal displacements is the response of the system. From here we have to get the control force. In other words we know what the modal force is, but for implementation, we need to obtain the physical forces. At the time of implementation a procedure had not been developed to get the physical forces for cases when there is damping. Consult the section on the experiment for details on how implementation was carried out at that time.

One can solve for the physical forces, from the known modal forces directly in the time domain. Recall that we have,

$$f_1 = B_{11}\dot{F}_1 + B_{12}\dot{F}_2 + C_{11}F_1 + C_{12}F_2 \quad (26)$$

and

$$f_2 = B_{22}\dot{F}_1 + B_{21}\dot{F}_2 + C_{22}F_1 + C_{21}F_2 \quad (27)$$

With a bit of manipulation, one can get the following matrix equation form:

$$\begin{bmatrix} F_1(t) \\ F_2(t) \end{bmatrix} = \begin{bmatrix} \frac{1}{K_1} \left(\frac{B_{12}C_{21}}{B_{11}B_{22}} - \frac{C_{11}}{B_{11}} \right) & \frac{1}{K_1} \left(\frac{B_{12}C_{22}}{B_{11}B_{22}} - \frac{C_{12}}{B_{11}} \right) \\ \frac{1}{K_2} \left(\frac{B_{21}C_{11}}{B_{22}B_{11}} - \frac{C_{21}}{B_{22}} \right) & \frac{1}{K_2} \left(\frac{B_{21}C_{12}}{B_{22}B_{11}} - \frac{C_{22}}{B_{22}} \right) \end{bmatrix} \begin{bmatrix} F_1 \\ F_2 \end{bmatrix} + \begin{bmatrix} \frac{1}{K_1 B_{11}} & -\frac{B_{12}}{K_1 B_{11} B_{22}} \\ -\frac{1}{K_2 B_{22} B_{11}} & \frac{1}{K_2 B_{22}} \end{bmatrix} \begin{bmatrix} f_1 \\ f_2 \end{bmatrix}$$

This can be easily implemented using State-Space methods where

$$A_{force} = \begin{bmatrix} \frac{1}{K_1} \left(\frac{B_{12}C_{21}}{B_{11}B_{22}} - \frac{C_{11}}{B_{11}} \right) & \frac{1}{K_1} \left(\frac{B_{12}C_{22}}{B_{11}B_{22}} - \frac{C_{12}}{B_{11}} \right) \\ \frac{1}{K_2} \left(\frac{B_{21}C_{11}}{B_{22}B_{11}} - \frac{C_{21}}{B_{22}} \right) & \frac{1}{K_2} \left(\frac{B_{21}C_{12}}{B_{22}B_{11}} - \frac{C_{22}}{B_{22}} \right) \end{bmatrix} \quad (28)$$

$$B_{force} = \begin{bmatrix} \frac{1}{K_1 B_{11}} & -\frac{B_{12}}{K_1 B_{11} B_{22}} \\ -\frac{1}{K_2 B_{22} B_{11}} & \frac{1}{K_2 B_{22}} \end{bmatrix} \quad (29)$$

$$C_{force} = \begin{bmatrix} 1 & 0 \\ 0 & 1 \end{bmatrix} \quad D_{force} = \begin{bmatrix} 0 & 0 \\ 0 & 0 \end{bmatrix} \quad (30)$$

This result is the same as before and can be called the force thing. The state vector here is $[F_1 F_2]^T$. So notice that from (30), the outputs of the force thing are the physical forces. The force thing can be appended to the compensator using series connection theory for State-Space systems. Since this is still the same force thing, only in a different form, it will still go to zero relatively quickly. For the beam experiment used in this thesis, the force thing would not be adequate, due to the lack of control authority. If there was enough control authority, the fact that control from the force thing diminishes would not matter because the system has already been damped. The question is, what else would cause this to not work or under what conditions would it work?

Meirovitch [13] says that in general, damping produces coupling of the normal modes, in some special cases there is no coupling introduced by damping. One such case is when the damping matrix is diagonal or

$$c_{rs} = c_r \delta_{rs} = 2\zeta_r \omega_r \delta_{rs} \quad r, s = 1, 2, \dots \quad (31)$$

He also notes that when the damping matrix does produce coupling, approximate methods are the only solution. Later he states that in the case of light damping, it is possible to obtain an approximate solution

by considering the coupling due to damping as a secondary effect and simply setting subsequent terms to zero. Harrell concludes [14] that uniform damping is just a mathematical fascination for control engineers. Harrell also notes that IMSC control can be applied to a lightly damped structure with fully populated damping matrix only if it is diagonally dominant. With this background we can present the following hypothesis; The physical modes can only be found for systems whose modal participation factors obey the following rule,

$$\frac{B_{22}C_{11} + B_{11}C_{21}}{B_{22}B_{11} - B_{21}B_{12}} > \frac{B_{12}C_{21} + B_{21}C_{12}}{B_{22}B_{11} - B_{21}B_{12}} \quad (32)$$

These modal participation factors are dependent on damping. To get a closed form solution as to what damping will work and what damping will not, would mean solving for the B_{ij} and C_{ij} terms, which are the residues of the partial fraction expansion, symbolically. From this closed form solution inferences could be drawn on what damping would cause the \bar{r} to be positive or negative.

The force thing is a dynamical system, thus stability requirements still hold. In-other-words the eigenvalues of A_{force} must have negative real parts. To demonstrate this, first let's consider the following damping for the five mode beam model.

$$\zeta_i = [0.001 \ 0.001 \ 0.001 \ 0.001 \ 0.001] \quad (33)$$

The B_{ij} and C_{ij} terms were calculated and put into A_{force} . The eigenvalues that result are -1.2693×10^5 and 1.9911×10^5 . Since one of the eigenvalues has a positive real part then the system is considered unstable. Thus the force thing could not be used for this system under this damping. Alternatively if we assume proportional damping, with $\zeta_1 = 0.001$, the damping vector takes on the form

$$\zeta_i = [0.001 \ 0.000339 \ 0.000184 \ 0.00011 \ 0.0000685] \quad (34)$$

The B_{ij} and C_{ij} terms were calculated and put into A_{force} . The eigenvalues that result are $-1.3246 \times 10^5 + 1.7854 \times 10^5 j$ and $-1.3246 \times 10^5 - 1.7854 \times 10^5 j$. These eigenvalues have negative real parts. Therefore for this beam system, under proportional damping, the force thing is stable. However if we use the damping from the passive damping design

$$\zeta_i = [0.0602 \ 0.0615 \ 0.0580 \ 0.0500 \ 0.0425] \quad (35)$$

which is neither uniform nor proportional, the force thing has eigenvalues with negative real parts, $-1.5445 \times 10^4 + 0.544 \times 10^5 j$ and $-1.5445 \times 10^5 - 0.544 \times 10^4 j$.

4 Controller Implementation/Verification

Up to this point a differential equation of motion has been derived and solved. Also two transfer functions have been derived, rationalized and expanded into partial fractions and converted to modal coordinates.

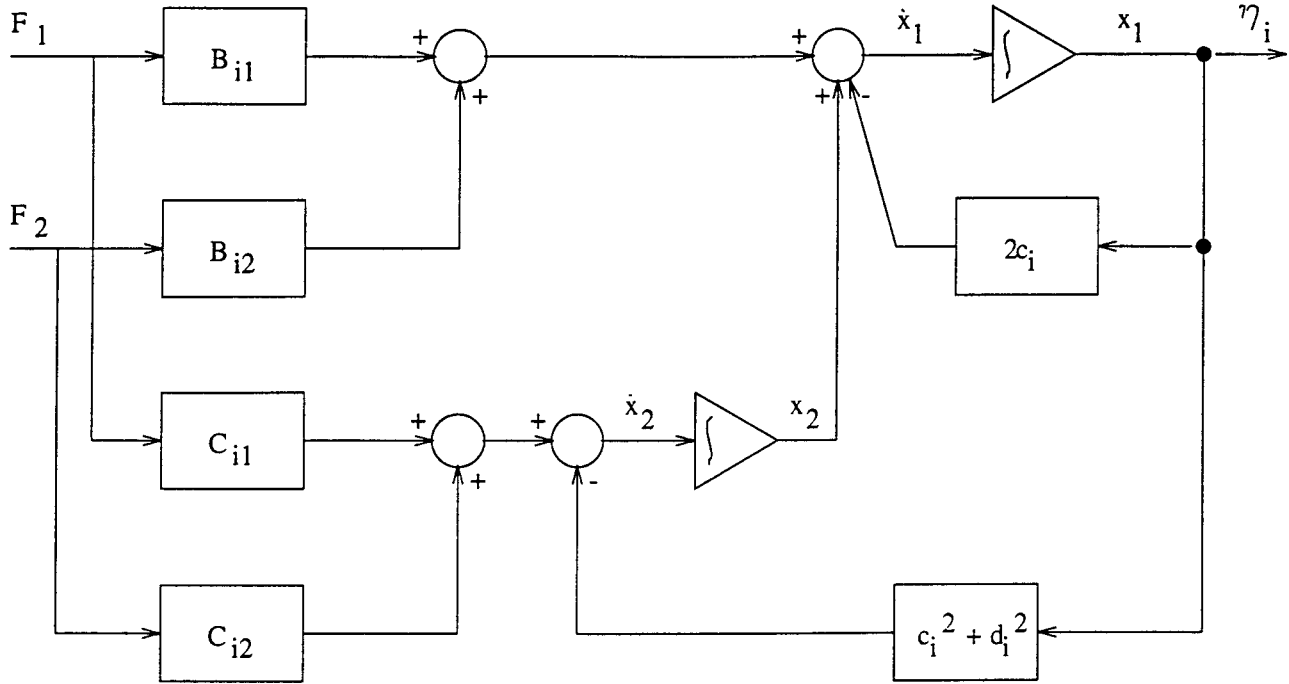


Figure 3: Block Diagram Showing Relationship of Input Control Force to Modal Displacement

An IMSC has been developed to use the transformed transfer functions and then converted the calculated control forces back to physical coordinates. Now an experiment to validate the effects of compensation on the system will be presented.

4.1 Experimental Set Up

A mechanical description of the experimental system has been given in section 2.1. A signal generator, tuned to a specific frequency, was used as input to the patches for excitation. When the beam's motion reached what appeared to be steady-state the generator was turned off and the controller, on. The controller was implemented on a Sun SPARCstation equipped with a Solflower input/output device where the Kaman sensor signal was the input and the two control voltages for the patches was the output. A C-language program which read the discretized A, B, C, D matrices from a file was used and operated at 600 Hz. The two signals from the Solflower were each sent to an amplifier and then to their respective piezoelectric patch-pairs. A Tektronix model 2630 Fourier Analyzer was used for data acquisition.

On this beam there are two actuators so two modes can be simultaneously controlled using IMSC. Due to a lack of voltage amplification the controller was implemented for one mode at a time. The amplifiers used had a maximum power output of ± 35 volts. It isn't until about ± 25 volts that these particular patches seem to respond with sufficient control authority. As it turned out for a particular α , the voltage

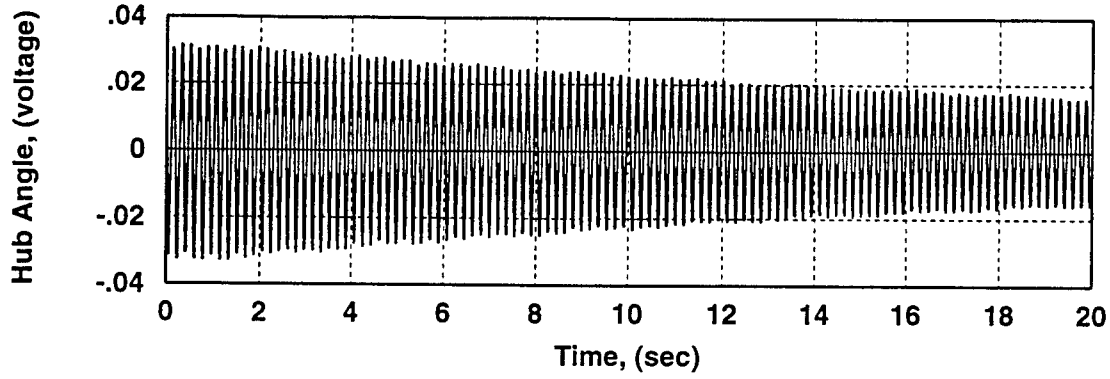


Figure 4: Mode 1, Free Decay, (experimental)

for patch-pair one was an order of magnitude higher than that for patch two. So for example with the beam vibrating in the first mode, and α adjusted so the voltage for patch-pair one was just saturating its amplifier at ± 35 volts, the voltage to patch-pair two would be near ± 3.5 volts. Therefore the second patch-pair would not be activated. This is acceptable for controlling the second mode. Yet the first mode is best controlled with the middle patch. So it was decided to implement the controller for each mode separately. Since mode one is best controlled from the second patch-pair, α was adjusted so that when the controller was first turned on, the amplifier for patch-pair two just barely saturated. This of course makes for a control voltage for the first patch-pair that is far too high for the available amplifier. Therefore the connection for the first patch-pair was disconnected. In this configuration, significant damping was achieved as seen by comparing Figures (4.1) and (4.1). The simulation for controlling mode one is shown in Figure (4.1) and correlates well with (4.1). Similar results were obtained for mode 2, however the plots are excluded here due to space limitations. Future implementations will include optimal passive damping in conjunction with this optimal active control.

So it was much easier to assume small damping and drop the $B_{ij}\dot{F}_j$ terms in (21). Therefore

$$f_i = C_{i1}F_1 + C_{i2}F_2 \quad (36)$$

Now we have to keep in mind that f_i is the modal input to mode i and not the input to any one particular actuator. The individual actuator inputs are the F_j 's. To make it clearer what has to be done, (36) rewritten for two modes is

$$\begin{bmatrix} f_1 \\ f_2 \end{bmatrix} = \begin{bmatrix} C_{11} & C_{12} \\ C_{21} & C_{22} \end{bmatrix} \begin{bmatrix} F_1 \\ F_2 \end{bmatrix} \quad (37)$$

The matrix containing the C_{ij} terms will be denoted as C . By multiplying (37) by C^{-1}

$$\begin{bmatrix} F_1 \\ F_2 \end{bmatrix} = \begin{bmatrix} C_{11} & C_{12} \\ C_{21} & C_{22} \end{bmatrix}^{-1} \begin{bmatrix} f_1 \\ f_2 \end{bmatrix} \quad (38)$$

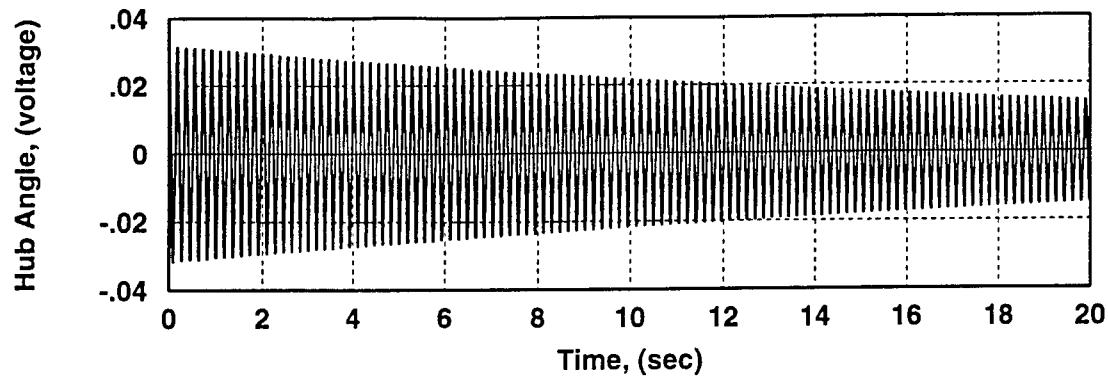


Figure 5: Mode 1, Free Decay, (simulated)

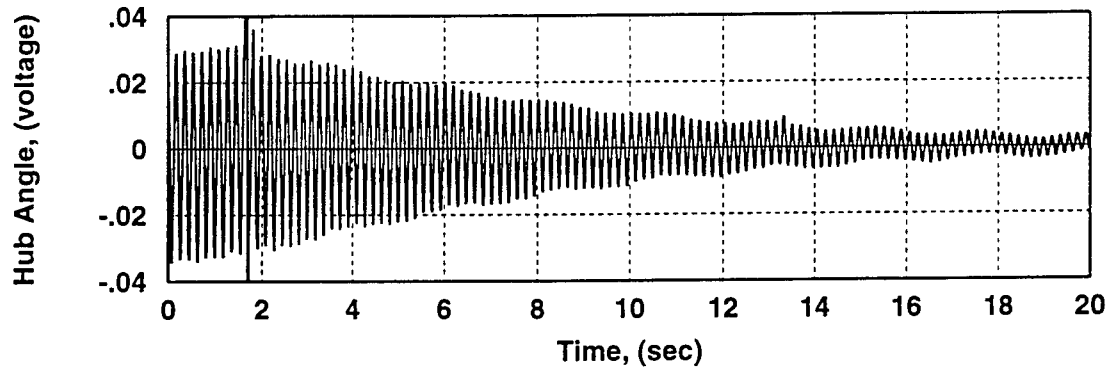


Figure 6: Mode 1, Controller On, Time Response, (experimental)

We also have to remember the feed-forward term from (17), δ .

5 Optimal Passive Damping

One of the methods of passively damping structural vibrations is with the use of a distributed damping treatment. This treatment utilizes a viscoelastic layer with a sectioned constraining layer. The thin viscoelastic film is bonded to the structure or flexible member. Then a constraining layer is bonded to the viscoelastic film. The result is a sandwich like structure, Figure (8). The idea is when the structure undergoes an elastic deformation, the viscoelastic layer undergoes a shear induced, plastic deformation. This plastic deformation dissipates energy, thus providing mechanical damping. This damping method was chosen because of its lightweight, ease of application, it is inexpensive, and has a proven reliability. One of the outcomes of this

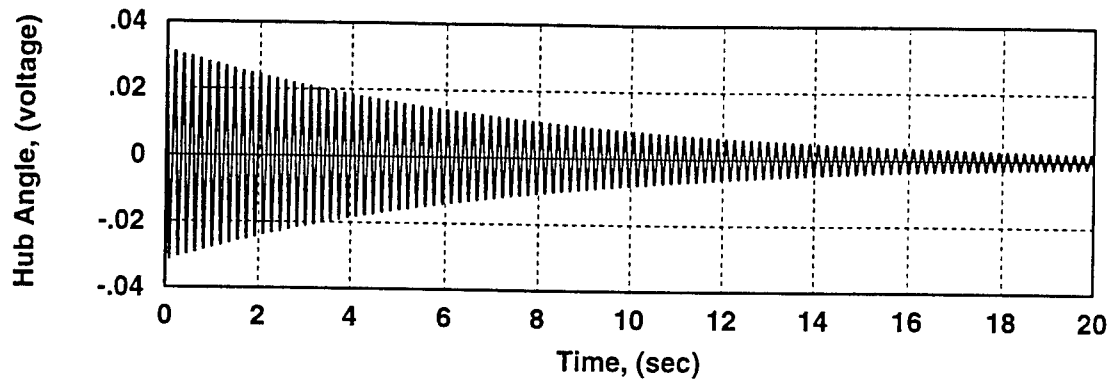


Figure 7: Mode 1, Controller On, Time Response, (simulated)

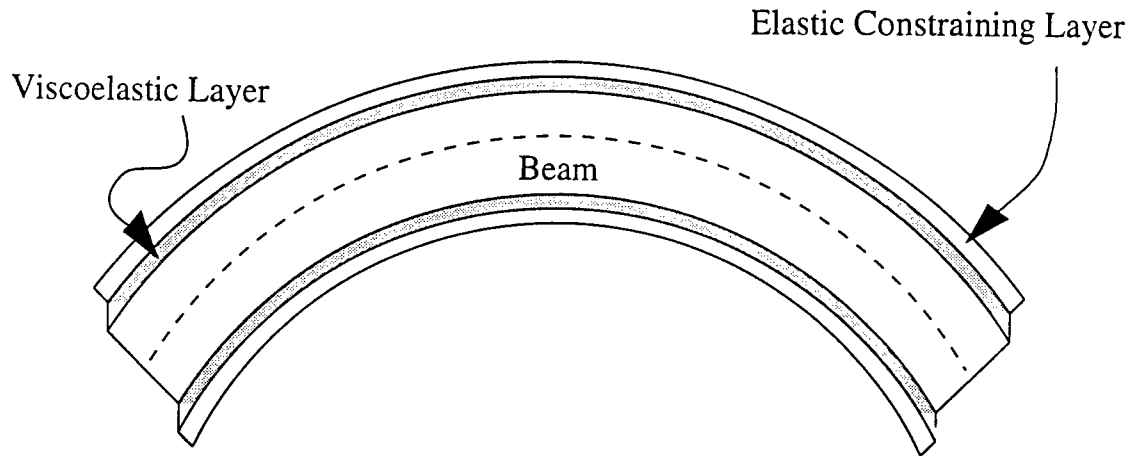


Figure 8: Treated Beam Element Under Flexure

passive damping theory is that it is frequency dependent. So the damping can be designed for a particular frequency. The result is damping that is optimum in the area of the prescribed frequency. To have an optimal actively and passively damped beam it is necessary to determine this target frequency.

5.1 Optimal Constraining Layer Section Length

Plunkett and Lee [1] observed that a relationship exists between the section length of the constraining layer and the amount of damping provided by the treatment. Their reasoning is as follows. If the length of the constraining layer is very long, then the strain imposed at the end due to shear stress will be the same as that of the base structure. Thus there is no shear in the viscoelastic layer, except near the ends and the resulting damping is small. Yet if the constraining layer is very short, there is no shearing of the viscoelastic material and the damping effect is small. These two extreme cases suggest that there exists an optimal constraining

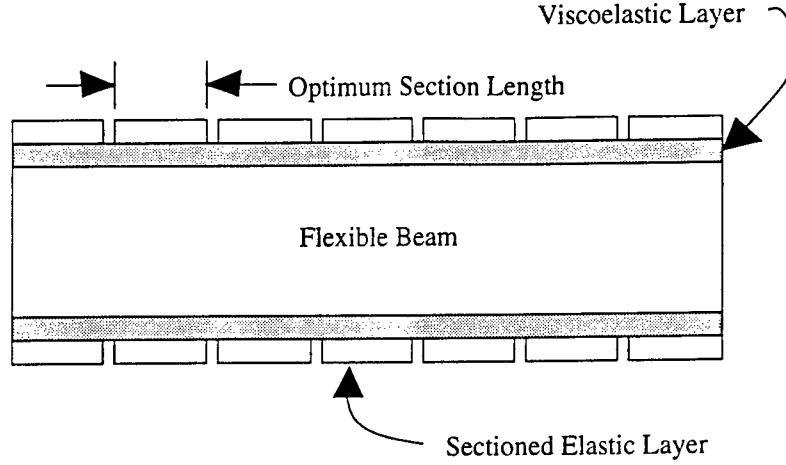


Figure 9: Sectioned Constraining Layer Treatment

layer section length that can provide maximum damping. Details on their analysis can be found in [1].

Equation 10 from [1], the dimensionless loss coefficient is

$$\eta_l = 4\pi \frac{1}{w} \left[\frac{\sinh(w \cos(\theta/2)) \sin(\theta/2) - \sin(w \sin(\theta/2)) \cos(\theta/2)}{\cosh(w \cos(\theta/2)) + \cos(w \sin(\theta/2))} \right] \quad (39)$$

where θ is the “loss angle”, defined as $\theta = \tan^{-1} \eta_G$ and η_G called the loss factor, is a property of the viscoelastic material. Notice too that $\eta_l = \eta_l(\eta_G, w)$. Also $w = \frac{L_c}{B_0}$, where L_c is the section length and

$$B_0 = \sqrt{\frac{t_v t_c E_c}{G \sqrt{1 + \eta_G^2}}} \quad (40)$$

The modified loss coefficient, η_L of the system, incorporates geometry and material properties of the beam and the constraining layer as follows

$$\eta_L = \eta_l \frac{3E_c t_c \int_a^{a+L} \left(\frac{d^2 y}{dx^2} \right)^2 dx}{\pi E_b t_b \int_0^L \left(\frac{d^2 y}{dx^2} \right)^2 dx} \quad (41)$$

where a is the distance from the root of the beam to the beginning of the damping layer, L is the length of the constrained portion of the beam, and l is the total length. For the beam studied in this thesis, η_L could be represented as

$$\eta_L = \eta_l \frac{3E_c t_c \int_{x/2}^{x/3} \left(\frac{d^2 y}{dx^2} \right)^2 dx + \int_{x/4}^l \left(\frac{d^2 y}{dx^2} \right)^2 dx}{\pi E_b t_b \int_0^L \left(\frac{d^2 y}{dx^2} \right)^2 dx} \quad (42)$$

Since the piezoelectric patches are only ‘interrupting’ about 1/12 of the viscoelastic damping layer, it is justifiable to say the integral (42) cancels itself. It would be possible to substitute the expression for the curvature of a uniform cantilever beam, vibrating at the mode being considered, into the integral. However

when a non-natural frequency is under investigation, interpolation between the natural frequencies for the mode shape equation, would be required. Therefore the modified loss coefficient for this case becomes

$$\eta_L = \frac{12E_c t_c}{w E_b t_b} \left[\frac{\sinh(w \cos(\theta/2)) \sin(\theta/2) - \sin(w \sin(\theta/2)) \cos(\theta/2)}{\cosh(w \cos(\theta/2)) + \cos(w \sin(\theta/2))} \right] \quad (43)$$

The variable w is a dimensionless characteristic length given by

$$w = \frac{L_c}{\sqrt{\frac{t_v t_c E_c}{G \sqrt{1 + \eta_G^2}}}} \quad (44)$$

L_c is the section length of the constraining layer, t_r is the thickness of the viscoelastic layer, and t_c is the thickness of the constraining layer. It turns out that the loss factor η_l has a maximum when w is equal to 3.28 [1], no matter what the loss factor is. So in (44) if we let $w = 3.28$ and solve for the L_c which we can now call L_o , we get the optimal characteristic length.

5.2 Optimal Viscoelastic Damping for the Active/Passive Beam

So at this point we know that for a prescribed frequency there is an optimal section length and it can be calculated as described above. Now the question is, for what frequency do we want to design the viscoelastic damping. To do this we will minimize (7), where J_i is the performance index (9).

So first of all determine a frequency range in which the passive damping design will be considered, say 1Hz-100Hz with an increment of 1Hz for the first decade then increments of 10Hz for the range 10Hz-100Hz. Build a list of the viscoelastic material properties (shear modulus G and loss factor η_G) to be used. Also include the natural frequencies of the system in the frequency list and the respective material properties at those frequencies. Then calculate the optimal section length for each frequency in the list.

$$L_{o_j} = 3.28 \sqrt{\frac{t_v t_c E_c}{G_j \sqrt{1 + \eta_{G_j}^2}}} \quad (45)$$

Compute w_{ij} for each frequency i , under each section length design j

$$w_{ij} = L_{o_j} \sqrt{\frac{G_i \sqrt{1 + \eta_{G_i}^2}}{t_v t_c E_c}} \quad (46)$$

Note that G_i and η_{G_i} here are the material properties of the viscoelastic material at frequency i . Now compute the system loss factors of the damped structure for each frequency under each section length design

$$\eta_{L_{ij}} = \frac{12E_c t_c}{w_{ij} E_b t_b} \left[\frac{\sinh(w_{ij} \cos(\theta/2)) \sin(\theta/2) - \sin(w_{ij} \sin(\theta/2)) \cos(\theta/2)}{\cosh(w_{ij} \cos(\theta/2)) + \cos(w_{ij} \sin(\theta/2))} \right] \quad (47)$$

Now the resultant damping from design j for frequency i is

$$\zeta_{ij} = 0.5 / \eta_{L_{ij}} \quad (48)$$

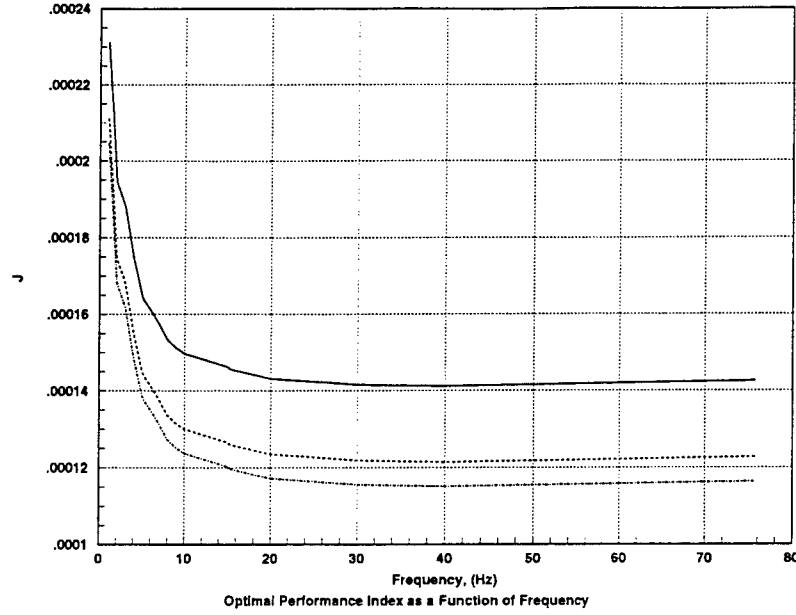


Figure 10: Plot For Determining Target Frequency For Passive Design

Now compute J , (7), for each frequency under each section length design which will be the sum of J_i (9) for the passive damping optimized at each natural frequency. Next plot J^{opt} vs. frequency. From the plot pick the frequency that minimizes J^{opt} . Then compute the optimal section length for that frequency.

At this point in the design, one would have an optimal active design for the case of no structural damping and an optimal passive design based on the outcome of the active design. Gaudreault, Liebst and Bagley [16] suggest that the active design should be modified based upon the new characteristics of the beam caused by the passive damping. Then recalculation of the passive design in an iterative fashion. This iteration is computationally expensive however and convergence of an optimization cannot be guaranteed. Therefore for this thesis a one step optimization is presented. To clarify these steps, one should consult the following example.

5.3 Optimal Active and Passive Beam Example

This example will show the steps taken and the subsequent results of an optimal passive damping design applied to an already optimal active damping design. To reiterate, the beam is aluminum, 2 m long, 3 in wide, 0.25 in thick, in a pinned-free configuration, with piezoelectric patches at the root and about midway down the beam.

5.4 Optimal Passive Design

An optimal passive damping design is desired. The materials selected for the prototype damping treatment include, mild steel shim stock (0.012 in thick) for the constraining layer, and 10 mil Scotchdamp SJ-2015X Type 110 Viscoelastic Polymer. Steel was chosen for the constraining layer, due to its relatively high stiffness, low cost, well known mechanical properties, and ease of workability. For space applications where weight is of concern, graphite fiber layers may be used very effectively. The 10 mil thickness Scotchdamp renders optimal constraining layer sections of practical length for easy construction. Mechanical data for the viscoelastic polymer was extrapolated from a nomogram provided by 3M, for a temperature of 68° and is tabulated in Table (3)

Frequency (Hz)	Shear Modulus G , (psi)	Loss Factor η_G	Section Length L_o , (in)
1	155	1.20	12.65
1.5	190	1.15	11.57
2	240	1.15	10.30
3	275	1.05	9.86
4	335	1.05	8.93
5	400	1.05	8.18
5.19	410	1.05	8.08
6	445	0.99	7.86
7	490	0.96	7.55
8	550	0.94	7.16
9	585	0.94	6.95
10	620	0.91	6.80
15	730	0.84	6.38
15.31	750	0.84	6.30
20	870	0.80	5.90
28.25	1000	0.74	5.59
30	1045	0.72	5.48
40	1300	0.65	5.04
47.25	1400	0.61	4.86
75.75	1625	0.51	4.61

Table 3: Scotchdamp SJ-2015X Type 110 Viscoelastic Polymer Properties at 68° and Calculated Optimal Section Length

Next, (45) was utilized to make a list of section lengths that are optimal for each frequency in the list of Table (3). The damping was found by first using (46) to calculate w_{ij} and then plugging w_{ij} into (47). Then ζ_{ij} was computed using (48). At this point compute J_{i_n} , equation (9) and sum this calculation for each natural frequency i_n . This sum is J^{opt} . Do this calculation and summation for each frequency in the frequency vector. Then plot J^{opt} verses the frequency vector as shown in Figure (10). This final

determination of J was done three times in Figure (10), for a different control penalty α .

From observation of this plot, one can see that an optimal passive damping design targeted at 40 Hz minimizes the performance index. This is between the third and fourth natural frequencies which are the next two frequencies that are not controlled actively. Thus it makes sense that they are targeted for the passive damping, to minimize the energy of the system. So now go back to the matrix of damping ratios, ζ_{ij} and for the natural frequencies in rows i_n , choose the damping ratios from the column that represents 40 Hz. This corresponds to column 18 in this example. The damping ratios under this optimal passive design are shown in Table (4)

Natural Frequency	5.19	15.31	28.25	47.25	75.75
Damping Ratio	0.0602	0.0615	0.0580	0.0500	0.0425

Table 4: Damping ratios resulting in passive design at 40 Hz.

5.5 Optimal Active and Passive Design Results

At this point we have determined the optimum passive damping design and have computed the resulting damping ratios. The optimal actively and passively damped beam was simulated similarly as it was in Chapter 5, except with the new structural damping coefficients. Plots comparing free decay for mode 1 with no damping treatment, Figure (4.1) can be compared with that of the optimally damped beam under mode 1 vibration, Figure (11).

5.6 Evaluation of the Simultaneously Optimal Control

To evaluate the effectiveness of the simultaneously optimal active and passive control design for the slewing beam, the mechanical energy and control efforts are examined for the following cases:

Case 1: The optimal active control for the beam presented in this thesis with $\alpha = 10$.

Case 2: The optimal active and passive design for the beam presented with $\alpha = 10$, and the passive damping design for 40 Hz.

Case 3: An optimal active design for the slewing beam with $\alpha = 1500$.

Case 4: An optimal active design for the slewing beam with $\alpha = 1500$ and a passive damping design picked arbitrarily for a target freq of 2 Hz.

Case 5: An optimal active design for the slewing beam with $\alpha = 1500$ and an optimal passive damping design with target freq of 40 Hz.

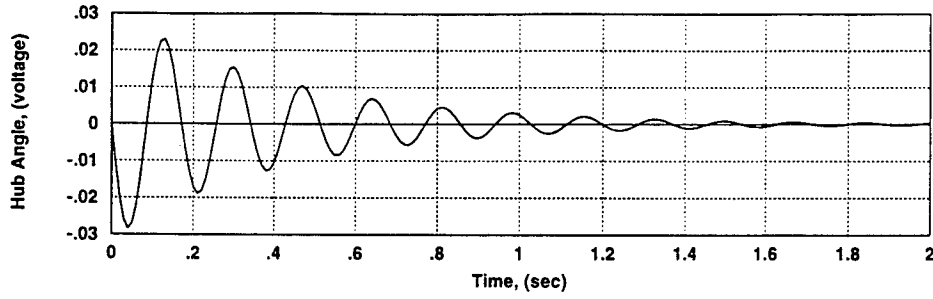


Figure 11: Mode 1, Controller On, Time Response for Optimally Damped Beam, (simulated)

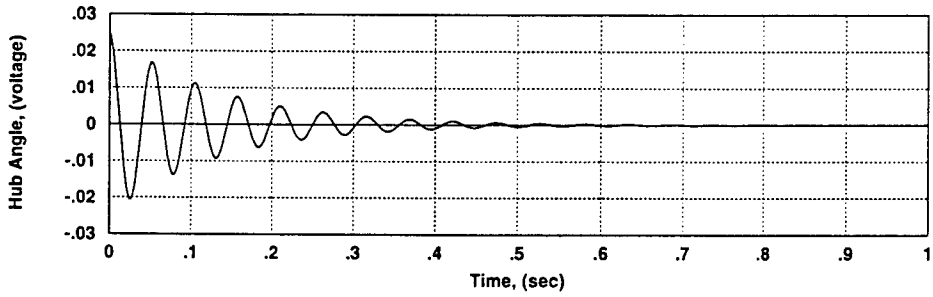


Figure 12: Mode 2, Controller On, Time Response for Optimally Damped Beam, (simulated)

The mechanical energy was calculated using

$$E_{mech} = \sum_{i=1}^n \int_0^{\infty} [\dot{\eta}_i^2 + (p_i^2 + g_i)\eta_i^2] dt \quad (49)$$

which is the mechanical energy portion of the performance index J_i . The energy due to control was calculated using

$$E_{cont} = \sum_{i=1}^n \int_0^{\infty} \left[\frac{1}{2\alpha^2} f_i^2 \right] dt \quad (50)$$

Results of cases 1 and 2 are shown in Figure (13). As expected, due to a lack of control authority under active control alone for this design, the addition of an optimal passive damping decreased the mechanical energy and the energy due to control, significantly. Mechanical energy due to the passive design, decreased

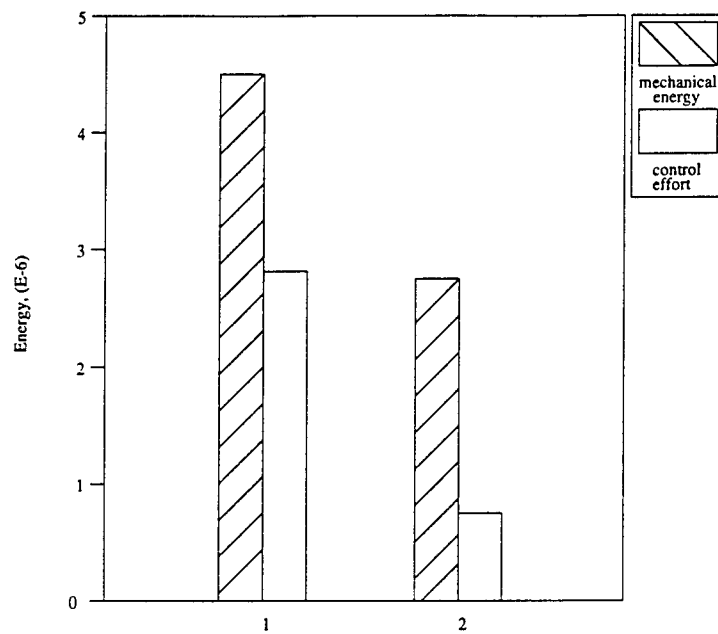


Figure 13: Comparisons of system energy

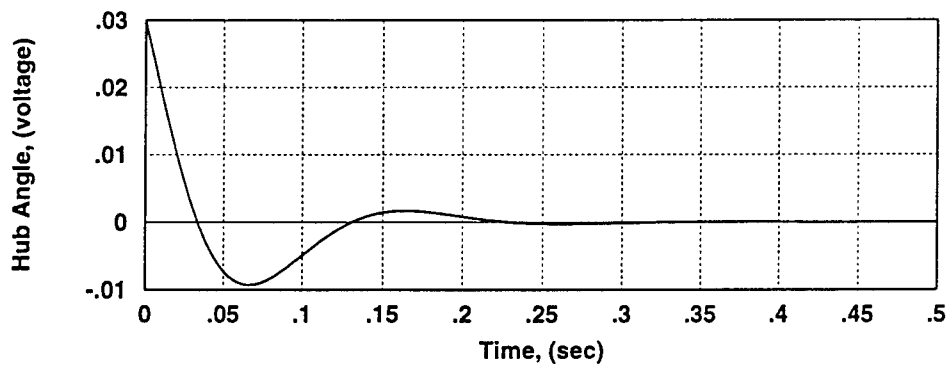


Figure 14: Mode 1, Controller On, Optimal Actively Damped Beam, $\alpha = 1500$, (simulated)

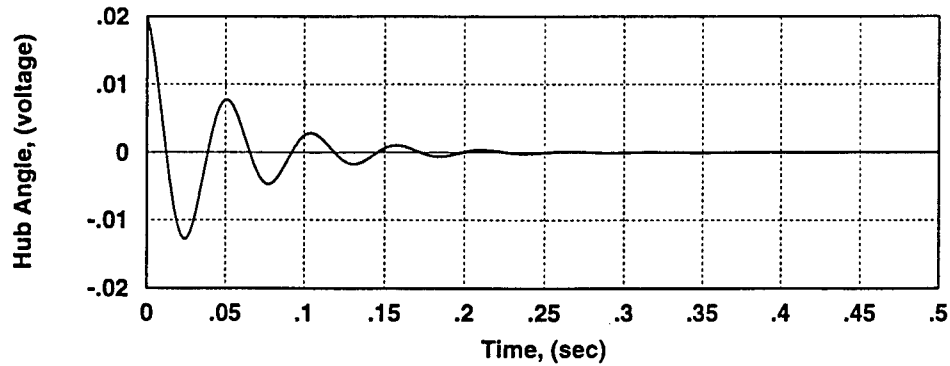


Figure 15: Mode 2, Controller On, Optimal Actively Damped Beam, $\alpha = 1500$, (simulated)

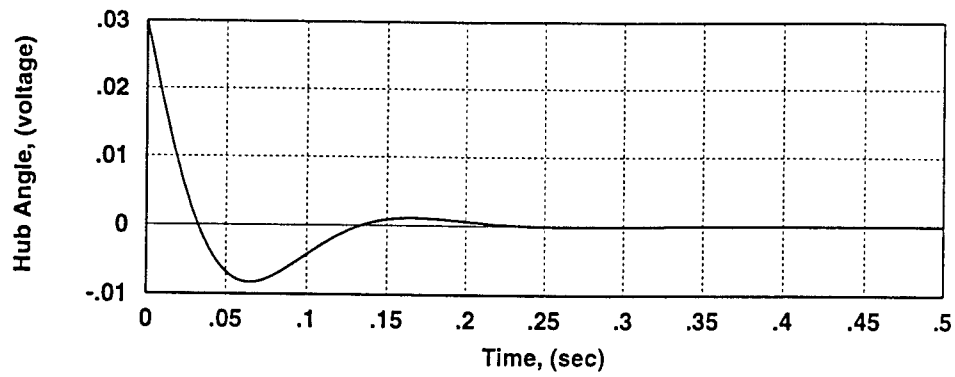


Figure 16: Mode 1, Controller On, Optimal Actively and Passively Damped Beam, $\alpha = 1500$, (simulated)

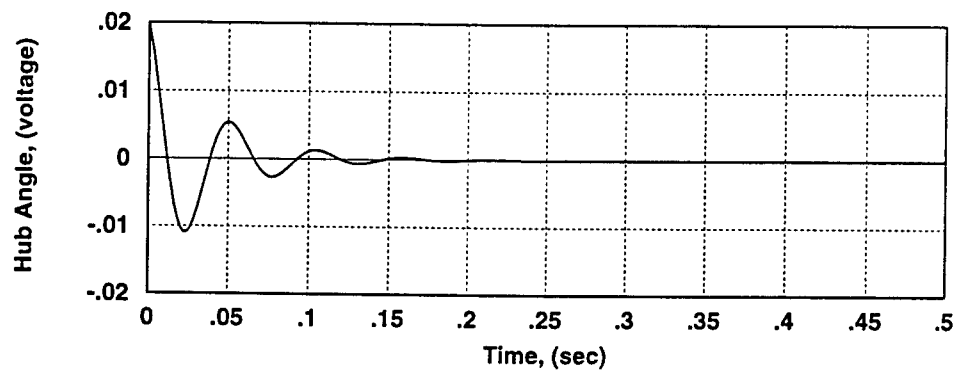


Figure 17: Mode 2, Controller On, Time Response for Optimal Actively and Passively Damped Beam, $\alpha = 1500$, (simulated)

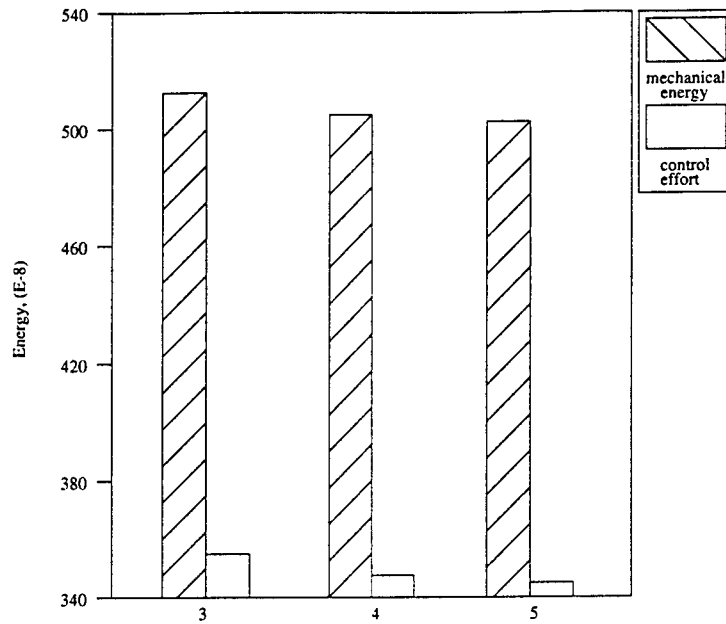


Figure 18: Comparisons of system energy

6 Planar Truss

This section describes and documents the preliminary model development for the planar truss system. The model is intended for future development using an approach similar to that described in the previous sections for the slewing beam model. A nastran model of the planer truss was made by first constructing a PATRAN model and assigning material properties. The longitudinal and diagonal bars were then represented as cbar elements in nastran. The transverse bars were assumed to consist of only the steel bars as the aluminum tubes added only weight to the truss not stiffness. The heavy steel bars were modeled using cbar elements also. It was assumed that the first bar of bay 1 was constrained for all six degrees of freedom. The nastran code for the truss is included in the Appendix. It was desired to actively control the truss using air jet thrusters due to excitation from a motor and slewing link at the end as shown in Figure(19). The nastran code for the slewing link is shown in the Appendix.

6.1 LQG Design for the FJSRL Planer Truss with Air Jet Thrusters

For a four mode model

$$\dot{x} = Ax + Bu \quad (51)$$

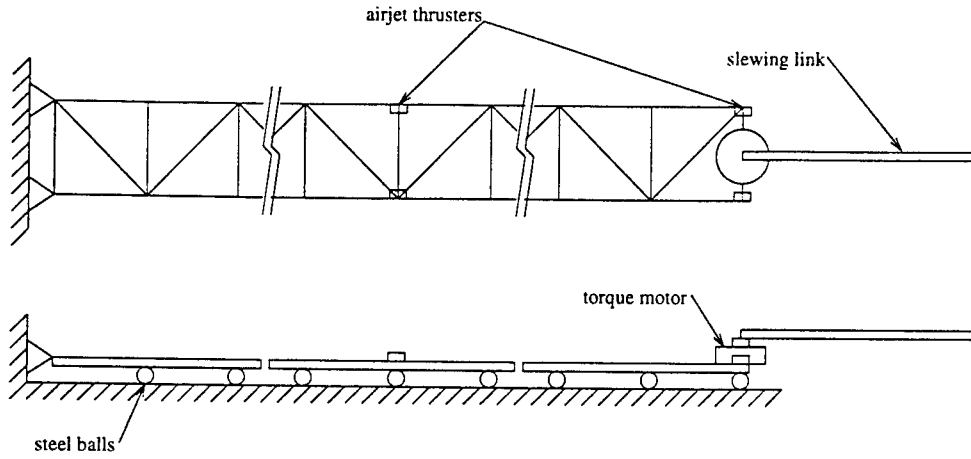


Figure 19: Planer Truss with Slewing Link

where

$$x = \begin{bmatrix} x_1 \\ x_2 \\ x_3 \\ x_4 \\ \dot{x}_1 \\ \dot{x}_2 \\ \dot{x}_3 \\ \dot{x}_4 \end{bmatrix} \quad \dot{x} = \begin{bmatrix} \dot{x}_1 \\ \dot{x}_2 \\ \dot{x}_3 \\ \dot{x}_4 \\ \ddot{x}_1 \\ \ddot{x}_2 \\ \ddot{x}_3 \\ \ddot{x}_4 \end{bmatrix} \quad (52)$$

$$\ddot{x} + 2\zeta\omega\dot{x} + \omega^2x = F \quad (53)$$

Putting this into a state space representation results in in block diagonals of the following form

$$A = \begin{bmatrix} 0 & 1 \\ -\omega & -2\zeta\omega \end{bmatrix} \quad (54)$$

$$B = \begin{bmatrix} 0 \\ \Phi_{mod}^T \end{bmatrix} \quad (55)$$

$$C = [\Phi \ 0] \quad (56)$$

$$D = [0] \quad (57)$$

$$(58)$$

where Φ_{mod}^T is a 4×4 matrix due to the four air jet thrusters. Two of which are at bay 10 and two at bay 20. The rows represent modes 1 through 4, the first two columns are mode shape displacements at bay 10 and the second two columns are mode shape displacements at bay 20. Columns one and two are opposite in sign as well as columns three and four. This is due to the thrusters acting in opposing directions. Φ^T represents the eigenvector at each actuator.

The weighting matrices for the LQG design are as follows

$$Q_{8 \times 8} = \text{diag}[0.1] \quad (59)$$

$$R_{8 \times 8} = \text{diag}[0.1] \quad (60)$$

Using the linear regulator design command REGULATOR in *Matrixx*, the closed loop eigenvalues, optimal state feedback control gains and the Riccati solution matrix P_r were found. Using the kalman filter design ESTIMATOR, the CL eigenvalues, optimal estimator gains and the Riccati solution matrix P_e were found. For base line Performance index, $\text{Trace}(P_r \times P_e)$ was computed and equals 0.8042. The closed loop eigenvalues from above, $[A - BK R]$ are in Table (5)

Now for a comparison with the dads model.

$$u = \begin{bmatrix} G_1 & 0 \\ 0 & G_2 \end{bmatrix} [\Phi] \begin{bmatrix} \dot{x}_1 \\ \dot{x}_2 \\ \dot{x}_3 \end{bmatrix} \quad (61)$$

where $G_1 = G_2 = 1$. Therefore for the Closed Loop eigenvalues of the existing DADS Model are

$$[A - B[0\Phi]] = [A - BB^T]. \quad (62)$$

These Closed Loop eigenvalues are given in Table (5) and are the result of DADS position-derivative control blocks.

LQG design	DADS
$-0.130 \pm j1.577$	$-0.071 \pm j1.578$
$-1.775 \pm j9.242$	$-1.796 \pm j9.237$
$-11.907 \pm j21.297$	$-11.919 \pm j21.291$
$-38.194 \pm j21.235$	$-38.213 \pm j21.201$

Table 5: Closed Loop Eigenvalues for LQG design and DADS Simulation

The DADS simulation consisted of a flexible link being slewed one radian with air-jet thrusters both active and not active, Figures(20-22).

7 Conclusion

A differential equation of motion was previously derived for a PZT/aluminum laminate beam. The equation was solved in the Laplace domain and expressed for twelve different transfer functions. These functions were later experimentally verified. Next two of these transfer functions, $G_{V_{a1},\theta}$ and $G_{V_{a2},\theta}$ were truncated to include five modes and converted into modal coordinates. Modal coordinates allow the use of Independent Modal Space Control, (IMSC). A performance index was minimized and the IMSC control gains for modal

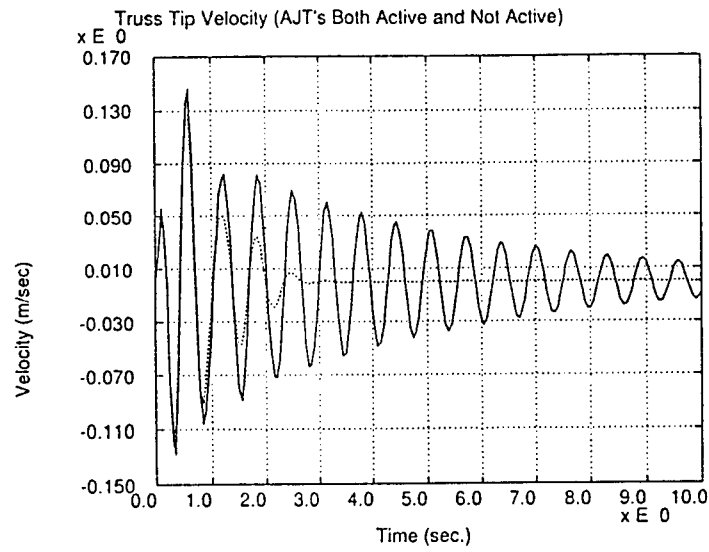


Figure 20: Truss Tip Velocity (AJT's Both Active and Not Active)

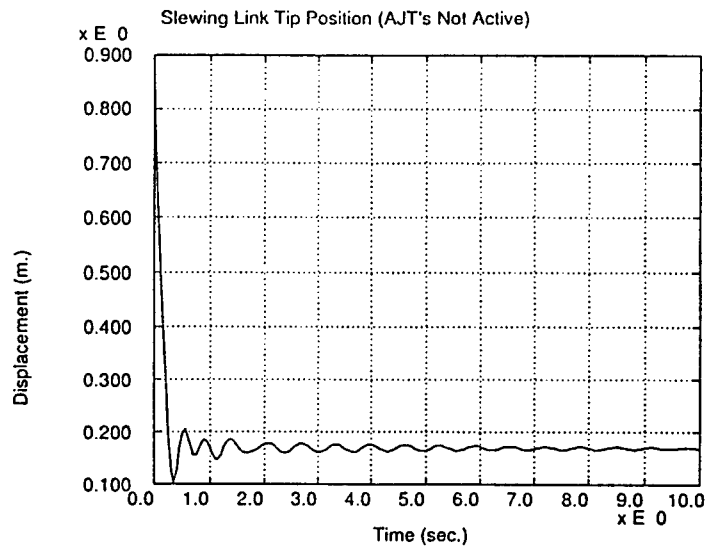


Figure 21: Slewing Link Tip Position (AJT's Not Active)

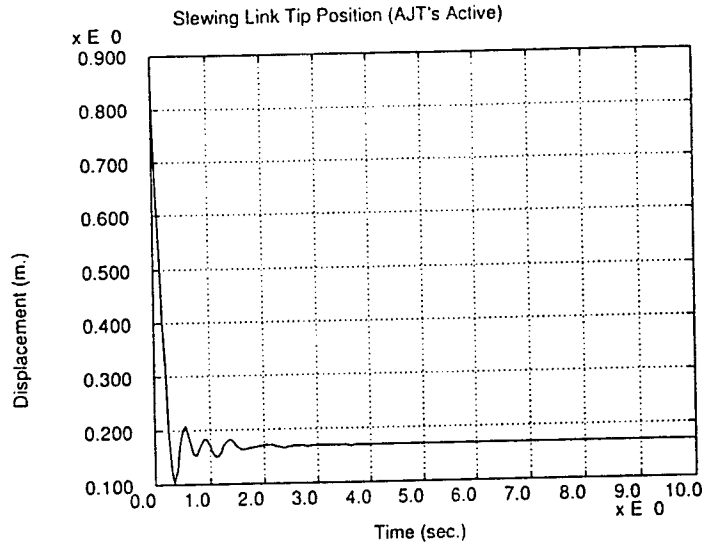


Figure 22: Slewing Link Tip Position (AJT's Active)

displacement and modal velocity were found. When zero structural damping for the beam was assumed, the results agreed with previous results. However an iterative scheme was developed to solve for the gains numerically when structural damping was not assumed to be zero. An experiment was conducted to verify the control law and model for a system where zero structural damping was assumed. The simulation matched the experimental results however more control authority would have been nice to demonstrate the usefulness of active control. A five mode model was used to watch for any effects of spillover. The problem of determining physical forces from the modal forces was presented and preliminary solutions to this problem were addressed. An optimal passive damping design using viscoelastic damping was also presented. A performance index was again minimized to determine the optimal design frequency for the frequency dependent, passive damping. A detailed example has been included for determining the optimal passive damping target frequency to aid in future work. The simulated results of the optimal active and passively damped beam were also presented.

7.1 Preliminary Planar Truss Development

A NASTRAN model of the planar truss system has been developed and incorporated into a DADS simulation model which includes a slewing link attached to the distal end of the truss. An LQG control design and simulation for this system have also been performed. Passive damping design for this system has been considered in the Ph.D dissertation of Xia [17]. It is our intention to continue this work to extend the results obtained with the slewing link to this structure. Nonlinear control may also be considered.

8 Appendix

A NASTRAN Code For the Planer Truss

```
ID TWO DIMENSIONAL MODEL
APP DISP
SOL 3
TIME 20
COMPILE DMAP=SOL3,SOUIN=MSCSOU
ALTER 24
OUTPUT2 GPL,BGPDT,,,/-1/11
ALTER 26
OUTPUT2 ECT,,,/0/11
ALTER 73
OUTPUT4 MGG,,,/-1/12
OUTPUT4 ,,,,/-2/12
OUTPUT2 OGPWG,,,/0/11
ALTER 416
OUTPUT2 LAMA,,,/0/11
ALTER 439
OUTPUT2 OUGV1,,,/0/11
OUTPUT2 ,,,,/-9/11
ALTER 100
OUTPUT4 KGG,,,/-1/13
OUTPUT4 ,,,,/-2/13
ENDALTER
CEND
$ CASE CONTROL DECK
TITLE=VIBRATION ANALYSIS OF THE PLANER TRUSS
OUTPUT
LINES=40
DISP=ALL
SPC=100
METHOD=1
BEGIN BULK
$FJSRL PLANER TRUSS
$--BULK DATA CARDS PRODUCED BY "PATNAS" VERSION1.7 : 1993-02-16 10:15:05
PARAM GRDPNT 0
EIGR,1,SINV,1.,50.,,5
SPC1,100,123456,1,2
GRDSET,,,,,,345
GRID      1      0.      0.      0.
GRID      2      0.      .35350 0.
GRID      3      .35350 0.      0.
GRID      4      .35350 .35350 0.
GRID      5      .70700 0.      0.
GRID      6      .70700 .35350 0.
GRID      7      1.06050 0.      0.
GRID      8      1.06050 .35350 0.
GRID      9      1.41400 0.      0.
GRID     10      1.41400 .35350 0.
```

GRID	11		1.76750	0.	0.	
GRID	12		1.76750	.35350	0.	
GRID	13		2.12100	0.	0.	
GRID	14		2.12100	.35350	0.	
GRID	15		2.47450	0.	0.	
GRID	16		2.47450	.35350	0.	
GRID	17		2.82800	0.	0.	
GRID	18		2.82800	.35350	0.	
GRID	19		3.18150	0.	0.	
GRID	20		3.18150	.35350	0.	
GRID	21		3.53500	0.	0.	
GRID	22		3.53500	.35350	0.	
GRID	23		3.88850	0.	0.	
GRID	24		3.88850	.35350	0.	
GRID	25		4.24200	0.	0.	
GRID	26		4.24200	.35350	0.	
GRID	27		4.59550	0.	0.	
GRID	28		4.59550	.35350	0.	
GRID	29		4.94900	0.	0.	
GRID	30		4.94900	.35350	0.	
GRID	31		5.30250	0.	0.	
GRID	32		5.30250	.35350	0.	
GRID	33		5.65600	0.	0.	
GRID	34		5.65600	.35350	0.	
GRID	35		6.00950	0.	0.	
GRID	36		6.00950	.35350	0.	
GRID	37		6.36300	0.	0.	
GRID	38		6.36300	.35350	0.	
GRID	39		6.71650	0.	0.	
GRID	40		6.71650	.35350	0.	
GRID	41		7.07000	0.	0.	
GRID	42		7.07000	.35350	0.	
CBAR	1	1	1	2	0.	1.00000
CBAR	2	1	3	4	0.	1.00000
CBAR	3	1	5	6	0.	1.00000
CBAR	4	1	7	8	0.	1.00000
CBAR	5	1	9	10	0.	1.00000
CBAR	6	1	11	12	0.	1.00000
CBAR	7	1	13	14	0.	1.00000
CBAR	8	1	15	16	0.	1.00000
CBAR	9	1	17	18	0.	1.00000
CBAR	10	1	19	20	0.	1.00000
CBAR	11	1	21	22	0.	1.00000
CBAR	12	1	23	24	0.	1.00000
CBAR	13	1	25	26	0.	1.00000
CBAR	14	1	27	28	0.	1.00000
CBAR	15	1	29	30	0.	1.00000
CBAR	16	1	31	32	0.	1.00000
CBAR	17	1	33	34	0.	1.00000
CBAR	18	1	35	36	0.	1.00000
CBAR	19	1	37	38	0.	1.00000

CBAR	20	1	39	40 0.	0.	1.00000
CBAR	21	1	41	42 0.	0.	1.00000
CBAR	22	22	2	3 0.	0.	1.00000
CBAR	23	22	6	7 0.	0.	1.00000
CBAR	24	22	10	11 0.	0.	1.00000
CBAR	25	22	14	15 0.	0.	1.00000
CBAR	26	22	18	19 0.	0.	1.00000
CBAR	27	22	22	23 0.	0.	1.00000
CBAR	28	22	26	27 0.	0.	1.00000
CBAR	29	22	30	31 0.	0.	1.00000
CBAR	30	22	34	35 0.	0.	1.00000
CBAR	31	22	38	39 0.	0.	1.00000
CBAR	32	22	3	6 0.	0.	1.00000
CBAR	33	22	7	10 0.	0.	1.00000
CBAR	34	22	11	14 0.	0.	1.00000
CBAR	35	22	15	18 0.	0.	1.00000
CBAR	36	22	19	22 0.	0.	1.00000
CBAR	37	22	23	26 0.	0.	1.00000
CBAR	38	22	27	30 0.	0.	1.00000
CBAR	39	22	31	34 0.	0.	1.00000
CBAR	40	22	35	38 0.	0.	1.00000
CBAR	41	22	39	42 0.	0.	1.00000
CBAR	42	22	1	3 0.	0.	1.00000
CBAR	43	22	3	5 0.	0.	1.00000
CBAR	44	22	5	7 0.	0.	1.00000
CBAR	45	22	7	9 0.	0.	1.00000
CBAR	46	22	9	11 0.	0.	1.00000
CBAR	47	22	11	13 0.	0.	1.00000
CBAR	48	22	13	15 0.	0.	1.00000
CBAR	49	22	15	17 0.	0.	1.00000
CBAR	50	22	17	19 0.	0.	1.00000
CBAR	51	22	19	21 0.	0.	1.00000
CBAR	52	22	21	23 0.	0.	1.00000
CBAR	53	22	23	25 0.	0.	1.00000
CBAR	54	22	25	27 0.	0.	1.00000
CBAR	55	22	27	29 0.	0.	1.00000
CBAR	56	22	29	31 0.	0.	1.00000
CBAR	57	22	31	33 0.	0.	1.00000
CBAR	58	22	33	35 0.	0.	1.00000
CBAR	59	22	35	37 0.	0.	1.00000
CBAR	60	22	37	39 0.	0.	1.00000
CBAR	61	22	39	41 0.	0.	1.00000
CBAR	62	22	2	4 0.	0.	1.00000
CBAR	63	22	4	6 0.	0.	1.00000
CBAR	64	22	6	8 0.	0.	1.00000
CBAR	65	22	8	10 0.	0.	1.00000
CBAR	66	22	10	12 0.	0.	1.00000
CBAR	67	22	12	14 0.	0.	1.00000
CBAR	68	22	14	16 0.	0.	1.00000
CBAR	69	22	16	18 0.	0.	1.00000
CBAR	70	22	18	20 0.	0.	1.00000

CBAR	71	22	20	22 0.	0.	1.00000				
CBAR	72	22	22	24 0.	0.	1.00000				
CBAR	73	22	24	26 0.	0.	1.00000				
CBAR	74	22	26	28 0.	0.	1.00000				
CBAR	75	22	28	30 0.	0.	1.00000				
CBAR	76	22	30	32 0.	0.	1.00000				
CBAR	77	22	32	34 0.	0.	1.00000				
CBAR	78	22	34	36 0.	0.	1.00000				
CBAR	79	22	36	38 0.	0.	1.00000				
CBAR	80	22	38	40 0.	0.	1.00000				
CBAR	81	22	40	42 0.	0.	1.00000				
PBAR	1	1	1.290-3	6.937-8	2.775-7					
PBAR	22	2	6.600-5	3.645-9	3.645-9					
MAT1	1	207.0+9	79.62+9	.30000	10246.0	0.	0.	0.	M	1
+M	1	0.	0.							
MAT1	2	75.00+9	28.20+9	.33000	2700.00	0.	0.	0.	M	2
+M	2	0.	0.							
ENDDATA										

B NASTRAN Code For the Slewing Link

```
ID TWO DIMINSIONAL MODEL
APP DISP
SOL 3
TIME 20
COMPILE DMAP=SOL3,SOUIN=MSCSOU
ALTER 24
OUTPUT2 GPL,BGPDT,,,/-1/11
ALTER 26
OUTPUT2 ECT,,,/0/11
ALTER 73
OUTPUT4 MGG,,,/-1/12
OUTPUT4 ,,,,/-2/12
OUTPUT2 OGPWG,,,/0/11
ALTER 416
OUTPUT2 LAMA,,,/0/11
ALTER 439
OUTPUT2 OUGV1,,,/0/11
OUTPUT2 ,,,,/-9/11
ALTER 100
OUTPUT4 KGG,,,/-1/13
OUTPUT4 ,,,,/-2/13
ENDALTER
CEND
$ CASE CONTROL DECK
TITLE=VIBRATION ANALYSIS OF a slewing link
OUTPUT
LINES=40
DISP=ALL
SPC=100
METHOD=1
BEGIN BULK
$1x.25 slewing link
PARAM GRDPNT 0
EIGR,1,SINV,1.,50.,,5
SPC1,100,123456,1
GRDSET,,,,,,,,345
GRID 1 0. 0. 0.
GRID 2 0. 1.00000 0.
CBAR 1 22 1 2 0. 0. 1.00000
PBAR 22 1 8.065-5 1.050-7 4.329-9

MAT1 1 75.00+9 28.20+9 .33000 2700.00 0. 0. 0. M 2
+M 2 0. 0. 0.
ENDDATA
```

References

- [1] R. Plunkett and C.T. Lee, "Length Optimization for Constrained Viscoelastic Layer Damping," J. Acoust. Soc. Amer., Vol. 48, No. 1, 1970, pp. 150-161.
- [2] M.J. Balas, "Feedback Control of Flexible Systems", IEEE Transactions on Automatic Control, VOL.AC-23, No.4, Aug. 1978, pp. 673-679.
- [3] T. E. Alberts and J. A. Colvin. 1991, "Observations on the nature of transfer functions for control of piezoelectric laminates," *J. of Intelligent Material Systems & Structures*, Vol.2, No.4, pp.528-541.
- [4] J. Fanson, G. Blackwood, and C.-C. Chu, "Experimental Evaluation of Active-Member Control of Precision Structures", Presented at the NASA/DOD CSI Conference, Jan.29 - Feb.2, 1989.
- [5] T.E. Alberts, "Augmenting the Control of a Flexible Manipulator with Passive Mechanical Damping", Ph.D. Dissertation, Georgia Institute of Technology, Sept. 1986.
- [6] L. Meirovitch and L.M. Silverberg, "Globally Optimal Control of Self-Adjoint Distributed Systems", Optimal Control Applications and Methods, Vol. 4, 1983, pp. 365-386.
- [7] L.M. Silverberg, "Uniform Damping Control of Spacecraft", Journal of Guidance Control, and Dynamics, Vol. 9, 1986, pp. 221-226.
- [8] H. Baruh and L. Meirovitch. "Implementation of the IMSC Method by Means of a Varying Number of Actuators", Proceedings of the Fourth VPI&SU/AIAA Symposium on Dynamics and Control of Flexible Structures, 1983, pp. 605-616.
- [9] E. Schmitz, "Experiments on the End-Point Position Control of A Very Flexible One-Link Manipulator," Ph.D. Dissertation, Stanford University, Stanford CA., 1985.
- [10] T.E. Alberts, and T.V. DuBois. "Multivariable Transfer Functions and Optimal Passive Damping for a Slewing Piezoelectric Laminate Beam," Final Report for the AFOSR Summer Research Program, FJSRL, Jul. 31, 1992. In review for publication in the AMSE *Journal of Dynamic Systems, Measurement, and Control*, also presented in IFAC 1993, Sydney, Australia.
- [11] T.E. Alberts and Joseph V. Harrell, "Optimal Passive/Active Control Design Synergism for Flexible Structures," Submitted to the AIAA Journal of Guidance, Control and Dynamics, July 12, 1991.
- [12] B. Friedland, *Control System Design, An Introduction to State-Space Methods*, McGraw-Hill, 1986.
- [13] L. Meirovitch, *Analytical Methods In Vibrations*, Macmillan Publishing Co., Inc., 1967.
- [14] J.V. Harrell, "Some Theoretical Results Supporting the Use of Passive Damping As Augmentation of the Active Control of Multi-Dimensional Systems", Ph.D. Dissertation, Old Dominion University, Dec. 1993.
- [15] T.E. Alberts, H. Xia and J.V. Harrell, "Simultaneously Optimal Active and Passive Control Design for a Slewing Piezoelectric and Viscoelastic Laminate Beam", Flexible Structures, pp 693-704, 1993.
- [16] M.L.D. Gaudreault, B.S. Liebst, and R.L. Bagley, "Simultaneous Design of Active Vibration Control and Passive Viscous Damping," J. Guidance, Control and Dynamics, Vol. 16, No. 4, pp 654-661, 1993.
- [17] H. Xia, "Fiber Enhanced Viscoelastic Damping Polymers and Their Application to Passive Vibration Control," Ph.D. Dissertation, Old Dominion University, Aug. 1993.

**Three Dimensional Characterization
of
Non-Linear Optical Thin Films**

Thomas M. Christensen
Assistant Professor
Department of Physics and Energy Science

University of Colorado at Colorado Springs
1420 Austin Bluffs Parkway
Colorado Springs, CO 80933-7150

Final Report for:
Summer Research Extension Program

Sponsored by:
Air Force Office of Scientific Research
Bolling Air Force Base, Washington D.C.

and

the University of Colorado

December, 1993

Three Dimensional Characterization of Non-linear Optical Thin Films

Thomas M. Christensen
Assistant Professor
Department of Physics and Energy Science
University of Colorado at Colorado Springs

Abstract

Second harmonic generation has been observed in SiO_2 fibers doped with GeO_2 and more recently in thin films of similar materials. The observation of these effects in thin films opens up new opportunities for characterizing these materials. This may lead to a more fundamental understanding of the non-linear processes occurring in these materials. We have modified an existing ellipsometer to employ spectroscopic, multiple-angle ellipsometry to the characterization of these materials. We show how this technique can be used to examine the optical properties and structure of the film and the variations in these properties across the film. The use of spectroscopic and multiple angle ellipsometry allows us to examine more complicated systems because of the large amount of additional information available when compared to standard single wavelength, single angle ellipsometry measurements. We review several applications: First a non-film application involving the optical rotation dispersion of a sucrose solution. Second we examine several thin films of SiO_2 on Si using combined spectroscopic and multiple angle ellipsometry. Third, we examine spectroscopically glass slides which exhibit non-linear behavior when poled. Finally, we discuss the spatial variations in thickness and index of refraction determined from multiple angle ellipsometry studies of laser ablated Ge oxide films.

Three Dimensional Characterization of Non-Linear Optical Thin Films

Thomas M. Christensen

Introduction

Second harmonic generation is an inherently non-linear optical phenomenon in which light incident on a material with a particular frequency, ω , leaves the material with a mix of frequencies, ω and 2ω . It has long been known that this phenomenon is not allowed in materials which are centro-symmetric. It was a surprise, therefore, in late 1985 when second harmonic generation was observed [1] from amorphous SiO_2 fibers doped with GeO_2 . These glass fibers were believed to be centro-symmetric, yet a second harmonic signal was observed to grow in over the course of several hours. It was later observed [2] that by "seeding" the fibers with the 2ω light, the second harmonic generation could be enhanced. Since the index of refraction in a material depends on the frequency of the light, the ω and 2ω light should propagate at different velocities through the fiber and thus be out of phase with one another. The strong observed second harmonic signal indicated that phase matching was occurring. This could be accomplished by creating a spatial periodicity in the material. In the eight years since the first observations, a great deal of effort has gone into trying to explain the source and formation of the non-linear properties in fibers. Many models have been proposed, but no consensus has yet been reached on the fundamental physics behind

these effects.

More recently, similar effects have been observed at F. J. Seiler Research Laboratory (FJSRL/NP) in thin films of the same material. The observation in thin films opens up new possibilities in characterizing the materials in order to understand the underlying physics. In thin films, the seeding of the material is done by waveguiding the fundamental and second harmonic light through the film. This activates the non-linear optical properties in a thin (about 25 μm wide) path across the sample. The rest of the sample remains unchanged and does not exhibit non-linear properties. We are, therefore, interested in being able to characterize changes in the film associated with this activation process. This requires being able to examine variations in film properties with good spatial resolution. The use of waveguiding requires some knowledge of the optical properties of the film and their variations in three dimensions in order to optimize the waveguiding conditions. We discuss the optical characterization of these materials in terms of optical properties, chemical composition, and morphology and discuss how we can obtain information on the spatial variations of these properties in three dimensions using spectroscopic, multiple-angle ellipsometry.

Films are being produced at FJSRL/NP by laser ablation. These films can

vary in composition, optical properties, and morphology depending on the deposition conditions. The material property variations can change the non-linear optical properties of the films. A thorough understanding of the variations of these material properties, both across the film and in depth through the film, is necessary to understand both the deposition process itself and the relationship of material properties to non-linear optical properties.

Experimental Technique

Ellipsometry [3] uses the change in polarization of light reflected from a material to determine information about the optical properties of the material. These optical properties depend on the composition, thickness, and morphology of layers of material in the sample. Prior to beginning this program, our existing ellipsometer was a standard, single-wavelength, multiple angle of incidence ellipsometer which was computer controlled by an old PDP-11 computer. The optics in the ellipsometer are all UV grade to allow operation of the instrument at various wavelengths.

As part of this project we made several modifications to the ellipsometer to enhance its capabilities. The first of these was to couple an existing monochromator and light source to the ellipsometer to allow us to perform spectroscopic ellipsometry. We also switched computers from

the older, and relatively slow, PDP11 to a much faster IBM 486 compatible computer. With the expanded amount of information obtained in spectroscopic ellipsometry, a faster computer with advanced graphics capabilities was necessary. We developed some of the necessary software to analyze the spectroscopic data.

The improved experimental configuration is shown in Figure 1.

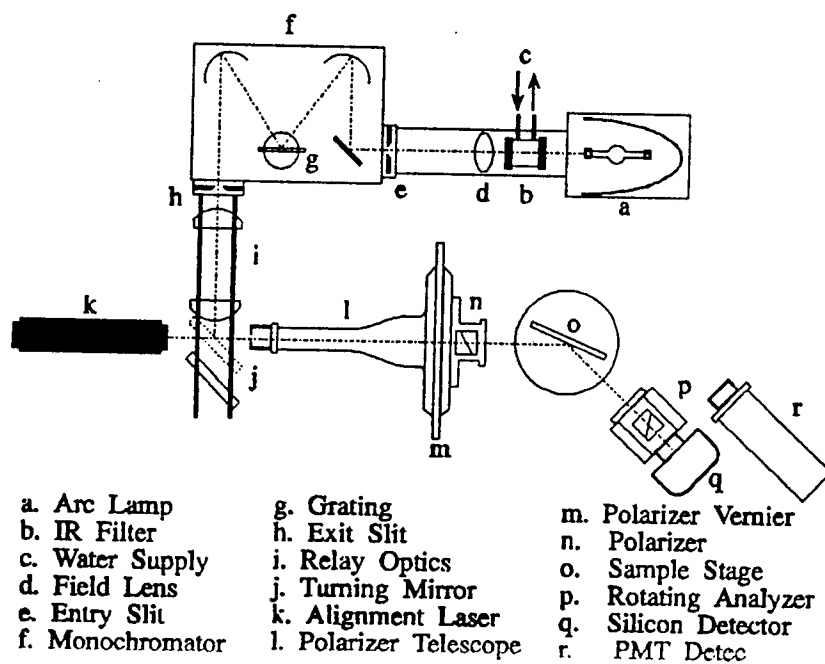


Figure 1. Spectroscopic Ellipsometer Configuration

We attempted to add optics to reduce our beam size down to approximately 26 microns across from the current value of about 1 mm.

Difficulty with coupling the optics to the source and with divergence after reflection from the sample have so far prevented us from achieving this goal. We have just obtained some additional lenses and hope to try again in the near future.

Most ellipsometry analysis involves application of some type of multiple layer model where the sample is treated as consisting of one or more layers each with specific optical properties and thickness. Each layer is assumed to be flat (uniform thickness) and to have uniform optical properties. Interfacial features like roughness or interdiffusion are treated by including more layers at the interfaces. A film deposited on a substrate might be treated as a two layer system: film (with some uniform thickness) and a substrate with infinite thickness. The same system might have to be modeled as a four layer system if the surface is rough and some type of interfacial region is suspected at the substrate-film interface.

Since single wavelength, single angle ellipsometry measurements yield only two experimental parameters, even the simplest film system can not be determined from ellipsometry alone. Each layer has three unknowns (index of refraction, extinction coefficient, and layer thickness) so additional information is necessary to determine the film properties. One

method of obtaining this additional information is to vary instrumental parameters like the wavelength and angle of incidence.

The effects of varying experimental parameters can be demonstrated by considering a data space made up of the ellipsometric parameters, angle of incidence, and wavelength of the incident light. In the standard ellipsometer experiment (with only one wavelength and one angle of incidence), two ellipsometric parameters (ψ and Δ) are obtained. These two parameters are all that we have available as we try to model the properties of the sample. If we consider our data space, we see (Figure 2) that the simple ellipsometer gives us two points in this space which can be fit by a large number of solutions.

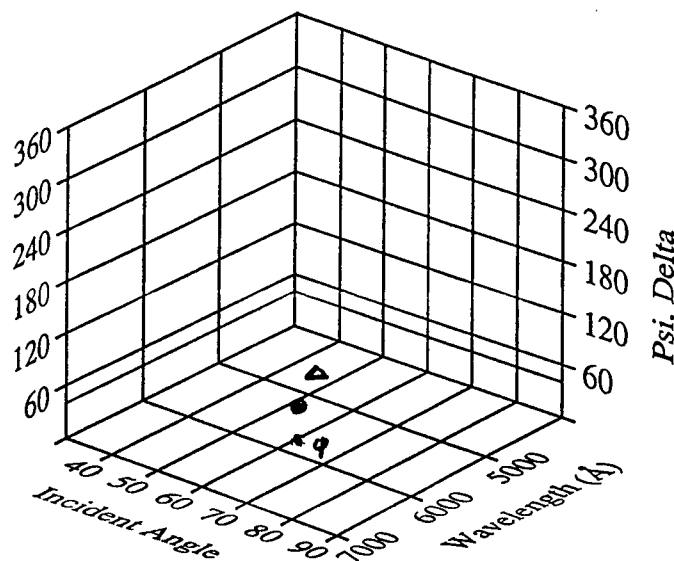


Figure 2. Data from single angle, single wavelength ellipsometer.

By considering either multiple angle of incidence or spectroscopic ellipsometry we can increase the amount of information available for modeling since now we have two curves which need to be fit as in Figure 3 which shows the multiple angle case.

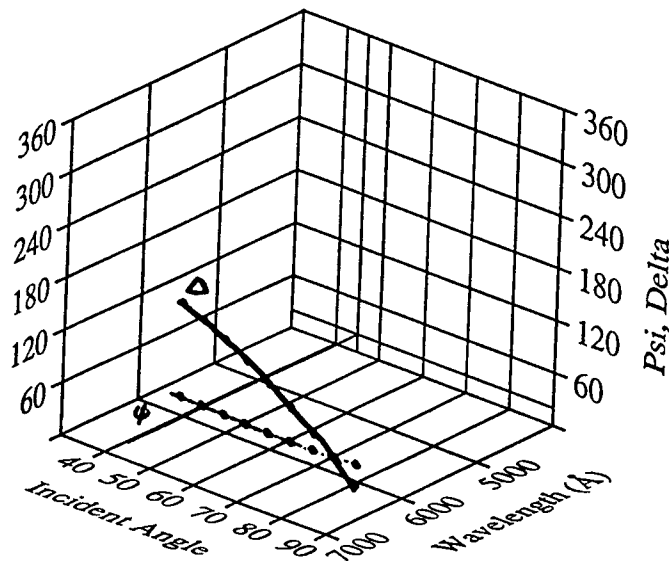


Figure 3. Data from multiple angle, single wavelength ellipsometry

Finally if we combine spectroscopic and multiple angle of incidence ellipsometry, we are trying to fit two surfaces and our ability to determine unique solutions is significantly enhanced. This is indicated in Figure 4. The tremendous amount of data available now also lets us examine considerably more complicated systems.

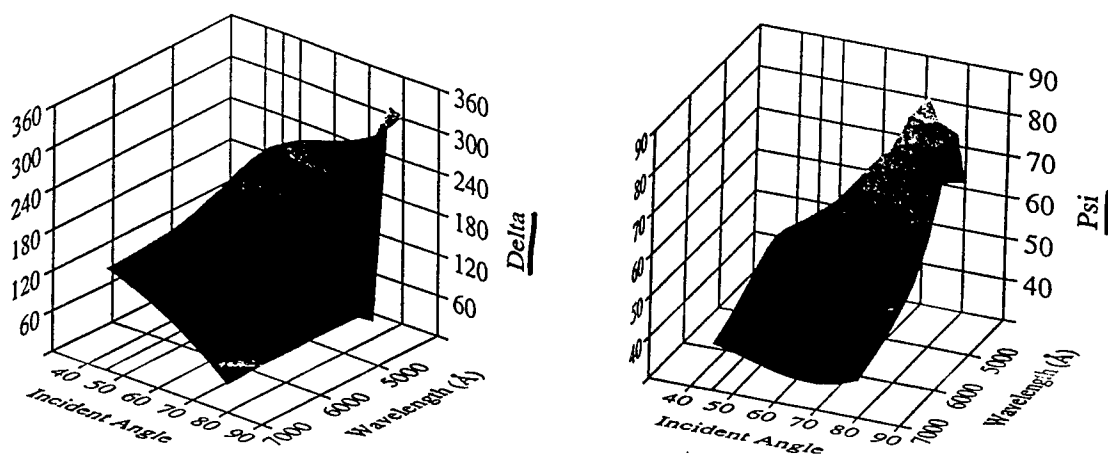


Figure 4. Data from multiple angle, spectroscopic ellipsometry

Results

Although the main thrust of this work was toward understanding GeO_x films which show non-linear optical properties, the improvements in the ellipsometer allowed a variety of other experiments to be performed. We will briefly discuss some results from sucrose solutions, SiO_2 films, and poled quartz slides (which show non-linear optical properties) before examining in detail the properties of GeO_x films.

Optical rotation dispersion of a sucrose solution

Another interesting application of spectroscopic ellipsometry is to use the instrument as a transmission polarimeter. Some materials have the property that the electric vector of plane polarized light is rotated as it passes through the material as shown in Figure 5.

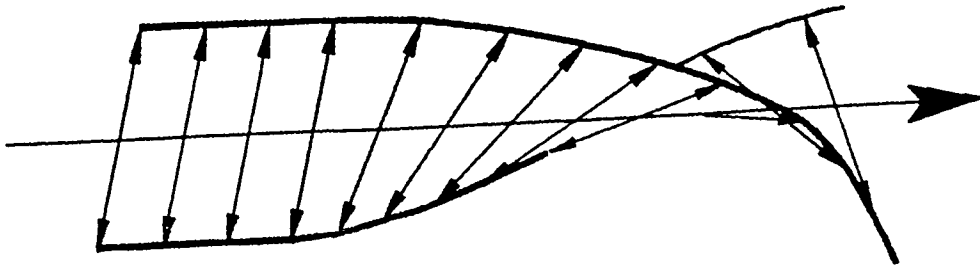


Figure 5. Rotation of electric field vector by an optically active medium.

The total amount of rotation, θ , depends on the wavelength of the light and the length of material traversed. Fresnel explained this effect as circular birefringence. Each of the two circular eigenpolarizations, right circular and left circular, sees a different index of refraction, n_r and n_l respectively. Since n_r and n_l are not the same, one polarization of light propagates faster than the other. The result is that one polarization incurs a relative phase shift with respect to the other. When the wave leaves the material, the relative phase shift appears as a rotation from the initial linear polarization state. It can be shown [4] that the positive angle of rotation for a material of length L will be

$$\theta = (n_r - n_l) \pi L / \lambda$$

Optical activity can be described with an expansion of the polarization of the material. Symmetry arguments about the dielectric and susceptibility

tensors lead to an approximate relationship between the circular indices and the susceptibility term χ_{xyz} [4]

$$(n_r - n_l) = (k/n^2) \chi_{xyz}$$

where n is the first order index of refraction and k is the wave number.

Combining these two equations, and using $k = 2\pi n/\lambda$ gives

$$\theta = 2\pi^2 L \chi_{xyz} / n \lambda^2$$

The net rotation of the electric vector as it traverses the media is therefore inversely dependent on the square of the wavelength. An additional wavelength dependence arises indirectly through the dispersion of the first order index of refraction n .

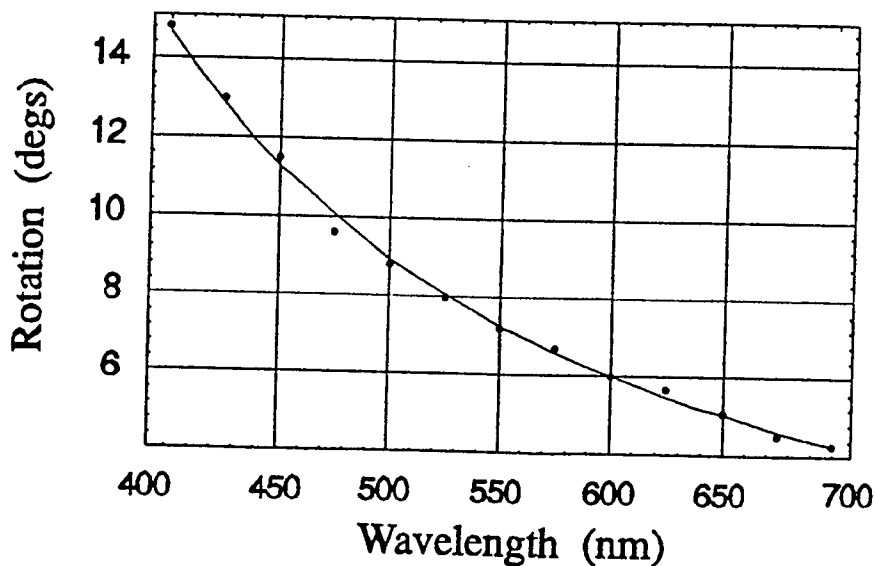


Figure 6. Optical rotation dispersion of a sucrose solution.

Figure 6 shows the results of a measurement of the rotation dispersion of light passing through a 20 cm length of a 5% sucrose in water solution. A least squares fit reveals an exponent of -2.2 for a power law relationship. The discrepancy from -2.0 is likely due to the additional dispersion of the first order index of refraction.

SiO₂ films on Si - spectroscopic, multiple angle ellipsometry

To test the ellipsometer more fully we examined a relatively simple system of SiO₂ films thermally grown on Si substrates. We examined three samples of varying thicknesses. The nominal thicknesses of the samples were 500 Å, 1000 Å and 4300 Å. We examined the samples over the wavelengths 350 - 700 nm and over incident angles of 45 - 80 degrees. This allowed us to make three dimensional plots of the ellipsometric parameters ψ and Δ as a function of both wavelength and incident angle. These plots could be compared to models to exactly determine the optical properties and thickness of the film and to test the performance of the instrument and software.

The experimental data and models are compared in the following figure. The parameter ψ is shown for all three samples in Figure 7. The experimental data and models are in reasonably good agreement.

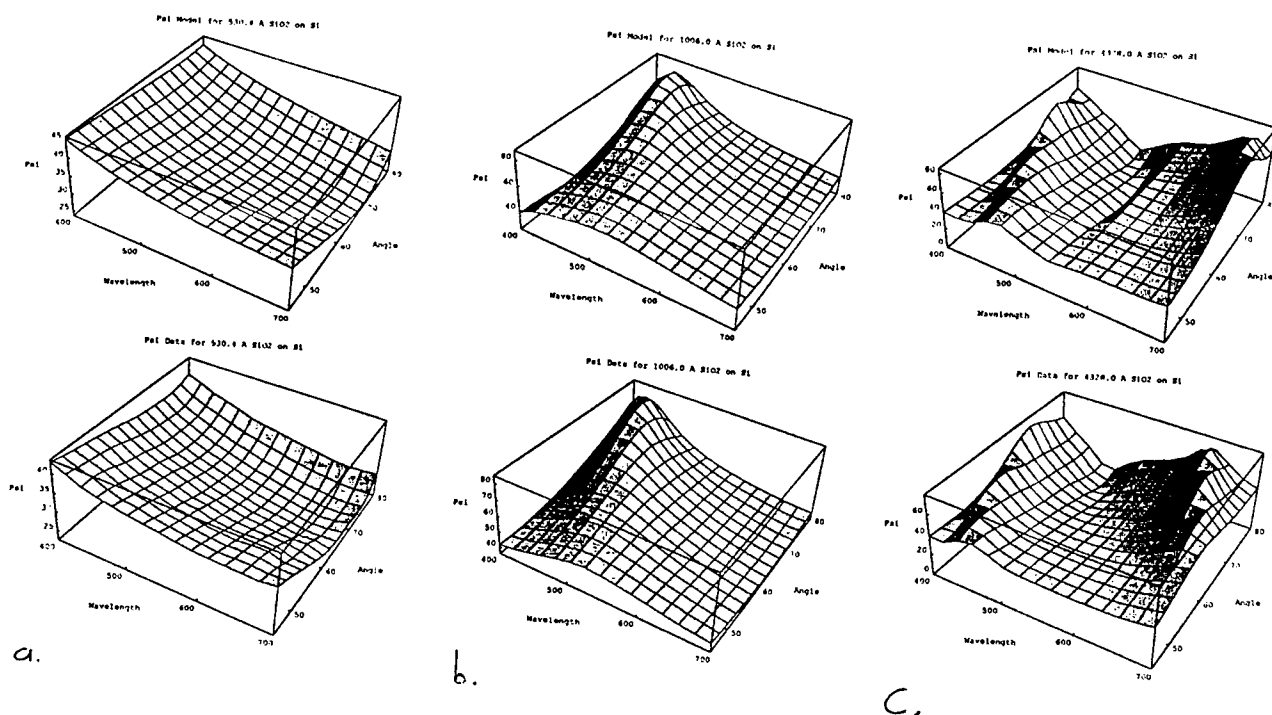


Figure 7. Psi vs. wavelength and angle for SiO_2 films of varying thickness: a) 530 Å, b) 1006 Å, c) 4328 Å on Si. The models are presented above the experimental data.

Poled Quartz Slide

Personnel at F. J. Seiler Lab have been examining quartz slides to attempt to understand a phenomenon in which these slides, once placed between two electrodes and poled with a high voltage will display non-linear optical properties. Several models exist for this behavior which depend either on bulk diffusion or surface effects. The cause of the effect is

believed to be located near one side of the sample based on etching studies. We examined one of these poled quartz samples using spectroscopic ellipsometry to attempt to find a change in the index of refraction between the two sides of the sample. The sample was placed on a thicker quartz substrate using an index matching fluid for the 632 nm wavelength index of quartz. Since data was taken at various wavelengths, this will lead to systematic errors in the actual values for n - but will still allow a comparison between the two sides of the slide.

The results are presented in Figure 8 and show no clear differences beyond the error range between the two sides of the sample. The solid lines represent 2nd order polynomial fits to the data. This suggests that the process responsible for the non-linear behavior does not involve production of a region with significantly different optical properties ($\Delta n = 0.005$).

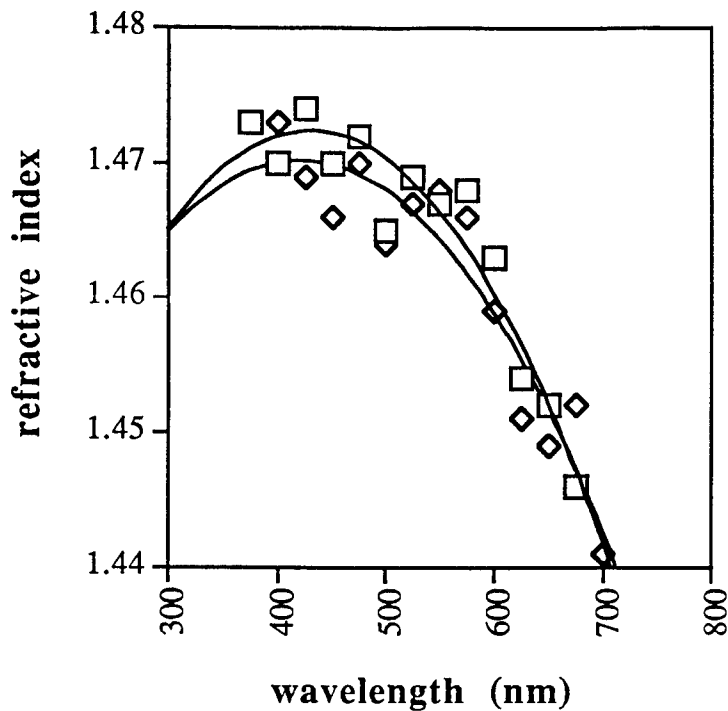


Figure 8. Variation in n for two sides of a poled quartz slide.

GeO_x Films Deposited by Laser Ablation

Previously we had examined some undoped GeO_x films produced by laser ablation at Seiler Labs. We examined films produced in various oxygen partial pressures and found that films produced in vacuum had a composition which varied from having a high Ge/O ratio near the center (and thus a higher index of refraction) to a more GeO₂-like composition (lower Ge/O ratio) near the edges.

Films deposited in 100 mTorr of oxygen show much smaller and more

random variations across the film. The values, however, are lower than the expected index for GeO or GeO₂ (around $n = 1.6$) suggesting that the films may be somewhat porous.

Since this time, Seiler Laboratory has revised the method in which they produce the films. They are now using an oxygen plasma during the laser ablation to attempt to better control the properties of the films. We examined a series of eight films grown under various oxygen pressures and temperatures. Unlike the films examined earlier, these were relatively uniform in optical properties. The results are presented in Table 1. The films grown at 200 and 400 C show somewhat lower indexes which may indicate that the films were somewhat porous. The film grown in 15 mTorr of Oxygen is the only one which was not transparent. It required a small k value of 0.006. This may indicate that it was not fully oxidized.

Oxygen pressure (mTorr)	Substrate deposition temperature (C)				
	0	100	200	300	400
15				1.588	
30	1.602	1.597	1.388	1.599	
50				1.584	1.519
100				1.589	

Table 1. Index of refraction for GeO_x films grown on Si substrates.

We also examined in detail the spatial variation of thickness and index of refraction on another sample which was GeO_x deposited onto a polished fused quartz substrate. The substrate was a disk approximately 25 mm in diameter and 6 mm thick. From waveguide experiments, the film was believed to have an index of refraction of approximately 1.57 - 1.58 at a wavelength of 457 nm and a thickness of 1.7 - 2 micrometers. We examined this sample using multiple angle of incidence spectroscopic ellipsometry to determine more exactly the optical properties and film thickness and their variation across the sample.

We began the study using a single wavelength (633 nm) and multiple angle of incidence. We examined a blank substrate to determine the effective optical properties to be used in examining the film-covered substrate. Since the substrate was transparent, we used an aperture to block the back surface reflection. We then calculated the effective optical properties using multiple angle ellipsometry. These were found to be $n = 1.426 \pm 0.014$ and $k = 0.039 \pm 0.04$. These values were used for the substrate of the film covered sample which was similarly mounted.

We next examined the film covered sample. A point at the center was chosen to perform a multiple angle analysis at 633 nm to determine the optical properties and thickness of the center of the film. This analysis involved measuring the ellipsometric parameters at 5 degree increments

between 45 and 80 degrees angle of incidence. The resulting data was fit with a standard single layer on substrate model with n , k , and thickness of the film as parameters. Three fits were found to be within experimental error. All had $k = 0$ as expected for a transparent film. The n values were 1.563, 1.573, and 1.588 (± 0.002) with corresponding thicknesses of 1760nm, 1980nm, and 2185nm (± 5 nm). These fits are shown in Figure 9 a and b for the parameters ψ and δ respectively. The best fit for both plots occurs for the case of $n = 1.588$.

Next we examined the spatial variation across the sample at a single wavelength and angle of incidence. We chose 60 degrees angle of incidence which appears to be near the Brewster angle for the film where ellipsometry is most sensitive [5] and 633 nm. We took data every 2 mm across the film.

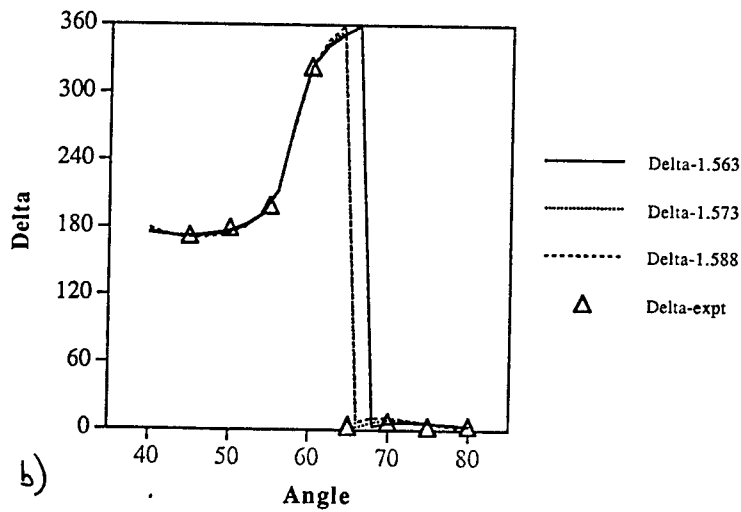
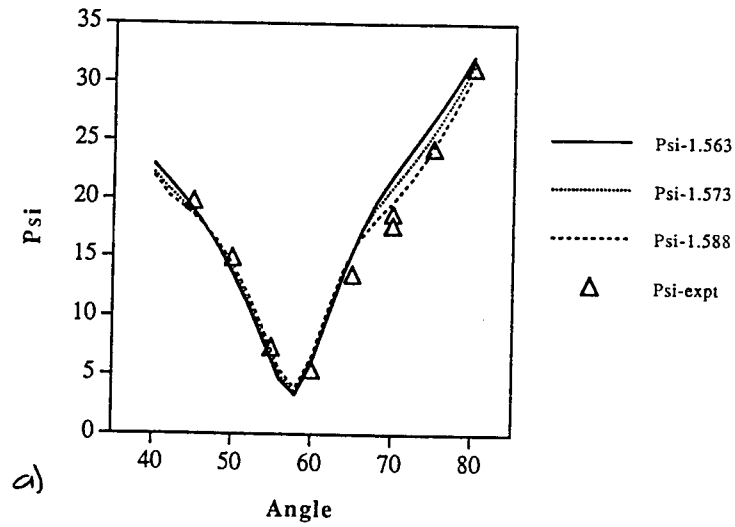


Figure 9. Ellipsometric parameters ψ (a) and Δ (b) at various angles of incidence and models for $n_{\text{film}} = 1.563, 1.573, \text{ and } 1.588$.

Thickness variations can be examined by considering the expected path a

sample with constant n but changing thickness would follow in Delta-Psi space. For transparent samples like these, this path will be closed and the values of ψ and δ will repeat themselves approximately every $\lambda/2$ change in film thickness. Figure 10 shows the data points and three curves, one for each of the three indices determined for the center point. If we assume, for the moment, that the index is constant across the film, then the best fit to the experimental data is the $n = 1.588$ curve. Since this was also the best fit to the Ψ data in Figure 9, we believe that a good average index for the film is 1.588.

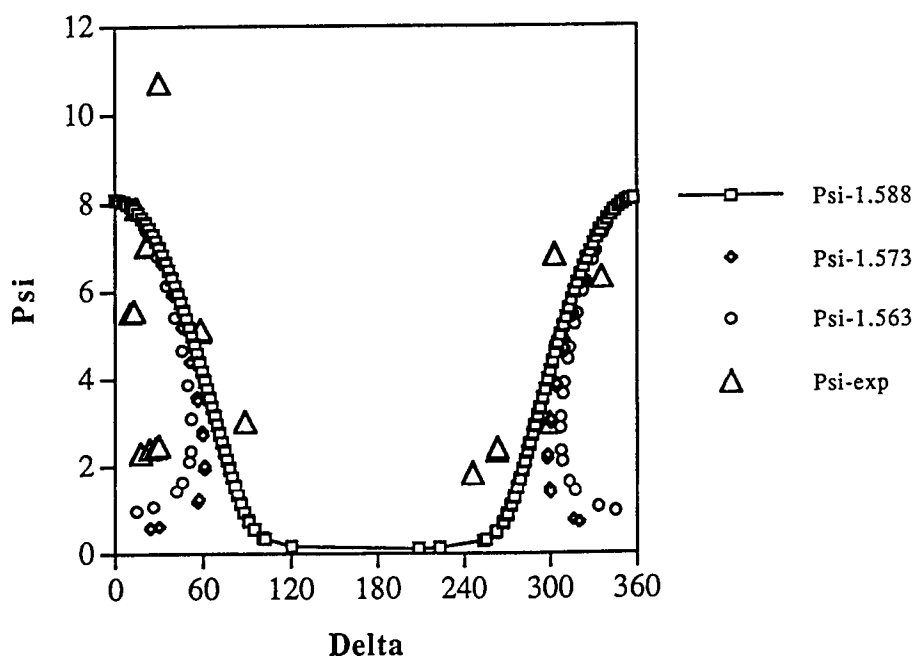


Figure 10. Experimental data and models in ψ - Δ space.

Spatial variation (x direction)

We can now examine the thickness variation across the film assuming a constant index of 1.588. Thickness increases as you go from right to left across the model curve in Figure 11. The data points are now labeled with their position (in mm) from one edge of the sample. If we start with the $x = 4$ mm position, we see a steady increase in thickness as we move to higher positions across the sample. After $x = 10$, we wrap back around on the right side to continue the progression on the next cycle of the curve. We know the center position ($x = 12.5$) is around 2185 nm, so we can determine which cycle of the curve we are on. The data points do not lie exactly on the curve which may indicate some variation in index across the sample. If we simply find the closest point on the curve to each data point we can determine the thickness variation across the sample. This data is presented in Figure 12. The data shows an almost linear variation across the sample from about 1930 nm to 2400 nm.

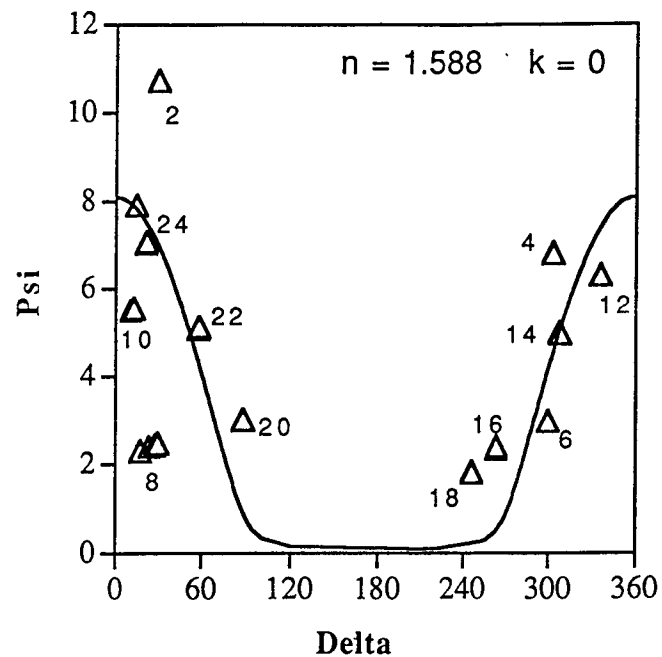


Figure 11. Variation in ψ and Δ with sample position in x-direction. Numbers indicate position from edge in mm.

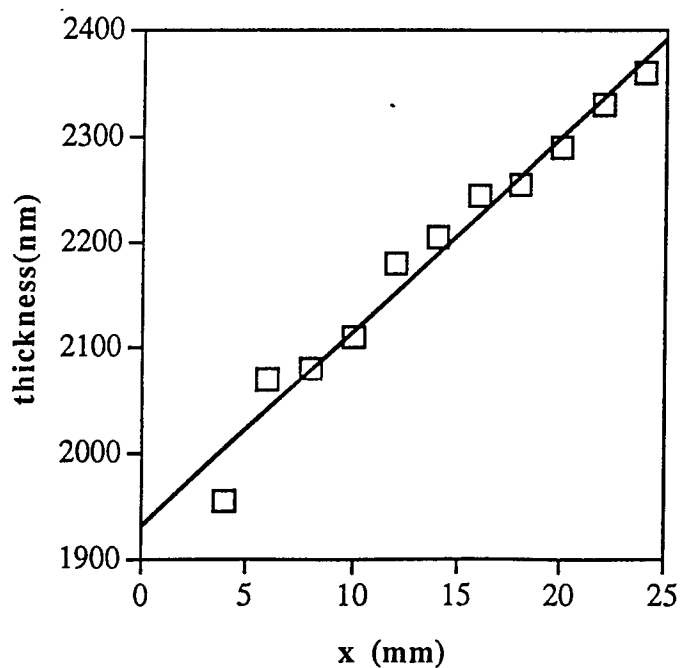


Figure 12. Film thickness variation across the sample in x direction.

Looking back, however, at Figure 11, we note that the data taken at positions on one side of the sample ($x = 6 - 10$ mm) tends to fall outside the curve which would correspond to a lower value of n . The data from positions on the other side ($x = 16 - 20$ mm) tends to fall inside the curve which suggests a higher value of n . Figure 13 shows a series of curves for different n values. From these we can, with some uncertainty, estimate the index of refraction at various points across the sample. A plot of index vs. x position on the sample is shown in Figure 14. The data appears to almost show a step function at the middle of the sample. We are reexamining this sample to see if these variations may have been caused by systematic errors introduced as we moved the sample stage.

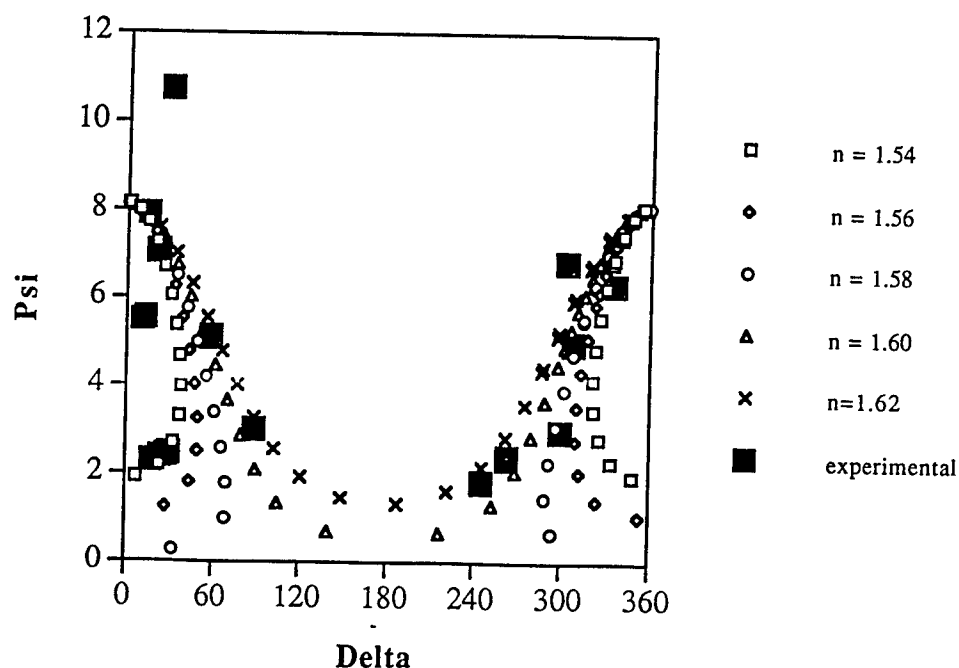


Figure 13. Experimental data compared to several models with different film refractive indexes.

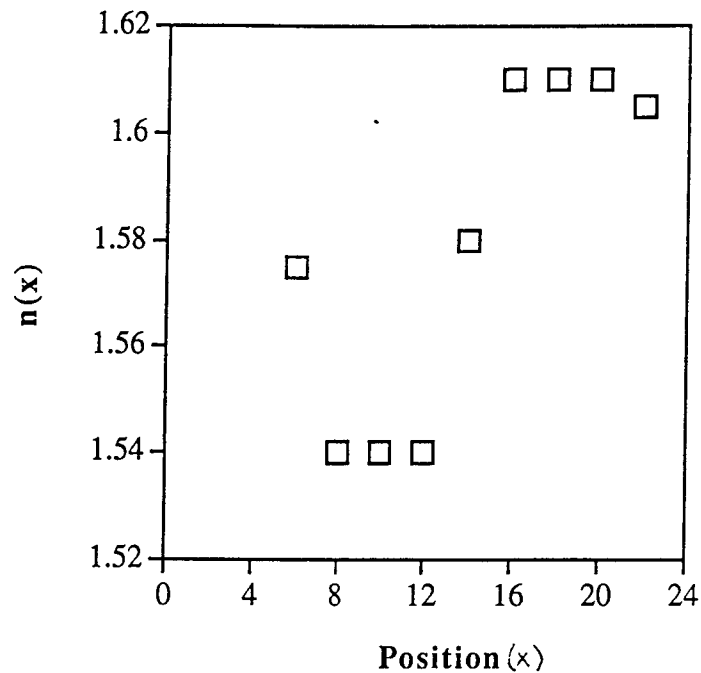


Figure 14. Variation of index of refraction with position across the sample in the x direction (mm).

Spatial variation (y direction - waveguide direction)

The sample was rotated 90 degrees about its normal to examine spatial variations in the other direction. This is the direction along which the waveguide experiments were performed. Again data was taken at 633nm wavelength and 60 degrees angle of incidence every 2 mm across the sample. The results, in delta-psi space are shown in Figure 15. The data is clearly much more clustered about a point on the $n = 1.588$ model curve indicating that the film is relatively uniform in thickness in this

direction. Figure 16 shows an enlargement of the region in delta-psi space which is of interest. The model curve has markers space every 5 nm starting in the lower right at 2055 nm and going up to 2115 nm in the upper left. With the exception of the point at the near edge ($y = 2\text{mm}$) all of the data lies within about 5 nm of an average value of 2095 nm.

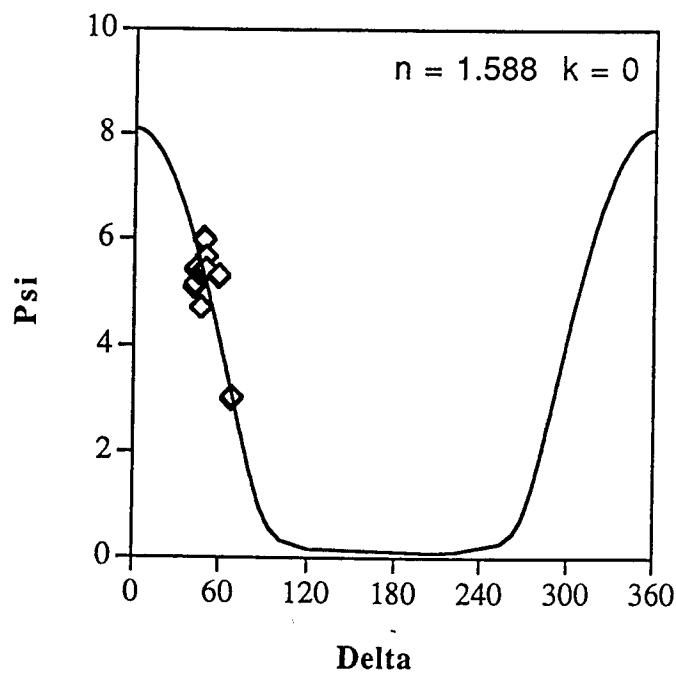


Figure 15. Variation in ψ and Δ with sample position in y-direction.

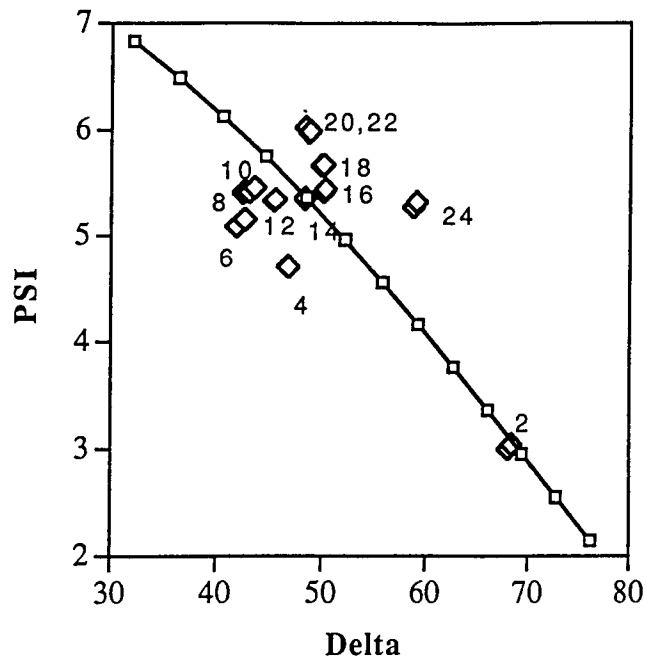


Figure 16. Enlargement of region from Figure 15. Numbers indicate the position from the edge of the sample in mm.

Again in Figure 16 we note a pattern to the data. The points for $y = 4 - 12$ mm tend to lie below the $n = 1.588$ curve. The points for $y = 16 - 24$ mm tend to lie above the curve. This suggests a variation in index of refraction across the sample in this direction as well. The data is plotted along with models for several indices of refraction in Figure 17. From this figure we can determine the index of refraction at each point across the sample. The variation of n with y position is shown in Figure 18. There appears to be a smooth variation in index from about 1.55 on one side of the sample to 1.61 on the other. We are examining this sample again to see

the sample to 1.61 on the other. We are examining this sample again to see whether these small changes in the ellipsometric parameters were caused by systematic error during sample translation or are real effects.

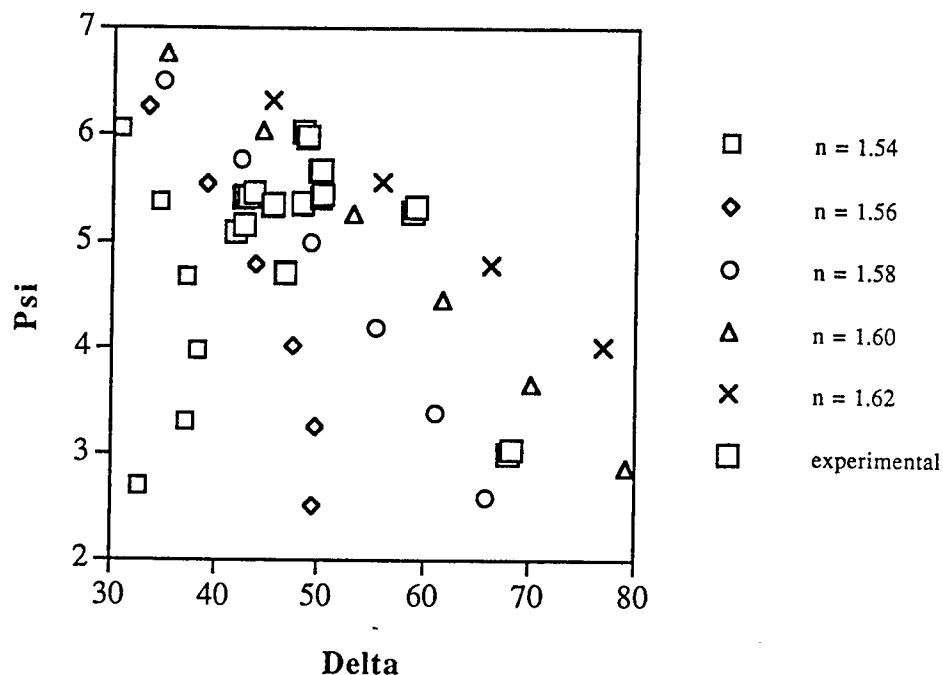


Figure 17. Experimental data compared to several models with different film refractive indexes.

Spectroscopic data from this sample revealed several shortcomings in our analysis software when the index of a film was unknown. We are presently revising this software to allow easier analysis of general spectroscopic data.

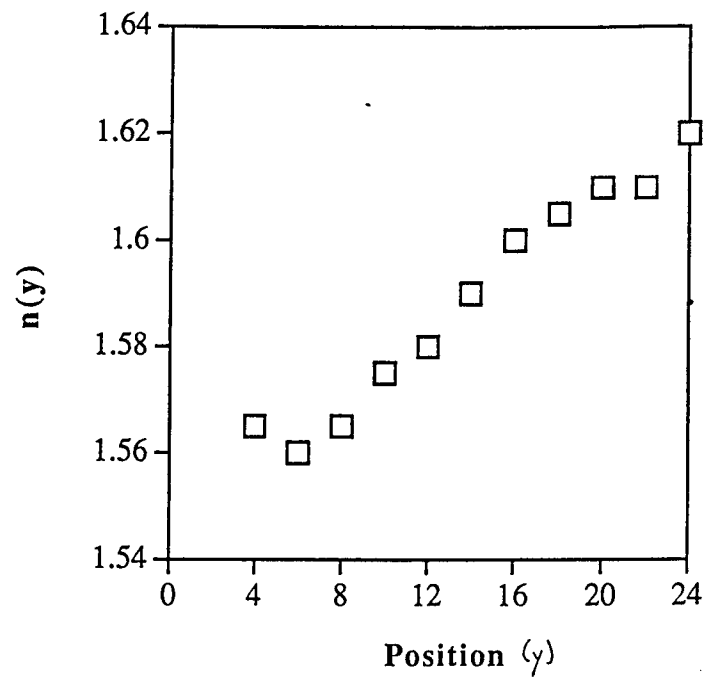


Figure 18. Variation of index of refraction with position across the sample in the y direction (mm).

References

1. U. Osterberg and W. Margulis "Dye laser pumped by Nd:YAG laser pulses frequency doubled in a glass optical fiber" Opt. Lett. 11, 516 (1986).
2. R. H. Stolen and H. W. K. Tom "Self-organized phase matched harmonic generation in optical fibers" Opt. Lett. 12, 585 (1987).
3. R. M. A. Azzam and N. M. Bashara, "Ellipsometry and Polarized Light" (North-Holland, Amsterdam, 1989).
4. A. Nussbaum and R. Phillips, "Contemporary Optics for Scientist and Engineers", (Prentice-Hall, Englewood Cliffs, NJ, 1976).
5. D. E. Aspnes in "Optical Properties of Solids: New Developments", B. O. Seraphin ed., (North-Holland, Amsterdam, 1976) p. 809.

ELECTROCHEMISTRY OF LITHIUM IN
ROOM TEMPERATURE MOLTEN SALT ELECTROLYTES

Bernard J. Piersma
Professor of Physical Chemistry
Department of Chemistry

Houghton College
Houghton, NY 14744

Final Report for:
Summer Research Extension Program

Sponsored by:
Air Force Office of Scientific Research
Bolling Air Force Base, Washington, D.C.

and

Houghton College

December 1993

ELECTROCHEMISTRY OF LITHIUM IN
ROOM TEMPERATURE MOLTEN SALT ELECTROLYTES

Bernard J. Piersma
Professor of Physical Chemistry
Department of Chemistry
Houghton College

Abstract

The demonstration of a stable reversible lithium anode is an important step in the development of practical secondary batteries using room temperature chloroaluminate melts as electrolytes. In this research extension program we have explored the conditions necessary for establishing stable redox behavior of lithium in buffered neutral EMIC-AlCl₃ melt. The role of protons in the reversible stripping of deposited lithium has been examined and a stable source for protons in the melt has been found. Nearly reversible deposition-stripping behavior of lithium is obtained when 0.2 M triethanolamine•hydrogen chloride is added to LiCl-buffered neutral melt, however stability of the lithium deposit remains a problem. In this study we have begun on investigation of Li-Al alloy as a means of improving electrode stability.

ELECTROCHEMISTRY OF LITHIUM IN
ROOM TEMPERATURE MOLTEN SALT ELECTROLYTES

Bernard J. Piersma

INTRODUCTION

Room temperature molten salts formed by mixing 1-ethyl-3-methylimidazolium chloride (EMIC) with aluminum chloride have been intensively studied, particularly by Wilkes and coworkers at FJSRL, for more than a decade with the goal of developing high energy density batteries. Alkali metals have high oxidation-reduction potentials and relatively low atomic masses making them very attractive candidates as battery anodes. Lithium is of particular interest because it has the highest electricity storage density of the active metals.

The Lewis acid-base behavior of these melts has a substantial influence on their physical and electrochemical properties. Melt acidity is easily ascertained electrochemically since Al deposition only occurs from acidic melts and the melt window is significantly greater in neutral melts than in either basic or acidic melts. Because of the wide electrochemical window it is desirable to work with a melt which is exactly neutral but, as with most acid-base systems, maintaining neutrality is not easily achieved unless the system is buffered. The use of sodium chloride to buffer the melt to neutral composition has been demonstrated by Wilkes, et.al.(1) More recently it was found that proton added to the melt as 1-ethyl-3-methylimidazolium hydrogen dichloride (EMIHCl_2) provides a more negative voltage window and nearly reversible deposition-stripping behavior of sodium when proper proton concentration is maintained.(2) During the 1992 Summer Research Project at FJSRL we studied lithium chloride-buffered neutral melts by first removing protonic impurity (resulting from contamination by H_2O during synthesis and purification of EMIC) with ethylaluminum dichloride. By adding proper amounts of EMIHCl_2 nearly reversible deposition-stripping behavior of lithium could be observed at tungsten electrodes.

While EMIHCl_2 is a proven proton source, its stability in the melt is limited with HCl being lost into the vapor phase relatively rapidly in an open

system. A major focus of this Summer Research Extension Program has been to develop a method for maintaining a stable proton concentration in the melt. We investigated many possible alternative proton sources and found triethanolamine•hydrogen chloride (TEOA•HCl) to be an effective source. TEOA•HCl is electrochemically stable within the melt window, except for proton reduction which is expected, and maintains a stable proton concentration in the neutral melt for times two orders of magnitude greater than that obtained with EMHCl₂. Proton enrichment of the melt with TEOA•HCl has been very successful in bringing a lithium chloride buffered melt to exactly neutral acidity which presents aluminum deposition and stripping and in extending the cathodic limit of the melt but has not provided the desired stability of deposited Li in the melt. We have made some attempts to understand the role of added protons (or HCl) in the observed electrochemistry of lithium in the melt. In addition we have initiated a study of LiAl alloys in these melts and this is being continued.

DISCUSSION OF PROBLEM

Lithium electrodes do not work very long as anodes in many organic solvents because of passivation.(3) Yeager, et.al. have stated that small amounts of atmospheric contaminants such as oxygen and water that unavoidably remain in nonaqueous solvent systems exert a profound influence on the electrochemical behavior of lithium.(4) They found that a film comprised of at least two components, lithium superoxide/peroxide (LiO₂ or Li₂O₂) and LiOH layers is present when lithium is deposited on a noble metal electrode. Electrodes in similar systems but not containing lithium salts were not passivated showing that the blocking film was, in fact, formed by lithium compounds.

Zavadil and Armstrong have studied the surface chemical and electrochemical properties of thin films formed in the gas phase on atomically clean lithium surfaces.(5) Exposure of clean Li to oxygen in the 10⁻⁵-10⁻⁶ torr range of partial pressures produces a Li₂O film on the order of 50Å in 3 - 5 minutes. At 10⁻⁵ torr oxygen the buildup of oxide was found to be 600 monolayers in 300

seconds. Reaction of a clean Li surface with H_2O produced a mixture of oxide and hydroxide at low H_2O exposure levels. The initial reaction was found from spectral data to involve complete dissociation on the Li surface to form Li_2O with probable evolution of H_2 . After the first monolayer formed, hydroxide also formed and with sufficiently high H_2O exposure, the $LiOH$ was the predominate surface species. Zavadil and Armstrong also found that Li_2O was not a good passivating layer.

Exposure of a clean Li surface to acetonitrile (CH_3CN) resulted in formation of a CN^- product and a lithium hydrocarbon complex (CHx). (5) Oxidation of the Li surface by O_2 or H_2O has a passivating effect which reduces corrosion. They conclude: Differences in electrochemical behavior of lithium films is most noticeable for applied current densities of about m/cm^2 . At low current densities, it is apparent that the surface layer, regardless of composition, has little effect on the migration of the lithium ion during discharge. At high current densities the act of passage of a high flux of lithium ion through the overlayer undoubtedly has the effect of structurally changing this layer and making lithium transport more facile."

Reaction with H_2O has a less passivating effect on the Li electrode than prereaction with O_2 and H_2O prereacted electrodes produce higher exchange currents densities for discharge. The higher electrochemical activity of the H_2O prereacted surfaces (as compared with O_2 treated surfaces) is consistent with the notion that the oxide/hydroxide surface layer formed from H_2O exposures is more permeable to both Li^+ and Li^0 than the surface layer formed from O_2 exposures. (5) In a study to determine the influence of H_2O on cycling efficiency of Li in $LiClO_4/2$ -methyltetrahydrofuran and $LiI/2$ -methyltetrahydrofuran solutions, Hefer, et.al., found a positive effect for water up to 200-300 ppm on the efficiency for LiI but not for $LiClO_4$. (6) For $LiClO_4$ the average cycling efficiency was about 81% with no H_2O added, decreasing to about 60% with 500 ppm H_2O content. No explanation was offered for the observed differences in behavior. The improved

cycling efficiency with LiI was presumed to be the formation of a protective film. Hefer, et.al., also reported improvement in cycling efficiencies to greater than 90% were achieved when lithium hexafluoroarsenate (LiAsF_6) was added to the LiClO_4 solutions. The improved cycling properties of Li in LiAsF_6 solutions is attributed to the formation of a protective film.

From comparative studies for Li deposited on W electrodes, Perichon, et.al., found that cycling efficiencies increased in the order $1/2 \text{ LiAlCl}_4/\text{SO}_2\text{Cl}_2 < 1/1 \text{ LiAlCl}_4/\text{SO}_2\text{Cl}_2 < 1/3 \text{ LiAlCl}_4/\text{SO}_2$. (7) In $1/1 \text{ LiAlCl}_4/\text{SO}_2\text{Cl}_2$ solution the Li cycling efficiency was about 90% at low plating charge and decreased slightly with increasing plating charge. For $1/3 \text{ LiAlCl}_4/\text{SO}_2$, the cycling efficiency was about 92% at low plating charge and increased to nearly 100% at higher plating charge. The deposited lithium is presumed to be protected by a passivating film formed by reaction of Li with the solvent. Perichon, et.al., discussed the kinetics of reactivity of the electrodeposited Li with solvent assuming zero order kinetics, with the dissolution rate being constant. The dissolution of Li in the $1/3 \text{ LiAlCl}_4/\text{SO}_2$ was relatively slow process with a decrease in cyclic efficiency from about 95% to 50% after approximately 60 hours, and appeared to follow the assumed zero order kinetics. Their results indicate that about 20% of the deposited Li remained on the surface after 120 hours at open circuit. (7)

Odziemkowski and Irish have stated that even in the best equipped argon atmosphere dry boxes a clean Li metal surface is covered very rapidly with more than a monolayer of Li_2O film. (8) "A clean lithium surface cannot be achieved by electrochemical methods because the passive layer, which acts as a solid electrolyte interface (SEI) or a polymer electrolyte interface, is unique compared to passive films formed on other nonalkali metals. Anodic stripping cannot work efficiently because SEI-controlled diffusion takes place by lithium cation transport through such films." They suggest that cathodic deposition would be more promising if reduction by the solvent could be eliminated. Thus they have developed an in situ method for cutting Li metal electrodes to provide new and hence clean surfaces. The open circuit potential of clean Li surfaces

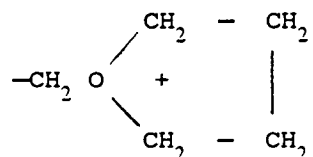
decay very rapidly (times on the order of 0.1 to 1 sec) in the several electrolyte systems studied indicating a high rate of passivation. They conclude that films formed on lithium surfaces are formed in most cases by electrochemical reduction of the electrolyte anions confirming the suggestion made previously by Campbell, et.al.(9)

Extending their study to unpurified solvents, Odziemkowski and Irich found that even in unpurified electrolytes for which water content exceeds 300 ppm, a major reaction of the clean Li metal is anion reduction.(10) They conclude that the behavior of lithium/surface film/electrolyte interphase is determined by two factors:

1. The transport of lithium cations through a surface film which controls the anodic part of the process and
2. The transport of oxidizing agents into the interphase where they encounter electrons and are reduced, controlling the cathodic reaction at the interface.

They suggest that equilibrium between these two processes is established within a few seconds after a clean Li surface is exposed. Using scanning electron microscopy they observed a thick, porous dark-brown film on clean Li surfaces undergoing anodic dissolution in purified LiAsF_6 / THF solution.

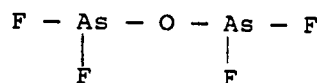
The passivating film and the brown film formed on clean Li surfaces was studied by Irish, et.al. using a Raman microprobe.(11) They concluded that the passivating film which protects the Li surface is a polymer formed from the tetrahydrofuran (THF) and initiated by the Lewis acid AsF_5 . The propagating species is thought to be the tertiary oxonium ion



and the counter ion is AsF_6^- . The initiating catalyst is formed e.g., by the reaction $\text{LiAsF}_6 \rightleftharpoons \text{LiF} + \text{AsF}_5$ and only very small amounts of the AsF_5 are required for the polymerization. Very small amounts of H_2O were found to

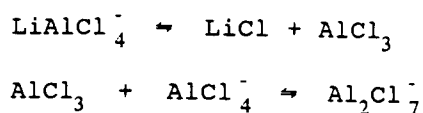
terminate chain growth. For this acid-base catalyzed polymerization the ratio of impurity concentration to catalyst concentration (C_{imp}/C_{cat}) governs the reaction. When the ratio C_{im}/C_{cat} is sufficiently large the polymerization of THF is terminated. Species like H_2O and O_2 are the effective impurities.

The brown film is an inorganic (brown) substance formed in the absence of the polymeric protective film. Analysis of decomposition products of the brown film indicate a structure composed of As_2O_3 and LiF with the probable structure



and not necessarily polymeric. (11)

Applying the conclusions of Irish, et.al. for Li in solutions of $LiAsF_6$ in THF by analogy to our studies of Li in the $LiCl$ -buffered EMIC/ $AlCl_3$ melts we can expect that a protective film is formed on Li by polymerization of EMI^+ with $AlCl_4^-$ as the counter ion. The Lewis acid catalyst then might be $Al_2Cl_7^-$ resulting from



In light of the experimental observations in the EMIC/ $AlCl_3$ systems with Li showing the importance of proton for reversible deposition-stripping behavior, the polymer initiating catalyst may likely involve some form of HCl . No similar analogy appears to exist for the brown film formed on Li in the EMIC/ $AlCl_3$ melt since there is no apparent source of arsenic compounds. We have consistently observed that the brown film is not formed on deposited Li when the proton concentration in the melt is maintained to yield essentially reversible deposition-stripping behavior or approximately 100% cycling efficiency. This clearly indicates that proton (or HCl) in our system is important in formation of the protective (polymer) film on Li and the brown non-protective film.

In an attempt to improve the stability of Li anodes in various battery electrolytes, several research groups have studied electrochemically prepared Li-Al alloys. Biallozor and Lieder have studied the formation and

electrochemical properties of Li-Al alloy in γ -butyrolactone solutions with several lithium salts or electrolytes.(12) They were able to confirm with x-ray studies that Li atoms intercalate the Al lattice to form β -Al-Li alloy. They obtained the best results for Li cycling efficiency with LiAsF_6 electrolyte, which was about 70% and remained unchanged after 25 cycles. Using other electrolytes like LiClO_4 , LiCl and LiBF_4 resulted in formation of passivating layers with greatly decreased cycling efficiency.

Fung and Chau have recently reported a study of LiAl alloy formed by electrodeposition from EMIC-AlCl_3 / LiAlCl_4 melts with a remarkable cycling efficiency of over 90% after 350 cycles.(13) Their success is apparently the result of first reacting LiCl with AlCl_3 to form LiAlCl_4 before it is added to a 1/1 EMIC-AlCl_3 melt. In this way they claim to be able to dissolve up to 1.59 moles of LiAlCl_4 per mole of the neutral $\text{EMIC} - \text{AlCl}_3$ melt. This results in a significantly higher concentration of Li^+ in the melt than can be obtained by adding LiCl to an acidic melt, the technique that we have employed. They further report no apparent reaction of the Li-Al alloy with the melt and essentially reversible deposition and dissolution of Li at the Al electrode.(13) We have not been able to confirm these results and they are not consistent with what we have done with Li in these melts up to this point. This approach is receiving priority in our continuing work on this project.

The use of Li-Al alloys appears to be a very promising direction for the development of practical lithium electrodes. Kumagai, et.al. has reported good success in electrochemical formation of Li-Al alloy in 1 M LiClO_4 in propylene carbonate solution.(14) They obtained cycling efficiencies of close to 90% for over 100 cycles. Aluminum proved to be a much better substrate than several other metals examined. In a following study Kumagai, et.al. determined the diffusion coefficient of Li into the β -Li-Al layer to be on the order of $10^{-10} \text{ cm}^2 \text{ sec}^{-1}$.(15) In this work the formation of a passivation layer on the surface of the alloy was mentioned and LiCl was suggested as one possible source. Kumagai, et.al., indicates that the passivating layer thickness increased with

time at open circuit but was apparently disrupted with application of a current pulse and a constant potential.(15)

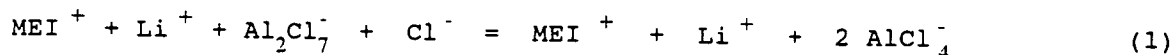
METHODOLOGY

All experimental work was performed with materials and electrochemical cell contained a Vacuum Atmospheres dry box system with a helium atmosphere. Electrochemical measurements were accomplished with an EG and G Princeton Applied Research (PAR) Model 263 Potentiostat/Galvanostat interfaced with an IBM 486 personal computer using EG and G PAR 270 software and a Hewlett Packard plotter model HP 7475A. A three-electrode arrangement in a single compartment cell used a molybdenum foil counter electrode and Bioanalytical System (BAS) working electrodes of platinum, tungsten, or glassy carbon. Most of the work reported here was obtained with tungsten working electrodes. The reference electrode was an Al wire in 0.60 EMIC/ AlCl_3 melt contained in a pyrex glass tube constructed with an asbestos tip to provide solution contact.

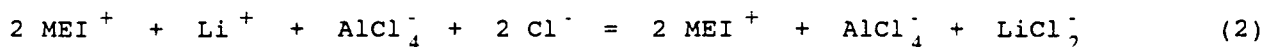
Components for the melt were synthesized and purified following the procedures developed by Wilkes and coworkers at FJSRL.(1,16) LiCl was dried for a minimum of 10 days in a vacuum oven at 130°C . The many compounds tested for improving proton stability in the melts were used as obtained from Johnson-Matthey or Aldrich. These included in addition to the triethanolamine•hydrogen chloride, a number of mono -, di - and tri - substituted amine•hydrogen chlorides, LiH and LiAlH_4 . In general the purity of melt components and additives were tested by preparing exactly neutral melts and observing the melt window using cyclic voltammetry.

BUFFERED NEUTRAL MELTS

We expected that the composition of buffered-neutral melts might vary depending on the initial melt acidity. Buffering with LiCl starting from an acidic melt should follow the reaction

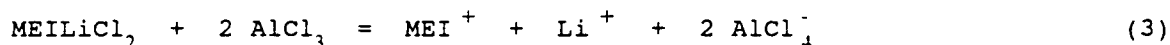


From a basic melt the reaction should be

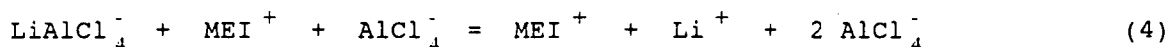


An acidic melt (0.55 mole fraction of AlCl_3) was prepared by adding the amount of AlCl_3 calculated to give the desired composition to an exactly neutral melt which had been treated with ethylaluminum dichloride. Then LiCl was added (with a calculated 25% excess) to buffer the melt back to neutral (eq. 1). LiCl was found to dissolve much more slowly than NaCl , requiring several days with occasional heating to 50°C for attainment of a neutral melt. Neutrality of this melt was demonstrated by the absence of Al deposition and stripping during a cyclic voltammetric scan. In a slightly acidic melt Al deposition could be observed at a cathodic potential approximately one volt more negative than in 0.55 melt. This Al deposition and stripping could be observed in buffered melts even after several days (up to 5 days) of stirring with LiCl in the melt. As with NaCl , LiCl was found to be insoluble in basic melt and all attempts to buffer a melt to neutral from the basic side with LiCl were unsuccessful.

Some other possibilities for preparing a buffered-neutral melt were explored according to the following reactions:



and



Following reaction (3), equimolar amounts of MEICl_2 and LiCl were mixed and heated. Formation of a clear colorless melt required heating to about 125°C . This melt was extremely viscous and exhibited a considerable range (approximately 50 degrees) of superheating and supercooling. On cooling the melt solidified as a clear colorless glass at about 70°C . With repeated careful heating and cooling cycles, crystallization was induced and a white crystalline solid (assumed to be MEILiCl_2) was recovered. Crystals suitable for x-ray analysis could not be obtained from this sample. When AlCl_3 was mixed with this solid in a 2:1 molar ration, a clear colorless melt was readily formed. Adequate proportions of the melt were not prepared for electrochemical studies but a sample was retained for

NMR studies. This method of preparing a Li-containing neutral melt merits further attention.

Following the outline of reaction (4), solid LiAlCl_4 (Johnson-Matthey) was added to an exactly neutral melt in equimolar proportions. After prolonged stirring most of the solid had not dissolved in the melt. This method for preparing a Li-containing neutral melt does not appear to be fruitful.

RESULTS AND DISCUSSION

After MEIC of acceptable purity had been obtained as in Fig. 1 a LiCl buffered melt was prepared as described above. The buffered melt remained slightly acidic even after seven days of stirring with excess LiCl, similar to the observed behavior of NaCl buffered melts reported by Riechel and Wilkes.(17) The acidity of the buffered melt was demonstrated by the deposition and stripping of Al as seen in Fig. 2. All of the cyclic voltammograms presented in this report were recorded at a sweep rate of 100 mV/sec using a W working electrode. Al deposition occurs at about -0.90 V and stripping at about -0.191 V (depending on melt acidity). The potential for Al deposition in this melt is more cathodic than the potential for the same process in more acidic melts by almost one volt. The Al stripping in this melt occurred at a potential that reported for a corresponding NaCl buffered melt having an AlCl_3 mole fraction of 0.5002,(17) suggesting that the LiCl buffered melt has a composition between 0.501 and exactly neutral. The deposition of Li at -1.6 V, (Fig. 2) significantly changes the Al stripping behavior as discussed in our 1992 Summer Research Program Final Report.

STABLE PROTON SOURCE

The effects of adding protons via EMIHCl_2 to the LiCl-buffered neutral melt on Li deposition-stripping behavior and the relatively rapid loss of proton from the melt were documented in our 1992 Summer Final Report. In the search for a stable proton source three criteria were used:

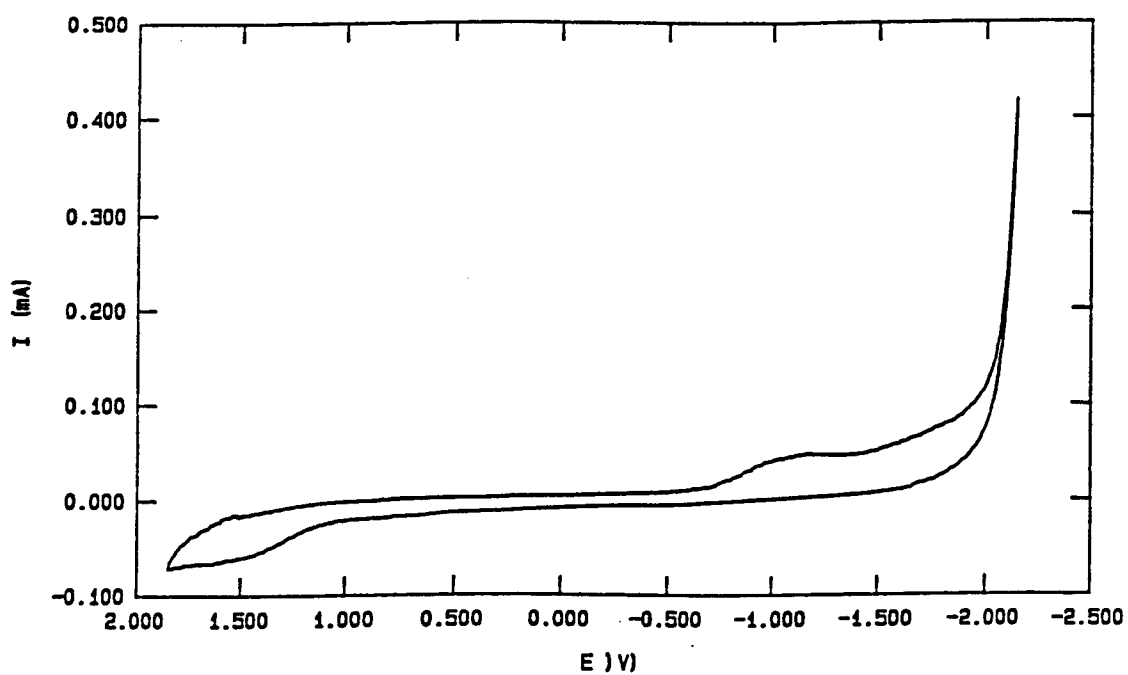


FIG 1

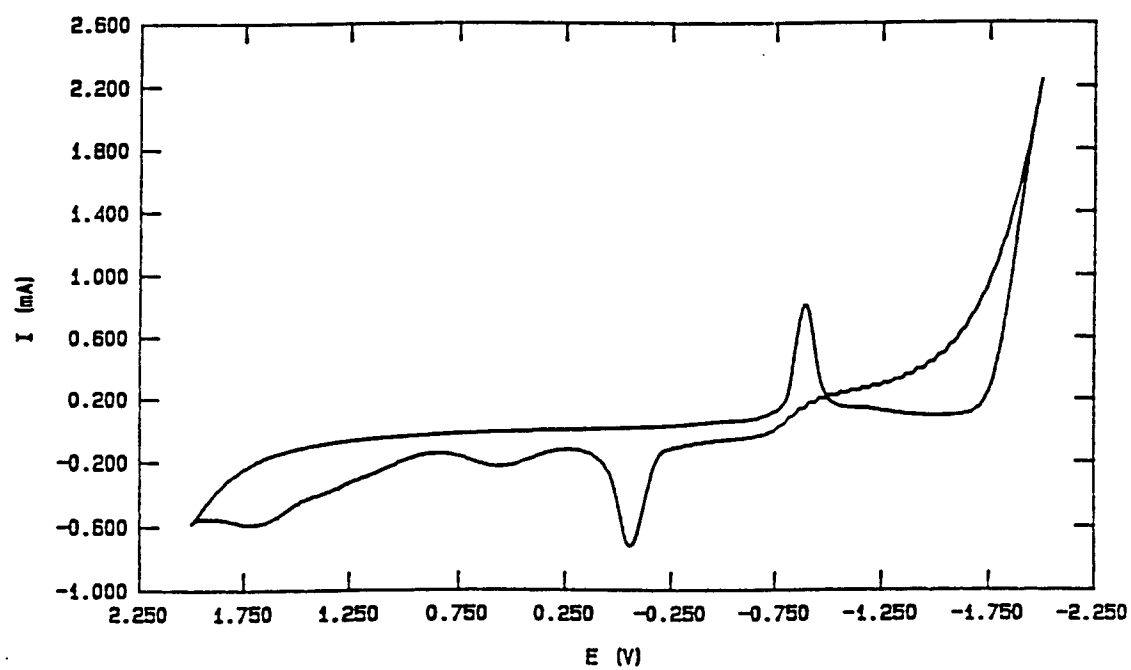


FIG 2

1) the electrochemical stability of the proton source compared within the electrochemical window of the melt, except for the desired proton reduction, as demonstrated in Fig. 3 for a neutral melt with added triethanolamine·hydrogen chloride (TEOA·HCl).

2) essentially reversible deposition-stripping behavior of lithium (nearly 100% cycling efficiency) which is reproducible without cleaning the electrode, as seen e.g., in Fig 4 which displays the CV behavior after 5 cycles.

3) relatively constant proton content of the melt over a period of several days (as determined by criteria 1 and 2).

Of the ten compounds selected and tested as potential proton sources, only triethanolamine·hydrogen chloride satisfied our three criteria.

As background for our discussion, Fig. 5 shows CV behavior, at a W working electrode, for an exactly neutral melt and for LiCl-buffered neutral melt. Fig. 5a represents typical CV behavior in a neutral melt showing the melt limits with a window of about 4.0 volts and no Al deposition or stripping. Behavior in a LiCl-buffered melt which is near to but not exactly neutral is shown in curves b-e with cathodic sweep limits respectively of -2.20 V, -2.50 V, -1.80 V and -2.70 V. Al deposition is clearly evident at about -1.0 V but the stripping, clearly seen in curve b at about 0.0V is significantly altered by Li deposition which occurs at about -1.7 V.

To explore the possibility that added proton may be reacting with lithium ion in the melt we added LiH and LiAlH_4 to LiCl-buffered melts. Fig. 6 is for 0.1 M LiH and the cathodic sweep limits are respectively for a-e: -1.00 V, -1.50 V, -1.70 V, -2.20 V and -2.50 V. The cathodic and anodic peaks prominent in curves (a) and (b) are due to Al deposition and stripping characteristic of a slightly acidic melt. The Al stripping peak decreases in (c) as Li deposition begins and is not evident in curves (d) and (e) where Li deposition is greater with increasing cathodic sweep limits. The curves of Fig. 6 demonstrate that LiH does not have any influence on melt acidity as expected, and has essentially no electrochemical activity. Fig. 7 shows similar results for 0.1 M LiAlH_4 added

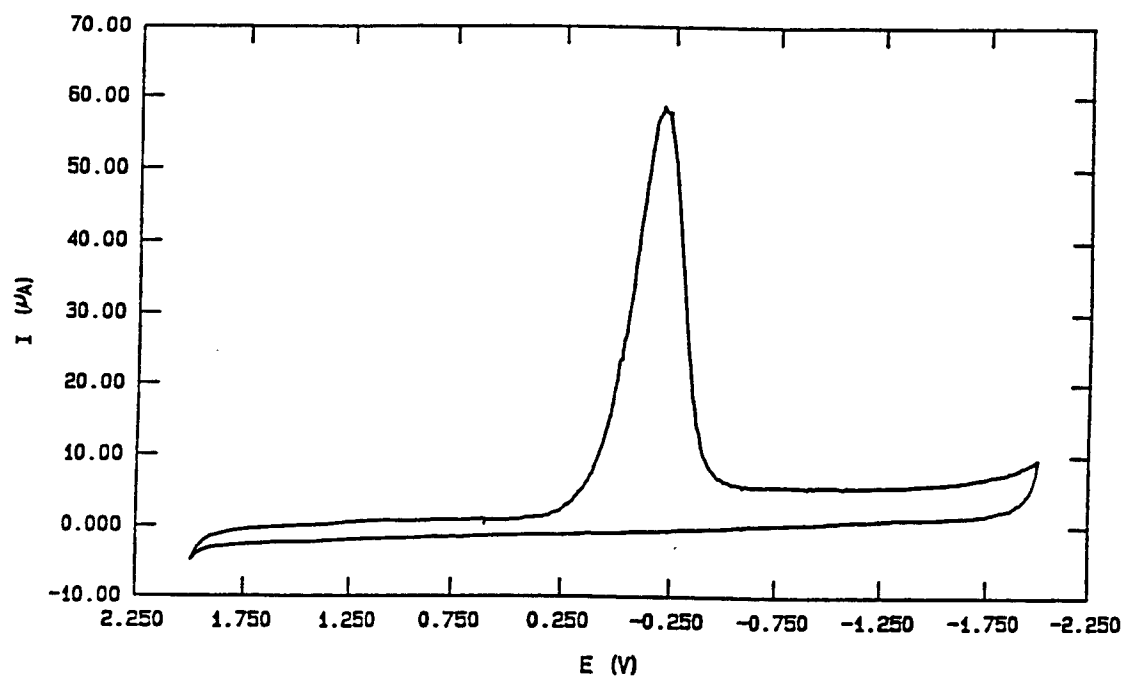


FIG 3

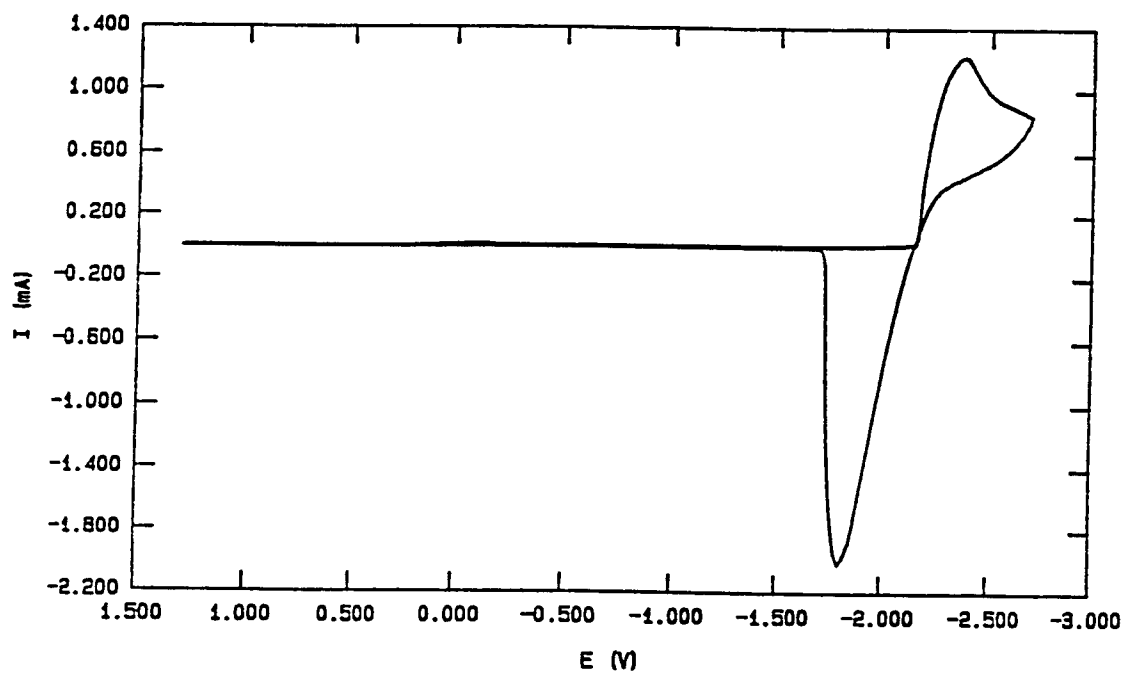


FIG 4

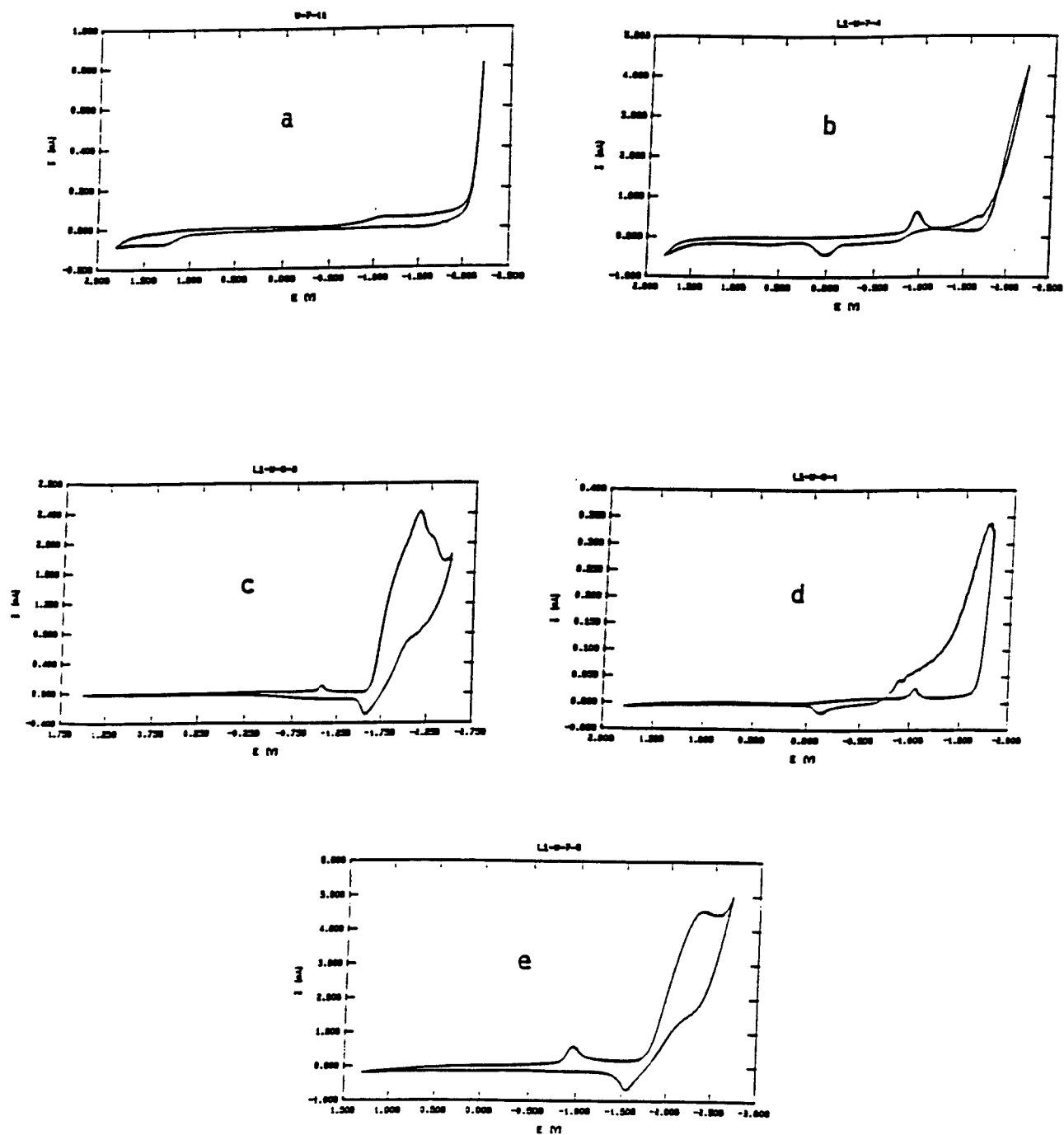


FIG 5

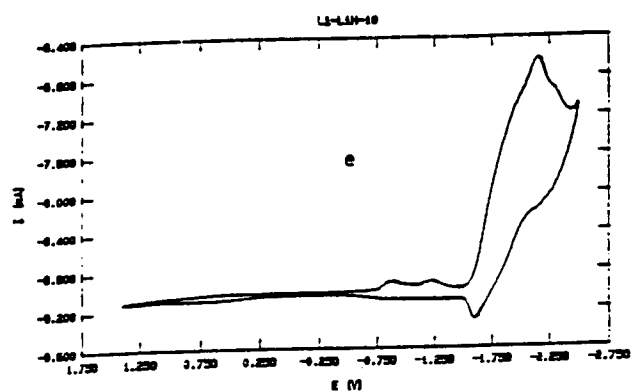
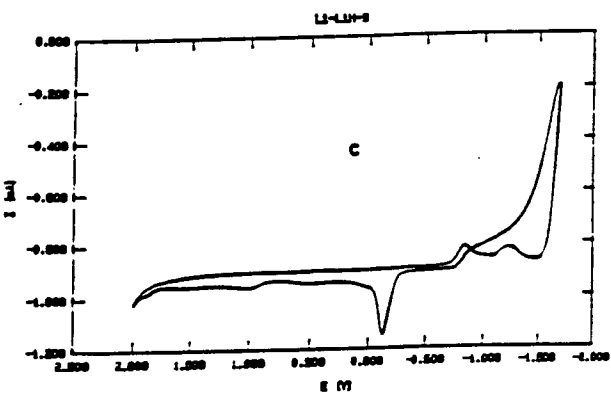
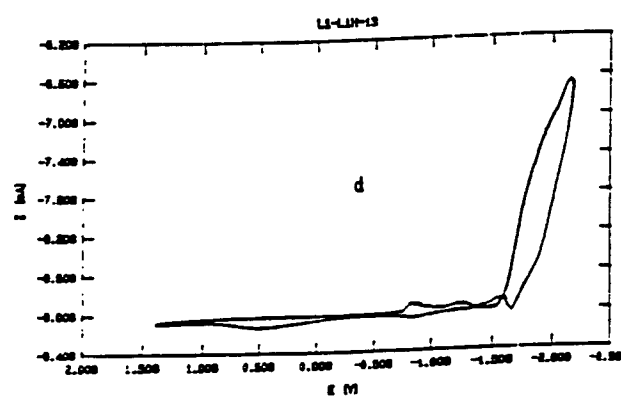
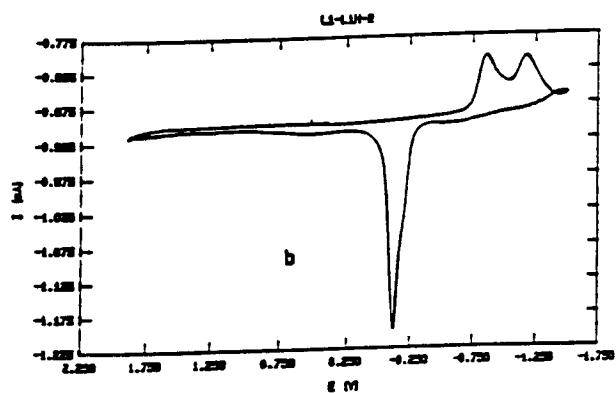
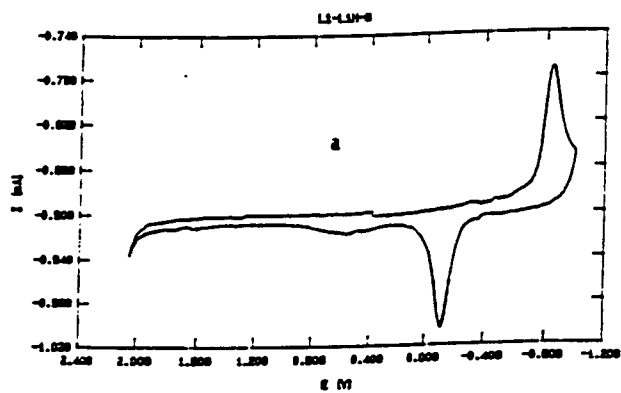


FIG 6

to LiCl-buffered melt. The cathodic sweep limits are for a-c respectively: -2.2 V, -2.3 V, and -2.5 V. The second cathodic peak observed beginning at about -1.3 V was also observed as a much smaller peak with LiH, but not seen in any other systems studied. We have not determined whether this is an impurity peak, which is considered rather unlikely, or perhaps a Li-Al alloy deposition peak since it occurs approximately half-way between Al deposition and Li deposition. In future work we will examine this peak more closely.

Figures 8 and 9 give CV behavior typical for most of the compounds which were studied as possible proton sources. Fig. 8 shows results for (a) 0.2 M trimethylamine·hydrogen chloride and (b) 0.2 M ethylamine·hydrogen chloride added to LiCl-buffered melt. No proton reduction peak is observed in the expected potential range, some Al deposition and stripping is seen indicating that the melt is still slightly acidic and Li deposition begins at about 01.6 V with no stripping. Fig. 9 for 0.2 M diethylamine·hydrogen chloride added to LiCl-buffered melt with cathodic sweep limits of (a) -1.8 V and (b) -2.5 V shows the system apparently closer to exactly neutral, but no proton reduction and no Li stripping are observed.

Figures 10-13 present representative CV data for the addition of triethanolamine·hydrogen chloride to LiCl-buffered melt. Fig. 10 is for 0.10 M TEOA·HCl with (a) clearly showing the proton reduction peak and the anodic melt limit and (b) showing the deposition of Li but very little stripping. The cathodic sweep limits are -1.6 V for (a) and -2.5 V for (b). Figs. 11 and 12 are for 0.20 M TEOA·HCl added to LiCl buffered melt showing essentially reversible deposition-stripping behavior for Li as a function of cathodic sweep limit. Fig. 11 a-d are for cathodic limits respectively of: -2.15 V, -2.20 V, -2.30 V, and -2.40 V. Fig 12, a-d are for cathodic limits respectively of: 02.50 V, -2.60 V, -2.70 V, and -2.80 V. This series of CV curves shows clearly that when the proton concentration is maintained at the proper level (in this case 0.20 M) the Li deposition-stripping behavior or cycle efficiency is not dependent on the cathodic sweep limit. We also note that no Al deposition is observed indicating

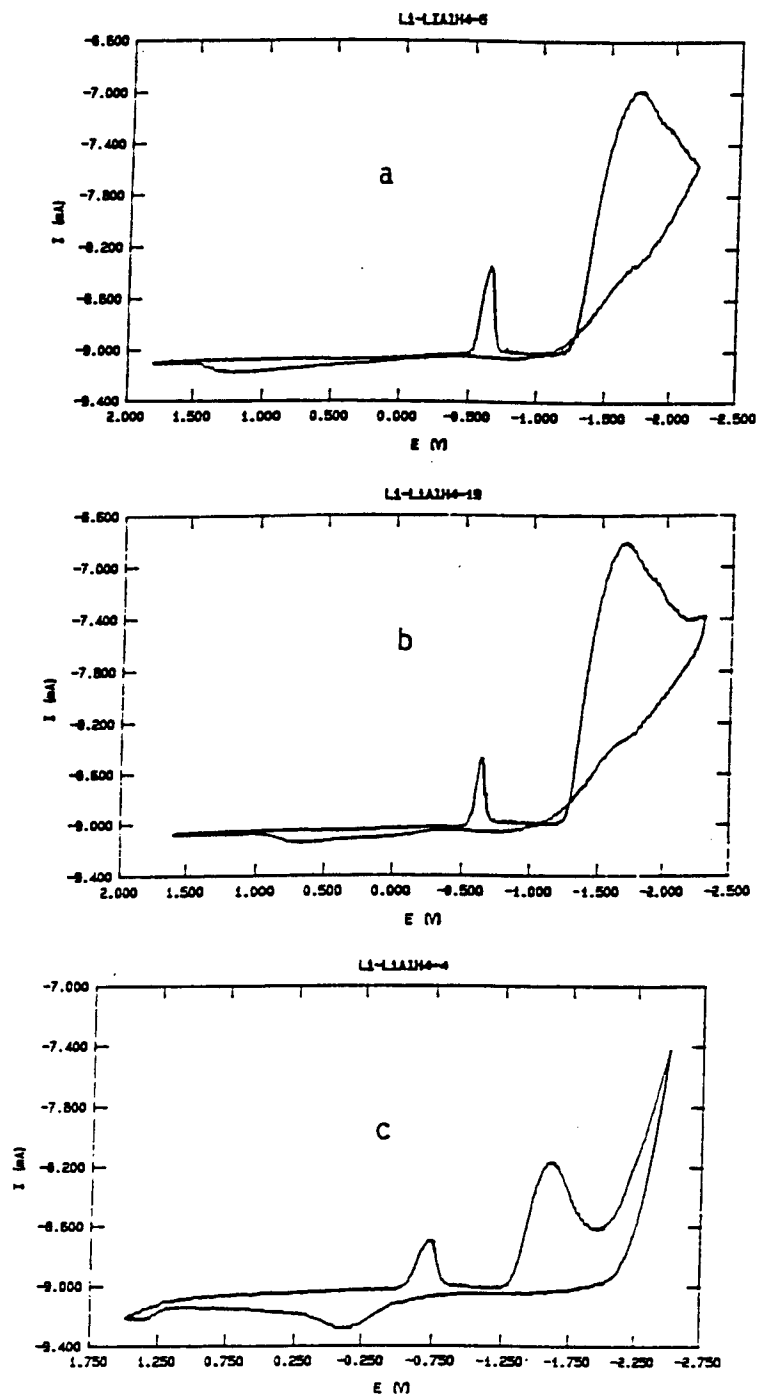


FIG 7

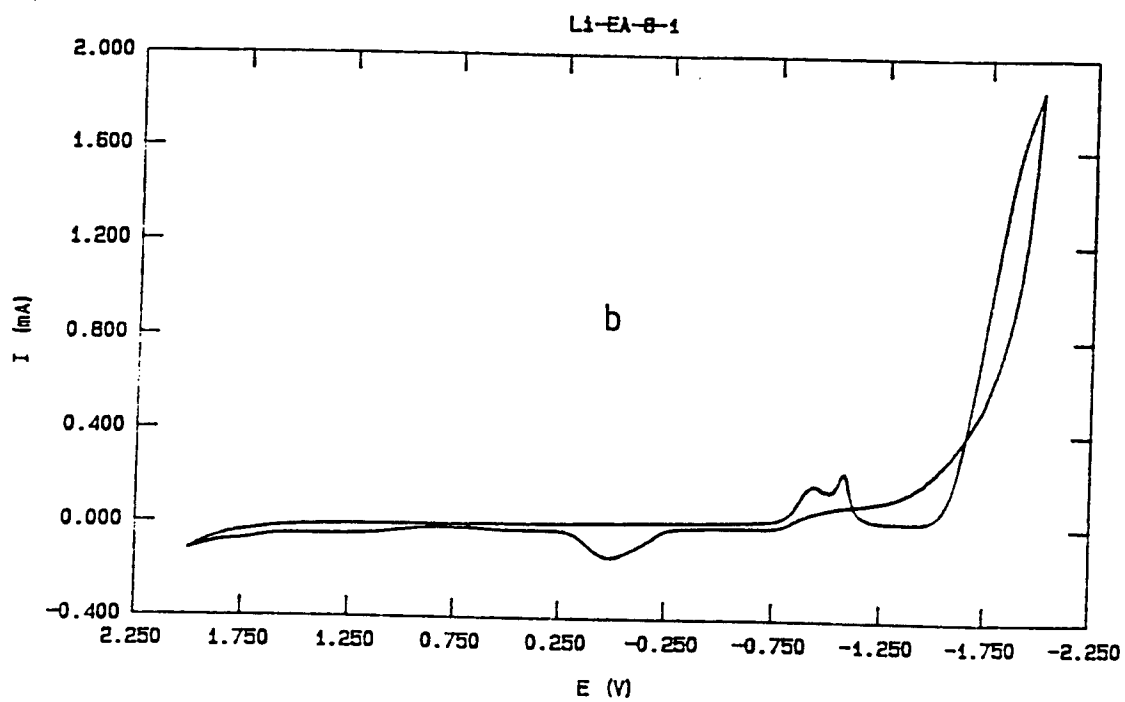
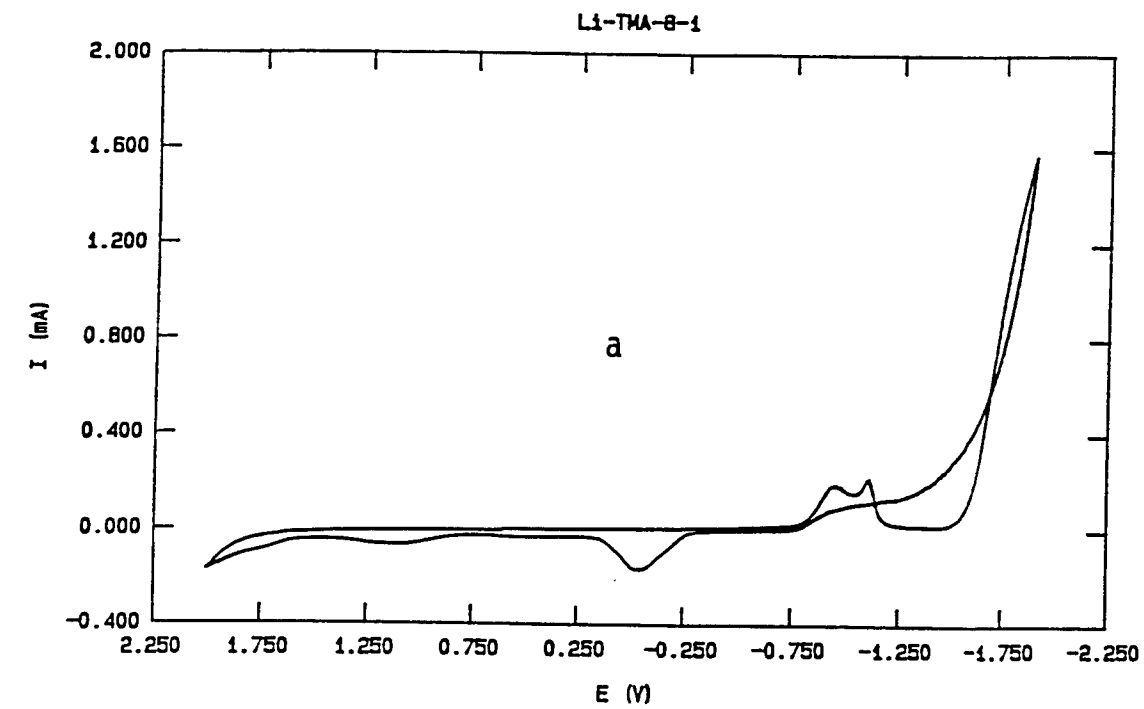


FIG 8

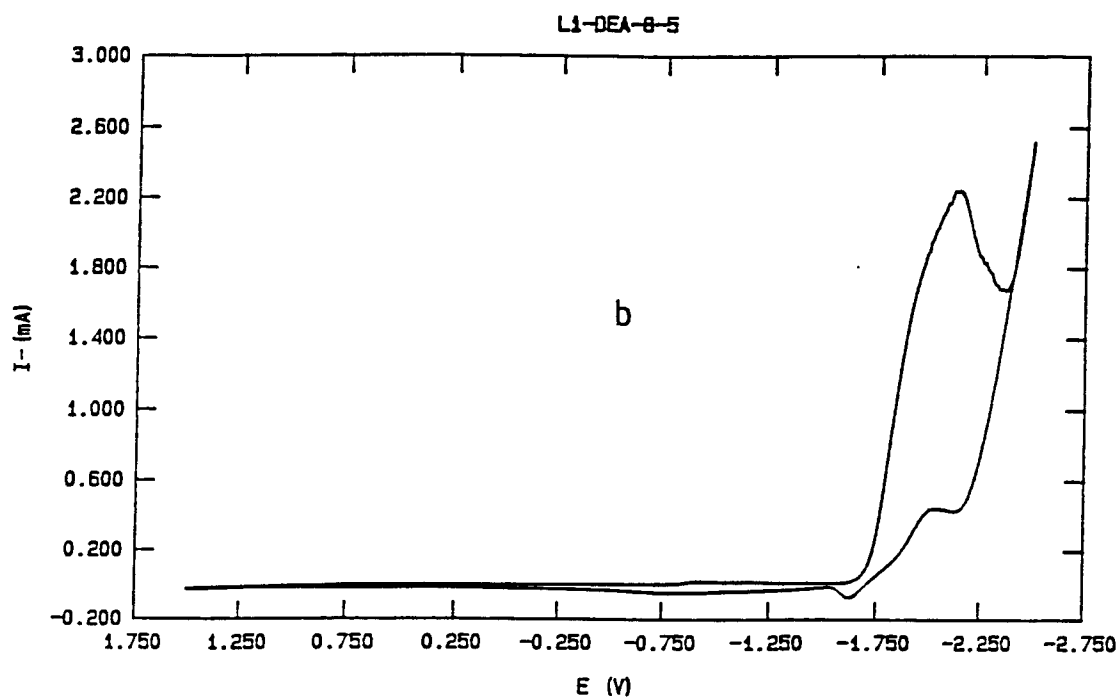
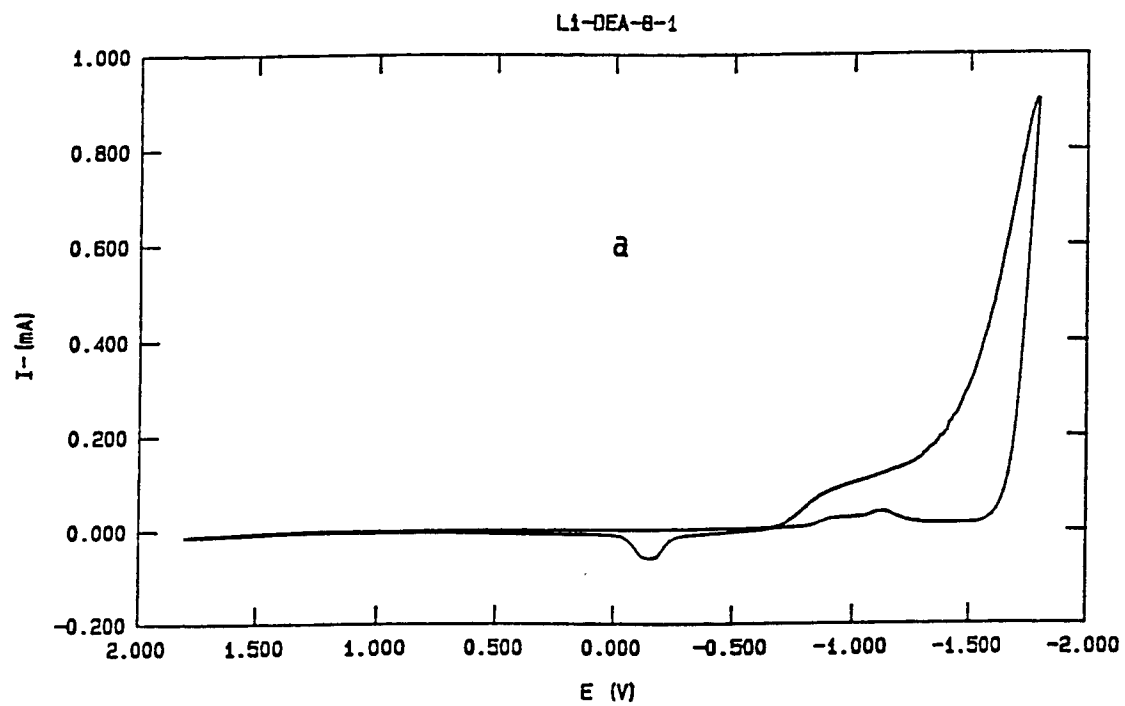


FIG 9

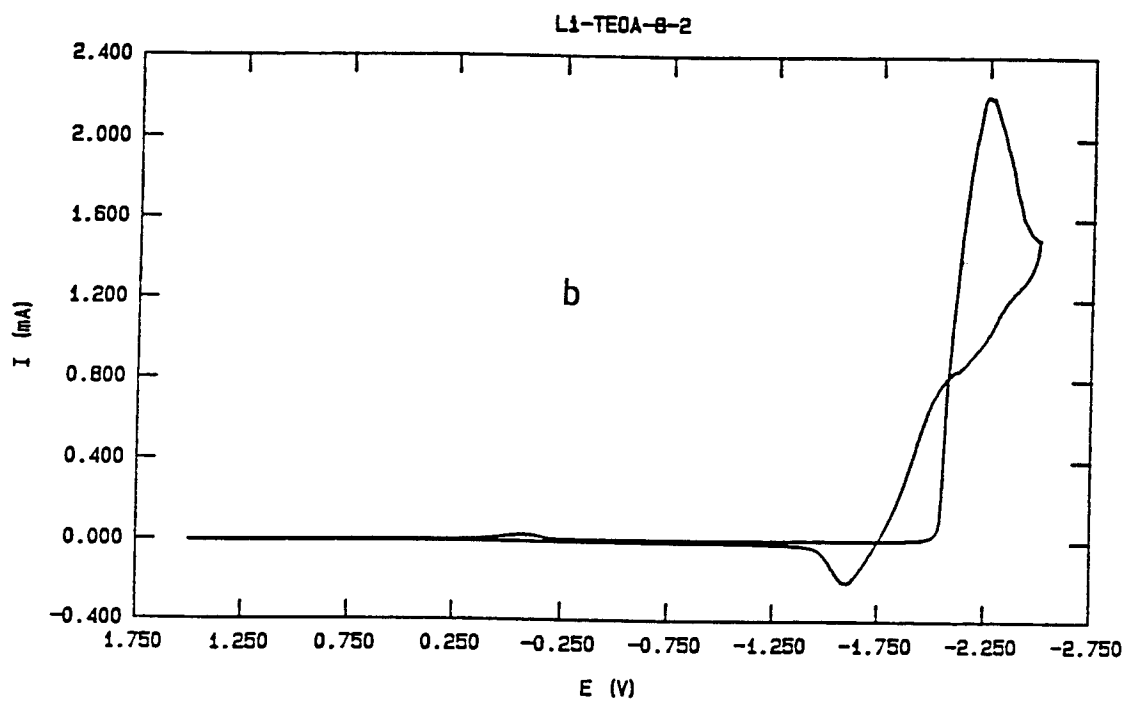
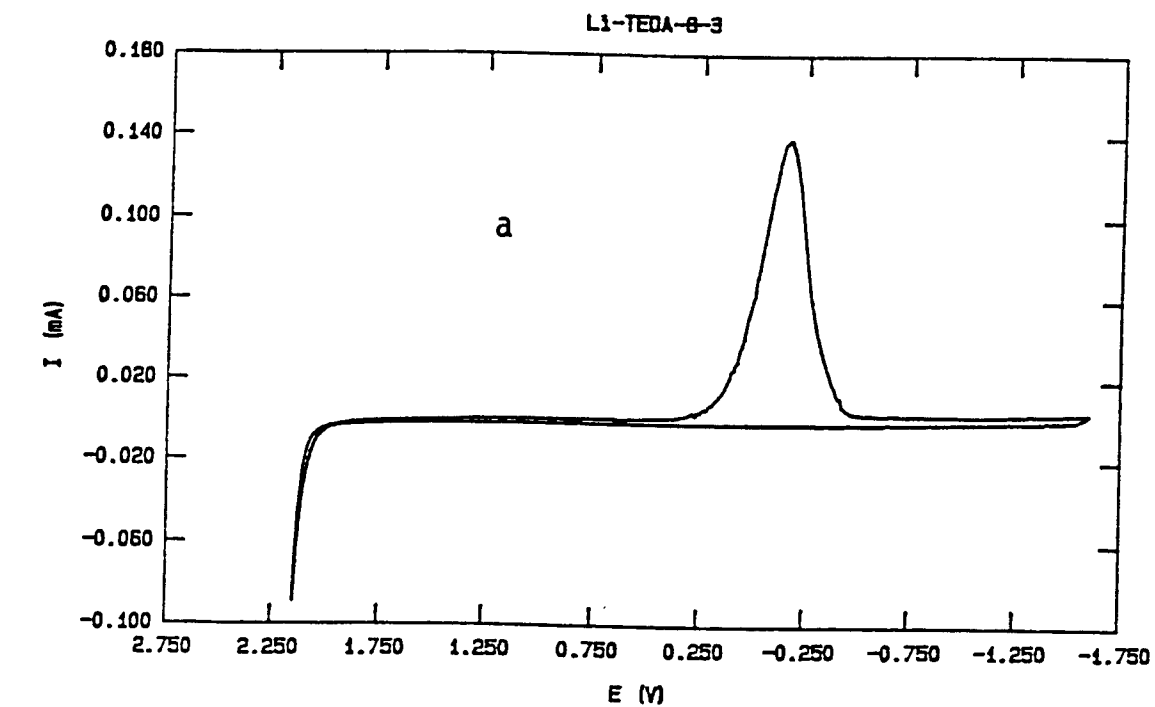


FIG 10

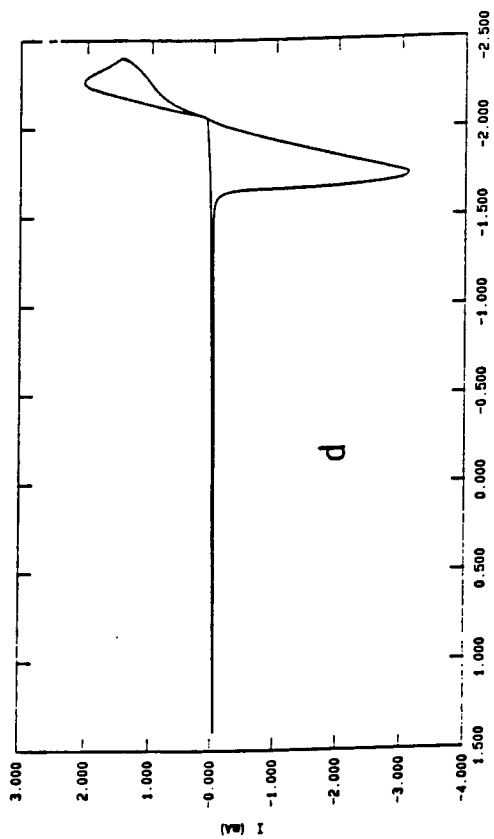
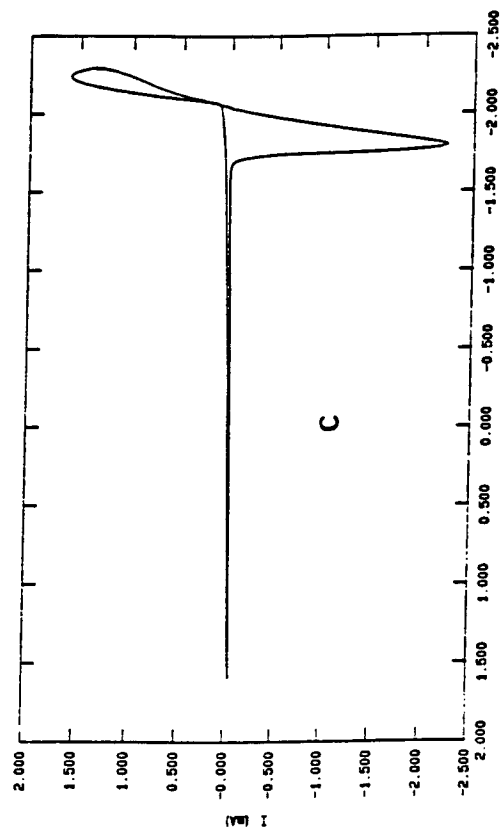
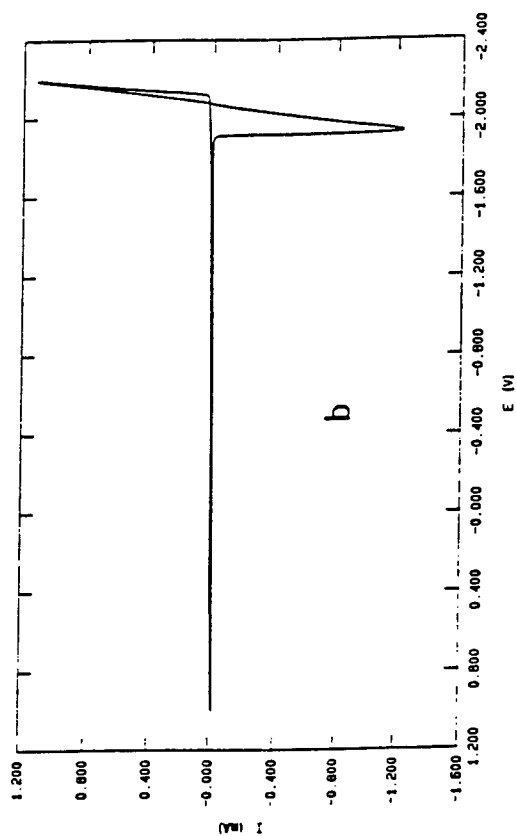
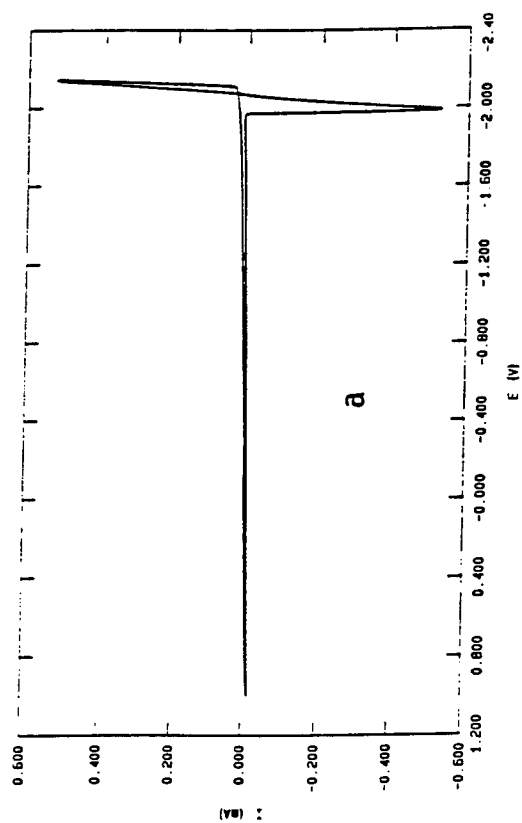


FIG 11

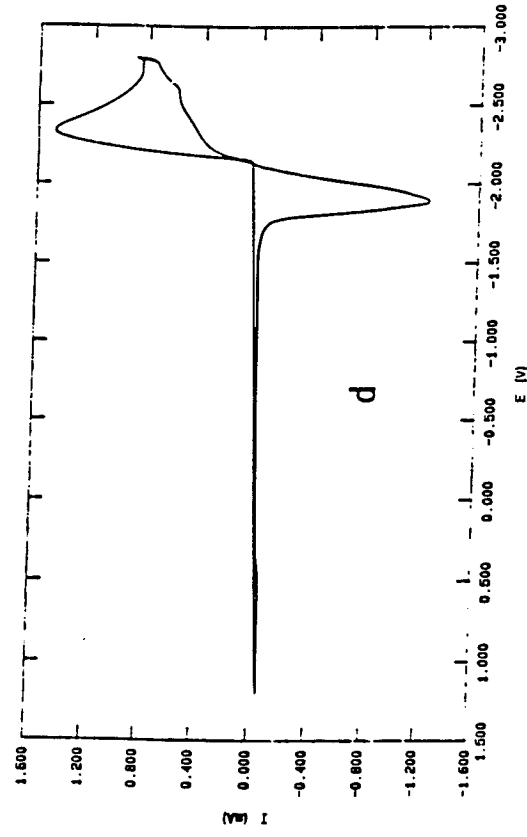
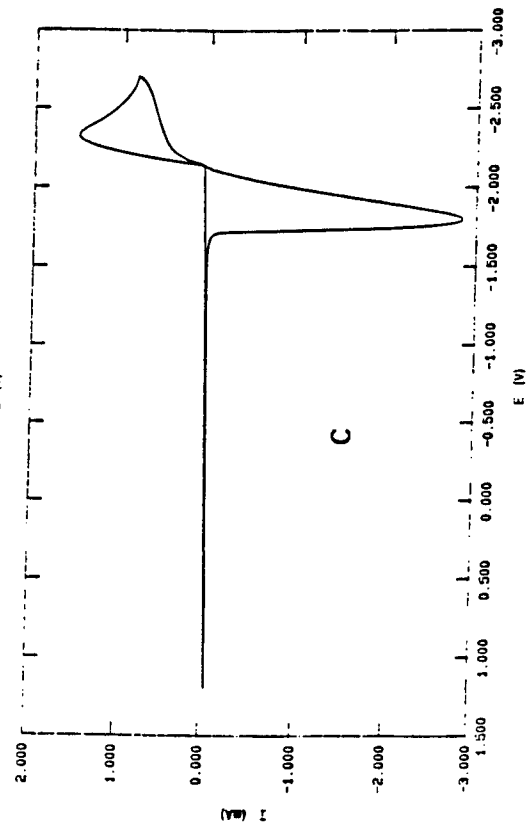
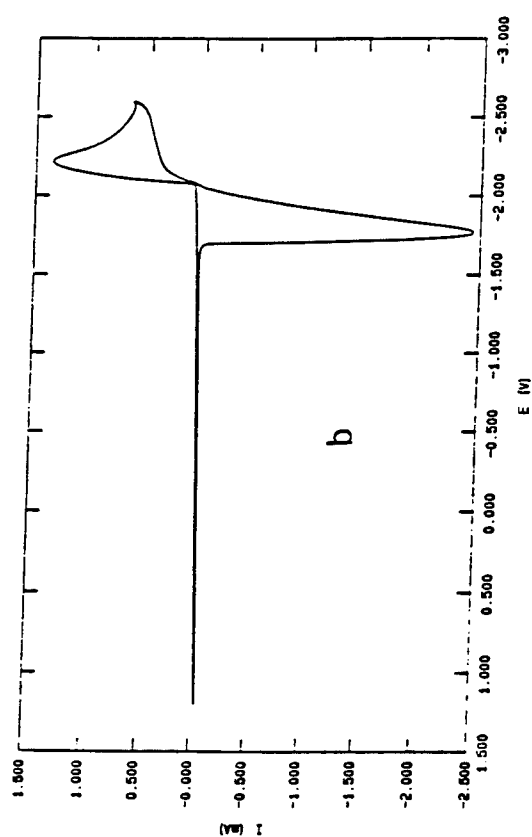
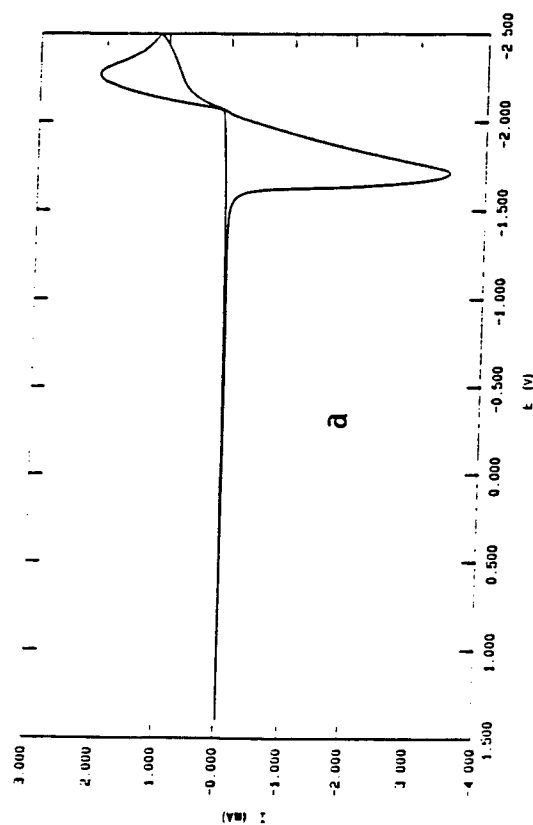


FIG 12

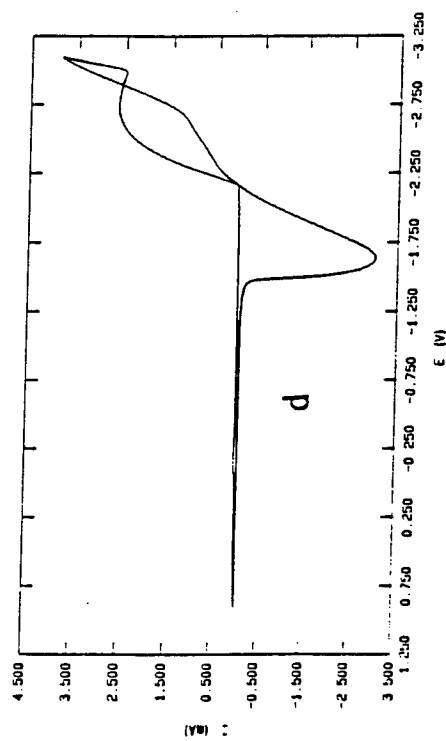
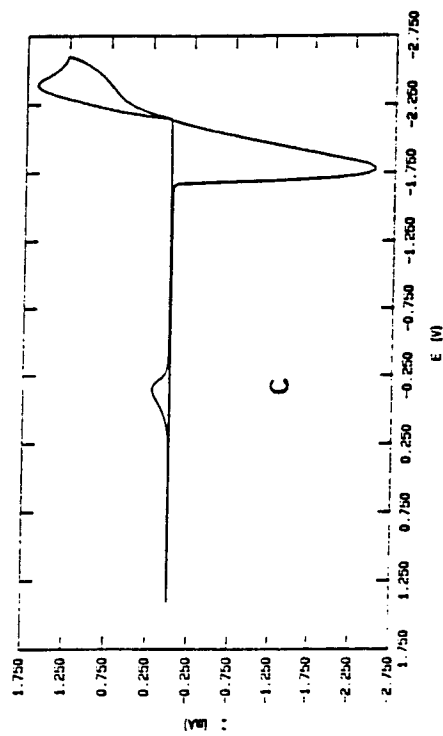
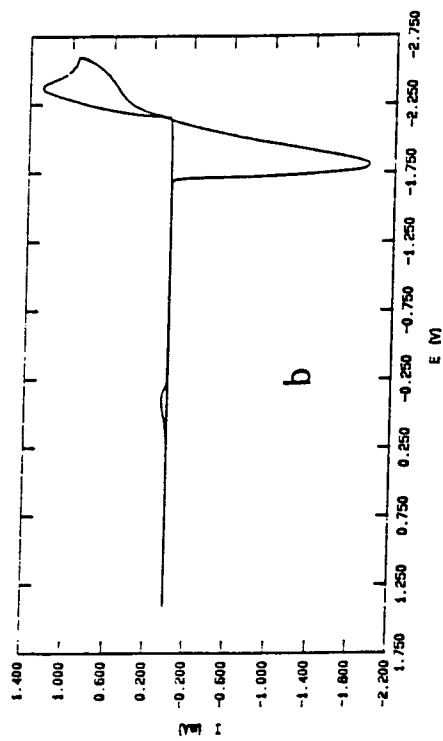
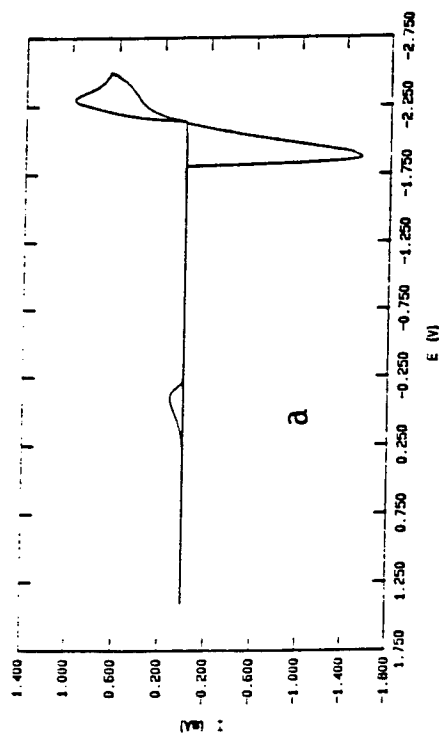


FIG 13

that the melt composition is exactly neutral. Fig. 13 shows typical results for varying the sweep rate for 0.2 M TEOA·HCl in LiCl-buffered melt with (a) 50 MV/sec, (b) 100 MV/sec, (c) 200 MV/sec, and (d) 1 V/sec. We note that at a sweep rate of 1 V/sec the cathodic melt limit in this system is extended to -3.0 V.

The following summarizes the important cyclic voltometric characteristics for 0.2 M TEOA·HCl in LiCl buffered melt:

For sweep rates from 10 MV/sec to 1 V/sec and cathodic sweep limits from -2.40 V to -2.90 V:

Li deposition begins at -2.15 ± 0.02 V

Li deposition peak at -2.40 ± 0.15 V

Li stripping peak at -1.85 ± 0.15 V

Cycle efficiency 0.74 ± 0.10

These results are comparable with those obtained using EM 1 HCl₂ as a proton source as summarized in TABLE I.

TABLE I
Sweep Rate Dependence

mv/sec	Li Deposition				Li Stripping		
	E _{begin} (V)	E _{peak} (V)	I _{peak} (mA)	A _{peak} (mC)	E _{peak} (V)	I _{peak} (mA)	A _{peak} (mC)
5	-2.09	-2.23	0.85	91.3	-1.94	0.80	17.4
10	-2.10	-2.34	1.13	53.9	-1.90	1.20	18.4
20	-2.10	-2.34	1.51	34.6	-1.82	1.88	17.9
50	-2.11	-2.35	2.07	18.6	-1.80	2.77	12.7
100	-2.12	-2.44	2.67	12.8	-1.76	3.16	9.00
250	-2.14	*	3.53	6.21	-1.67	4.01	4.71
500	-2.16	*	3.67	3.36	-1.67	4.14	2.45
1000	-2.16	*	3.52	1.55	-1.68	4.13	1.16

* Cathodic limit was set at -2.50 V to avoid reduction of melt.

Melts which did not have the proper composition to exhibit Li stripping and extended melt limit always resulted in a brown (copper-colored) film deposited on the electrode, even at potentials positive to the detectable melt limit. This film was easily removed by wiping the electrode but was not electrochemically removed up to the anodic melt limit. This film significantly influenced electrode behavior necessitating cleaning of the electrode after every CV to obtain reproducible results. Peak currents for Li deposition were reduced by a factor of two or more after a single CV cycle if the electrode was not cleaned by removal of this film. With proper melt composition the brown film was no longer a problem and electrode cleaning was not required. In some cases when the melt composition was intermediate between the brown film stage and that necessary for desired CV response, Li deposition resulted in coating of the electrode with a gray deposit that could not be removed by wiping. This deposit also had a significant influence on any subsequent measurements and required removal. On removal of the electrode from the dry box this gray deposit immediately disappeared when brought in contact with water. We speculate that this deposit contained Li strongly bound to the W surface, hence it could not be removed by wiping but readily dissolved in water. The reason for its electrochemical inertness is not readily apparent.

Melts which have the proton composition to give exactly neutral conditions and reversible deposition-stripping behavior of lithium, whether from addition of EMIHCl_2 or from addition of $\text{TEOA}\cdot\text{HCl}$, exhibit finely divided white precipitates in rather significant amounts. We have speculated that this may be LiCl precipitating out because of the decreased solubility in neutral, as compared to acidic melt. To identify the white solid we carried out the following series of experiments. Samples of the melt containing the white precipitate were removed from the dry box, the melt was decanted as far as possible and the remaining melt was removed, again as much as possible, with a disposable pipet. The precipitate was washed six times with acetonitrile with the solution removed each time after centrifuging using a disposable pipet. The washed precipitate was dried in a microwave oven, then dissolved in water, in

which it was readily soluble. The aqueous solution was treated with silver nitrate until precipitation of chloride was complete. The clear solution was separated from the AgCl and on addition of 6M NH_4OH formed a gelatinous precipitate. On completion of precipitation, the clear gelatinous precipitate was separated from solution and identified by standard qualitative analysis to be $\text{Al}(\text{OH})_3$. The relative quantity of this precipitate indicated that a major constituent of the original white solid was aluminum. The clear solution separated from the $\text{Al}(\text{OH})_3$ was neutralized with HNO_3 and then evaporated to dryness, leaving a white crystalline solid. This salt was dissolved in a small portion of water and lithium was clearly identified using a flame test. With positive identification of lithium, aluminum and chloride, we conclude that the white precipitate is LiAlCl_4 , not LiCl as initially suspected.

LITHIUM-ALUMINUM ALLOY

An aluminum rod was placed in heat-shrinkable teflon tubing so that only the end was exposed to the melt solution and then used as a working electrode. Cyclic voltammetry was carried out in proton rich LiCl -buffered melt of the proper composition to give reversible deposition-stripping behavior on W and the results for cycle efficiency are summarized in Table II, along with results obtained on Al. The cycle efficiency is defined as $Q_{\text{stripping}}/Q_{\text{deposition}}$ as

TABLE II

Cathodic Limit (v)	Cycle Efficiency on W	Cycle Efficiency on Al
-2.10	—	0.68
-2.20	0.73	0.72
-2.30	0.72	0.72
-2.40	0.76	0.72
-2.50	0.78	0.68
-2.60	0.80	0.62
-2.70	0.73	—
-2.80	0.68	—

obtained from integration of the CV curves.

The cycle efficiencies represent averages of several determinations and are valid to ± 0.05 . The Al electrode required several cycles for conditioning before stable efficiencies could be obtained.

With Li deposited on W we found that cycle efficiency decreased fairly rapidly with time at open circuit before the anodic cycle was begun as represented in Table III reported for a deposition potential of -2.20 V and stripping at -1.6 V.

TABLE III

Time at open circuit between deposition and stripping	Cycle Efficiency
10 sec	0.75
30 sec	0.62
60 sec	0.37
300 sec	0.12

With Li-Al alloy, we are not ready to report similar data but we have observed open circuit potentials which are much more stable than with Li deposited on W. Table IV shows how the open circuit potential changes for an Al electrode on which Li was deposited at -2.3 V for 30 sec.

At the end of this time the Al electrode was observed to have a black deposit which could not be removed by wiping but which readily dissolved in water when the electrode was removed from the dry box. We are planning much more extensive studies with Li-Al alloy in these melts.

CONCLUSIONS

1. We have found that triethanolamine•hydrogen chloride provides a better proton source than ethylmethylimidazolium hydrogen dichloride with stability in the melts studied measured in weeks rather than hours.

TABLE IV

Time	Open Circuit Potential
0	-2.30 V
15 sec	-1.85
30 sec	-1.78
60 sec	-1.75
90 sec	-1.73
2 min	-1.71
3 min	-1.70
4 min	-1.69
5 min	-1.68
7 min	-1.68
10 min	-1.68
15 min	-1.68
20 min	-1.68
30 min	-1.67
45 min	-1.67
60 min	-1.67
75 min	-1.67
90 min	-1.67
2 hr	-1.67
4 hr	-1.67

2. Nearly reversible deposition-stripping of lithium is obtained in LiCl-buffered melts when the TEOA·HCl concentration is between about 0.20 and 0.225

M. It does not appear however, that the Li deposit on W is stable in this system.

3. The protective film which has been reported to form on Li by several groups cited in the review of recent literature presented in this report does not form on the Li deposits under conditions in our melts where reversible deposition-stripping behavior is observed. The brown films which we observe with proton concentrations below the minimum concentration of 0.20 M may possibly be

identified with the lithium oxide or lithium hydroxide films reported by other groups. The increased proton concentration appears to be related to the lack of this film formation and to the reversible deposition-stripping behavior.

4. The white precipitate formed when sufficient EMIHCl_2 or $\text{TEOA}\cdot\text{HCl}$ is added to provide reversible deposition-stripping behavior has been identified as LiAlCl_4 .

5. Li-Al alloy has been shown to be a possible attractive alternative with a much improved stability over deposited Li in the these melt systems. We have not been able to reproduce the results of Fung and Chau cited above but are continuing to work along the lines they have suggested.

REFERENCES

1. Melton, T.J., Joyce, J., Maloy, J.T., Boon, J.A. and Wilkes, J.S., J. Electrochem. Soc. 137, 3865 (1990)
2. Riechel, T.L. and Wilkes, J.S., J. Electrochem. Soc. 139, 977 (1992)
3. Biallozar, S. and Lieder, M., J. Electrochem. Soc. 140, 2537 (1993)
4. Aurbach, D., Daroux, M., Faguy, P. and Yeager, E., J. Electroanal. Chem. 297, 225 (1991)
5. Zavadil, K.R. and Armstrong, N.R., J. Electrochem. Soc. 137, 2371 (1990)
6. Barthel, J., Wühr, M., Sauerer, W. and Hefer, B., J. Electrochem. Soc. 140, 6 (1993)
7. Auboy, M., Lojou, E., Messina, R. and Perichon, J., J. Electrochem. Soc. 140, 879 (1993)
8. Odziemkowski, M. and Irish, D.E., J. Electrochem. Soc. 139, 3063 (1992)
9. Campbell, S.A., Boures, C. and McMillan, R.S., J. Electroanal. Chem. 284, 195 (1990)
10. Odziemkowski, M. and Irish, D.E., J. Electrochem. Soc. 140, 1546 (1993)
11. Odziemkowski, M., Krell, M. and Irish, D.E., J. Electrochem. Soc. 139, 3052 (1992)
12. Biallozar, S. and Lieder, M., J. Electrochem. Soc. 140, 2537 (1993)
13. Fung, Y.S. and Chau, S.M., J. Applied Electrochem. 23, 346 (1993)
14. Kumagai, N., Kikuchi, Y. and Tanno, K., J. Applied Electrochem. 22, 620 (1992)
15. Kumagai, N., Kikuchi, Y., Tanno, K., Lantelme, F. and Chemla, M., J. Applied Electrochem. 22, 728 (1992)
16. Wilkes, J.S., Levisky, J.A., Wilson, R.A. and Hussey, C.L., Indry. Chem. 21, 1263 (1982)
17. Riechel, T.L. and Wilkes, J.S., J. Electrochem. Soc. 140, 3104 (1993)

**ENHANCED PHYSIOLOGIC MONITORING OF PATIENTS WITH
CLOSED HEAD-INJURY**

Michael L. Daley
Associate Professor
Department of Electrical Engineering

Memphis State University
Memphis, TN 38152

Final Report for:
Research Initiation Program
Wilford Hall Medical Center
Lackland AFB, TX

Sponsored by:
Air Force Office of Scientific Research
Bolling Air Force Base, Washington, D.C.

and

Memphis State University

September, 1992

ENHANCED PHYSIOLOGIC MONITORING OF PATIENTS WITH CLOSED HEAD-INJURY

Michael L. Daley
Associate Professor
Department of Electrical Engineering
Memphis State University

Abstract

With the use of a laboratory model, arterial and intracranial pressure signals were obtained under conditions of intact regulation of cerebral blood flow and massive dilation. During elevated intracranial pressure and intact regulation, positive pressure inhalation appears to briefly occlude venous flow into the cranial sinuses during inspiration. As a result, the intracranial pressure and arterial pressure signals are not similar. In contrast when maximal dilation causes failure of regulation of cerebral blood flow, the intracranial pressure signal is approximately proportional to the arterial pressure signal. Comparison of the crosscorrelation function derived from the intracranial and arterial pressure signals to the autocorrelation function of the arterial signal reveals that the two correlation functions are: 1) different during intact regulation and 2) nearly identical during dilation induced failure of regulation of cerebral blood flow.

ENHANCED PHYSIOLOGIC MONITORING OF PATIENTS WITH CLOSED HEAD-INJURY

Michael L. Daley

INTRODUCTION:

Raised intracranial pressure occurs in most cases involving severe head-injury [1] and is a major cause of morbidity and mortality [2]. While there is no universally accepted method for treating raised intracranial pressure, knowledge of as to whether the rise in intracranial pressure is predominantly due to vascular or non-vascular causes would improve the efficacy of treatment [1].

Management of the patient with severe head-injury includes bedside physiologic monitoring of arterial and intracranial pressure. The goal of our work has been to develop enhanced physiologic monitoring techniques which can be used to evaluate the status of control of cerebral blood flow. The present paper describes a correlation method for detecting the loss of control of cerebral blood flow. In particular, during dilation induced failure of regulation, the autocorrelation function derived from the arterial pressure signal is nearly identical to the corresponding crosscorrelation function derived from the arterial and intracranial pressure signals.

MATERIALS AND METHODS:

Animal Model of Closed Head Injury: Eight pigs ranging in weight from 2 to 33 kg were used in this study. The procedures used were similar to those described for other animal studies employing this model [3]. Initially each animal was intramuscularly administered ketamine (33 mg/kg) and acepromazine (3 mg/kg). Animals were intubated and ventilated with a positive pressure respirator at a rate ranging between 8 and 20 breaths/min. with a pulse ventilation pattern. The ratio of inspiration to expiration time was maintained between 20 and 25 %. Anesthesia was maintained with a chloralose (50 mg/kg iv initially, followed by 10 mg/kg hourly). Rectal temperature of animals was kept at 38-39°. Following each experiment, the animal was euthanized.

A pressure recording via a fluid-filled catheter inserted in the brachial artery and a three lead electrocardiographic signal were used to record arterial pressure and ECG activity. Internal jugular venous pressure or sagittal sinus pressure recordings were obtained via a fluid filled catheter. Intracranial pressure was recorded using the Camino fiber optics system. The skull was trephined approximately 1 cm lateral to midline and 2 cm below the coronal suture, a hole was made in the dura, and the fiber optic transducer was placed in the parenchyma and secured to the skull. To manipulate intracranial volume, the skull was trephined at a location contralateral to the fiber optic pressure transducer, and a small fluid-filled balloon was extradurally placed.

Induction of Dilation Failure of Cerebral Blood Flow Regulation: Two methods were used to disrupt regulation of cerebral blood flow. In one method which was done in three experiments the extradurally placed balloon was used to raise intracranial pressure above arterial pressure for more than three to five minutes, producing cerebral ischemia. Upon deflating the balloon, intracranial pressure decreased rapidly to an elevated steady-state condition. Generally, but not always, apparent massive cerebral vasodilation occurred. Large pulsations of jugular pressure were observed and the variation of the baseline of intracranial pressure during positive pressure inhalation was not observed. Sometimes, this state lasted for between five to ten minutes after which the jugular pressure pulsations disappeared and the synchronized variation in the baseline of intracranial pressure with positive pressure inhalation returned. Other times the impaired state was permanent. In the second method, severe hypercapnia was used to maximally dilate the arterial vasculature. Specifically the model was ventilated with 8.5% CO₂. Each time the intracranial pressure increased and arterial pressure decreased over a time course of approximately 5 to 8 minutes to a new steady-state condition which was characterized by an arterial carbon dioxide tension (PaCO₂) above 70 mm Hg and a loss the synchronized variation of the baseline of intracranial pressure with positive pressure inhalation. In most cases, this physiologic state was reversed with reventilation and the return of PaCO₂ to below 50 mm Hg.

Data Acquisition: An IBM compatible 486DX, 33 MHZ, computer with four analog to digital channels was connected to a physiologic recording system (EVR physiologic monitor or a

Bechman physiologic recorder). The three physiologic signals, ECG, arterial pressure, and intracranial pressure were simultaneously acquired at a rate of 250 samples/sec by procedures similar to those previously described [4,5]. Each physiologic channel was calibrated prior to the start of each experiment. Unlike the clinical situation [5], artifact screening was not required for this preparation.

Signal Analysis Methods: Data obtained from the laboratory experiments were imported into DADISP (DSP Development Corp., Cambridge, MA 02139), a signal processing software package. With the use of this software the crosscorrelation function derived from the sampled intracranial and arterial pressure signals was computed. In addition, the autocorrelation of the sampled arterial signal for the same recording period was also calculated with this software. The accuracy of this commercial software was verified with a known analytical signal.

RESULTS:

Three coupled volume compartments are contained within the craniospinal sac: 1) the cerebrospinal fluid volume; 2) the tissue volume containing brain, spinal cord, and supporting tissue; and 3) the blood volume. Insertion of the extradurally placed balloon creates a fourth volume compartment which can be manipulated by infusing or extracting fluid from the balloon. Over short time periods, the compartments containing cerebral spinal fluid volume and tissue volume are assumed to be constant. Therefore, when the extradurally placed balloon volume is maintained at a constant value, rapid changes of intracranial pressure reflect changes of the blood volume within the craniospinal sac. Examples of the arterial and intracranial pressure signals recorded with and without intact autoregulation of cerebral blood flow are shown (see Fig. 1). Each pulsation of arterial pressure produces a corresponding pulsation of intracranial pressure which is produced by the difference between arterial and venous flow over each cardiac cycle. As indicated by the intracranial signal during intact regulation, intracranial pressure increases during positive pressure inhalation and decreases rapidly at the onset of expiration suggesting corresponding increases and decreases of cerebral blood volume (see Fig. 1 a). For this regulatory

condition, the arterial and intracranial pressure signals are not similar. During unregulated vasodilation, abrupt increases and decreases of intracranial pressure are not evident. As expected during impaired autoregulation due to maximal dilation of the arterial vasculature, changes in intracranial pressure are similar to the corresponding arterial pressure.

Since the arterial and intracranial pressure are not similar during intact cerebral blood flow regulation and similar during periods of impaired regulation due to maximal dilation of the vasculature, a comparison of the autocorrelation of the arterial pressure signal to the corresponding crosscorrelation function of the arterial and intracranial pressure signals provides a method for evaluating integrity of regulation of cerebral blood flow. The details of this derivation are presented in Appendix I. For the 16 second recordings of arterial and intracranial pressure signals shown in Fig. 1, the corresponding autocorrelation functions of the arterial signals and crosscorrelation functions of the arterial and intracranial pressure (ICP) signals are shown in Fig. 2. For both recording conditions, with and without intact regulation, the normalized autocorrelation function of the arterial pressure signal has a characteristic diamond shape. During intact regulation, the arterial and intracranial pressure signals are not similar. Thus, the autocorrelation function of the arterial pressure signal and the crosscorrelation function of the arterial and ICP signals are not similar. As shown (see Fig. 2a), the crosscorrelation function is not diamond shaped and it has wave-like features corresponding to each respiratory cycle. In contrast, with dilation and failure of regulation, the arterial and intracranial pressure signals are similar. For this condition, the autocorrelation of the arterial pressure signal and the crosscorrelation function between the arterial and intracranial pressure signals should be similar (see Appendix I). As shown in Fig. 2b, the crosscorrelation function has a characteristic diamond shape similar to that of the corresponding autocorrelation function of the arterial pressure signal.

DISCUSSION:

During the elevated intracranial pressure rapid changes of intracranial pressure primarily reflect changes of cerebral blood volume. For the condition of intact regulation of cerebral blood flow with

normal vascular tone, cyclic variations in the baseline of intracranial pressure are synchronized with positive-pressure inhalation. Similar variations in the baseline of the ICP signal are observed in recordings from our animal model (see Fig. 1). At the onset of inhalation, intracranial pressure rises in apparent response to a steady accumulation of intracranial cerebral blood volume. At the onset of expiration, the accumulated blood volume appears to be rapidly released. This pattern suggests that during the positive pressure phase of ventilation cerebral blood volume slightly increases and when cessation of the positive pressure occurs the accumulated venous blood is rapidly released. One explanation for this cyclic behavior is the possible presence of a valve-like mechanism at the outlets of the venous bridging vasculature between the cerebral veins and the cranial sinuses. To maintain adequate intrinsic venous pressure for blood flow during elevated ICP, these bridging veins appear to be selectively compressed (pinched) at localized sites near their outlets to the sinuses[6]. Because the outlet of the compressed site has a small cross-sectional area [6] and is at low intrinsic pressure, it is the most likely site for occluded flow due to the extramural pressure increase during positive pressure inhalation. At the cessation of positive pressure, this severe restriction is immediately released, flow through the restricted site occurs, and cerebral venous blood volume rapidly decreases. This apparent cyclic accumulation and release of cerebral blood volume during inhalation produces an intracranial pressure signal which is very different than the corresponding arterial pressure signal. In contrast, extensive, unregulated cerebral dilation produces high intrinsic cerebral venous pressure and reduced vascular compliance. For this condition, because of the high intrinsic cerebral venous pressure, it is unlikely that selective compression within the bridging vasculature occurs. Thus, the cyclic valving action of venous flow associated with positive pressure inhalation is not present. In addition, because of reduced arterial compliance due to maximal dilation of the vasculature, arterial flow is essentially through a resistive network. For this condition, the contour of the arterial pressure signal reflects arterial flow [7]. Furthermore, arterial flow into the venous bed produces a change of cerebral blood volume and a corresponding change of intracranial pressure. Thus, during impaired regulation due to maximal dilation of the arterial vasculature, the changes

of arterial pressure are followed by corresponding changes of intracranial pressure. The intracranial pressure signal is approximately proportional to the arterial pressure signal.

In summary, during intact regulation of cerebral blood flow and elevated intracranial pressure, intrinsic cerebral venous pressure appears to be maintained slightly above intracranial pressure by localized compression of the bridging vasculature just proximal to the outlets to the cranial sinuses [6]. The action of this venous regulatory mechanism coupled with positive pressure inhalation appears to briefly occlude venous flow out of the cranialspinal sac during inspiration. The cyclic accumulation and decrease of cerebral blood volume produces an intracranial signal that is saliently different than the corresponding arterial pressure signal (see Fig. 1a). As a result the autocorrelation function of the arterial pressure signal and crosscorrelation of function of the arterial and intracranial pressure signals are not similar (see Fig. 2a). In contrast, with loss of arterial tone the intrinsic cerebral venous pressure is high and vascular compliance is reduced. The intracranial pressure signal is proportional to the arterial pressure signal (see Fig. 1b). Furthermore, the autocorrelation function of the arterial pressure signal and the crosscorrelation function of the arterial and intracranial pressure signals are similar (see Fig. 2b). Thus, comparison of the arterial autocorrelation function to the corresponding arterial and intracranial pressure crosscorrelation function provides a means for evaluating the status of the integrity cerebral blood flow regulation.

REFERENCES:

- [1] J. D. Miller, N. M. Dearden, I. R. Piper, and K. H. Chan, "Control of intracranial pressure in patients with severe head injury, " J. Neurotrauma vol. 9, pp. S317-S525.
- [2] D. P. Becker, J. D. Miller, J. D. Ward, R.P. Greenberg, H. F. Young, and R. Sakalar, "The outcome from severe head-injury with early diagnosis and intensive management," J. Neurosurgery vol 47, pp. 491-502.
- [3] C.J.J. Avezatt, J.H.M. Van Eijndhoven, and D.J. Wyper, "Cerebrospinal fluid pulse pressure and intracranial volume-pressure relationships," J. Neurology, Neurosurgery, and Psychiatry vol. 42, pp. 687-700, 1979.

- [4] M. L. Daley, A.E. Gallo, G.F. Gehling, J.B. Isom, W. Mauch, and P.D. Kingsley, "Fluctuation of intracranial pressure associated with the cardiac cycle," Neurosurgery vol. 11, pp. 617-621, 1982.
- [5] M.L. Daley, A.E. Gallo, and W. Mauch, "Analysis of the intracranial pressure pulsation associated with the cardiac cycle," Innovation Et Tech. En Biologie Et Medicine vol. 7, pp. 537-544, 1986.
- [6] Y. Nakagawa, M. Tsuru, and K. Yada, "Site and mechanism for compression of the venous system experimental intracranial hypertension," J. Neurosurg. vol. 41, pp. 427-434, 1974.
- [7] W. Nichols and M.F. O'Rourke, "Contours of pressure and flow waves in arteries," In McDonald's Blood Flow in Arteries, Philadelphia, Lea & Febinger, 1990, pp. 216-245.

APPENDIX:

Variations in the baseline of intracranial pressure follow the variations in arterial pressure over the respiratory cycle. This observation can be mathematically approximated as:

$$P_{icp}(t) = kP_{art}(t) \quad (1).$$

Furthermore, assuming a deterministic system the crosscorrelation of the intracranial and arterial pressure signals can be expressed as:

$$C(\tau) = \langle P_{icp}(t), P_{art}(t) \rangle \quad (2)$$

where the notation $\langle x, y \rangle$ denotes the correlation of the two functions on the time-difference interval $\tau \in [-T, T]$. Since loss of cerebral vascular tone produces an intracranial signal which is approximately proportional to the arterial signal, the crosscorrelation of the two signals can be expressed as:

$$C(\tau) = k \langle P_{art}, P_{art} \rangle. \quad (3).$$

Moreover, the autocorrelation of the arterial signal is expressed as:

$$A(\tau) = \langle P_{art}, P_{art} \rangle. \quad (4).$$

Therefore, for physiologic recordings obtained during cerebral vasodilation, the crosscorrelation function generated by correlating the intracranial pressure and arterial pressure signals should be proportional to the autocorrelation function of the arterial signal recorded over the same time period. Mathematically, this relationship can be expressed as:

$$C(\tau) = kA(\tau). \quad (5).$$

A similar relationship is valid for the a.c. components of each signal which are shown for detail visual analysis in Fig. 2.

ACKNOWLEDGMENTS:

This study was supported in part by a Faculty Research Grant from Memphis State University, a USAF Research Initiative Proposal awarded to M. L. D. and the National Institutes of Health to C.W.L.. We wish to thank Col. John Cissik and the technical staff at Wilford Hall Medical Center, Lackland AFB, TX, for their help and suggestions.

FIGURE LEGENDS

Figure 1. Arterial and Intracranial Pressure Signals Recorded During Intact Cerebral Blood Flow Regulation and Massive Dilation. a) Arterial Pressure and Intracranial Pressure recorded during positive pressure inhalation and intact autoregulation. Both arterial and intracranial pressure signals have a rhythmic variation in baseline associated with respiratory cycle. Unlike arterial pressure, the intracranial pressure increases rapidly during inhalation and abruptly decreases at the onset of expiration. The recorded pressure signals are not similar. b) Arterial pressure and intracranial pressure signals recorded during cerebral vasodilation. Cerebral vasodilation was induced by severe hypercapnia which produces maximal dilation for the arterial vasculature. For this condition, the recorded arterial and intracranial pressure signals are similar.

Figure 2. Autocorrelation and Crosscorrelation Functions Derived from Arterial and Intracranial

Pressure Signals During Intact Cerebral Blood Flow Regulation and Massive Dilation. a)

Autocorrelation and crosscorrelation of the a.c. components of the arterial and intracranial pressure signals recorded during intact regulation (see Fig. 1a. above). Wave-like features in the crosscorrelation function reflect cyclic increases of intracranial pressure during inhalation. b)

Autocorrelation and crosscorrelation of the a.c. components of the arterial and intracranial pressure signals recorded during maximal dilation of the arterial vascular induced by severe hypercapnia ($\text{PCO}_2 > 85$ mm of Hg). During loss of regulation, the intracranial pressure signal is proportional to the arterial signal (see Fig. 1b.). For this condition, the crosscorrelation function lacks the wave-like features which are evident during intact regulation and is very similar to the autocorrelation of the arterial function.

FIGURE 1
Arterial and Intracranial Pressure Signals Recorded During Intact and
Failed Cerebral Blood Flow

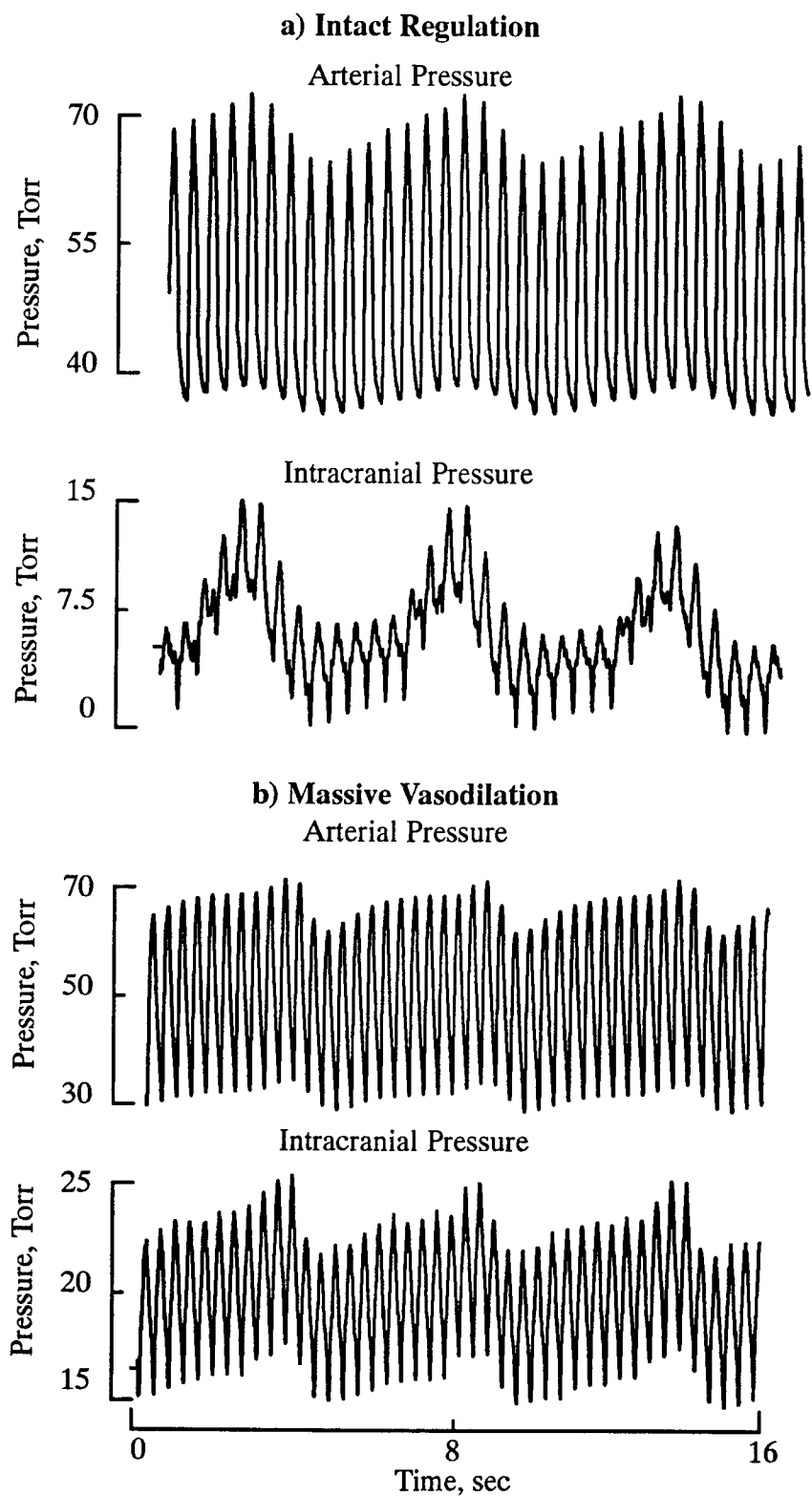
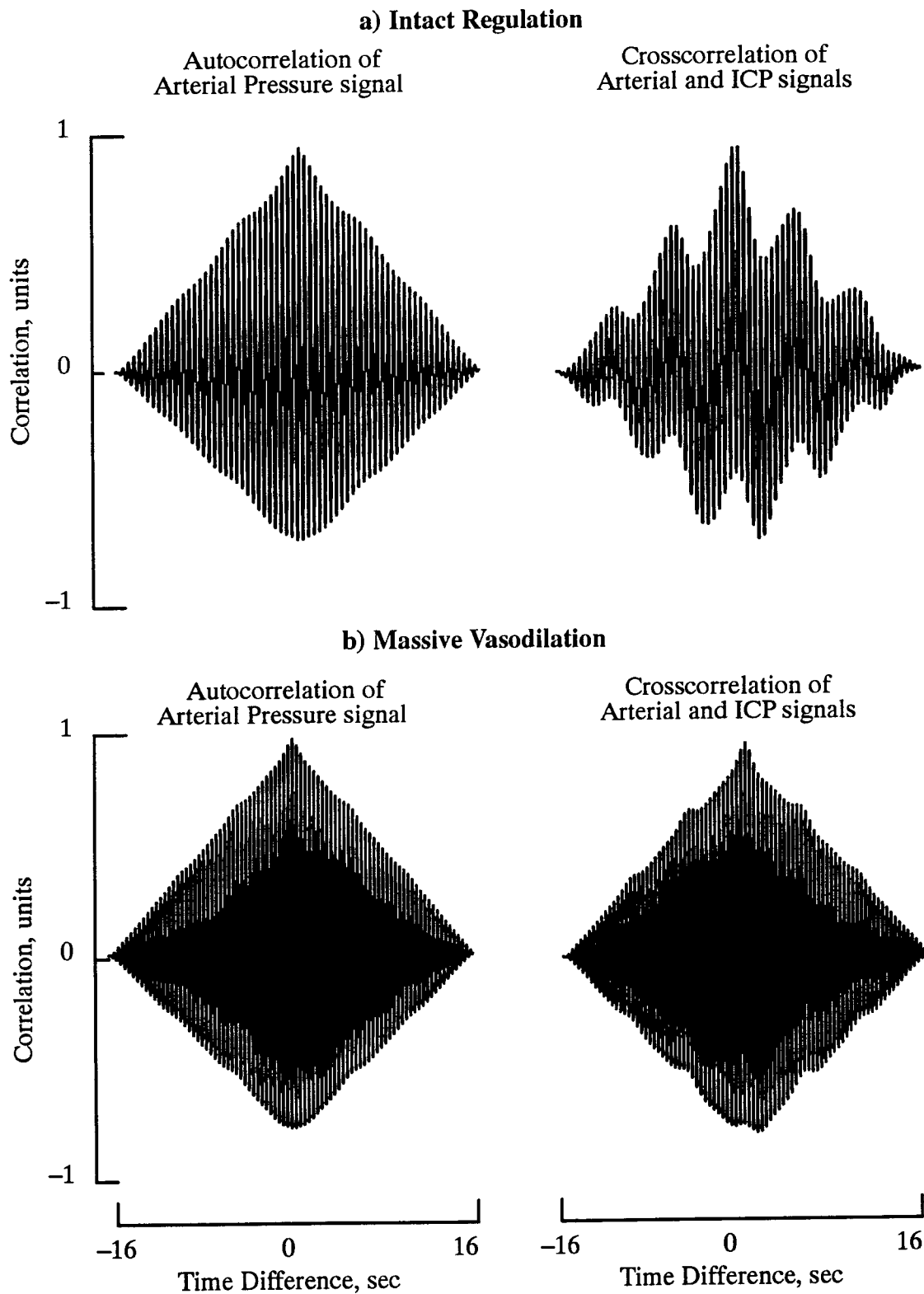


FIGURE 2
Autocorrelation and Crosscorrelation Functions During Intact and Failed Cerebral Blood Flow



RHEOLOGICAL, BIOCHEMICAL AND BIOPHYSICAL STUDIES OF BLOOD AT
ELEVATED TEMPERATURES

FINAL REPORT ON RESEARCH INITIATION GRANT, BASED ON WORK
INITIATED AT THE CLINICAL INVESTIGATION DIRECTORATE,
WILFORD HALL MEDICAL CENTER, LACKLAND AFB, SAN ANTONIO, TX.

Sponsored by the Air Force Office of Scientific Research,
Bolling AFB, Washington, DC.

by
W. DROST-HANSEN
LABORATORY FOR WATER RESEARCH
DEPARTMENT OF CHEMISTRY
UNIVERSITY OF MIAMI,
CORAL GABLES, FLORIDA, 33124.

Period covered: December 1991 - December 1992.

ABSTRACT

RHEOLOGICAL, BIOCHEMICAL AND BIOPHYSICAL STUDIES OF BLOOD AT ELEVATED TEMPERATURES.

W. Drost-Hansen
Laboratory for Water Research
Department of Chemistry, University of Miami
Coral Gables, FL, 33124.

In spite of over 70 years of use in clinical diagnosis, no quantitative theory exists which adequately describes the Erythrocyte Sedimentation Rate (ESR.) In an attempt to understand the dynamics of the ESR we have over the past four years studied a variety of parameters related to the ESR, including the rheology of blood plasma and model biopolymers (effects of temperature and shear-rate), red cell volumes, rate of diffusion of solutes and colloidal particles, and related physical parameters likely to play a role in the transport processes of whole blood. In the present study we have particularly studied rheological aspects of model macromolecules and bio-polymers as function of shear-rate and temperature. The main findings are: I) *large polymers in aqueous solution appear to be "vicinally hydrated" -- i.e., these polymers have hydration "shells" of interfacially modified water of the type expected at most (or all) solid surfaces. Small solutes in water are not similarly hydrated; hence it is likely that vicinal hydration of macromolecules occurs only for molecules larger than a certain critical minimum size. Most likely this critical size is about 1 kDa.* Furthermore, we find that II) *the vicinal hydration of large macromolecules is strongly shear-rate dependent.* III) *Once the vicinal structures have been disrupted by shear, the original hydration structures reform only slowly;* this is in agreement with earlier findings by the Author and his coworkers. In all cases studied, IV) *the viscosity of the polymer solutions (with MW above the critical range) exhibit distinct (and often dramatic) changes as a function of temperature at the thermal transition temperatures (T_k) of vicinal water.* However, with *increasing shear rate the thermal anomalies tend to become less and less pronounced.* This suggests that the vicinal water structures are highly labile. Finally, V) *measurements by a Photon Correlation Spectrometric method of the apparent particle diameters of solid, submicroscopic Polystyrene spheres in aqueous suspensions yield values which decrease quite abruptly near 30 ° - 32 °C.* It appears that this effect is most pronounced in stagnant suspensions, and that stirring such suspensions remove the abrupt change at T_k in the apparent diameters; this view is consistent with the observation mentioned above that the vicinal hydration structures are very labile. It is conceivable that similar considerations may apply to erythrocytes in whole blood. Estimates for the thickness of the vicinal hydration shells of the Polystyrene spheres below 30 °C are of the order of 30 nm, in good agreement with a number of independent estimates.

INTRODUCTION

The famous biochemist/biologist Albert Szent-Györgyi repeatedly stressed that water is the "mother and matrix" of life. It is indeed hard to overemphasize the "aqueous connection": most living organisms contain, on the average, about 70 % water but while this may seem high the truly aqueous nature of life becomes much more readily envisioned when it is realized that because of the low molecular weight of water, the mole-fraction of water in a living cell is overwhelming. Thus, in a typical assembly of eukaryotic cells, say a muscle, the number of ions and molecules (large and small) is very low compared to the number of water molecules. Thus, per 20 000 water molecules there are only about 100 small ions and non-electrolytes; somewhat fewer larger non-electrolytes and only 75 lipid molecules with one (or at most, two) protein molecules and one or a few other macromolecules (say polypeptides, nucleic acids, or polysaccharides.) In view of this, it seems reasonable to seek a description of *life in terms of the physical chemistry of aqueous interfacial systems*. Indeed, this is the underlying "leitmotif" for most of the work in the LABORATORY FOR WATER RESEARCH at the University of Miami.

For several decades we have investigated various aspects of the role of the aqueous phase in cell biology [a list of pertinent papers are given in the Reference Section at the end of this report.] These papers will serve to "set the stage" for the investigations to be described below. In the present report the main emphasis will be on the role of interfacial water in modeling hemorheology, both as far as the dynamics of transport processes are concerned, as well as external surface hydration effects which may affect the apparent volumes (and effective cross-sectional areas) of erythrocytes. To this discussion will be added some of the conclusions reached from the results of three years of Summer Research Programs (sponsored by the AFOSR) and an integration sought between the various pieces of information obtained.

Hemodynamics is concerned with the flow of blood in the circulatory systems of those organisms which have a closed circulatory system -- from earthworms to fish, amphibians and reptiles, and from birds to mammals. In man, malfunctioning of the circulatory system, traceable to hemodynamics, accounts for a large fraction of all medical problems such as high blood pressure, ischaemic heart disease, peripheral arterial disease and stroke.

Hemorheology is concerned with the rheological aspects of the flow of the exceedingly complex fluid, the blood. The complexities are overwhelming; the blood is a non-homogeneous suspension of various types of living cells, all deformable and non-spherical (of different ages and in varying numbers) in an extremely complex fluid, the plasma, which is non-newtonian, containing high concentrations of both electrolytes and non-electrolytes, including a large number of different biopolymers in varying ratios, in which the number-density of the dispersed blood cells vary with shear rate. As an example of the role of hemorheology, consider the apparent correlation between

blood plasma viscosity and ischaemic heart disease as recently discussed by Lowe et al. (1991) and earlier by Dintenfass (1981.)

The Erythrocyte Sedimentation Rate (ESR or "sed rate") is a measure of the rate of hindered settling of red cells in whole, anti-coagulated blood. This quantity has been used empirically for about 70 years as a non-specific indicator of disease. Given the complexity of blood, indicated above, it is hardly surprising that no satisfactory theory is extant for the calculation of the ESR from first principles and added to the physico-chemical problems involved in calculating the rate of hindered settling (of non-spherical, deformable "particles") under the conditions prevailing in whole blood one must add the complexity of rouleaux formation -- itself reflecting some complex, aqueous adsorption processes of biopolymers on the red cell surface -- which dramatically affects the net observed sed rates.

While the ESR may seem a "subspecialty" within hemorheology (as part of the larger realm of hemodynamics) it is worth noting that the ESR assumes a uniquely interesting position as bridging the gap between Chemical and Industrial Engineering on the one hand -- for instance through the processes of settling tanks in chemical industrial operations and hydrological considerations in Reservoir Engineering for dams -- and the physical processes of hindered settling as an exercise in theoretical hydrodynamics of heterogeneous dispersions on the other hand. Add to this difficult "mix" the likely role of classical, physico-chemical hydration and electrical double layer aspects of solid surfaces in contact with an aqueous phase. Finally, as will be emphasized in the present report, to this description must be added the unique features of "vicinal hydration" of the interface between a "solid surface" and the aqueous phase -- immensely complicating the dynamic description of the ESR.

One of the main objectives of the author's research is to elucidate the role of vicinal water in cell functioning. In the context of the AF Grant, our interests have primarily been in the role of vicinal water in the Erythrocyte Sedimentation Rate and rheological aspects of blood and aqueous solutions of biopolymers, such as plasma and serum. In addition to work on the AF Grant, the author has spent three summers at an AF Clinical Laboratory (namely, the Clinical Investigation Directorate of Wilford Hall Medical Center at Lackland AFB) and has there had the opportunity to make a large number of ESR measurements and rheological observations. Since the results of these studies have greatly influenced the selection of topics pursued under the AF Grant to LWR it is important briefly to review these related studies as well as to mention some significant results obtained from the literature.

BACKGROUND.

The two main, interrelated themes of the present report are:

A) the dynamics of the Erythrocyte Sedimentation Rate [ESR] and
B) the rheology of aq. polymer solutions and dispersions -- particularly those of biophysical interests, such as protein solutions, plasma, serum and whole blood. A vast literature exists on these subjects, yet our understanding of the transport properties in question is still incomplete and in certain aspects totally inadequate. However, the main point of the present study is not to attempt an extension of current insight by the study of further "classical " details but instead *to examine the likely role that interfacially modified water structures [the so-called vicinal water] may play in these areas*. In this respect, then, the research reported here breaks new ground and some previous "unusual results" now find natural explanations in terms of the vicinal water effects. As some readers may be unfamiliar with the current state of vicinal water research the next several Sections of this Report will attempt briefly to "set the stage" by reviewing the essence of vicinal water theory. This "diversion" is critically important in order to understand the selection of subjects chosen for AF Grant study and for the interpretation of the results we have obtained.

The dynamics of transport processes in blood must depend on a variety of variables; in this and our earlier studies we have, somewhat arbitrarily, chosen to limit our studies to the following parameters: the viscosity of the plasma; the surface hydration of the erythrocytes (in part modeled by Polystyrene spheres), and the volumes of the blood cells (red cells, white cells and platelets.) As will become apparent in the following sections, we are particularly interested in the effects of the hydration of macromolecules on the overall rheological properties. However, our primary interest is not in the "classical" aspects of polymer hydration [such as the first layer of water of hydration, frequently associated with the hydration of surface charges or surface dipoles.] Instead, we have proposed (Etzler & Drost-Hansen, 1983) that macromolecules in aqueous solution (at least those with a Molecular Weight, MW, larger than about 1000 Dalton) are VICINALLY hydrated, -- akin to the vicinal hydration of solid surfaces (please see the list of General Papers in the Reference Section.)

A ubiquitous aspect of vicinal hydration is the occurrence of thermal anomalies in the temperature dependence of many or most parameters. Thus, anomalies - such as more or less abrupt changes in the temperature coefficient - over rather small temperature intervals [say one to two degrees] are frequently seen. The temperatures of the anomalies, T_k , are near 15, 30, 45 and 60 °C. Conversely, the occurrence of these thermal anomalies strongly suggest the presence of vicinal water --- a point which is of crucial importance for the discussion which follows. Again the reader is referred to the list of General Papers.

PHYSICO-CHEMICAL ASPECTS OF THE ESR: DYNAMICS OF HINDERED SETTLING.

Much of the impetus for the work performed under the AF Grant comes from a desire to understand the dynamics of hindered settling of red cells in whole, anticoagulated blood. The reasons are two-fold: A) the ESR has a long, distinguished career as a cheap, "quick-and easy", non-specific indicator of disease, yet the dynamics of the process is still far from well understood, and B) settling of red cells in the body may occur at low flow rates in the venous system, and thus be an important factor in the overall hemodynamics of the patient, especially in those cases where the sed rate is notably elevated due to the presence of various diseases.

ERYTHROCYTE SEDIMENTATION RATE (ESR)

After 70 years the ESR continues to be a useful, if rather non-discriminating, indicator of disease. It is not only a cheap diagnostic test, but where more sophisticated biomedical Laboratory equipment is not available, it may still be an important aid to the physician. In other circumstances it may serve as a cheap, fast and relatively reliable monitor of the progress of a disease or as an indicator of the effectiveness of the therapies employed over a period of time.

No satisfactory theory of the ESR is presently available. This is hardly surprising as the dynamics is extremely complicated. Briefly, the initial settling rate is nearly zero (particularly in healthy subjects) until a significant degree of rouleaux formation has occurred. The rate of rouleaux formation itself must be a complicated function of the adsorption of various proteins on the red cell surface, and further depend on the rates of diffusion of the cells and the proteins involved in the binding between the cell surfaces. Only when the rouleaux formation has progressed sufficiently will these larger entities begin to settle: a process bearing very little resemblance to the simple settling of a single, spherical particle implied in the Stokes treatment of sedimentation. The process is further complicated by the chemical and rheological complexity of the plasma, including the fact that the plasma is non-newtonian (at low shear-rates) and the individual red cells are deformable. Even in those rare cases where a reasonably complete biochemical analysis is available of the proteins present in the plasma it is still difficult to predict the viscosity of the plasma with any degree of certainty.

Notwithstanding the obvious shortcomings of the Stokes treatment of sedimentation when applied to whole blood, the "Stokesian approach" underlies all current theories of the ESR. It is important to point out that even the theory of hindered settling of perfect, non-interacting spherical particles in low concentration in newtonian liquids, is approximate (and extremely difficult mathematically, see Batchelor, 1972, and Happel and Brenner, 1973) and does certainly not apply to concentrations corresponding to normal hematocrit values, nor to the less-than-rigid, totally non-spherical red cells or the rouleaux aggregates of red cells. On the other hand, it is intuitively reasonable that the viscosity of the plasma -- or of the whole blood itself -- must play a role, as

must the "effective cross-sectional area" of the sedimenting entities. It is indeed for these reasons that much of our work has been concerned with viscosity measurements of protein solutions (and other polymers and biopolymers) and with the determination of the sizes of the (individual) red cells (as well as white cells and platelets.)

VICINAL WATER

Notwithstanding a century of study, the structure of water has not yet been fully delineated -- and may indeed escape a rigorous description for several more decades. By the same token, our understanding of aqueous solutions also remains incomplete; thus not only do we not have adequate, quantitative theories for any but the most dilute electrolyte solutions but far less is known with certainty about solutions with multiple solutes, especially mixtures of electrolytes and non-electrolytes. Concentrated solutions - say a few molar - present additional significant problems and again mixtures of solutes in this concentration range are even less well understood. Finally, polymer behaviour in water is not only difficult because of the enormous complexity of the polymers themselves, but for lack of a detailed description of water structure our insight into the specifics of water/polymer interactions remain largely obscure (notwithstanding decades of research.)

Consider now a typical living cell, say a eukaryotic cell. The most overwhelming aspect of all cells is not their vast biochemical complexity; instead, the two totally dominant factors are A) the enormous mole fraction of water compared to all other solutes [Drost-Hansen and Singleton, 1992] and B) the gigantic interfacial area within the cell [see for instance Clegg, 1979, 1982.] In short, a living cell is essentially only a highly dispersed aqueous system serving as the structured medium in which the biochemical processes take place. The prevailing biochemistry, then, may not necessarily bear any resemblance to the relatively simple chemistry of the same molecular moities in dilute, bulk solution. No wonder, then, that a study of cell functioning on the molecular level must now begin with an understanding of how interfaces in general affect the struture and properties of water (and aq. solutions.)

In the older literature (say, before 1925) - the idea that a solid surface might alter the structure of an adjacent liquid to a significant extent was quite readily appreciated -- notwithstanding the fact that the evidence provided for such structural effects was often rather weak or circumstantial. Since the mid twenties, however, the notion of "long-range ordering" in liquids near surfaces fell from favor for a variety of reasons. The Debye-Huckel theory of dilute aqueous solution of electrolytes was spectacularly successful without making any specific reference to the detailed structure of water - a fortunate circumstance as not even an approximate, first-order theory of liquid water existed at the time of the original Debye-Huckel paper. At that time, most (but not all) studies of liquid water, for instance by x-ray diffraction, found no evidence whatever for long-range ordering in the liquid and thus it did not seem unreasonable to conclude that "water is water is water", right up to any interface, and that for many or most purposes water might be treated as a continuum dielectric fluid with no structural

characteristics. Furthermore, as far as interfaces are concerned, the theory of Deryaguin-Landau-Verwey-Overbeek (at the time of WW II) for colloidal systems was enormously successful without any reference to specific structural aspects of water. [It is of interest to note that Deryaguin did *not* ignore possible interfacial structure modifications. In fact, as early as 1933 Deryaguin published papers showing long-range modifications of water near solid interfaces: over nearly five decades a great many of his roughly 1000 papers have continued to explore the nature and extent of long-range structure.] The idea that an interface might significantly affect the structure of the adjacent water became notably unpopular and only during the past one or two decades have serious attempts been made to re-examine the structural properties of interfacial water. However, at this time a considerable number of investigators would agree that there does indeed exist evidence for structural effects in water (and aq. solutions) induced by most interfaces. What is missing is a consensus opinion as to how far from the interface such structural effects may propagate into the liquid and what type of structural effects are indeed operating. Again, we are seriously hampered by not knowing the detailed structure of bulk water (and aqueous solutions.)

The behavior of dispersed aqueous systems is enormously complicated. Thus, it is extremely difficult to disentangle the effects of the multitude of classical forces which operate in such systems from the specific effects due to a possible long-range structural effect of the surfaces on the adjacent water structure. It is easy to understand, therefore why many (or most) authors have ignored the solvent structural effects in favor of studying more immediately accessible, "classical" effects. However, a growing number of investigators are paying some attention to the role of the solvent structure; among those currently most active are Israelachvili (1977 - 1992) and other investigators working with surface-force balance devices. See also the numerous writings by Parsegian and co-workers (1976 - 1992), van Oss and co-workers (1991, 1992) and the myriad of papers by Deryaguin, Churaev and colleagues spanning many decades.

THE NATURE OF VICINAL WATER.

It appears that most (and possibly ALL) solid interfaces in contact with an aqueous phase create vicinal water. The properties of such interfacially modified water differ from the equilibrium and transport properties of the corresponding bulk water (and solutions) and hence it must be concluded that the structure of the vicinal water also differs from the (still unknown) structure of the bulk aqueous phases. The principal questions regarding vicinal water are: 1) to what extent do the properties differ from the bulk; 2) what is the geometric extent of the structurally modified layers; 3) how does the energetics of vicinal water differ from the bulk, and 4) what is the difference in structure between bulk and vicinal water. For detailed considerations of these and related questions the reader is referred to the writings by Etzler, Wiggins, Peschel, Low and others, as well as the studies by the present author. Below are outlined briefly some of the more unusual properties of vicinal water -- including the existence of thermal anomalies in a great variety of properties.

Etzler and Fagundus (1983, 1987) have carefully measured the density of vicinal water in narrow pores of a silica gel. The density is distinctly lower than that of the bulk phase -- by as much as 3 (to 4) %. To compress bulk water 3% would require a pressure of about 750 atm. and to achieve a 3% expansion of the bulk would require heating the water from about room temperature to 70 °C. The density of the vicinal water assumes its lowest value near the actual interface (or at least within a few molecular layers of the interface) and decreases (probably roughly exponentially) as a function of distance from the interface; a "decay-length" of say 30 (to 50) molecular layers may be involved (i.e. a drop of 50 % in the degree of "vicinal ordering" over distances of about 100 Angstrom = 10 nm, or 0.01 micron.) Such distances *far exceed* most previous estimates of the depth of structurally modified interfacial water which traditionally have been taken to be merely one to three molecular layers.

The low density of vicinal water has been used to explain an unexpected volume contraction observed when dispersions of rather inert particles settle out of an aqueous suspension. Thus we have shown (Drost-Hansen, Braun et al. 1987) by high-precision dilatometry that when suspensions of Polystyrene (PS) spheres settle, a distinct volume contraction occurs. This observation is readily understandable if it is assumed that in the suspended state each particle is surrounded by a "vicinal hydration shell". As the particles settle, these hydration shells overlap and the modified water in the overlap-region is converted to bulk water; as the bulk water has higher density (and thus lower specific volume) a volume contraction takes place. From these volume contraction data it is possible to obtain rough estimates of the water layer thicknesses; typically values are of the order of 300 - 400 Å (or about 100 molecular layers) in excellent agreement with independent estimates based on a variety of other methods. It is of interest to note that *similar volume contractions were observed in a study of the settling of silica particles.*

The specific heat of water is remarkably high (1.0 cal/gram °C) compared to most other liquids -- the result of its high degree of structure reflecting the extensive H-bonding. Measurements of the specific heat (c_p) of vicinal water (Braun and Drost-Hansen, 1976, Etzler, 1988 Etzler and Connors 1990, 1991) have shown even larger values than observed in the bulk, namely about 1.25 cal/gram °C or 25 % larger ! Thus it must be concluded that vicinal water is notably more structured than the bulk. The fact that the specific volume of vicinal water is greater than that of the bulk, and the larger degree of structuring required to explain the enhanced specific heat suggest that vicinal water likely resembles ice (Ice-Ih) -- at least in the sense of being more open and more structured. Etzler (1983) has proposed a statistical mechanical theory of vicinal water in which the increased specific heat is explained in terms of a displacement in the distribution of the "connectivity" of the H-bonds of the vicinal water molecules.

In connection with the increased values for c_p it is also of interest to point out that we have observed essentially identical values for c_p of water adjacent to such chemically and structurally different surfaces as quartz, glass, activated charcoal, diamond and a zeolite. In fact, this behaviour has been confirmed in many other studies: *the specific detailed chemistry of the solid interface plays only a minor role (if a role at all) in the formation of vicinal water structuring at interfaces!* We have named this phenomenon the "*Paradoxical Effect*" because of its unexpected nature. In this connection, however, it should be noted that of course the specific nature of the surface chemistry does indeed play a crucial role in the short-range, highly energetic interactions which determine the nature and extent of the innermost ("primary") hydration structures -- i.e. all the aspects of the classical hydration of surfaces. Another example of the Paradoxical effect was mentioned earlier in this Section, namely that the same volume contraction is observed for the settling of Polystyrene spheres and silica particles.

Over the past five to ten years, the evidence for vicinal water has become greatly strengthened through the studies by such investigators as Etzler, Kurihara and Kunitake (1992), and several others. A recent example of an investigation suggesting truly long range effects of an interface on the adjacent water structure is the paper by Yanagimachi, Tamai and Masuhara (1993.) The authors have examined the rate of proton transfer of 1-naphthol at the sapphire/water interface by a total internal reflection fluorescence method. FIG. 1 shows the rate constant as a function of the distance from the interface. A notable reduction in rate is observed over distances of the order of 100 to 200 nm - in other words 1000 to 2000 Å or roughly 300 to 600 molecular diameters. Such large distances have been invoked earlier by other authors (for instance, Alpers and Hühnerfuss, 1983, Hühnerfuss (1983) and Hühnerfuss et al. 1983; see also Drost-Hansen, 1982) and this range for the vicinal water is indeed consistent with our own recent Photon Correlation Spectroscopy data on the hydration of Polystyrene sphere suspensions (to be discussed in the last Section of this Report.)

RATE CONSTANT OF THE PROTON TRANSFER
REACTION OF 1-NAPHTHOL IN AQUEOUS
SOLUTION AT THE WATER/SAPPHIRE INTERFACE.
DATA BY YANAGIMACHI ET AL., CHEM. PHYS. LETT.
201, p. 115 - 119, 1993. *NOTE THE LARGE DISTANCE
FROM THE INTERFACE OVER WHICH THE REACTION
IS AFFECTED.*

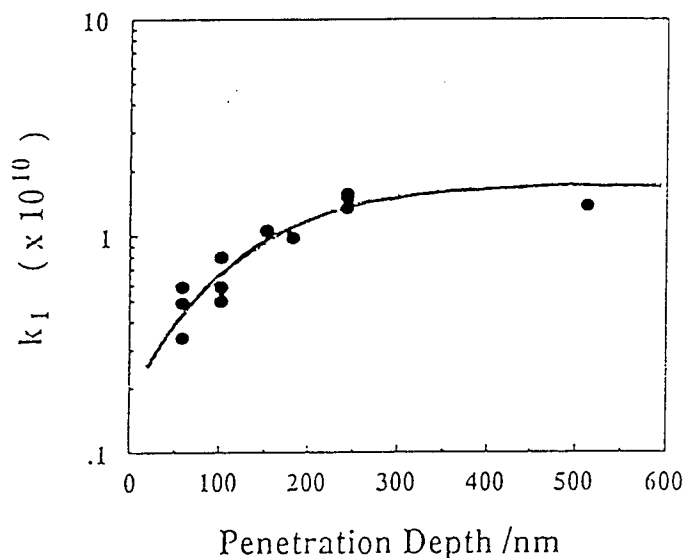


FIG. 1

ARRHENIUS GRAPH: LOG(VISC.) VS. RECIPROCAL
ABSOLUTE TEMPERATURE; WATER BETWEEN QUARTZ
PLATES SEPARATED (IN ORDER TOP TO BOTTOM) 30, 50,
70, AND 90 nm. DATA BY PESCHEL AND ADLFINGER, 1977

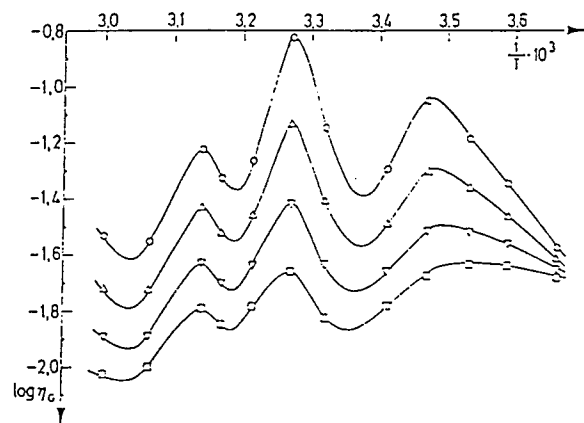


FIG. 2

ION DISTRIBUTION: K^+/Na^+ FOR EQUIMOLAR
K AND Na SALTS IN THE VICINAL WATER OF
PORES IN SILICA GEL AS A FUNCTION OF THE
TEMPERATURE. DATA BY WIGGINGS, 1975.

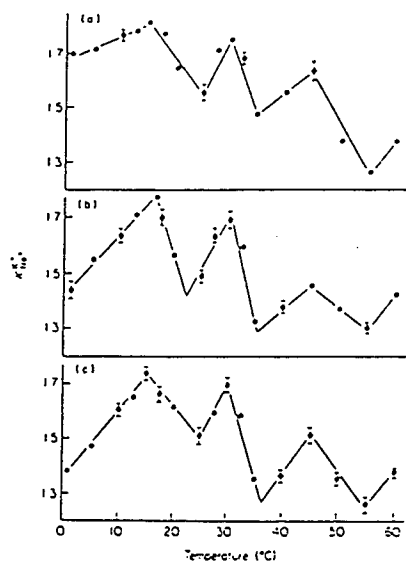


FIG. 3

TEMPERATURE DEPENDENCE OF THE
SELECTIVITY COEFFICIENT, K_{Na}^{K} , IN
RAT KIDNEY CORTEX SLICES. DATA:
WIGGINGS, 1975.

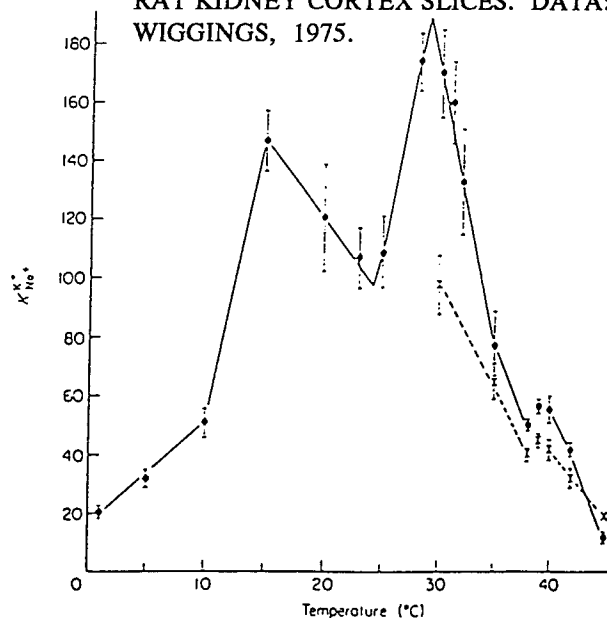


FIG. 4

THERMAL ANOMALIES.

One of the most characteristic features of vicinal water is the existence of thermal anomalies in the properties of large surface-to-volume ratio systems in which vicinal water is present. Typical examples of anomalies are more or less abrupt changes in the slope of a property [when plotted against temperature] over a rather narrow temperature range, say one (to two) Degrees. Between the melting and boiling points of water no less than four such transition ranges occur, namely around $14 - 16^{\circ}$, $29 - 32^{\circ}$, $44 - 46^{\circ}$ and $59 - 62^{\circ}\text{C}$. (The transition temperatures, T_k , are sometimes referred to as the "Drost-Hansen thermal anomaly temperatures".) While the anomalies are extremely well documented it is not at all obvious what molecular processes underlie these transitions; we have previously assumed that they represent higher-order phase transitions of the vicinal water structures but while not an unreasonable assumption we have no firm proof for this. (In fact, a recent neutron-scattering study [Davies, Dore, and Drost-Hansen, to be published, 1993] of water in porous silica gel did find that the water structure at the silica/water interface is indeed changed as expected for vicinal water, but no evidence was found for a phase transition (in any "crystallographic" sense) of this differently structured water near 30°C .)

Over the years a great number of studies have been reported showing sometimes dramatic evidence for the thermal anomalies. Using an early version of a high-precision force-balance, Peschel and co-workers (1971, 1979) have measured the disjoining pressure between two highly polished quartz plates immersed in water and various dilute solutions. For pure water, for instance, the disjoining pressure as a function of temperature goes through very distinct, sharp maxima and minima (the minima occurring near T_k .) Similarly, the viscosity of the water between the plates goes through somewhat broader maxima and minima, again relating to T_k ; (Peschel and Adlfinger, 1969) see Fig. 2. In view of these extreme examples of temperature effects on the viscosity of vicinal water it is perhaps not surprising that the viscosity of a large number of aqueous polymer solutions also show dramatic temperature responses. By the same token, in fact, much of the rheology of aqueous dispersed systems must be expected to show complicated responses to temperature; as will be discussed briefly below. Subsequent to the force-balance measurements by Peschel et al., Israelachvili has notably improved the force-balance method and the studies by Israelachvili and coworkers (see, for instance, 1977, 1986, 1987, 1992) have revealed a wealth of information regarding the nature of the interfacially modified water. Regrettably, no detailed studies appear to have been published where this improved surface-force balance has been used for closely spaced temperature measurements as would be necessary to delineate the thermal anomalies of the vicinal water.

Among the many reported studies of thermal anomalies the results by Wiggins (1975, 1979) deserve special mentioning as the implications for cell physiology of Wiggins data are highly significant. Wiggins measured the distribution of K and Na ions (from

equimolar solutions of the two kinds of salts) between the vicinal water in the pores of a silica gel and the outside, bulk solution. Her results are shown in Fig. 3. Note first the values of the ion partitioning coefficient for K/Na: apparently the vicinal water enhances the concentration of the K ions at the expense of the Na ions. This is of course qualitatively exactly the essence of cell functioning in nearly all eukaryotic cells but achieved here without any membrane or membrane-situated, active transport "ion-pumps". Note also the sharp peaks in the partition coefficient near the thermal transition temperatures. Because of the signal importance these findings may have for cell volume regulation we have repeated Wiggins measurements (Huertado and Drost-Hansen, 1979) and confirmed, quantitatively, her findings for the K/Na ions. That similar processes may indeed play a major role in cell physiology is illustrated in Fig. 4: instead of using silica gel Wiggins used slices of rat kidney cortex and once again measured the K/Na partitioning as a function of temperature. Note that qualitatively the results resemble those observed in Fig. 3 with the silica gel, namely sharp peaks near 15 and 30 °C. The obvious conclusion is that vicinal water must play a major role in the ion distribution between a cell and the surrounding fluid! For a discussion of these results see the papers by Wiggins et al., and by the present author (1976, 1985.) Independently, Etzler and Liles (1987) has demonstrated the existence of similar peaks in the distribution of Li and K ions between a silica gel and both aqueous solutions and D₂O solutions.

Thermal anomalies are also frequently seen in the properties of aqueous solutions of large macromolecules. For instance, a substantial number of such anomalies are found in reaction rates of various enzymes (see, for instance Drost-Hansen, 1978 and Etzler and Drost-Hansen, 1979.) In most of these cases, the temperatures where the anomalies occur are indeed the same temperatures at which anomalies are seen in the properties of vicinal water at the solid/water interface. We return to that aspect later in this report.

A vast literature exists on the hydration of proteins, particularly in solution, but while these studies include extensive viscosity measurements there is a notable paucity of reports on the viscosity of macromolecules in aqueous solutions measured as a function of temperature, - especially at closely spaced temperature intervals. Interestingly, however, a number of other rheological studies have been reported on aqueous biopolymer systems at closely spaced temperatures, particularly by investigators in the food industry.

As an example of unexpected temperature effect, FIG. 5 shows the viscosity of a dilute actomyosin solution as a function of temperature during slow heating (1 °C per min.) at a shear-rate of 1.02 sec⁻¹ (Wu et al., 1985.) Note the distinct minimum near 30 °C and the very low value around 45 °C. Somewhat similar results are shown in FIG. 6 and FIG. 7, respectively for the rigidity of actomyosin solutions during heating (at 1 °C/min.) at low shear-rate: 0.0684 sec⁻¹, and changes in rigidity of actomyosin

VISCOSITY OF ACTOMYOSIN SOLUTION.
HEATING RATE: 1 °C/MIN. SHEAR-RATE
1.02 SEC⁻¹; CONCENTRATION: 14 MG/ML.
DATA: WU ET AL., J.FOOD TECH., 50, 1985.

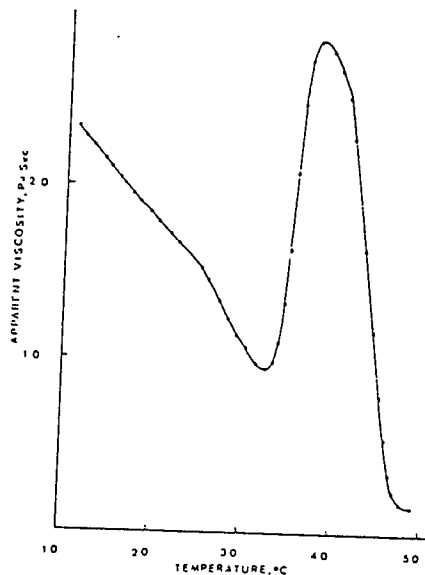


FIG. 5

VISCOSITY/RIGIDITY ACTOMYOSIN
SOLUTIONS; HEATING RATE: 1 °C/MIN.
SHEAR RATE: 0.0684 SEC⁻¹. DATA:
WU ET AL., (IBID)

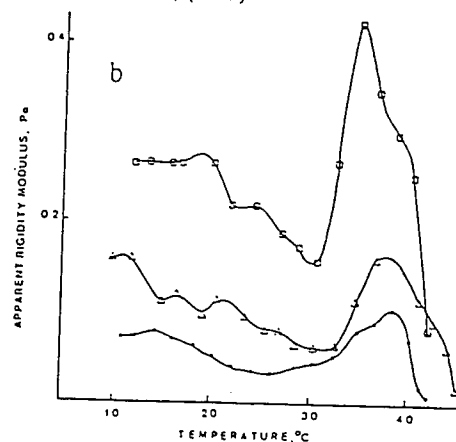


FIG. 6

RIGIDITY OF ACTOMYOSIN PASTES
(AT DIFFERENT CONCENTRATIONS)
DURING HEATING (°). 1 °C/MIN. DATA:
WU ET AL., (IBID.)

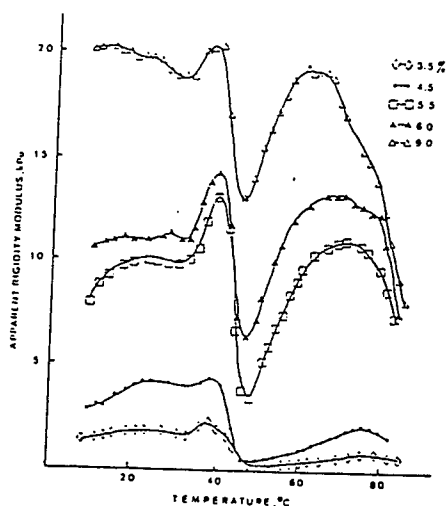


FIG. 7

RIGIDITY OF MINCED FISH PASTE;
HEATING RATE: 0.5 °C/MIN. DATA:
MONTEJANO ET. AL, JOURNAL OF
RHEOLOGY, 27 p. 557 - 579, 1983.

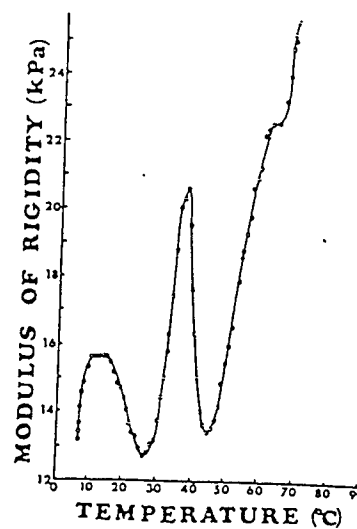


FIG. 8

pastes (being heated at 1 °C/min.) The anomalies at both 30 ° and 45 °C are pronounced.

Other rheological studies of concentrated protein/water systems from the Laboratory of Hamann and Lanier are shown in FIG. 8 where the modulus of rigidity of a minced fish paste is plotted as a function of temperature: again distinct minima near 28 °- 29 °C and 45 °C are observed and these anomalies persist at different rates of heating as shown in FIG. 9.

Since 1991 we have measured the viscosities of a number of solutions of both model polymers and biologically important macromolecules. Thus measurements have been made with a Brookfield variable shear-rate cone-&-plate viscometer on solutions of such model polymers as Polyethylene oxide (PEO, = PEG), Polyvinyl pyrrolidone (PVP), and Dextran as well as on solutions of BSA, fibrinogen and cytochrome-c. Measurements have also been made on blood plasma and serum. In addition to varying the shear-rates in these experiments, we have also made measurements over rather large temperature intervals (usually from about 20 °C and up to 50 or 60 °C.) Nearly all measurements have been made at closely spaced temperatures: usually at two [or one] degree intervals.

The viscosities of solutions of larger polymers, including many of biochemical interest, usually depend very strongly on the temperature. Over the past few years we have collected a large amount of such data in connection with the AF SUMMER RESEARCH PROGRAMS. Measurements have been made on aqueous solutions of a variety of model polymers and biopolymers (such as albumin, fibrinogen, cytochrome-c and blood plasma and serum.) In all the cases, A) thermal anomalies have been found at one or more of the thermal transition temperatures for vicinal water (T_k); and B) the observed thermal anomalies are very strongly shear-rate dependent: as the shear-rate increases the degree of change in the viscosity decreases, specifically, the thermal anomalies become far less pronounced. Again this is consistent with the idea that the vicinal hydration structures are very readily disturbed or destroyed. As an example of the temperature effects on the viscosity of a polymer solution, FIG. 10 shows the viscosity of a 5 % Dextran solution, (MW 82 kDa.) as a function of temperature. The anomaly near 30 °C is clearly seen. A detailed paper describing all our viscosity measurements is in preparation.

The experimental evidence for vicinal water structuring at the solid/water interface is now very substantial while the evidence for thermal anomalies in the properties of vicinal water is even more firmly established. It is obvious that the thermal anomalies reflect the presence of vicinal water and vice versa: the presence of vicinal water makes it likely that thermal anomalies exist in some properties of the system. Note that the properties of *bulk* water (and bulk aqueous solutions of small solutes) do not reveal any anomalies as a function of temperature at T_k (i.e. at the temperatures of the thermal anomalies for vicinal water.) On the other hand, the properties of *bulk*

RIGIDITY OF FISH PASTE FOR VARIOUS HEATING RATES; MEASURED IN THE ORDER: a, b, c. DATA BY MONTEJANO ET AL., (IBID.)

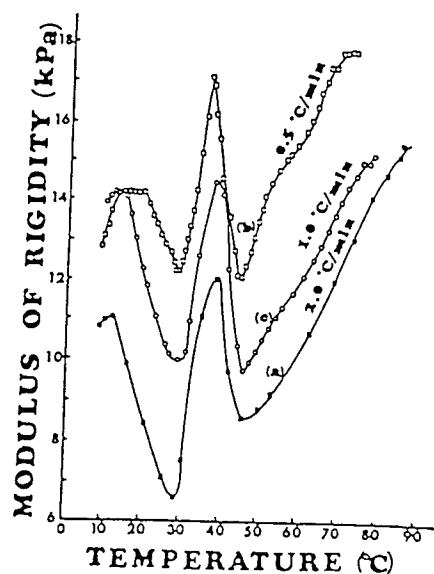


FIG. 9

VISCOSITY OF 5 % DEXTRAN SOLUTION (MEASURED IN BROOKFELD VISCOMETER) AS FUNCTION OF TEMPERATURE. SHEAR-RATE: 90 SEC⁻¹. DATA: DROST-HANSEN AND CAMACHIO, UNPUBL. 1992.

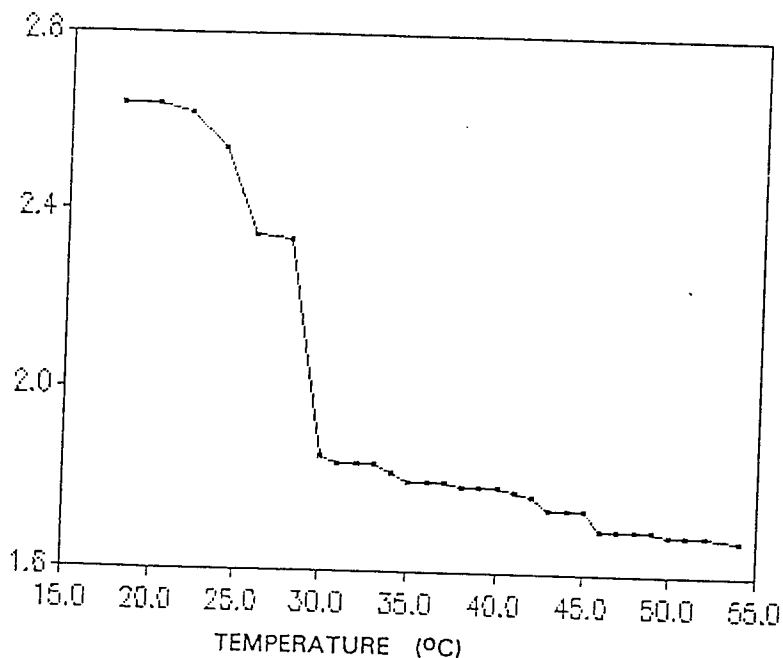


FIG. 10

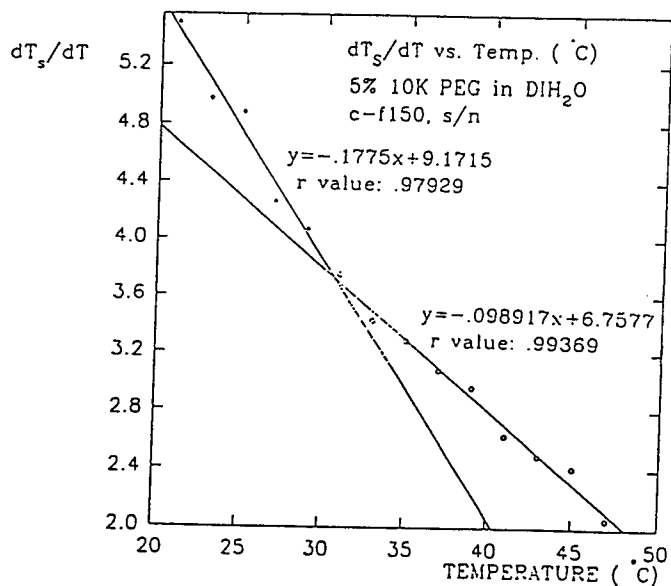


FIG. 11

VISCOSITY OF 10 % PEO SOLUTIONS AS FUNCTION OF MW AT 20 AND 26 °C. [SIZE 200 VISCOMETER.] DATA: VOUGHT AND DROST-HANSEN, UNPUBL. NOV. 1992

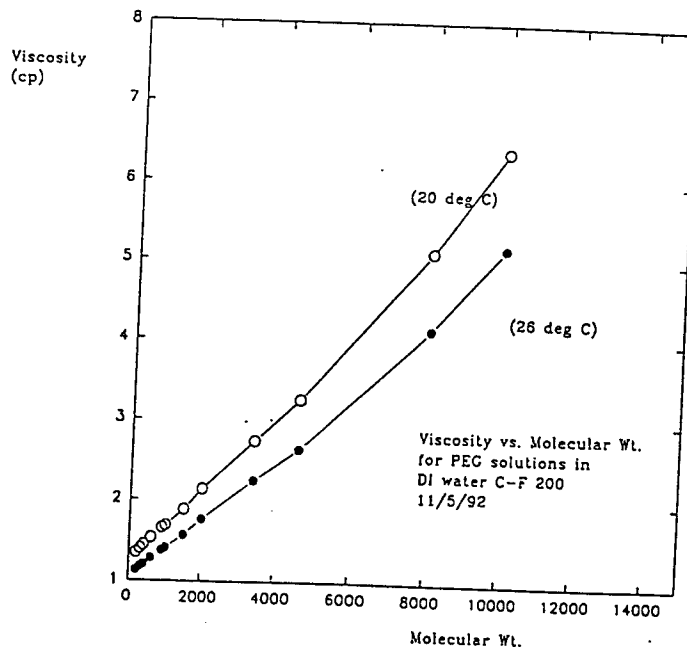


FIG. 12

aqueous solutions of some macromolecules, for instance many enzymes, do show anomalies at T_k (notably in reaction rates) suggesting that these solutes are vicinally hydrated in (bulk) solution. In view of this it is of interest to consider if there exists a critical molecular size above which most (or all) macromolecules in solution are hydrated in the same manner that a solid surface is vicinally hydrated. We have considered this question for some time (Etzler and Drost-Hansen, 1983) and based on an examination of data from the literature have concluded that indeed a critical molecular weight (MW) range may exist above which the molecules are vicinally hydrated. This critical MW range appears to be in the range from about 600 (or 1000) to a few thousand Dalton. The reader is referred to the references listed at the end of this report for more details about this conjecture; in the present study we have examined the viscosity of some polymer solutions, mostly Poly-ethylene oxides [PEO - sometimes also referred to as PEG, Polyethylene glycols] as function of MW using both capillary and variable shear-rate cone-&-plate viscometers. The question of vicinal hydration of the macromolecules in the cell is of obvious importance to all of cell biology considering the prevalence of biopolymers in cellular systems: solid-like interfaces abound in the cell, for example the endoplasmic reticulum and the membrane surfaces of the cell wall and the various organelles. IF, in addition, to these vicinally hydrated "solid" surfaces the larger biopolymer molecules are also vicinally hydrated, it becomes difficult to see how one can be anywhere within a living cell without the aqueous environment being vicinal water!

EXPERIMENTAL. PART A: VISCOSITY MEASUREMENTS.

To elucidate the nature of macromolecular hydration in aqueous solutions -and its likely role in determining plasma viscosities - measurements were made on a number of polymer solutes as functions of concentration, temperature, molecular weight (MW) and shear rates. Most of the measurements were made on polyethylene oxide (PEO) polymers (= polyethylene glycols, PEG) with MWs ranging from about 300 to 300 000 Dalton.

As mentioned briefly in the Introduction, our preliminary studies have suggested that a distinct change in the nature of the hydration may occur for macromolecular solutes in water in the MW-range of about 1000 Dalton. To investigate this possibility for PEO, measurements were made on various PEO polymers covering the suggested critical MW-range at various temperatures (in some cases only two temperatures, - see below) in order to obtain the apparent energy of activation for the flow process (ΔE^*). It was assumed that the flow of the PEO solutions were essentially newtonian, -- or, at least, that the non-newtonian effects would only slightly affect the difference in flow times at two relatively closely spaced temperatures (say, usually only two to six degrees apart.)

Unless otherwise stated, the measurements discussed in this Part of the report were made with capillary viscometers of the Cannon-Fenske or Ubbelohde type with the following specifications:

Viscometer A size 150, serial # I795
 B size 200, serial # A284
 C size 100, serial # D364

At each temperature at least three determinations were made with each viscometer. RSD were calculated and usually found to be 0.5 % or less.

The viscosity measurements were all made in a constant temperature water bath with heavy external insulation (including the top surface of the bath) through which was cut an opening for use as a viewing port. Temperatures were generally constant throughout each run to within ± 0.01 °C (or better.) Viscosity data for pure water and values for the apparent energies of activation were taken from Korson, Drost-Hansen and Millero (1969.)

Materials: the PEO samples were obtained from the Aldrich Company (except for the 14 100 Dalton sample from American Polymer Standards, Corp). The polymers were used as received without any purification or fractionation. The MW estimates listed are those provided by the Distributor. All solutions were prepared by weight.

To utilize the observed flow times (measured to within 0.01 sec.) for the calculation of relative viscosities, density measurements were made on all solutions prepared by simple pycnometry, using a Gay-Lussac type pycnometer; the samples were

equilibrated in a separate water bath at various temperatures covering the range of temperatures used for the viscosity measurements. In general the estimated precision on the density measurements is ± 0.0001 g/ml.

No surface tension or kinetic energy end-effect corrections were applied to the viscosity data as the primary use of these data were for comparative purposes on systems differing only slightly in the flow parameters; any corrections were estimated to be minimal.

The two main features of vicinal hydration examined in this study are:

- a) the existence of thermal anomalies in solution viscosities at the vicinal water thermal transition temperatures, T_k , and
- b) the possibility that a critical macromolecular size exists above which aqueous polymers are vicinally hydrated.

Once again the reader is reminded that our interest is not primarily in the "classical" type of primary polymer hydration but rather in the far more subtle type of vicinal hydration which is readily observed near most [or all] water/solid interfaces.

Fig. 11 shows the temperature coefficient of the flow times for a 5.0 % aq. solution of PEO, MW = 10 000 Dalton. The ordinate is the *change in flow time per two degree ($^{\circ}\text{C}$)*; the abscissa is the temperature. It is obvious that a change in slope occurs at $31 (\pm 1) ^{\circ}\text{C}$. As the densities of the solutions generally have been found to change in a perfectly smooth manner with temperature, the change in slope seen in Fig. 11 must be due to a change in the energy of activation for the viscous flow of this solution. The difference in the slopes below and above the transition temperature corresponds to a difference of 257 cal/mol in the energy of activation, or a change of 5.6 % in ΔE^{\ddagger} (from $\Delta E^{\ddagger} = 4714$ cal/mole to 4457 cal/mole.) A comparison with the flow properties of pure water is shown in the table below;

$T_{av} (^{\circ}\text{C})$	25	38.5	Ratio [25 $^{\circ}$ /38.5 $^{\circ}$]
$\Delta E^{\ddagger}_{\text{water}} \text{ (CAL/MOLE)}$	3700	3560	1.039
$\Delta E^{\ddagger}_{\text{polym.}} \text{ (CAL/MOLE)}$	4714	4457	1.058
Ratio [polymer/water]	1.274	1.228	1.037

Further discussion of thermal anomalies in viscosity data will be presented at the end of this Section. Before proceeding it is of interest to examine the effect of Molecular Weight on the hydration properties of polymers in aqueous solution.

As mentioned above, it has been proposed (Etzler and Drost-Hansen, 1983) that macromolecules in aqueous solutions are vicinally hydrated - similar to the vicinal hydration of solid surfaces - but only if the molecules are sufficiently large! The critical size appears to be around 1000 Dalton. This idea was suggested on the basis of a variety of measurements reported in the literature, such as the intrinsic viscosity of PEO as a function of MW and the diffusion coefficient of some thirty solutes (Nir and Stein, 1971) plotted as a function of MW. Other examples of dramatic changes in solute properties have been reported by Gekko and Noguchi (1971) from a study of ultrasonic properties of dextrans of different MW: the behaviour of these solutions change notably near 1 (to 2) kDa. Because of the importance of the suggestion that a critical size of macromolecules in solution might exist we have investigated in detail the viscosities of a number of PEO samples with different MW, spanning a range from 300 to 300 000 Dalton. All the measurements were carried out two different temperatures (20 ° and either 25 ° or 26 °C) - so as to allow estimates to be made of the apparent energies of activation for viscous flow. Some of the results are discussed below.

Bailey and Koleski (1976) reported a change in slope of the *intrinsic* viscosity of PEO solutions (as a function of MW) near 2 to 3 kDa. In our own work we have frequently plotted the *actual* viscosities of PEO solutions as a function of MW without noting any distinct change near this MW range; see FIG. 12. In an attempt to provide a more sensitive test of the MW dependence we have measured viscosities of various PEO solutions (with different MW) at two different temperatures in order to examine the effects of MW on the apparent energies of activation for the flow of such solutions. Two sets of data were obtained, using different sizes of viscometers to elucidate any possible effects of shear rate on the activation energies. FIG. 13 and FIG. 14 show some of our results. In both sets of data it appears that the apparent energy of activation levels off above approximately 2000 Da. [Note that the division of the data in each graph into two sets of data was done by inspection and the curves fitted to the points therefore carry little weight.] The scatter in the data for the larger solutes makes a quantitative comparison somewhat uncertain, but it does appear that two flow regimes exist, respectively below and above a MW range centered around 2 kDa. This finding is at least consistent with all the other evidence for a change in polymer hydration in a MW range around 1 to 2 kDa.

That the resulting hydration is indeed similar to the vicinal hydration which occurs at solid/water interfaces is supported by the occurrence of thermal anomalies in the properties of such solutions. as discussed later in this Section.

Other indications of notable differences in solute behaviour of PEO, respectively with MW below and above 1 kD, have come from a recent study by Antonsen and Hoffman (1992.) These authors observe a small, but distinct jump in the amount of bound water/repeat unit between 1 and 2 kD; see FIG. 15. Similarly, transition temperatures from melts of the PEO in water show a dramatic increase around a MW of 1.2 kD (see

APPARENT ENERGIES OF ACTIVATION FOR
VISCIOUS FLOW OF PEO SOLUTIONS, 10 %, AS
FUNCTION OF MW. [SIZE 200 VISCOMETER.]
DATA: VOUGHT AND DROST-HANSEN, UNPUBL.
NOV. 1992.

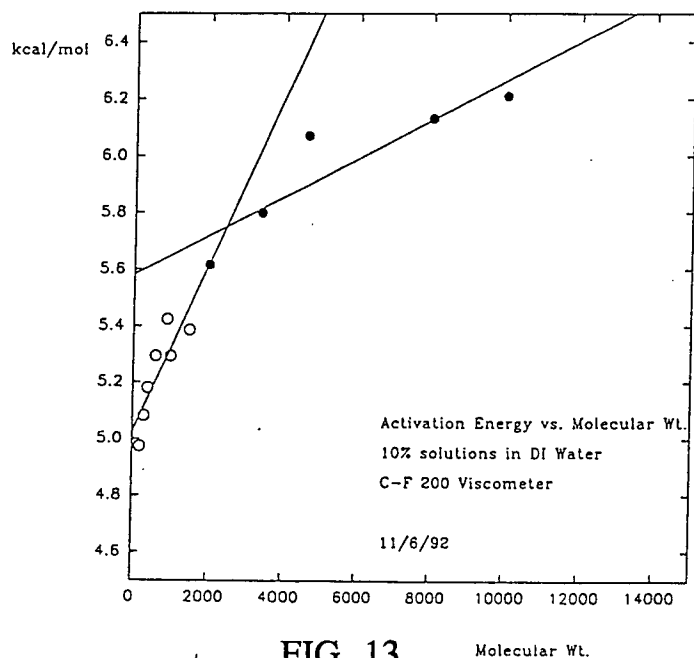


FIG. 13

APPARENT ENERGIES OF ACTIVATION FOR
VISCIOUS FLOW OF PEO SOLUTIONS, 10 %, AS
FUNCTION OF MW. [SIZE 150 VISCOMETER.]
DATA: VOUGHT AND DROST-HANSEN, UNPUBL.
NOV. 1992.

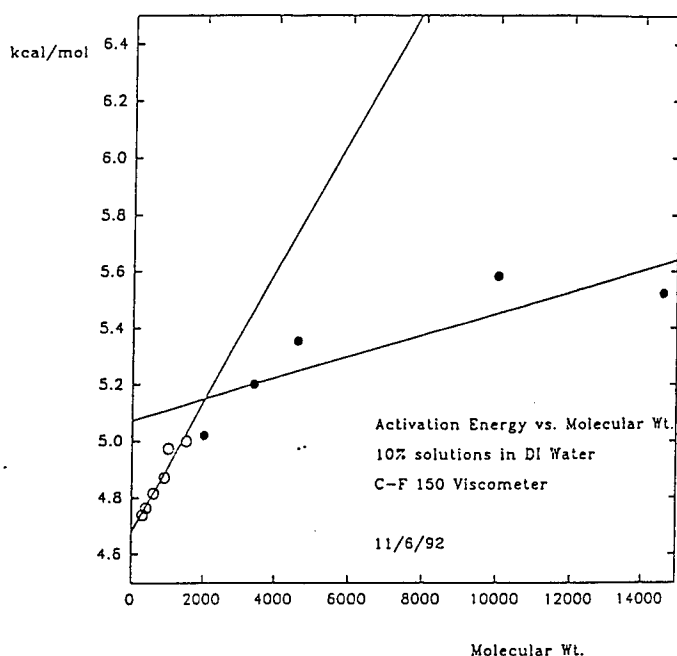


FIG. 14

AMOUNT OF BOUND WATER (PER REPEAT UNIT)
IN 30 % PEO (AND MPEO) SOLUTIONS AS FUNCTION
OF MW. OPEN CIRCLES: PEO; CLOSED: MPEO.
DATA BY ANTONSEN AND HOFFMAN (IN HARRIS, ED.
"POLY(ETHYLENE GLYCOL) CHEMISTRY", PLENUM
PRESS, 1992.)

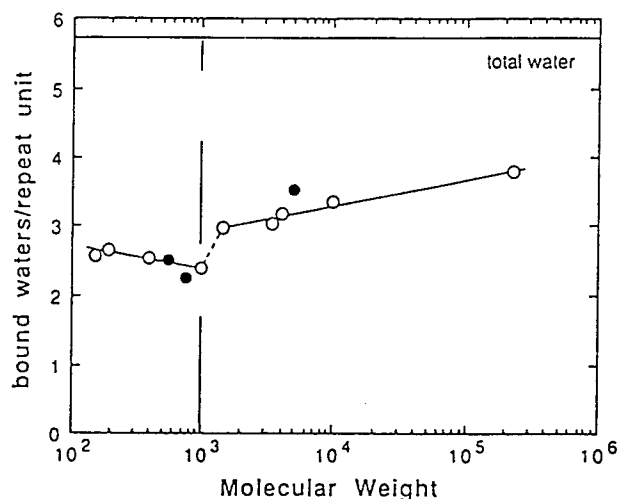


FIG. 15

TRANSITION TEMPERATURE FOR 30 % PEO
SOLUTIONS AS FUNCTION OF MW. DATA BY
ANTONSEN AND HOFFMAN (IBID.)

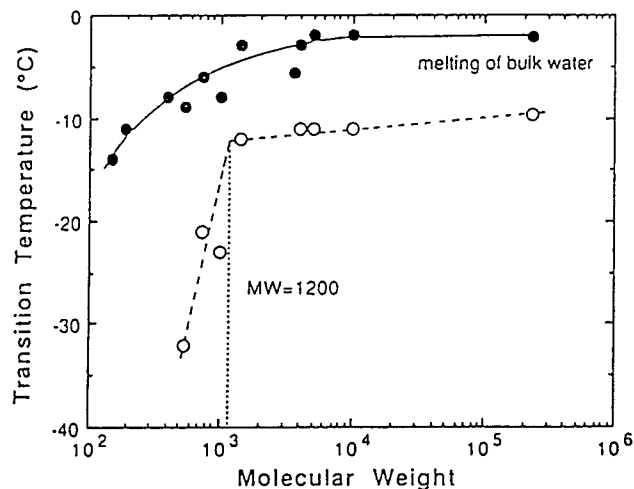


FIG. 16

FIG. 16) and the heats of fusion a similarly distinct jump between 400 and 1000 D. See Fig. 17.

It is of interest also in the study by Antonsen and Hoffman, that large differences exist between data collected upon heating the samples compared to data collected during subsequent cooling of the samples, as shown in Fig. 18. This is eminently consistent with our own measurements on vicinal water: upon heating, a particular vicinal water structure appears to be destroyed (and a new one formed) when heating a sample above one of the critical transition temperatures (T_k) for the vicinal water. Upon cooling, the vicinal water structure is only "regenerated" very slowly; sometimes 24 hrs may be necessary to reform the specific prior structure in question. For a discussion of such hysteresis see the discussions elsewhere by the present author (1971; see also Braun and Drost-Hansen, 1976.)

As discussed elsewhere in this report, the vicinal water -- or at least a significant fraction of the vicinal water -- is extremely sensitive to its past thermal and mechanical history. Thus, heating the vicinal water past one of its transition temperatures will apparently destroy the structure which is stable below that T_k ; upon subsequent cooling down of the sample below this critical point *the original vw structure reforms only slowly*. Similarly, shearing the vicinal water appears to break down the prevailing vw structure [compare for instance the viscosity data by Peschel and Adlfinger, 1970] and again the original vw structure reforms only slowly when the shear is removed.

An entirely different study of MW effects have been reported by Bayer and Rapp (1992) who measured the ^{13}C -NMR-Relaxation of free (and of bound) PEO as a function of the MW. Their results are shown in FIG. 19. It is obvious that a decisive "levelling off" in T_1 occurs for the free PEO at about 1 - 2 kDa.

It should be noted that much of the evidence for a change in solute behaviour of polymers near a MW of 1 kDalton has come from studies on PEO, both those described in this report as well as some derived from the literature. However, it is unlikely that the change in solute properties merely reflect some peculiarity of the PEO polymers. Recall, for instance, the rather abrupt change in $d[\text{diff.coeff.}]/d[\text{MW}]$ near approx. 1 kD reported by Nir and Stein; this study was based on diffusion data from about 31 different solutes, ranging from He to very large proteins. Note also, that remarkably sharp changes in solute behaviour (especially ultrasonic properties) near 1 kD were observed by Gekko and Noguchi for solutions of Dextrans. This observation is likely of considerable importance because of what has been suspected to be widely differing types of the hydration between PEO and Dextrans. (Recall, for instance, that two mutually *immiscible* liquid phases exist at room temperature between aqueous solutions of PEO and Dextrans -- even though each may be 90 % water.)

TOTAL HEAT OF FUSION FOR 30 % SOLUTION OF PEO.
DATA BY ANTONSEN AND HOFFMAN (IBID.)

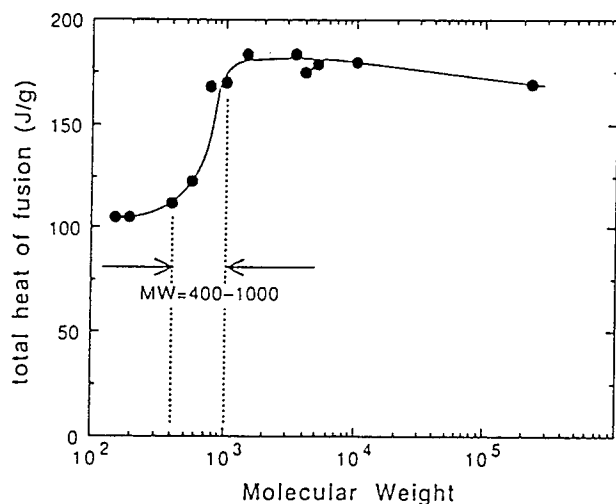


FIG. 17

AMOUNT OF BOUND WATER PER REPEAT UNIT
IN 30 % PEO SOLUTION AS FUNCTION OF MW. DATA
BY ANTONSEN AND HOFFMAN (IBID.) NOTE:
DIFFERENCE BETWEEN HEATING AND COOLING.

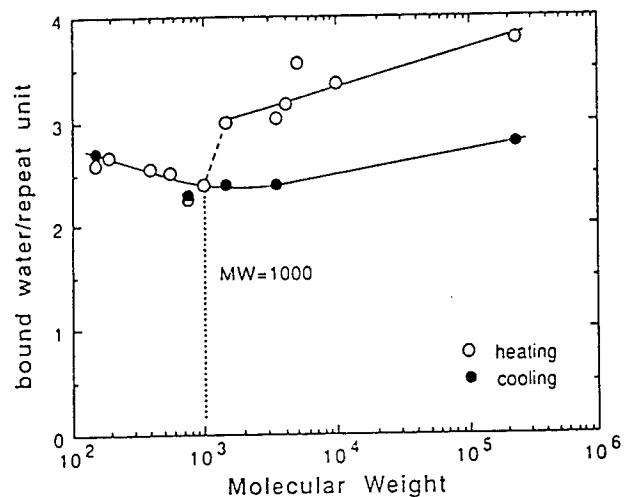


FIG. 18

¹³C-NMR-RELAXATION TIMES T_1 OF FREE
PEO (a) AND OF PS-IMMOBILIZED PEO (b) AS
FUNCTION OF MW. DATA: BAYER AND RAPP,
(IN HARRIS, ED. "POLY(ETHYLENE GLYCOL)
CHEMISTRY" PLENUM PRESS, 1992.)

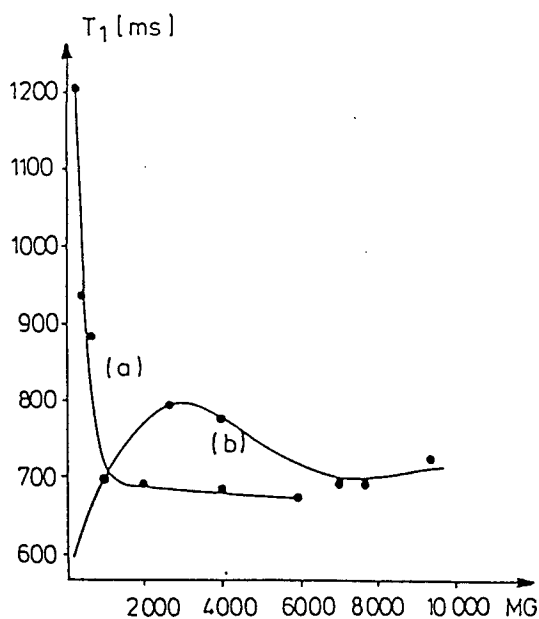


FIG. 19

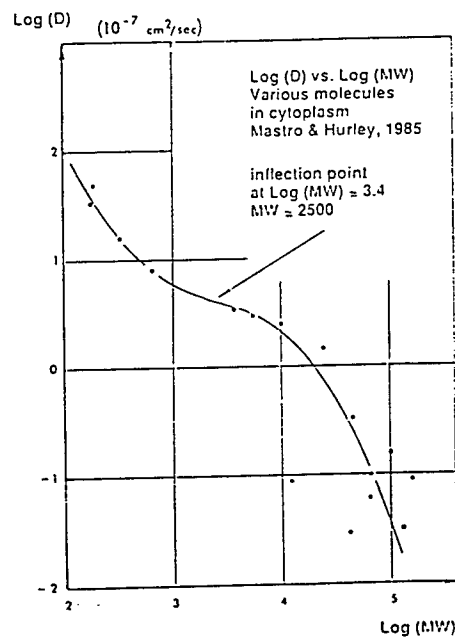


FIG. 20

We have demonstrated that the viscosities of aqueous polymer solutions (for polymers above a certain critical size) strongly suggest the vicinal hydration of the polymers. The significance of this finding to cell biology becomes particularly obvious when recalling the Walden rule: that diffusion coefficients and viscosities are inversely related. Thus it must be expected that the diffusion coefficients for solutes in the cytoplasm reflect the presence of the vicinal water. Mastro and Hurley (1986) have used an ingenious technique to follow the diffusion in cells of various solutes with different MW. Fig. 20 shows their results in terms of the logarithm of the observed diffusion coefficients as a function of the logarithm of the molecular weight of the diffusing species. A *distinct* inflection point occurs at approx. 2500 Da. -- just about the molecular weight range where it is proposed that macromolecules in aqueous solution become vicinal hydrated. This tendency is even more obvious in Fig. 21 where the product of the observed diffusion constant and the viscosity of the aqueous medium is plotted versus the log[MW]: an unmistakable change in slope occurs just about 1 kDa. -- as would be expected if this MW range indeed represents the lower limit for the onset of vicinal hydration.

As discussed above, we have proposed that polymers, above a certain critical size, in aqueous solutions are vicinally hydrated and that the type of extensive hydration found is the same type of vicinal hydration which occurs at the solid/water interface. We base this claim on the observation that thermal anomalies occur in the viscosities of the polymer solutions at [or very close to] the same temperatures where thermal anomalies are found for water near solid interfaces. A few examples of such data (obtained during the summer 1992 at the Clinical Investigation Directorate at Lackland AFB) are presented below.

In FIG. 22 is shown the viscosity of a 5 % PEO solution, measured in the Brookfield viscometer, as a function of temperature. The MW of the polymer was 100 kDa and the speed of rotation of the viscometer cone was 30 RPM [corresponding to a shear-rate of 225 sec^{-1} .] A distinct change in slope of the viscosity is seen near 31 or 32 °C as well as an abrupt change around 45 °C.

The unusual temperature responses are not restricted only to PEO. Recall for instance FIG. 10 for the viscosity of a 5% Dextran solution. In FIG. 23 is shown the viscosity as measured in the Brookfield viscometer, for a 10% Poly(vinyl pyrrolidone) [PVP] solution; MW = 40 kDa., at 6.0 RPM [shear-rate 45 sec^{-1} .]. Distinct anomalies are again seen near the thermal transition temperatures, in this case near 32 and 46 °C.

Anomalies in viscosities are seen also -- sometimes very dramatically -- in solutions of all biopolymers so far investigated! Thus FIG. 24 shows the viscosity of a 5% solution of Bovine Serum Albumin in distilled water, measured at 6.0 RPM [shear-rate 45 sec^{-1} .] A truly dramatic change in slope is seen at 28 °C. Somewhat similar data have been obtained with BSA in 0.9% NaCl solutions. Thus, FIGS. 25 and 26

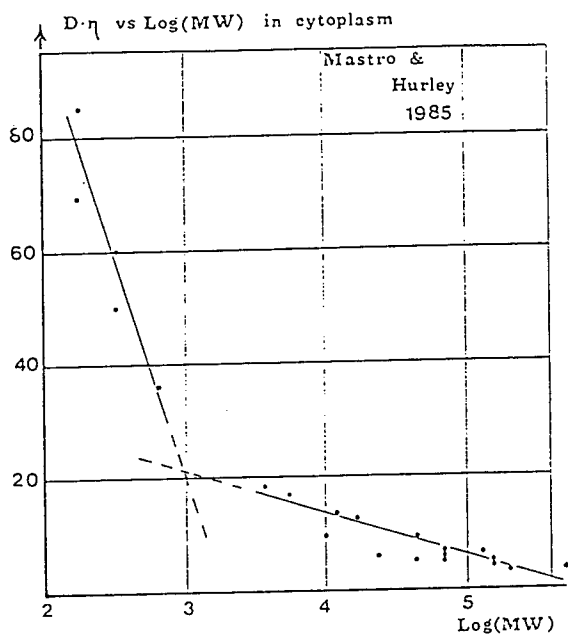


FIG. 21

VISCOSITY OF 5 % PEO, MW = 100 kDa.
AS A FUNCTION OF TEMPERATURE.
SHEAR-RATE 225 SEC^{-1} . DATA:
DROST-HANSEN & CAMACHO, 1992
UNPUBLISHED.

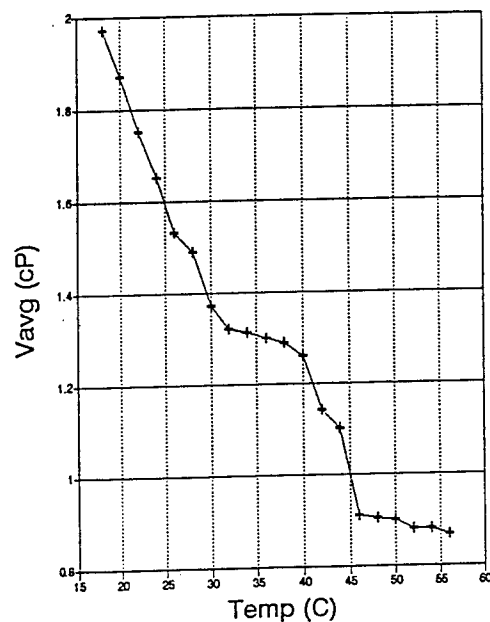


FIG. 22

VISCOSITY OF 10% PVP, MW = 40 kDa.
AS FUNCTION OF TEMPERATURE.
SHEAR-RATE 45 SEC^{-1} . DATA:
DROST-HANSEN & CAMACHO, 1992.
UNPUBLISHED.

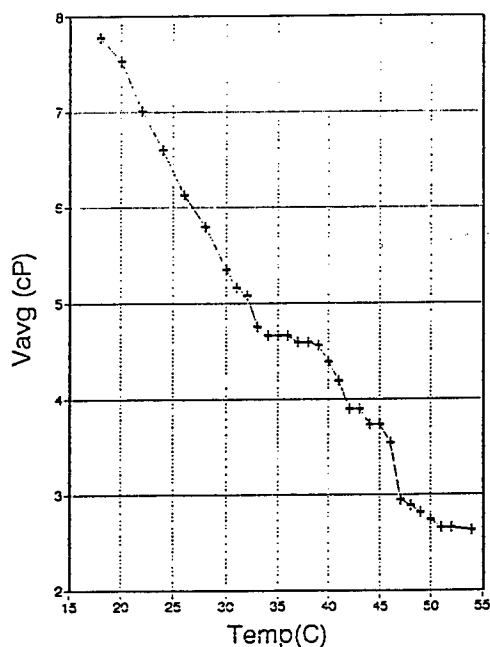


FIG. 23

$\text{LOG}_e(\text{VISCOSITY [cP]})$ OF 5% BSA
IN WATER. SHEAR-RATE 45 SEC^{-1} .
DATA: DROST-HANSEN & CAMACHO,
1992, UNPUBLISHED.

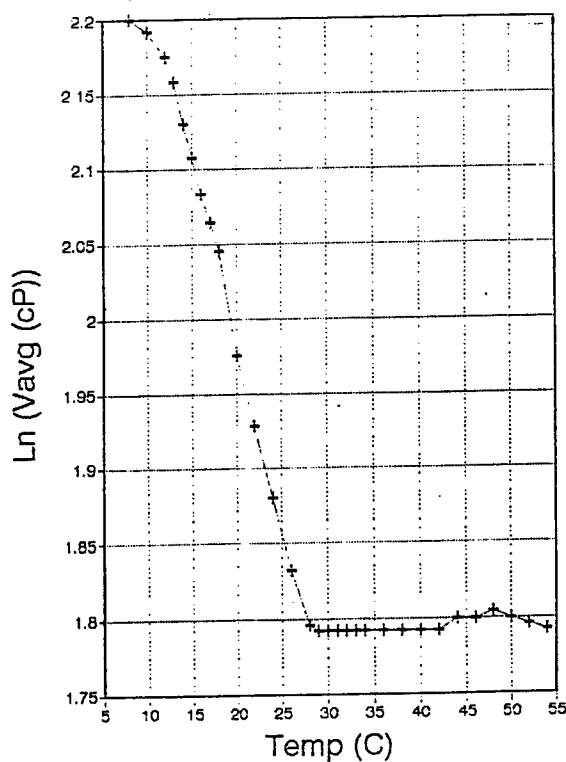


FIG. 24

show, respectively, the viscosities for 5% BSA measured at 3.0 and 30 RPM. Again the temperature range around 30 °C is seen to represent a critical region -- and this is surely can not be caused by any denaturation process of the protein (or all the world's cows would be in big trouble.)

Finally, a large number of viscosity measurements have been made on both mammalian blood plasma and serum. Invariably distinct thermal anomalies are seen in these data. As an example, FIG.27 shows the plasma viscosity of a California Harbor Seal, measured at 6 RPM [shear-rate 45 sec^{-1} .] The drop in viscosity over a 1 ° interval [at 30 °C] is a factor of three ! Compare this with the viscosity of 5% Dextran shown in FIG. 10 in which the viscosity also dropped precipitously at 30 °C. Note as well the abrupt increase above 45 °C. These and a great deal of other viscosity data for plasmas and sera from about a dozen different mammals are being prepared for publication.

In summary: thermal anomalies are seen in the viscosities of a wide variety of polymers in aq. solution. The anomalies occur at the same temperatures where anomalies are seen in various properties of water near solid surfaces. Thus, it seems reasonable to infer that the vicinal hydration of polymers is the same type as that found at the solid/liquid interface. Note also that the thermal anomalies are seen for a wide range of different chemical structures of the polymers (PEO, PVP, Dextran, BSA, and plasma from the blood of a Harbor Seal) as illustrated in this report. This is consistent with the Paradoxical Effect seen for water at the water/solid interface: the *detailed surface chemistry of the solids plays little or no role in the establishment of the vicinal water* [while the surface chemistry of course determines all of the far more familiar innermost hydration processes and electrical double layer effect of dispersed systems.]

VISCOSITY OF 5% BSA IN 0.9% NaCl
AS FUNCTION OF TEMPERATURE.
SHEAR-RATE 22.5 SEC⁻¹. DATA:
DROST-HANSEN & CAMACHIO, 1992
UNPUBLISHED.

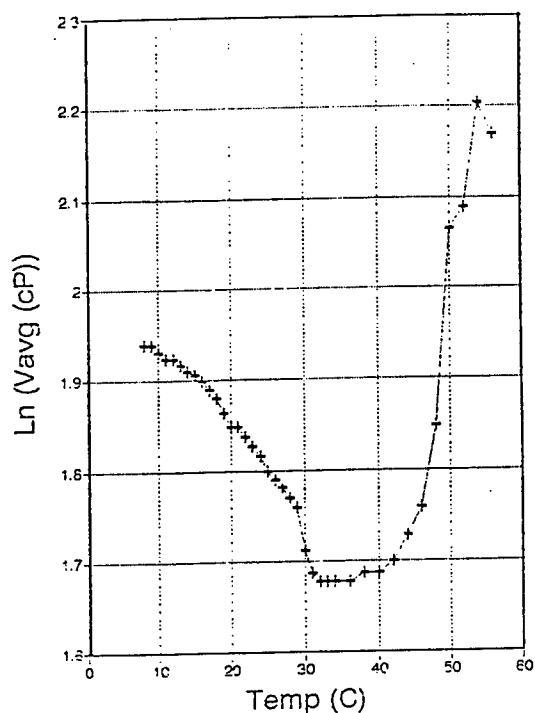


FIG. 25

VISCOSITY OF 5% BSA IN 0.9% NaCl
AS FUNCTION OF TEMPERATURE.
SHEAR-RATE 225 SEC⁻¹. DATA:
DROST-HANSEN & CAMACHIO, 1992
UNPUBLISHED.

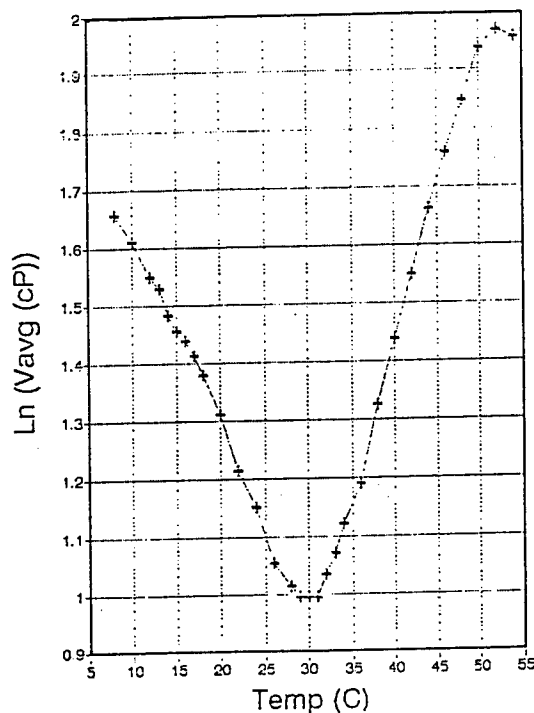


FIG. 26

VISCOSITY OF BLOOD PLASMA FROM
CALIFORNIA HARBOR SEAL.
SHEAR-RATE 45 SEC⁻¹. DATA:
DROST-HANSEN & CAMACHO, 1992.
UNPUBLISHED.

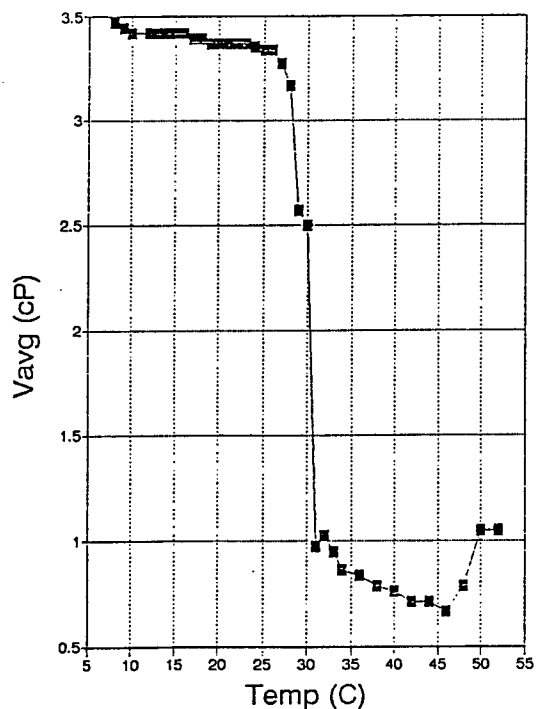


FIG. 27

EXPERIMENTAL. PART B: PHOTON CORRELATION SPECTROMETRY (PCS) (for particle sizing.)

The quantitative treatment of hindered settling -- such as observed in the sedimentation of erythrocytes in whole, anti-coagulated blood -- is generally based on the Stokes law for the sedimentation of a single (spherical) particle. So far, only approximate theories have been developed and only for low concentrations, usually less than one percent solids; no rigorous theory presently exists to account for the settling of concentrated suspensions of non-spherical [let alone non-rigid] particles in non-newtonian fluids. Nonetheless, it appears likely that any ultimate theory of hindered settling must somehow take into account the "effective" diameter of the settling particles -- including the red cells in the case of hindered settling of whole blood. It is proposed that one factor which may influence the overall, apparent "diameter" of particles (including the erythrocytes) is the possible existence of extensive, vicinal surface hydration. This idea is hardly new and over the years it has been severely criticized by many authors; indeed, the evidence for such surface hydration is weak but not entirely without merit. As discussed in the present report - based on our measurements in connection with the AF Grant - and in part based on the viscosity studies carried out during the author's AF Summer Research Programs - vicinal surface hydration effects are real but may be rather "delicate" in the sense of being highly shear rate dependent. Thus, the vicinal hydration structures envisioned in this study are notably different from the classically assumed, essentially high-energy hydration of surface charges or strongly polar surface molecules. Also, as discussed elsewhere in considerable detail, the vicinal water structures are believed to differ only slightly from the bulk structures and the difference in the energetics of the two forms of water is likely small, say ten to a few hundred cal/mole, -- in other words less (or far less) than kT at room temperature. This may in part explain why many previous investigators have failed to observe the vicinal water structures. Finally, recall the proposition stated earlier in this report: vicinal water undergoes more or less abrupt changes with temperature at a number of critical temperatures ranges, T_k (for instance near 14 - 16, 29 - 32 and 44 - 46 °C). Conversely, if anomalies are observed at any one of these temperatures (or especially at two or more of these critical temperature ranges) it suggests that vicinal water is likely present and influences the overall properties of the system.

Author's question to readers with exceptionally good eyesight: does anyone ever read these reports? or are we just spinning our wheels? Please advise me if you are reading this report, - especially if you might have an interest in our work..

We have carried out particles size measurements on some well-defined, rigid spherical particles by means of a Coulter Counter particle size analyzer based on a Photon Correlation Spectrometric (PCS) method. The particles were submicron-sized polystyrene (PS) spheres in pure water and measurements were made of the apparent particle sizes as a function of temperature.

Suspensions were prepared from PS sphere suspensions as obtained from Bangs Laboratories, Inc.. Nominal diameters for these particles were 0.170 and 0.50 microns. Suspensions of approx. 0.1 % were prepared and placed in plastic cuvettes (1 cm path length) and the cuvettes placed in the Coulter Co. Particle Size Analyzer (Model CN4 SD). A scan was made and the temperature of the sample holder increased to the next higher temperature wanted; a period of 2 min was allowed to elapse after reaching the new temperature before a subsequent run was initiated (to insure thermal equilibrium.) Note that in all of these runs measurements were made only with increasing temperatures. Note also, the samples were NOT stirred (or otherwise "disturbed" mechanically) during the whole measuring sequence. Some typical results are shown in Figs. 28 and 29.

The data for the apparent particle diameters are highly unusual and likely very significant. The measured particle diameters, for temperatures below about 30° - 32 °C, are about 30 % larger than the nominal, solid diameters. Above the transition temperature the apparent diameters decrease abruptly by about 60 nm (or 600 Å). We propose that the observed sizes reflect the actual "effective" diameters as determined by the hydrodynamics of the vicinally hydrated particles in view of the fact that the photon correlation spectroscopy actually measures the diffusion coefficient (from which in turn the apparent diameter is calculated.) The sharp drop at 30° - 32°C represents the structural transition in the vicinal hydration hull from the vicinal water structure stable below T_k to the vw structure stable above this thermal transition. The difference between the two values then leads to a minimum estimate of the thickness of the vicinal hydration hull, namely $0.5 \times 60 \text{ nm} = 30 \text{ nm} = 300 \text{ Å} = \text{approx. } 100 \text{ d[H}_2\text{O]}$ in good agreement with many other independent estimates for the thickness of the vicinal water structures. Note that these measurements were carried out with as little mechanical disturbance as possible of the particle suspensions. In a subsequent study (a continuation of the original project) we have repeated similar measurements but stirring the contents of the cuvettes with a small magnetic stirrer between each measurement (and allowing only a few minutes between consecutive scans.) In these measurements we find a distinct but less pronounced, more or less uniform decrease in apparent particle size as a function of temperature -- i.e. without an abrupt drop in the apparent diameter at T_k .

It appears from these and a considerable number of other studies in the authors Laboratory that vicinal water exhibits hysteresis: it is sensitive to the past thermal as well as mechanical history of the samples. Allowed sufficiently long times the vicinal water structures do regenerate. The time for the vicinal water to regenerate appears to depend somewhat on the specific nature of the systems studied; times of the order of hours to a day have been encountered. However, vicinal water is indeed the thermodynamically stable form of interfacial water. In view of the hysteresis mentioned above it is hardly surprising that many investigators have failed to observe any consistent behaviour of vicinal water.

Apparent Diameter (d) of PS spheres
(nominal: 500 nm) as meas. by PCS
6-29-92

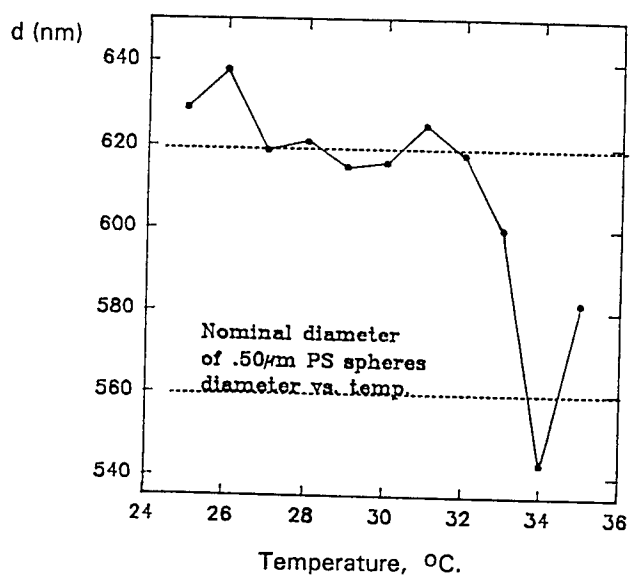


FIG. 28

Apparent Diameter (d) of PS spheres
(nominal: 500 nm) as meas. by PCS
6-22-92

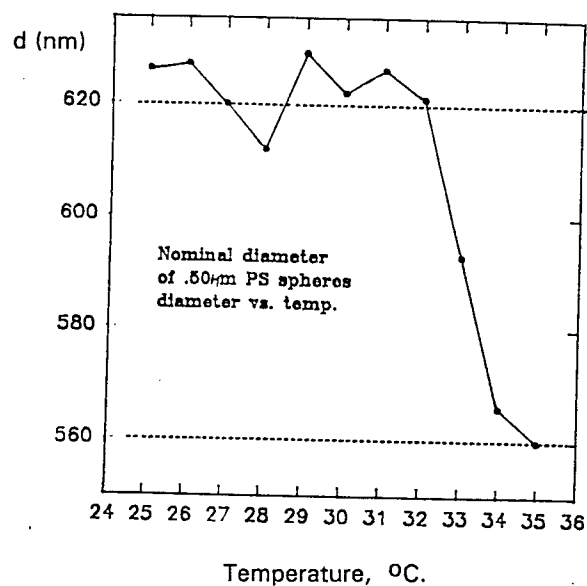


FIG. 29

SUMMARY AND CONCLUSIONS.

The viscosity measurement on aqueous polymer solutions have shown that:

A) Anomalies occur in the viscosity of aqueous polymer solutions at the thermal anomaly temperatures (T_K) of vicinal water. This has been observed with both PEO, Polyvinyl pyrrolidone and Dextran solutions, at least for polymers above a certain critical Molecular Weight (about 1000 Dalton.) This suggests that polymers in aqueous solution are vicinally hydrated, akin to the vicinal hydration structures at the solid/water interface.

The above conclusions agree with thermal anomalies previously reported in the literature from rheological data on both aqueous solutions and polymer gels (for instance gels made of fish meal, etc., i.e. primarily concentrated protein systems.)

B) Measurements of the temperature dependence of viscous flow of PEO solutions have yielded apparent Energies of Activation (ΔE^\ddagger) for viscous flow of these solutions. When plotted against the MW of the polymer, ΔE^\ddagger is found to change rather abruptly for MW of the order of 1000 Dalton -- in agreement with our earlier expectations based on published data in the literature.

C) Based on the above observations, together with various reports in the literature, we are lead to the conclusion that most (or all) macro-molecules in aqueous solutions are vicinally hydrated. Such vicinal hydration must significantly influence the intracellular phase of all living cells, and -- in the context of the present study -- very likely affect the volume (and possibly the shape) as well as the tendency to aggregate of all erythrocytes. Thus the ESR must be expected to reflect the structural properties of vicinal water -- as we have indeed observed in our in-vitro studies of the hindered settling of red cells in whole blood.

Our measurements of particles sizes have shown that:

D) Well-defined, monodisperse solid Polystyrene spheres have apparent radii far larger the nominal, solid-sphere diameters of the particles, *when measured with a Photon Correlation Spectrometer* (Coulter Co., Model CN4 SD). We believe these larger, apparent diameters reflect the vicinal hydration hulls of the particles. It is hard to overestimate the significance of this finding: if vicinal hydration occurs to such an extent, then rates of diffusion of the particles must be notably affected and "classical" estimates of diffusion coefficients/particle sizes will likely be in error!

E) The apparent, enhanced particle diameters are highly temperature sensitive. Thus upon heating, for instance, from 25 °C to 37 °C, the observed, apparent particle diameters appear to decrease abruptly near 30 - 32°C, suggesting that the observed diameters are indeed those determined by the vicinal hydration hulls of the PS spheres. We propose, if only tentatively, that *erythrocytes may likewise be vicinally hydrated*.

F) At higher temperatures, say from 40 ° to 50 °C the behaviour of the PS spheres are more complicated. In these cases, *increases* in the apparent diameters are usually observed but NOT necessarily right at T_k for the third, vicinal water transition at 44 - 46°C.

G) If one accepts as real the apparent, observed effective diameters of the PS spheres, the change in the effective thickness of the vicinal hydration hull around 30 - 32 °C amounts to about $0.5 \times 60 \text{ nm}$ or 300 Å. Such a distance is indeed in good agreement with the order of magnitude estimates for the effective thickness of vicinal water obtained by a variety of other methods.

In Summary: all our results continue to support the idea that interfacial water is restructured at solid interfaces and that the depth of the "vicinal" layers [of the order of a hundred Angstrom - or more] far exceeds more classical estimates (of only one or a few molecular layers of water.) In addition to finding vicinal water at the solid/water interface we now also observe vicinal hydration of macromolecules in solution, at least for sufficiently large polymers. Our results suggest that the critical minimum size above which vicinal hydration occurs is about 1 kDalton.

The findings summarized above have a direct bearing on the ultimate objective of our research, namely providing a molecular basis for hemorheology [and, in turn, hemodynamics.] The vicinal hydration of "solid" surfaces must affect the multitude of internal membrane surfaces of the erythrocytes; in addition, all the larger macromolecules present in the erythrocyte -- as well as in the plasma -- now also appear to be vicinally hydrated. No wonder then that red cell volumes reflect the presence of vicinal water, for instance by abrupt changes at 45 °C (and to a lesser degree near 30 °C.). Furthermore, the surfaces of erythrocytes are likely vicinally hydrated and this must affect such processes as diffusion rates of the cells; extent and dynamics of surface adsorption of proteins and tendency to rouleaux formation. Finally, if indeed all polymers in aqueous solution are vicinally hydrated, then one must expect the macromolecules in the plasma (and serum) to be similarly hydrated and in turn influence the rheological behavior. Strong evidence for this has been obtained independently in our viscosity data on both plasma and serum.

ACKNOWLEDGEMENTS

The author gratefully acknowledges the US Air Force (AFOSR and RDL) for the award of a Research Initiation Grant making possible this study, and Col. J.H. Cissik and Lt. Col. W. R. Patterson of the Clinical Investigation Directorate (Wilford Hall Medical Center at Lackland AFB) for their longstanding help, encouragement and logistical support. The author also gratefully acknowledges the expert assistance of Mr. Franklin K. Vought in the Laboratory for Water Research who has been responsible for most of the Laboratory operations during the Contract Period and particularly the viscosity measurements. Thanks also go to Mr. Shahram Shahmohamady for his extensive particle size measurements with the Coulter Particle Size Analyzer.

GENERAL REFERENCES

Braun, C.V. and W. Drost-Hansen. A DSC study of the heat capacity of vicinal water. In: *Colloid and Interface Science. Vol. III*, edited by M. Kerker, New York: Academic Press, 1976, pp

- 1) Drost-Hansen, W. and H.W. Neill, Temperature anomalies in the properties of liquid water. *Physical Reviews (Abstract)*, 100: p. 1600, 1955.
- 2) Drost-Hansen, W. Temperature anomalies and biological temperature optima in the process of evolution. *Naturwissenschaften*, 43: 512, 1956.
- 3) Drost-Hansen, W. The effects on biological systems of higher-order phase transitions in water. *New York Academy of Sciences, Annals*, 125, Art. 2.: 471 - 501, 1965.
- 4) Drost-Hansen, W. Structure of water near solid interfaces.. *Industrial and Engineering Chemistry*, 61(11): 10 - 47, 1969.
- 5) Drost-Hansen, W. Thermal anomalies in aqueous systems -- manifestations of interfacial phenomena. *Chem. Physics Letters*, 2: 647 - 652, 1969.
- 6) Drost-Hansen, W. Structure and properties of water at biological interfaces. In: *Chemistry of the Cell Interface*, edited by H.D. Brown. New York: Academic Press, 1971, pp. 1 - 184.
- 7) Drost-Hansen, W. Role of water structure in cell-wall interactions. *Federation Proceedings*, 20(5): 1539 - 1548, 1971.
- 8) Drost-Hansen, W. Effects of pressure on the structure of water in various aqueous systems. In: *Symposia of the Soc. for Exp. Biology, Nr. XXVI The Effects of Pressure on Organisms*. 1972, pp 61 - 101.
- 9) Drost-Hansen, W. Phase transitions in biological systems: manifestations of cooperative processes in vicinal water. *Annals N.Y.Acad. Sci.*, 204: 100 - 112, 1973.
- 10) Drost-Hansen, W. Thermal aspects of aquatic chemistry. Part. 2. In: *Senate Committee Print, 93d Congress, 1st session: Effects and Methods of Control of Thermal Discharges*, Serial 93-14, U.S Government Printing Office, Washington, 1973. pp. 999 - 1139.
- 11) Drost-Hansen, W. Structure and functional aspects of interfacial (vicinal) water as related to membrane and cellular systems. In: *Colloques internationaux du CNRS. No. 246 -L'eau et les Systemes Biologiques.*, 1976, pp 177 - 186.
- 12) Drost-Hansen, W. The nature and role of interfacial water in porous media. Preprint in: *Symposium on Advances in Petroleum Recovery; Division of Petroleum Chemistry. ACS New York Meeting*. 21(2): 278 - 280, 1976.
- 13) Drost-Hansen, W. Water at biological interfaces - Structural and functional aspects. *Physics and Chemistry of Liquids*, 7: 243 - 348, 1978.
- 14) Drost-Hansen, W. Gradient device for the study of temperature effects on biological systems. *J. Washington Academy of Science*, 71(4), 187 - 201, 1981.
- 15) Drost-Hansen, W. The occurrence and extent of vicinal water. In: *Biophysics of Water*, edited by F. Franks and S. Mathias. Chichester: John Wiley and Sons. 1982, pp 163 - 169.

- 16) Drost-Hansen, W. Role of vicinal water in cellular evolution. In: *Water and Ions in Biological Systems*, edited by A. Pullman, V. Vasilescu and L. Packer. New York: Plenum Press, 1985, pp. 523 - 534.
- 17) Drost-Hansen, W. Anomalous volume properties of vicinal water and some recent thermodynamic (DSC) measurements relevant to cell physiology. In: *Water and Ions in Biological Systems*, edited by A. Pullman, V. Vasilescu and L. Packer. New York: Plenum Press, 1985, pp 289 - 294.
- 18) Drost-Hansen, W., C.V. Braun Jr., R. Hochstim and G.W. Crowther. High-precision dilatometry on aqueous systems: Volume contraction upon settling. In: *Particulate and Multiphase Processes*, edited by T. Ariman and T.N. Veziroglu. Vol. 3. Washington DC: Hemisphere Publishing Co., 1987, pp 111 - 124.
- 19) Drost-Hansen, W. and J. Lin Singleton. Our aqueous heritage: Evidence for vicinal water in cells [Chapter 5] In: *Fundamentals of Medical Cell Biology*, Vol. 3A, edited by E.E. Bittar. Greenwich, Conn.: JAI Press, Inc., 1992, pp. 157 - 180.
- 20) Drost-Hansen, W. and J. Lin Singleton. Our aqueous heritage: Role of vicinal water in cells. [Chapter 6] In: *Fundamentals of Medical Cell Biology*, Vol. 3A, edited by E.E. Bittar. Greenwich, Conn.: JAI Press, Inc., 1992, pp. 181 - 202.

Etzler, F.M. and W. Drost-Hansen. A biophysical role for vicinal water in seed germination. In: *Colloid and Interface Science, Vol. III*, edited by Milton Kerker, New York: Academic Press Inc. 1976, pp 517 - 531.

Etzler, F.M. and W. Drost-Hansen. A role for water in biological rate processes. In: *Cell-Associated Water*, edited by W. Drost-Hansen and J.S. Clegg. New York: Academic Press, 1979, pp. 125 - 164.

Etzler, F.M. and W. Drost-Hansen. A role for vicinal water in growth, metabolism and cellular organization. *Adv. in Chemistry*, (Am Chem. Soc). 188: 485-497, 1980.

Etzler, F.M. and W. Drost-Hansen. Recent thermodynamic data on vicinal water and a model for their interpretation. *Croatica Chemica Acta*, 56(4): 563 - 592, 1983.

Schufle, J.A., C-T. Huang and W. Drost-Hansen. Temperature dependence of surface conductance and a model of vicinal (interfacial) water. *J. Colloid and Interface Science*, 54(2): 184 - 202, 1976

SPECIFIC REFERENCES.

Adlfinger, K.H. and G. Peschel. *Ber. Bunsenges., Physik. Chem.*, 74: 347, 1970. See also: *Z. Physik. Chem. (N.F.)* 70: 151, 1970.

Alpers, W. and H. Huhnerfuss. Molecular aspects of the system water/monomolecular surface film and the occurrence of a new anomalous dispersion region at 1.43 GHz. *J. Phys. Chem.*, 87: 525 - 5258, 1983.

Antonsen, K.P. and Allan S. Hoffman. Water structure of PEG solutions by differential scanning calorimetry measurements. In: *Poly(ethylene Glycol) Chemistry: Biotechnical and Biomedical Applications*. Edited by J. Milton Harris. New York: Plenum Press, 1992, pp 15 - 28.

Bailey, F.E. Jr. and J.V. Koleske. *Poly(ethylene oxide)*. New York: Academic Press, 1976.

Batchelor, G.K. Sedimentation in a dilute dispersion of spheres. *Fluid Mechanics*, 52: 245 - 268, 1972.

Bayer, E. and W. Rapp. Polystyrene-immobilized peptide synthesis, immunology, and chromatography. In: *Poly(ethylene Glycol) Chemistry: Biotechnical and Biomedical Applications*. Edited by J. Milton Harris. New York: Plenum Press, 1992, pp 325 - 345.

Berteaud, A.J. and W. Drost-Hansen. Studies of vicinal water structuring in suspensions. III. Dielectric loss properties at 5 GHz. In: *The Mechanisms of Microwave Biological Effects*, Report on Workshop, University of Maryland, edited by L.S. Taylor and A.Y. Cheung. 1979, paper 10.

Churaev, N.V. and B. V. Deryaguin. Inclusion of structural forces in the theory of stability of colloids and thin films. *J. Colloid and Interface Science*, 103(2): 542 - 553, 1985.

Clegg, J.S. Metabolism and the intracellular environment: the vicinal-water network model. In: *Cell-Associated Water*, edited by W. Drost-Hansen and J.S. Clegg; New York: Academic Press, 1979, pp 364 - 412.

Clegg, J.S. Alternative views on the role of water in cell functioning. In: *Biophysics of Water*, edited by F. Franks and S. Mathias, New York: Wiley and Sons, 1982, pp 365 - 383.

Clegg, J.S. Intracellular water and the cytomatrix: some methods of study and current views. *J. Cell Biology*, 99(1): 167s - 171s, 1984 (ref. A)

Clegg, J.S. Properties and metabolism of the aqueous cytoplasm and its boundaries. *Am. J. of Physiology*, 246: R133 - R151, 1984 (ref. B)

Clegg, J.S. Contrasting views on the organization of cytoplasm. In: *The State of Water in the Cell*, edited by W. Negendank and L. Edelman; Chicago, Ill.: Scanning Microscopy International, pp 105 - 114, 1988

Clegg, J.S. and W. Drost-Hansen. On the biochemistry and cell physiology of water. In: *Biochemistry and molecular biology of fishes, 1. Phylogenetic and Biochemical Perspectives*, edited by P.W. Hochachka and T.P. Mommsen. Amsterdam: Elsevier, 1991, pp. 1 - 23.

- Deryaguin, B.V. and Churaev, N.V. Properties of water layers adjacent to interfaces. In: *Fluid Interfacial Phenomena*, edited by C.A. Croxton,, New York: John Wiley and Sons, 1986, pp 663 - 738.
- Deryaguin, B.V. Modern state of the investigation of long-range surface forces. *Langmuir*, 3(5): 601 - 606, 1987.
- Deryaguin, B.V., N.V. Churaev and V.M. Muller. *Surface Forces*. Translated from Russian to English by V.I. Kisin [edited by J.A. Kitchener.] New York: Consultants Bureau, 1987. 440 pages
- Deryaguin, B.V. and N.V. Churaev. Structure of water in thin layers. *Langmuir*, 3: 607 - 612, 1987
- Dintenfass, L. *Hyperviscosity in Hypertension*. Sydney: Pergamon Press, 1981, pp 250
- Etzler, F.M. and D.M. Fagundus. The density of water and some other solvents in narrow pores. *J. Colloid and Interface Science*, 93: 585 - 588, 1983
- Etzler, F.M. A statistical thermodynamic model for water near solid interfaces. *J. Coll. & Interface Science*, 92: 43 - 56, 1983.
- Etzler, F.M. and T.L. Liles. Ion selectivity by solvents in narrow pore: Physical and biophysical significance. *Langmuir*, 2: 797 - 800, 1986.
- Etzler, F.M. and D.M. Liles. The extent of vicinal water. *J. Colloid and Interface Science*, 115(2): 513 - 519, 1987.
- Etzler, F.M. and P.J. White. The heat capacity of water in silica pores. *J. Colloid & Interface Science*, 120(1): 94 - 99, 1987.
- Etzler, F.M. Enhancement of hydrogen bonding in vicinal water: Heat capacity of water and deuterium oxide in silica pores. *Langmuir*, 4: 877 - 883, 1988.
- Etzler, F.M. and J.J. Connors. Temperature dependence of the heat capacity of water in small pores. *Langmuir*, 6: 1250 - 1253, 1990
- Etzler, F.M., R.A. Halcomb and R. Ross. A statistical approach for understanding the structure of liquid water. *Physica A*, 172: 161 - 173, 1991
- Etzler, F.M. and J.J. Connors. Structural transitions in vicinal water: Pore size and temperature dependence of the heat capacity of water in small pores. *Langmuir*, 7: 2293 - 2297, 1991.
- Gekko, K. and H. Noguchi. Physicochemical studies of oligodextran. I. Molecular weight dependence of intrinsic viscosity, partial specific compressibility and hydrated water. *Biopolymers*, 10: 1513 - 1524, 1971.
- Gericke, A. and H. Hühnerfuss. Thermal anomalies of the surface potential induced by monomolecular surface films. *J. Colloid and Interface Science*, 131(2): 588 - 591, 1989.
- Hamann, D.D. See: Montejano et al., 1983
- Happel, J. and H. Brenner. *Low Reynolds Number Hydrodynamics*. Leyden: Nordhoff International Publishing, 1973, 553 pages.
- Hühnerfuss, H. Molecular aspects of organic films on marine water and the modification of water waves. *La Chimica L'Industria* 65: 97 -101, 1983.
- Hühnerfuss, H. and W. Wolfgang. The thermal anomaly of relaxation effects in monomolecular surface films. *J. Coll. and Interface Sci.* 107: 476 - 480, 1983

Hurtado, R.M. and W. Drost-Hansen. Ionic selectivities of vicinal water in the pores of a silica gel. In: *Cell-Associated Water*, edited by W. Drost-Hansen and J.S. Clegg. New York: Academic Press, 1979, pp. 115 - 123.

Israelachvili, J. and G.E. Adams. Measurement of forces between two mica surfaces in aqueous electrolyte solutions in the range of 0 - 100 nm. *J. Chem. Soc.* 74: 975 - 1001, 1977

Israelachvili, J. and H.K. Christenson. Liquid structure and short-range forces between surfaces in liquids. *Physica*, 140A: 278 - 284, 1986.

Israelachvili, J. Hydrophobic interactions. In: *Physics of Complex and Supramolecular Liquids*", edited by S.A. Safran and N.A. Clark, New York: Wiley and Sons. 1987, pp 101 - 114.

Israelachvili, J. Solvation forces and liquid structure, as probed by direct force measurements. *Accounts of Chem Res.* 20: 415 - 421, 1987.

Israelachvili, J. and H. Wennerstrom. Entropic forces between amphiphilic surfaces in liquids. *J. Phys. Chem.* 96: 520 - 531, 1992.

Korson, L, F. J. Millero and W. Drost-Hansen. Viscosity of water at various temperatures. *J. Phys. Chem.* 73: 34 - 38, 1969.

Kurihara, K. and T. Kunitake. Submicron-range attraction between hydrophobic surfaces of monolayer-modified mica in water. *J.A.C.S.* 114: 10927 - 10933, 1992.

Low: see Viani, B.E., P.F. Low and C.B. Roth. Direct measurement of the relation between interlayer force and interlayer distance in the swelling of montmorillonite. *J. Colloid and Interface Science*, 96: 229 - 234 , 1983

Low, P.F. Nature and properties of water in montmorillonite-water systems. *Soil Sci. Soc. Amer.J.* 43: 651 - 658, 1979.

Lowe, G. D.O. Blood viscosity and cardiovascular disease. *Thrombosis and Hemostasis*, 67(5): 494 - 498, 1992.

Mastro, A.M. and D.J Hurley. Diffusion of small molecule in the aqueous compartment of mammalian cells. In: *The Organization of Cell Metabolism*, edited by G.R. Welch and J.S. Clegg. New York: Plenum Press, 1986, pp 57 - 74.

Montejano, J.G., D.D. Hamann and T.C. Lanier. Final strength and rheological changes during processing of thermally induced fish muscle gels. *J. of Rheology*, 27(6): 557 - 579, 1983.

Nir, S. and W.D. Stein. Two modes of diffusion. *J.Chem. Phys.*, 55: 1598 - 1603, 1971.

Parsegian, V. A. and coworkers: see, for instance, D.M. LeNeveu, P.R. Rand and V.A. Parsegian. Measurement of forces between lecithin bilayers. *Nature*, 259, 601 - 603, 1976. D.M. LeNeveu, R.P. Rand, V.A. Parsegian and D. Gingell. Measurements and modification of forces between lecithin bilayers. *Biophysical J.*, 18: 209 - 230, 1984. V.A. Parsegian, D. Rau and J. Zimmerberg. Structural transitions induced by osmotic stress. In: *Membranes, Metabolism, and Dry Organisms*, edited by A. C. Leopold, Ithaca: Comstock Publishing Associates, 1986, p. 306 - 317. R.P. Rand and V.A. Parsegian. Hydration forces between phospholipid bilayers. *BBA*, 988: 351 - 376, 1989. V.A. Parsegian, R.P. Rand and D. C. Rau. Swelling from the perspective of molecular assemblies and single functioning

biomolecules. In: *Mechanics of Swelling*, edited by T.K. Karalis, NATO ASI Series, Vol. H 64, Berlin: Springer Verlag, 1992, p 623 - 647, 1992. D.C. Rau and V.A. Parsegian. Direct measurement of the intermolecular forces between counterion-condensed DNA double helices. *Biophysical J.*, 61, 246 - 259, 1992. See also: *ibid*: p 260 - 271. K. Gawrisch, D. Ruston, J. Zimmerberg, V.A. Parsegian, R.P. Rand and N. Fuller. Membrane dipole potentials, hydration forces, and the ordering of water at membrane surfaces.. *Biophysical J.*, 61: 1213 - 1223, 1992. M. F. Colombo, D.C. Rau and V. A. Parsegian. Protein solvation in allosteric regulation: a water effect on hemoglobin. *Science*, 256, 655 - 659, 1992.

Peschel, G. and K.H. Adlfinger. Temperaturabhängigkeit der Viskosität sehr dünner Wasserschichten zwischen Quarzglasoberflächen. *Naturwissenschaften*, 56(11): 558 - 559, 1969. See also: Peschel, G. and K.H. Adlfinger. *J. Coll. Interface Sci.* 25: 131, 1970

Peschel, G. and K.H. Adlfinger. Viscosity anomalies in liquid surface zones. IV. The apparent viscosity of water in thin layers adjacent to hydroxylated fused silica surfaces. *J. Colloid and Interface Science.* 34(4): 505 - 510, 1970.

Peschel, G. and K.H. Adlfinger. Thermodynamic investigations of thin liquid layers between solid surfaces. II. Water between entirely hydroxylated fused silica surfaces. *Zeit. Naturforschung*, 26a: 707 - 715, 1971.

Peschel, G. and P. Belouschek. The problem of water structure in biological systems. In: *Cell-Associated Water*, edited by W. Drost-Hansen and J.S. Clegg. New York: Academic Press, 1979, pp. 3 - 52.

Peschel, G. and U. Furchtbar. Thermal anomalies in the DSC-diagrams of a highly disperse silicic acid wetted by different aqueous solutions. *Prog. Colloid Polym Sci.*, 83: 216 - 221, 1990.

Szent-Györgyi, A. Biology and the pathology of water. *Perspectives. Biol. Med.*, 13: 239, 1971.

van Oss, C.J. Interaction forces between biological and other polar entities in water: how many different primary forces are there? *J. Dispersion Sci. & Tech.*, 12(2): 201 - 219, 1991.

van Oss, C.J. Hydration forces. In: *Water and Biological Macromolecules*, edited by E. Westhof,, London: Macmillan Press, Ltd., in press.

Wiggins, P.M. Ionic partitioning between surface and bulk water in a silica gel. *Biophysics J.*, 13: 385 - 397, 1973.

Wiggins, P.M. Thermal anomalies in ion distribution in rat kidney slices and in a model system. *Clinical and Experimental Pharmacology and Physiology*, 2: 171 - 176, 1975.

Wiggins, P.M. Metabolic control of the properties of intracellular water as a universal driving force for active transport. In: *Cell-Associated Water*, edited by W. Drost-Hansen and J.S. Clegg. New York: Academic Press, 1979, pp. 69 - 114.

Wu, M.C., T.C. Lanier, and D.D. Hamann. Rigidity and viscosity changes of croaker actomyosin during thermal gelation. *J. Food Science*, 50(1): 14 - 19, 1985

Yanagimachi, M. N. Tamai and H. Masuhara. *Chem. Phys. Letters* 201: 115 - 119, 1993.

AIR FORCE REPORTS

The three reports to the US Air Force, listed below, summarizes the research done during three summers at the Clinical Investigation Directorate at Wilford Hall Medical Center, Lackland AFB, San Antonio, Texas.

Drost-Hansen, W. (with J.P. Lafferty IV.) Temperature effects on erythrocyte sedimentation rates in whole blood and on erythrocyte and platelet volumes. *Final Report, 1989 USAF-UES Summer Faculty Research Program*, 1989, 28 pages.

Drost-Hansen, W. (with R.R. McNeer) Temperature effects on erythrocyte sedimentation rates, cell volumes and viscosities in mammalian blood. *Final Report, 1991 USAF-RDL Summer Faculty Research Program*, 1991, 29 pages.

Drost-Hansen, W. (with J.L. Camacho.) Temperature effects on aq. polymer and biopolymer solution viscosities, and erythrocyte sedimentation rates and cell volumes in mammalian blood. *Final Report, 1992 USAF-RDL Summer Faculty Research Program*, 1992. 19 pages.